

Deposition of Droplets onto Solid Objects in Aerosol Flow

by

Bojan Petkovic

B.Sc., University of Novi Sad, Serbia, 2004

A THESIS SUBMITTED IN PARTIAL FULFILLMENT OF THE
REQUIREMENTS FOR THE DEGREE OF
MASTER OF APPLIED SCIENCE

in

THE FACULTY OF GRADUATE STUDIES
(Chemical and Biological Engineering)

THE UNIVERSITY OF BRITISH COLUMBIA
(Vancouver)

February 2010

© Bojan Petkovic, 2010

Abstract

In this work, the effect of velocity on deposition coefficients and capture efficiencies on a circular disk, placed normal to an aerosol flow was investigated. The superficial gas velocity was varied in the range of 0.1 m/s to 1.5 m/s, while the volume median diameter of the droplet size distribution varied between 3.9 and 7.5 microns. The morphology and distribution of deposits on the upstream and downstream surface of the disk were observed and measured. The effect of contact angles (20°, 51°, 94°) on deposition, and dry vs. wet surface effects were also investigated.

It was found that in the range of velocity and droplet sizes investigated, deposition on the upstream side was dominated by the inertial impaction mechanism. Capture efficiencies increased with velocity and droplet size, and could be explained by the inertial impaction mechanism from the upward flow, using the potential flow approximation. For the downstream side, capture efficiencies increased with droplet size and showed a minimum with velocity. It is postulated that the governing deposition mechanism for the downstream side is the inertial impaction mechanism with gravity in the flow direction.

On the upstream side, it was found that deposits were concentrated closer to the coupon edge, while on the downstream side, the distribution of deposits on the surface was uniform.

In the range of investigated contact angles, there was no significant difference observed between the deposition rates. The same can be said for the effect of dry vs. wet coupon surface.

Table of Contents

Abstract.....	ii
Table of Contents.....	iii
List of Tables.....	viii
List of Figures.....	xi
Nomenclature.....	xviii
Acknowledgments.....	xxvii
Chapter 1. Introduction.....	1
1.1. Bitumen upgrading and the Fluid Coker.....	2
1.2. Fouling in the Scrubber section of the Fluid Coker.....	4
1.3. Project objectives.....	5
1.4. Scope of the thesis.....	7
Chapter 2. Theory and Literature Review.....	8
2.1. Particle deposition from turbulent flow parallel to solid surfaces.....	8
2.2. Particle deposition from the flow around bluff bodies and surfaces.....	11
2.2.1. Upstream (front) side.....	13
2.2.2. Downstream (back) side.....	16
2.3. Distribution of deposits along the coupon radius.....	18
2.4. Contact angle effect.....	19
2.4.1. Wetting and contact angles.....	20
2.4.2. Impact of droplets on the solid surface (sticking vs. rebounding).....	22
2.4.3. Superoleophobicity.....	25
Chapter 3. Modeling.....	27
3.1. Particle deposition on the upstream and downstream side.....	27
3.2. Gas phase flow.....	29
3.2.1. Continuity and momentum conservation equations.....	29
3.2.2. Potential flow approximation.....	30
3.2.3. Potential flow with the viscous sublayer.....	31
3.3. Inertial impaction mechanism.....	31
3.4. Particle transport due to turbulence.....	34

3.4.1. Particle transport due to convective diffusion.....	34
3.4.2. Particle transport due to turbulent diffusion in the inertial regime.....	34
3.5. Surface coverage.....	35
3.5.1. Deposition model.....	35
3.5.2. Estimation of deposition rates.....	36
3.6. Deposition coefficients.....	37
3.7. Droplet size distribution fitting.....	38
3.7. Reaction.....	39
3.8. Drop size estimation in the Hot Unit.....	41
Chapter 4. Experimental Study.....	46
4.1. Cold Unit apparatus.....	46
4.1.1. Cold Unit details.....	48
4.1.1.1. Cold Unit Setup #1 and Setup #2.....	48
4.1.1.2. Atomizers.....	49
4.1.2.3. Gas distributor.....	50
4.1.2.4. Other settings.....	51
4.2. Hot Unit apparatus.....	53
4.3. Measurement techniques.....	55
4.3.1 Liquid flow and aerosol concentration measurements.....	55
4.3.1.1. Measurements of the liquid flow to the nozzle.....	55
4.3.1.2. Measurements of the liquid flow to the aerosol.....	55
4.3.2. Velocity measurements.....	59
4.3.3. Shadowgraphy measurements of aerosol drop size distribution.....	59
4.3.3.1. Shadowgraphy setup.....	59
4.3.3.2. Aerosol sampling.....	62
4.3.3.3. Hardware and software settings.....	65
a. Shadowgraphy hardware settings.....	65
b. RS Image software settings.....	66
4.3.3.4. Sample size.....	66
4.3.3.5. Image processing and image segmentation settings.....	67
4.3.3.6. Calibrations.....	68

a. Camera view field calibration.....	68
b. Calibration of the Internal focus module.....	69
c. Depth of field calibration.....	71
4.3.3.7. Corrections.....	73
a. Border correction.....	73
b. Depth of field correction.....	74
4.3.3.8. Shadowgraphy verification.....	74
4.3.3.9. Summary procedure.....	76
4.3.3.10. Suggestions for improvements.....	77
4.4.4. Coupon drop size distribution measurements.....	77
4.4.4.1. Deposition (sampling).....	78
4.4.4.2. Recording images along the coupon radius.....	79
4.4.4.3. Image analysis in Image Pro Plus.....	80
4.3.5. Deposition rate measurements.....	82
4.3.5.1. Load cell measurements.....	82
4.3.5.2. Analytical balance measurements.....	84
4.3.6. Contact angle measurements.....	85
4.3.6.1. Measurement procedure.....	85
4.3.6.2. Accuracy of contact angle measurements.....	86
Chapter 5. Results and Discussions.....	88
5.1. Effect of velocity	89
5.1.1. Effect of velocity with 50% sugar solution	89
5.1.2. Effect of velocity with triethylene glycol.....	90
5.1.2.1. Cold Unit nozzle, Setup #1.....	90
a. Upstream side.....	92
b. Downstream side.....	93
5.1.2.2. Hot Unit nozzle, Setup #2.....	95
5.2. Effect of droplet size distribution, Cold Unit nozzle, Setup #1.....	98
5.2.1. Upstream side.....	98
5.2.2. Downstream side.....	99

5.3. Calculation of capture efficiencies and deposition coefficients for individual drop sizes from experimental results.....	100
5.3.1. Effect of drop diameter at different velocities, downstream side.....	101
5.3.2. Effect of velocity for different drop diameters, downstream side.....	104
5.4. Simulations.....	106
5.4.1. Inertial particle transport.....	106
5.4.1.1. Particle trajectories.....	106
5.4.1.2. Discussion of the model validity.....	107
a. Analytical vs. numerical solutions for Stokesian particles, and non-Stokesian vs. Stokesian particles.....	107
b. Comparison with the CFD results.....	109
c. Potential flow with patched viscous sublayer.....	110
5.4.1.3. Effect of gravity on inertial particle transport.....	111
a. Capture efficiencies vs. Stokes number.....	112
b. Capture efficiencies vs. drop diameter and velocity.....	113
5.4.2. Particle transport due to turbulence.....	115
5.5. Comparison with experimental data.....	117
5.5.1. Upstream side.....	117
5.5.2. Downstream side.....	118
5.6. Morphology of deposits and their distribution along the disk radius.....	121
5.7. Contact angle and dry vs. irrigated surface effect.....	125
Chapter 6. Application of the Results to the High Temperature Unit Conditions..	128
6.1. Estimation of droplet size distribution in the Hot Unit.....	128
6.2. Deposition coefficients for high temperature unit conditions.....	129
6.3. Comparison of results.....	131
Chapter 7. Conclusions and Recommendations.....	134
7.1. Conclusions.....	134
7.2. Recommendations.....	136
7.2.1. Recommendations for further investigations in the Cold Unit.....	136
7.2.2. Recommendations for the industrial case	137
References.....	140

Appendix A. Cold Unit Operating Procedure.....	147
Appendix B. Calibrations.....	150
B.1. Pump calibration.....	150
B.2. Rotameter calibration.....	152
B.2.1. Theoretical background.....	152
B.2.2. Experimental.....	153
B.3. Load cell calibration.....	157
Appendix C. Equations Development.....	158
C.1. Inertial particle transport from potential flow.....	158
C.1.1. Equations of particle motion.....	158
C.1.2. Flow field from potential flow approximation.....	159
C.1.3. Capture efficiencies for Stokesian particles.....	160
C.1.3.1. X-component particle trajectory.....	160
a. Conjugate complex roots ($St > 1/16$).....	161
b. Real roots ($St < 1/16$).....	162
C.1.3.2. r-component particle trajectory.....	163
C.1.3.3. Capture efficiencies.....	164
a. No gravity ($p = 0$).....	164
b. With gravity ($p=1, p=-1$).....	165
C.1.4. Capture efficiencies for non-Stokesian particles.....	166
C.1.5. Distribution of deposits along the coupon radius.....	168
C.2. Drop diameter on a surface	169
Appendix D. Software Codes.....	171
D.1. Image Pro Plus macros.....	171
D.2. MATLAB [®] codes.....	174
D.3. Mathcad code.....	191
Appendix E. Tables.....	195

List of Tables

Table 1.1 Bitumen, Synthetic crude, and Conventional crude oil properties [5].....	2
Table 2.1 Summary of experimental data and simple theoretical treatments of inertial impaction on the front side of bluff bodies.....	15
Table 2.2 Summary of experimental investigations for the downstream (back) side of bluff bodies.....	18
Table 2.3 Degree of wetting explained in terms of solid-liquid and liquid-liquid interaction.....	21
Table 2.4 Contact angles of water at 20°C with solids of different surface energies [38].....	21
Table 2.5 Possible outcomes of droplet impact on a solid surface	23
Table 3.1 Summary of mechanisms of deposition on the circular disk from an upward flow.....	29
Table 3.2 Accumulation rate and mass of deposits as a function of time.....	41
Table 4.1 Variability in liquid flow rate measurements (g/min), with aqueous sugar solution and tri-ethylene glycol, at different superficial velocities (Setup #1, Fig. 4.3).....	58
Table 4.2 Exposures (in microseconds) needed for 50% blurriness of different drop diameters and different velocities.....	62
Table 4.3 Comparison of the volume median diameter measured right after the flow is stopped and 5 seconds after the flow is stopped, at 6× magnification and 110 microseconds exposure. Velocity 1 m/s, liquid flow to nozzle 40 ml/min.....	63
Table 4.4 Comparison of the volume mean diameter measured 5 seconds after the flow is stopped and when the aerosol flows upward.....	64
Table 4.5 Terminal velocities of tri-ethylene glycol in air at room temperature and the time needed to travel 80cm in free fall.....	64

Table 4.6 Main shadowgraphy hardware settings.....	66
Table 4.7 Main RS Image software settings.....	66
Table 4.8 Effect of sample size on measured volume median diameter (Run 33).....	67
Table 4.9 Internal focus module calibration at different magnifications.....	70
Table 4.10 Main settings for the image segmentation.....	72
Table 4.11 Detection probability for different particle sizes, at 6× magnification ($W = 718\mu\text{m}$, $H = 536\mu\text{m}$).....	74
Table 4.12 Glass beads in different focus position, captured and analyzed with shadowgraphy.....	76
Table 4.13 Relevant environment settings in the Image Pro Plus for coupon deposit analysis (1–set, 0–not set).....	81
Table 4.14 Variability in contact angle measurements using the sessile drop method.....	87
Table 5.1 Properties of 50% aqueous sugar solution and triethylene glycol at 20°C.....	90
Table 5.2 Operating conditions for contact angle tests.....	125
Table 5.3 Coupon material and roughness properties at initial dep. rate tests.....	125
Table B.1 Rotameter #1 calibration data.....	154
Table B.2 Rotameter #2 calibration data.....	155
Table B.3 Rotameter #3 calibration data.....	156
Table C.1 Correction factor for different contact angles.....	170
Table E.1 Summary results for the effect of velocity, triethylene glycol, Cold Unit nozzle, Setup #1.....	195
Table E.2 Summary results for the effect of velocity, triethylene glycol, Hot Unit nozzle, Setup #2.....	196
Table E.3 Summary results for the effect of droplet size distribution, triethylene glycol, Cold Unit nozzle, Setup #1.....	198

Table E.4 Deposition coefficients for the downstream side, m/hr.....	199
Table E.5 Weight of deposits (± 0.1 mg) at the end of experiment, $m(\tau)$, mg.....	200
Table E.6 Experimental integral deposition rates, $r_{d,i}^{\text{exp}}$, mg/hr.....	200
Table E.7 Correction factors (last column) obtained from several Cold Unit runs.....	201
Table E.8 Estimated volume median diameter after evaporation.....	201
Table E.9 Estimation of deposition rates at high temperature conditions from the deposition coefficients in the Cold Unit.....	201

List of Figures

Figure 1.1 Schematic representation of the bitumen upgrading process [9].....	2
Figure 1.2 Schematic of the Syncrude Fluid Coker.....	3
Figure 1.3 Segment of the packing elements in the Scrubber Section of the Fluid Coker, (a) before start up of the reactor and (b) after reactor shutdown.....	5
Figure 1.4 Side view of the scrubber packing elements, given in Fig. 1.3. The blades are inclined at a 30° angle with the vertical axis [8].....	5
Figure 1.5 Schematic representation of the side and top view of the 5 cm diameter disk in the 7.5 cm diameter column (aerosol droplets are presented disproportionately large).....	6
Figure 2.1 Summary of experimental data on particle deposition from turbulent pipe flow, adapted from Young and Leeming [18].....	10
Figure 2.2 Experimental and theoretical data on inertial deposition onto front surfaces of disks.....	14
Figure 2.3 Schematic representation of the surface tension forces acting on a droplet deposited on the surface.....	20
Figure 2.4 Droplet on a surface in the Cassie (metastable) state, showing superhydrophobic properties, and in the Wenzel (stable) state, wetting the surface.....	23
Figure 3.1 Schematic representation of the flow field around a disk, with particle transport mechanisms.....	28
Figure 3.2 Schematics of the patched viscous sublayer, linearly increasing from $\bar{v}_r = 0$ at $\bar{x} = 0$, to $\bar{v}_r = \bar{r}$ at $\bar{x} = -0.2$	31
Figure 3.3 Schematic representation of the discrete amounts of deposits on the coupon surface. Layer 1 had more time to react than layer n and release more volatiles.....	39
Figure 4.1 Schematic of the Cold Unit Apparatus.....	47
Figure 4.2 90° and 45° elbows used for removal of large droplets.....	48

Figure 4.3 Cold Unit Setup #1 and Setup #2, used in the experiments. Setup #1 was used with the Cold Unit nozzle and the nozzle from Spraying Systems Co., while Setup #2 was used for the experiments with the Hot Unit nozzle.....	49
Figure 4.4 Cold Unit nozzle details, used in the setup with elbows (Setup #1).....	49
Figure 4.5 Hot Unit nozzle details, used in the position below the column (Setup #2).....	50
Figure 4.6 1/4QMJ + SUQR220B QuickMist™ nozzle details, used in experiments for shadowgraphy validation.....	50
Figure 4.7 Drawing and the picture of the gas distributor in the Cold Unit.....	51
Figure 4.8 Fan positioned close to the load cell to remove aerosol droplets causing load cell failures.....	52
Figure 4.9 Rod motion and deposition constraints, installed to reduce oscillations of the coupon and prevent formation of significant amount of deposits on the rod.....	52
Figure 4.10 Process flow sheet diagram of the Hot Unit Apparatus [52].....	54
Figure 4.11 Picture of the RK-75211-10 Cole Parmer Console Drive and RK-07002-27 Micropump® A-mount Suction Shoe Pump Head with its scale.....	55
Figure 4.12 Schematic representation of the tank with the liquid that is pumped to the nozzle (4 liter), and the tank for collecting the washdown (2.5 liter), placed on the balance.....	56
Figure 4.13 Log of the liquid flow to the aerosol for Run 28 (Cold Unit at 1m/s, Setup #1). Short experiments and the presence of elbows reduce accuracy of droplet flow measurements.....	57
Figure 4.14 Log of the liquid flow to the aerosol for Run 53 (Cold Unit at 1m/s, Setup #2). Straight line from long experiment results in droplet flow measurement accuracy higher than 1%.....	57
Figure 4.15 Schematic representation of the Shadowgraphy system used on the Cold Unit and the path of light rays entering and leaving the droplet.....	60

Figure 4.16 Pictures of the Shadowgraphy system installed on the Cold Unit and details of the Optem ZOOM XL long distant lenses.....	61
Figure 4.17 Schematic of the solution for eliminating glass curvature.....	61
Figure 4.18 Schematic representation of the shape and intensity of droplet shadows captured at constant aerosol velocity and increased exposure. Sharpness of the images also decreases with a decrease in shadow intensity.....	62
Figure 4.19 Calibration lines of ‘Cool Snap Pro cf camera + OPTEM Zoom 70 XL lens’ and ‘Cool Snap Pro cf camera + OLYMPUS BX41 Microscope’ systems.....	69
Figure 4.20 Camera was moved with the help of the moving stage.....	70
Figure 4.21 Traveled camera distance in X-direction vs. internal focus module position, required to bring the Objective Micrometer back in focus, 6× magnification.....	71
Figure 4.22 Schematic representation of the depth of field. For larger particles, depth of field is larger.....	71
Figure 4.23 Glass beads (3.4-16.6 μm) and Polyamid particle (26.2 μm) in the focus, used for depth of field calibration; 6× magnification.....	72
Figure 4.24 Depth of field for the shadowgraphy system, using Image Pro Plus settings given in Table 4.10.....	73
Figure 4.25 Verification of shadowgraphy with glass beads on the microscopic glass slide.....	75
Figure 4.26 Picture of the Microscope and Camera setup, used for recording images of coupon deposits.....	78
Figure 4.27 Schematic representation of: (a) glass coupon used for deposit size distribution analysis and (b) placement of the coupon in the column	79
Figure 4.28 Locations of coupon deposit samples taken from the upstream and downstream side. First image starts as the coupon centre, last image is taken at the coupon edge.....	80
Figure 4.29 Supporting stage made of glass slides	80

Figure 4.30 Schematic representation of (a) light rays that pass through the spherical cap and (b) one example of deposits on the downstream side, Run 56.....	81
Figure 4.31 Identified droplets on the upstream surface, with (a) <i>Convex Hull</i> =0 and (b) <i>Convex Hull</i> =1 option. In the second case, measured diameter is much closer to the real diameter of droplets.....	82
Figure 4.32 GSO-50 load cell and DPM-3 data logger from Transducer Techniques.....	83
Figure 4.33 Typical response of the load cell, Run 15.....	84
Figure 4.34 Photo of the sessile drop measurement system. Lenses are at 1× magnification, 90 cm away from the drops.....	85
Figure 4.35 (a) Coupon on the camera when droplets are deposited from the pipette, and (b) schematics of the coupon on the stage as in Fig. 4.34.....	86
Figure 4.36 Images of TEG droplets on different surfaces, recorded with Image Pro Plus.....	87
Figure 5.1 Aerosol concentration vs. velocity for Cold Unit nozzle and Setup #1 experiments, calculated from washdown and shadowgraphy measurements of concentration, for triethylene glycol. 95% confidence intervals are estimated from three repeated experiments.....	91
Figure 5.2 Upstream side capture efficiencies, deposition coefficients and volume median diameter vs. velocity. 95% confidence intervals are estimated from three repeated experiments.....	93
Figure 5.3 Downstream side capture efficiencies, deposition coefficients and volume median diameter vs. velocity. 95% confidence intervals are estimated from three repeated experiments.....	94
Figure 5.4 Aerosol concentration vs. velocity, for Hot Unit nozzle and Setup #2 experiments, calculated from washdown and shadowgraphy measurements of concentration. 95% confidence intervals calculated from two repeated experiments.....	96

Figure 5.5 Capture efficiencies and deposition coefficients vs. velocity for the downstream side.....	97
Figure 5.6 Capture efficiency and deposition coefficient for the upstream side vs. volume median diameter, at $U = 1$ m/s. 95% confidence interval were estimated from three repeated experiments.....	98
Figure 5.7 Capture efficiency and deposition coefficient for the downstream side vs. volume median diameter, at $U = 1$ m/s. 95% confidence intervals were estimated from three repeated experiments.....	99
Figure 5.8 Images of triethylene glycol deposits on the (a) upstream and (b) downstream surface of the glass coupon, Run 26.....	100
Figure 5.9 Measured drop size distribution in the aerosol, and on the upstream and downstream side of the glass coupon at 1 m/s, Run 26.....	101
Figure 5.10 Calculated capture efficiencies vs. drop diameter for the downstream side, at different gas velocities.....	102
Figure 5.11 Calculated deposition coefficients vs. drop diameter for the downstream side, at different gas velocities.....	103
Figure 5.12 Calculated capture efficiencies vs. velocity for the downstream side, at different drop diameters.....	104
Figure 5.13 Calculated deposition coefficients vs. velocity for the downstream side, at different drop diameters.....	105
Figure 5.14 Trajectories of (a) 10, (b) 50 and (c) 140 micron droplets (pathlines) in the potential flow field (streamlines), for the upward flow at 1 m/s superficial gas velocity, using Stokes drag force.....	107
Figure 5.15 Comparison of analytical and numerical solutions for Stokesian particles, with numerical solutions for non-Stokesian particles, for upward, horizontal and downward flow, at 1 m/s superficial gas velocity.....	109
Figure 5.16 Comparison of numerical solutions for non-Stokesian particles for upward flow, at different velocities, with the CFD results (by Lakghomi [36]).....	110

Figure 5.17 Comparison of the capture efficiencies on the upstream side from potential flow with and without viscous sublayer, for non-Stokesian particles, with CFD (Lakghomi [36]).....	111
Figure 5.18 Calculated capture efficiencies vs. Stokes number for the horizontal, upward and downward flow, at different superficial gas velocities.....	112
Figure 5.19 Capture efficiencies vs. drop diameter for (a) horizontal, (b) upward, and (c) downward flow, at different superficial gas velocities. Capture efficiencies vs. velocity for downward flow are presented in (d).....	114
Figure 5.20 Simulation of deposition by convective diffusion and turbulent inertia from the flow parallel to the coupon surface, based on modeling described in Section 3.4...	116
Figure 5.21 Comparison of the simulation and experimental results for the upstream side at 1 m/s.....	118
Figure 5.22 Axisymmetric flow pattern about a disk (adapted from Humphries and Vincent [73]).....	119
Figure 5.23 Correlation between the calculated capture efficiencies from the downward flow and experimental data. Simulation over-predicts experimental data by a factor of 2.33.....	119
Figure 5.24 Typical appearance of (a) non-uniform distribution of deposits on the upstream side, and (b) uniform distribution on the downstream side.....	121
Figure 5.25 Distribution of deposits along the coupon radius on the (a) upstream and (b) downstream side, for Run 56. Solid lines were obtained by averaging measured values from four samples.....	123
Figure 5.26 Mass distribution of deposits on the (a) upstream and (b) downstream surface of the coupon, from Runs 46–59.....	124
Figure 5.27 Experimental integral deposition rates, $r_{d,i}^{\text{exp}}$, at $U=0.7$ m/s and $U=1.0$ m/s, on different surfaces, for the upstream side (a, c) and downstream side (b, d) (Table E.6). 95% confidence intervals are estimated from 3 repeated experiments.....	126

Figure 6.1 Calculated capture efficiencies (from exp. results) for the downstream side vs. Stokes number, in the range of droplet sizes (1–20 microns) and velocities (0–1.5 m/s).....	130
Figure 6.2 Comparison between Hot Unit deposition rates for 5% MEBR, with the predictions from the Cold Unit deposition coefficients, and CFD predictions.....	132
Figure 6.3 Comparison between Hot Unit deposition rates for 10% MEBR, with the predictions from the Cold Unit deposition coefficients, and CFD predictions.....	132
Figure 6.4 Comparison between Hot Unit deposition rates for the effect of velocity, with the predictions from the Cold Unit deposition coefficients.....	133
Figure A.1 Picture of the Cold Unit apparatus.....	149
Figure B.1 Gear pump calibration curve, with and without differential pressure (200–300 kPa).....	151
Figure B.2 Schematic representation of the rotameter float.....	152
Figure B.3 Rotameter #2 calibration setup. Rotameter #2 (A) is connected in series with the rotameter with the calibration curve from the manufacturer (B).....	153
Figure B.4 Calibration curve for the second GSO-50 load cell used. The curve is approximately linear and it can be seen that, in this case, true values are about 11% larger than measured.....	157
Figure C.1 Schematic representation of the flow field in front of the disk and fluid velocity components.....	158
Figure C.2 Schematic representation of limiting droplet trajectories and the way that capture efficiencies for disk are obtained.....	165
Figure C.3 Spherical cap model for droplets deposited on the coupon surface.....	169

Nomenclature

A	Upstream or downstream coupon (disk) surface area, $A = D_c^2 \pi / 4$, m^2
A_{column}	Column cross section area, m^2
A_{dry}	Dry coupon (disk) surface area, upstream or downstream, m^2
A_{an}	Annular area between the rotameter float and the rotameter tube, m^2
A_{tube}	Cross section area of the rotameter tube, m^2
A_{wet}	Wet coupon (disk) surface area, upstream or downstream, m^2
Br	Blockage ratio, $Br = A/A_{column}$, <i>dimensionless</i>
c_b	Aerosol concentration in the bulk, kg/m^3
C_c	Cunningham slip correction factor, <i>dimensionless</i>
C_p	Heat capacity, $J \cdot kg^{-1} K^{-1}$
c_{wake}	Aerosol concentration in the wake, kg/m^3
d	Characteristic length (total disk surface area divided by the perimeter of a disk, $D_c/2$), m
D	Brownian diffusivity, m^2/s
D_c	Coupon (disk) diameter, m
D_{min}	Minimum drop diameter, m
D_{max}	Maximum drop diameter, m
D_p	Particle (droplet) diameter, m
$D_{p,eq}$	Equivalent diameter for a given drop size distribution that has the same specific mass, m_s , as that size distribution, m

D_p'	Particle (droplet) diameter on a surface, having diameter D_p in the aerosol, $D_p' = k(\theta) \cdot D_p, m$
$D_{p,i}$	Drop diameter of the class i in the aerosol, m
$D_{p,max}$	Drop diameter of the last (maximum) class in the aerosol, m
$D_{p,reference}$	Reference particle (droplet) diameter, m
$D_{V,10}$	10% volume diameter, m
$D_{V,50}$	Volume median diameter, same as VMD , m
$\bar{D}_{V,50}$	Average volume median diameter, m
$D_{V,90}$	90% volume diameter, m
E	Capture efficiency, <i>dimensionless</i>
E_a	Activation energy, J/mol
$E_{i,downstream}$	Capture efficiency of the class i , for the downstream side, m/s
$E_{i,upstream}$	Capture efficiency of the class i , for the upstream side, m/s
F	Force, N
$F_{a,nozzle}$	Volumetric flow rate of air to the nozzle, at pressure p_{nozzle} , m^3/s
$F_{a,secondary}$	Volumetric flow rate of secondary air to the gas distributor, at pressure $p_{secondary}$, m^3/s
F_l	Droplet (liquid) flow rate to the aerosol, kg/s
g	Gravity acceleration, $g=9.81, m/s^2$
i_{max}	Largest diameter class in the distribution, <i>dimensionless</i>
h	Height of air annulus (in the nozzle), cm
H_f	Residence time of inertialess particles, <i>dimensionless</i>
H_p	Residence time of particles with inertia, <i>dimensionless</i>

k	Correction factor for the drop size estimated by correlation, <i>dimensionless</i>
$k(\theta)$	Drop diameter correction factor, for a drop sitting on a surface, <i>dimensionless</i>
k_B	Boltzmann's constant, $k_B = 1.386 \cdot 10^{-23}$, $kg \cdot m^2 \cdot s^{-2} \cdot K^{-1}$
k_d	Particle (droplet) deposition coefficient (velocity), <i>m/s</i>
$k_{i,downstream}$	Particle (droplet) deposition coefficient of the class i , for the downstream side, <i>m/s</i>
$k_{i,upstream}$	Particle (droplet) deposition coefficient of the class i , for the upstream side, <i>m/s</i>
k_m	Mass transfer coefficient, <i>m/s</i>
k_r	First-order reaction constant, s^{-1}
$k_{r,0}$	Pre-exponential factor for the first order reaction constant, s^{-1}
k_s	Deposition constant, $k_s = r_{d,1} / (m_s A)$, s^{-1}
k_t	Particle (droplet) transport coefficient, <i>m/s</i>
k_t^+	Nondimensional particle (droplet) transport coefficient, <i>dimensionless</i>
L	Plate (surface) length, <i>m</i>
m	Mass of deposits, <i>kg</i>
M	Mass of the rotameter float, <i>kg</i>
\dot{M}_g	Mass flow rate of a gas (in the nozzle), <i>g/s</i>
m_i	Mass of deposits in the i -th layer, <i>kg</i>
$m_{i,0}$	Mass of the freshly deposited i -th layer, <i>kg</i>
$m_{i,f}$	Mass of the i -th layer at the end of reaction ($t=\infty$), <i>kg</i>

\dot{M}_l	Mass flow rate of a liquid (in the nozzle), <i>g/s</i>
m_s	Specific mass of a droplet sitting on a surface, <i>kg/m²</i>
M_w	Molar mass of the gas, <i>kg/mol</i>
MCR	Micro Carbon Residue, <i>dimensionless</i>
N_i	Number of particles (droplets) in the class <i>i</i> , <i>dimensionless</i>
N'	Statistically corrected number of particles, <i>dimensionless</i>
p	Gravity orientation parameter $\{-1, 0, 1\}$, <i>dimensionless</i>
P	Pressure, <i>Pa</i>
P_0	Atmospheric pressure, $P_0 = 101\ 325\ Pa$
p_i	Total detection probability, <i>dimensionless</i>
$p_{i,Border}$	Detection probability due to the border correction, <i>dimensionless</i>
$p_{i,DOF}$	Detection probability due to the depth of field correction, <i>dimensionless</i>
P_{nozzle}	Pressure of the air in the nozzle, <i>Pa</i>
$P_{secondary}$	Pressure of the secondary air in the gas distributor, <i>Pa</i>
r	Radial coordinate, <i>m</i>
R	Universal gas constant, $R = 8.314\ J\cdot K^{-1}\cdot mol^{-1}$
R_c	Coupon (disk) radius, <i>m</i>
r_d	Deposition rate, <i>kg/s</i>
$r_{d,1}$	Deposition rate on a dry surface, <i>kg/s</i>
$r_{d,2}$	Deposition rate on a wet surface, <i>kg/s</i>
$r_{d,i}^{exp}$	Experimental integral deposition rate for experiment <i>i</i> , <i>kg/s</i>
$r_{d,i}^{int}$	Calculated integral deposition rate for experiment <i>i</i> , <i>kg/s</i>

Re	Reynolds number for a disk, $Re = \frac{Ud\rho_a}{\mu_a}$, <i>dimensionless</i>
R_I	Interception parameter, $R_I = D_p/D_c$, <i>dimensionless</i>
\bar{r}	Nondimensional radial coordinate, $\bar{r} = r/R_c$, <i>dimensionless</i>
\bar{r}_0	Initial nondimensional radial position at \bar{t}_0 , <i>dimensionless</i>
Sc	Schmidt number, $Sc = \frac{V_a}{D}$, <i>dimensionless</i>
Sh	Sherwood number for a disk, $Sh = \frac{k_m d}{D}$, <i>dimensionless</i>
$S_{D_v,50}$	Standard deviation of the volume median diameter, <i>m</i>
$S_{\bar{D}_v,50}$	Standard deviation of the average volume median diameter, <i>m</i>
S_p	Particle stopping distance, $S_p = t_p U$, <i>m</i>
St	Stokes number, $St = \frac{t_p U}{D_c}$, <i>dimensionless</i>
St_{cr}	Critical Stokes number, <i>dimensionless</i>
t	Time, <i>s</i>
T	Temperature, <i>K</i>
t_i	Moment of deposition of the <i>i</i> -th layer, <i>s</i>
t_p	Particle relaxation time, $t_p = \frac{\rho_p D_p^2 C_c}{18\mu_a}$, <i>s</i>
t_p^+	Nondimensional particle relaxation time, $t_p^+ = t_p \cdot \frac{(v^*)^2}{V_a}$, <i>dimensionless</i>
\bar{t}	Nondimensional time, $\bar{t} = t \cdot v_0 / R_c$, <i>dimensionless</i>

\bar{t}'	Nondimensional time needed for particle to reach the coupon surface plane ($\bar{x} = 0$), <i>dimensionless</i>
Q	Volumetric flow rate of air, m^3/s
U	Superficial gas velocity, m/s
U_{nozzle}	Superficial gas velocity in the column, from the nozzle air, m/s
$U_{secondary}$	Superficial gas velocity in the column, from the secondary air, m/s
u_r	Radial velocity component of a particle (droplet), m/s
u_x	Axial velocity component of a particle (droplet), m/s
\vec{u}	Particle (droplet) velocity vector, m/s
V	Yield of volatiles, <i>dimensionless</i>
v_0	Axial gas velocity, same as U , m/s
V_g	Gas velocity (in the nozzle), m/s
$V_{i,aerosol}$	Volume relative frequency of the class i in the aerosol, <i>dimensionless</i>
$V_{i,downstream}$	Volume relative frequency of the class i on the downstream side of the coupon, <i>dimensionless</i>
$V_{i,upstream}$	Volume relative frequency of the class i on the upstream side of the coupon, <i>dimensionless</i>
V_l	Liquid velocity (in the nozzle), m/s
v_r	Radial gas velocity component, m/s
V_t	Terminal velocity of a particle (droplet), m/s
v_x	Axial gas velocity component, m/s
v^*	Friction velocity, m/s
V^*	Maximum yield of volatiles, <i>dimensionless</i>

v^∞	Average gas free stream velocity, m/s
v_r^∞	Freestream gas velocity in radial direction, m/s
\vec{v}	Gas velocity vector, m/s
\bar{v}_r	Nondimensional radial gas velocity, $\bar{v}_r = v_r / v_0$, <i>dimensionless</i>
\bar{v}_x	Nondimensional axial gas velocity, $\bar{v}_x = v_x / v_0$, <i>dimensionless</i>
VMD	Volume median diameter, same as $D_{V,50}$, m
x	Axial coordinate, m
\bar{x}	Nondimensional axial coordinate, $\bar{x} = x / R_c$, <i>dimensionless</i>
\bar{x}_0	Initial nondimensional axial position at \bar{t}_0 , <i>dimensionless</i>
y	Surface coverage, <i>dimensionless</i>
z_1, z_2	Solutions of the characteristic equation, $z_{1,2} = \frac{-1 \pm \sqrt{1 - 16St}}{4St}$, <i>dimensionless</i>

Greek symbols

γ	Surface tension, J/m^2
γ_L	Liquid surface tension, J/m^2
γ_{LV}	Liquid-vapour surface tension, J/m^2
γ_S	Solid surface tension (surface energy), J/m^2
γ_{SL}	Solid-liquid surface tension, J/m^2
γ_{SV}	Solid-vapour surface tension, J/m^2
μ_a	Dynamic viscosity of air, $Pa \cdot s$

μ_{oil}	Dynamic viscosity of oil, $Pa \cdot s$
ν_a	Kinematic viscosity of air, m^2/s
ν_l	Kinematic viscosity of liquid (in the nozzle), $10^{-6} m^2/s$ (cSt)
θ	Equilibrium contact angle, $^\circ$
θ_{adv}	Advancing contact angle, $^\circ$
θ_{rec}	Receding contact angle, $^\circ$
ρ_a	Density of air, kg/m^3
ρ_f	Density of fluid flowing through the rotameter, kg/m^3
ρ_g	Density of gas (in the nozzle), g/cm^3
ρ_p	Particle (droplet) density, kg/m^3
σ_l	Liquid surface tension (in the nozzle), $10^{-3} J/m^2$ (dyn/cm)
τ_i	Duration of the experiment i , s

List of acronyms

ATB	Atmospheric Topped Bitumen
FBP	Final Boiling Point
HGO	Heavy Gas Oil
IBP	Initial Boiling Point
LGO	Light Gas Oil
MCR	Micro Carbon Residue
MEBR	Syn crude Canada Ltd. Plant 7 Bitumen product
VTB	Vacuum Topped Bitumen

TEG Triethylene glycol

Acknowledgments

I would like to use this opportunity to thank my supervisors, Dr. Paul Watkinson, Dr. Dusko Posarac and Dr. Fariborz Taghipour, for the supervision of my work on this thesis and all their suggestions and help.

Also, I would like to thank Syncrude Canada Ltd., for financing this project and for the opportunity to work on an interesting subject.

Finally, I would like to thank my parents for their understanding and support throughout the years.

Chapter 1. Introduction

Total oil sand reserves in Northern Alberta are estimated at around 1.7 trillion barrels of bitumen; this amount is comparable to the total proven world oil reserves of conventional petroleum, where the top seventeen countries hold about 1.24 trillion barrels [1]. One tenth of the bitumen deposits are considered economically recoverable at 2006 oil prices. This portion alone makes Canada's total oil reserves second-largest in the world, next only to Saudi Arabia's.

As the price of petroleum over the last decade showed a steady rise [2], petroleum production from unconventional oil reserves (oil sands, oil shales, biomass) [3] attracted more attention. Production of synthetic crude oil from bitumen which was extracted from oil sands, became more economically viable, resulting in a great expansion in Northern Canada. Today, 46% of the petroleum in Canada is produced from oil sands, while in 1992 that share was just 17% [4, 5].

Oil sands are a mixture of bitumen, sand, clay and water [6]. Typically, they contain about 84% wt. of solids, 11–12% wt. of crude bitumen and the rest is water. The solids are about 90% quartz, with some amounts of feldspar, muscovite, chert, and clay minerals [5]. Crude bitumen is a complex mixture of organic compounds that contains polymeric asphaltenes and resins of high molecular mass, and high levels of nitrogen, oxygen, sulfur, and metals. It is a highly viscous, black and sticky substance, entirely soluble in carbon disulfide. Its main characteristic is high viscosity in its natural state ($10^1 - 10^3 \text{ Pa}\cdot\text{s}$) – to the point of pseudoplasticity; it has to be heated or diluted before it will flow [5, 7].

For deep oil-sand deposits, steam injection is used, whereas for shallow deposits, extraction of bitumen begins with the mining process. Mining the oil sands includes removing the overlying overburden, recovering the oil sands and transporting them to a bitumen extraction plant. In the extraction plant, hot water is used to wash out bitumen from the oil sands. The bitumen is then upgraded and refined to produce synthetic crude oil.

1.1. Bitumen upgrading and the Fluid Coker

The purpose of bitumen upgrading is to reduce high boiling fractions, increase the hydrogen to carbon ratio, and remove impurities. Table 1.1 illustrates the property differences between bitumen and crude oils, which suggests a need for bitumen upgrading.

Table 1.1 Bitumen, Synthetic crude, and Conventional crude oil properties [5]

	Bitumen	Synthetic crude	Conventional crude
°API	8	32	41
Sulfur, wt %	4.8	0.08	0.2
Nitrogen, wt %	0.45	0.03	0.04
Viscosity at 40°C, cSt	3000	3.0	2.9
Pour point, °C	18	-4.5	-6
Metals, mg/kg	450	<1	
Distillate yield, vol %			
IBP – C5*	0	4	3
C5 – 195°C	0	18	36
195°C – 345°C	14	47	31
345°C – 560°C	86	31	18
560°C +		0	12

*IBP=Initial Boiling Point, C5=pentane

Upgrading consists of two steps: primary and secondary. A schematic diagram of the bitumen upgrading process and its two main steps is given in Fig. 1.1.

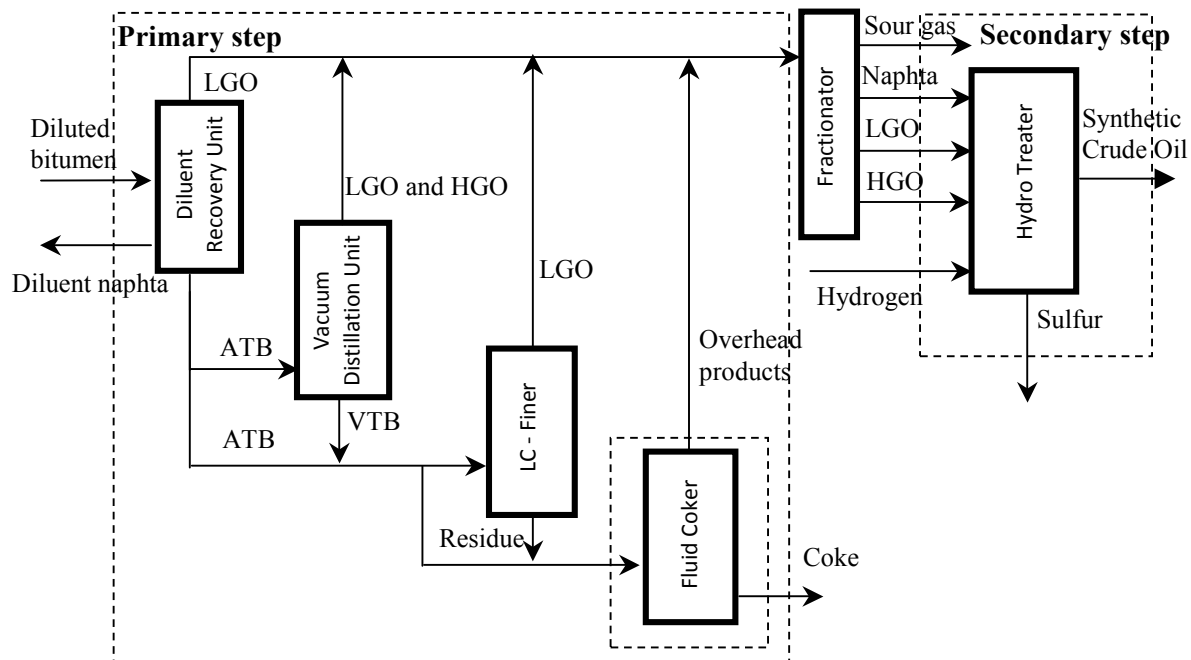


Figure 1.1 Schematic representation of the bitumen upgrading process [9]

The *primary step* converts high-molecular residues in the bitumen to a distillate. The *secondary step* includes separating the distillate into desired boiling ranges and adding hydrogen to saturate hydrocarbons and remove impurities.

In the primary step, bitumen from the froth treatment step is first sent to the Diluent Recovery Unit (atmospheric distillation column). This unit recovers diluent naphtha, and produces Light Gas Oil (LGO) and Atmospheric Topped Bitumen residue (ATB). Produced ATB is sent to the Vacuum Distillation Unit, where LGO and Heavy Gas Oil (HGO) are removed from the top, and the Vacuum Topped Bitumen (VTB) from the bottom is mixed with part of the ATB and sent to the LC-Finer. The LC-Finer is a catalytic reactor where hydrogen is added to increase the hydrogen to carbon ratio and produce cracked LGO. Residue from the LC-Finer is combined with parts of the feed and sent to the Fluid Coker reactor (Fig. 1.2).

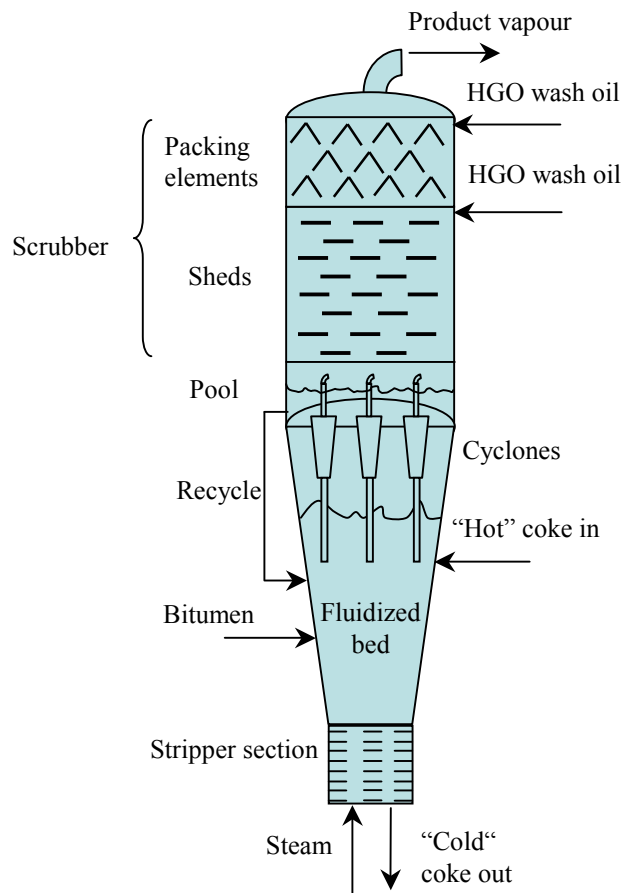


Figure 1.2 Schematic of the Syncrude Fluid Coker

In the Fluid Coker, bitumen is first sprayed into the fluidized bed reactor section. Coking reactions occur on the surface of introduced hot coke particles, at about 510°C to 530°C, where bitumen cracks and forms coke and lighter fractions in the form of vapour. Energy for the reaction is provided by burning in the coke burner part of the produced coke from the reactor, and by re-circulating the hot coke back into the reactor. In the stripping section, bitumen that remains on the surface of the coke particles is stripped off with steam. Product vapour from the coker reactor is then sent to the cyclones that remove unreacted bitumen droplets and particles above about 11 microns [7]. Vapour is then sent to the scrubber section, which consists of the pool, sheds and structured grid (Fig. 1.2). Heavy gas oil at 325°C is sprayed from the top of the structured packing and sheds, in order to cool down the gas and remove (scrub) heavy components from the vapour by condensation. The purpose of the heavy gas oil is to also remove small droplets and coke particles from the product vapour. However, if droplets and particles deposit on the surface of the packing in the Scrubber, they can cause fouling of the Scrubber and plugging of the reactor.

1.2. Fouling in the Scrubber section of the Fluid Coker

Fouling can be defined as the accumulation of unwanted material on solid surfaces. Fouling in the grid section of the scrubber in the Fluid Coker reactor increases pressure drop along the scrubber and changes the operating conditions of the reactor. The cause of fouling in the scrubber section of the reactor is deposition of fine bitumen droplets, and possibly coke particles, not removed in the cyclones from the product vapour. Under the effect of high temperatures, bitumen droplets deposited on the surface undergo thermal decomposition into volatiles and coke. Formed coke remains on the surface of the packing as a solid material. Build-up of deposits eventually results in plugging of the reactor and its shutdown for maintenance, with a costly disruption of the production. Figure 1.3 shows a comparison between the clean packing in the grid and the packing surface covered with coke.

If we could understand the fundamental phenomena that govern deposition on the packing elements of the scrubber, it would be possible to change operating conditions in

order to minimize the fouling, or change the geometry of the packing and prolong the reactor operation.

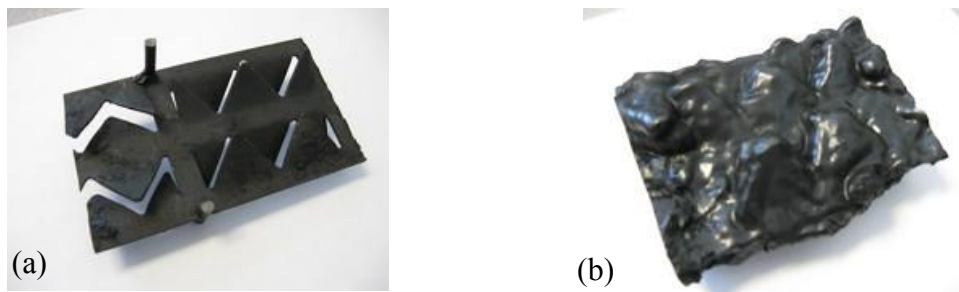


Figure 1.3 Segment of the packing elements in the Scrubber Section of the Fluid Coker, (a) before start up of the reactor and (b) after reactor shutdown

1.3. Project objectives

Fouling in the scrubber section of the Fluid Coker reactor was previously studied theoretically by Subudhi [8]. He simulated the increase in the pressure drop of the scrubber by modeling particle transport to the surface, assuming perfect sticking, and included the effect of the reaction. His model assumed flow *parallel* to the surface of the packing. Since the orientation of packing elements in the reactor is not fully parallel with the upward flow of the gas (Fig. 1.4), the fluid dynamics around such a geometry is certainly different. Since fluid dynamics plays a key role in particle transport to the surface, there was room for improvements to Subudhi's approach.

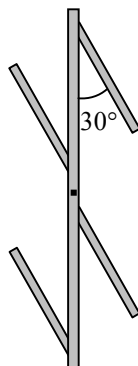


Figure 1.4 Side view of the scrubber packing elements, given in Fig. 1.3. The blades are inclined at a 30° angle with the vertical axis [8]

Because of the complex geometry of the actual packing, it was decided to study deposition onto single elements of simple geometries, placed normal to the flow of aerosol droplets in a gas-vapour mixture. A normal orientation of the disk to the flow, compared to the parallel orientation, yields a different flow field around the disk that is likely more similar to the flow field around the packing elements in the Scrubber. This is especially true for the vortex behind the disk, where flow separation occurs. The idea was to investigate deposition on the 5 cm diameter circular disk (coupon), placed in a 7.5 cm diameter column (Fig. 1.5). The aerosol flow was directed in the upward direction, as is the case in the Fluid Coker reactor.

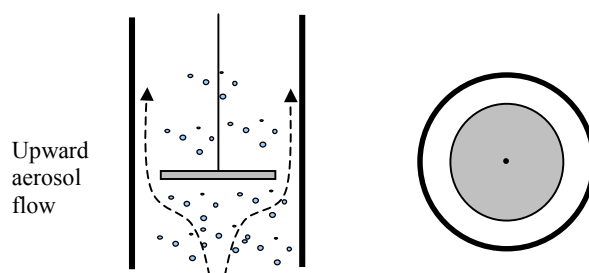


Figure 1.5 Schematic representation of the side and top view of the 5 cm diameter disk in the 7.5 cm diameter column (aerosol droplets are presented disproportionately large)

The deposition process was intended to be studied experimentally in two separate experimental units: a room temperature unit (called the Cold Unit) and a high temperature unit (called the Hot Unit). The Cold Unit was intended to be used to investigate the effect of velocity over the range that could not be covered in the Hot Unit (0–1.5 m/s), and the effect of other factors such as droplet size, which was not measured in the Hot Unit. The high temperature unit was used to study deposition of heavy oil hydrocarbons at temperatures of 290–425°C, similar to the conditions in the real Fluid Coker reactor, and the effect of heavy oil composition (Song [52]). Experimental results from both units were used for verification of the computational fluid dynamics (CFD) model predictions, undertaken as part of this overall study (Lakghomi [36]), and that would be later used for simulation of deposition on arbitrary geometries.

1.4. Scope of the thesis

The objective of this thesis was to carry out an experimental investigation of the deposition process at room temperature. For this purpose, the Cold Unit apparatus (Fig. 4.1) was constructed as part of this work. A limited set of experimental factors was selected. To investigate the effect of particle transport on deposition, velocity and droplet size distribution were varied (Sections 5.1–5.3); to quantify the distribution of deposits on the surface, distribution of deposits along the coupon radius was measured (Section 5.6). Lastly, to understand the effect of wettability on sticking and deposition, the effect of contact angles between the liquid and the solid surface was studied (Section 5.7). In particular, the factors to be investigated included:

1. Effect of superficial gas velocity on deposition rate, at a given droplet size distribution, over the range 0–1.5 m/s.
2. Effect of droplet size distribution on deposition rate, at a given velocity, over the range of volume median diameters between 3.9 and 7.5 microns.
3. Morphology of deposits and distribution of deposits along the radius of the disk.
4. Effect of contact angles (20° , 51° , and 94°) between the liquid and the solid surface on deposition rate.

In addition to the experimental investigation, the inviscid flow approximation was used to simulate particle transport to the surface and interpret the obtained experimental results (Section 5.4). Furthermore, deposition coefficients from the room temperature unit experiments (Section 5.3) were recalculated to the high temperature conditions, and compared with the independent set of data obtained in the high temperature unit experiments [52] (Chapter 6). The following chapter (Chapter 2) presents the relevant theory of particle deposition from parallel flow and flow around bluff bodies (transport and sticking) used in the modeling section (Chapter 3), and reviews significant work in this area.

Chapter 2. Theory and Literature Review

The deposition of small particles and droplets onto solid surfaces from gaseous streams was studied in the literature for two main classes of problems. First is the case when the flow is parallel to solid surfaces (laminar and turbulent flow) and the second is when the flow is normal to solid surfaces. The rationale for this division is that the flow field, and therefore the mechanisms that govern particle deposition, are different in each case. The main aspects of both are reviewed here, since both apply to the object of investigation.

2.1. Particle deposition from turbulent flow parallel to solid surfaces

Experimental work on particle deposition was reviewed by Cleaver and Yates [11], who validated their sublayer model for deposition from turbulent flow against the available experimental data. Papavergos and Hadley [10] were first to give a comprehensive review of theoretical developments and available experimental data on deposition from parallel turbulent flow. Epstein [12] presented a review of theory of particle transport, particle attachment and particle re-entrainment. Recently, deposition from parallel flows was also studied by the means of computational fluid dynamics. Tian and Ahmadi [14] compared different turbulent model predictions with the existing body of experimental data, while Zhang and Li [13] simulated deposition on the walls, roof and floor of horizontal ducts, thus distinguishing the effect of gravity.

Following Epstein [12], the main deposition phenomena can be summarized as follows. Starting from submicron particles, three mechanisms of deposition dominate as the particle size increases: diffusion, inertia and impaction. In the *diffusion regime*, particles are sufficiently small that they are carried to the wall through the viscous sublayer by Brownian diffusion. The Brownian diffusivity for a dilute suspension of spheres is given by the Stokes-Einstein equation,

$$D = \frac{k_B T}{3\pi\mu_a D_p} \quad (2.1)$$

where k_B is the Boltzmann constant, μ_a is the air dynamic viscosity and D_p is the particle diameter. It can be used in empirical correlations for convective mass transfer of the form $Sh = f(Re, Sc)$. The calculated Sherwood number yields a mass transfer coefficient, k_m , equal to the particle transport coefficient, k_t , for this case.

In the *inertia regime*, the particles are large enough so that turbulent eddies transfer to them some momentum that is normal to the walls. This momentum is not completely dissipated in the viscous sublayer and particles can reach the surface. A large body of experimental results on deposition in the inertial regime can be summarized by the following empirical correlation, to a good degree of accuracy,

$$k_t^+ = 3.5 \cdot 10^{-4} t_p^+, \quad 0.2 < t_p^+ < 20, \quad \text{horizontal wall} \quad (2.2)$$

where k_t^+ is the nondimensional deposition coefficient. The key independent variable for the inertia regime is the nondimensional particle relaxation time, t_p^+ , defined as

$t_p^+ = t_p \cdot \frac{(v^*)^2}{(\mu_a / \rho_a)}$. The dimensional particle relaxation time, t_p , represents the time needed for a particle to adjust or relax its velocity to a new fluid velocity,

$$t_p = \frac{\rho_p D_p^2 C_c}{18 \mu_a} \quad (2.3)$$

where D_p is the particle diameter. It includes fluid viscosity and the Cunningham slip correction factor, C_c , and is therefore affected by changes in temperature and pressure. The deposition coefficient, k_t , can be obtained from the nondimensional deposition coefficient, k_t^+ , using the relation $k_t^+ = k_t / v^*$. The friction velocity v^* , can be calculated from the shear stress or velocity gradient at the wall according to,

$$v^* = \left(\frac{\mu_a}{\rho_a} \cdot \frac{dv}{dx} \Big|_{x=0} \right)^{1/2} \quad (2.4)$$

The average velocity gradient, along a surface of length L , may be estimated from the correlations given in the literature (Schlichting [15], Lai and Nazaroff [16]),

$$\left. \frac{dv}{dx} \right|_{x=0} = \left(\frac{0.074}{\mu_a} \right) \left(\frac{\rho_a (v^\infty)^2}{2} \right) \left(\frac{v^\infty L}{\mu_a / \rho_a} \right)^{-1/5} \quad (2.5)$$

where v^∞ is the average free stream velocity. To account for the effect of gravity, Sehmel [17] extended this theory to predict deposition velocities on the floor and ceiling of horizontal ducts, and obtained,

$$k_t^+ = \begin{cases} 2 \cdot 10^{-3} t_p^+, & 0.2 < t_p^+ & \text{Floor} \\ 4 \cdot 10^{-5} t_p^+, & 1 < t_p^+ < 50, & \text{Ceiling} \end{cases} \quad (2.6a,b)$$

However, these equations fit only a limited set of data (Papavergos and Hadley [10]).

As particle size is increased, the inertia regime is followed by the *impaction regime*, which begins at $t_p^+ = 20$, where the response of such large particles to turbulent fluctuations becomes limited, and k_t^+ levels off at about 0.12–0.18. At $t_p^+ \geq 30$, deposition coefficients starts to fall gradually, since such large particles get even more sluggish in their response to turbulent eddies.

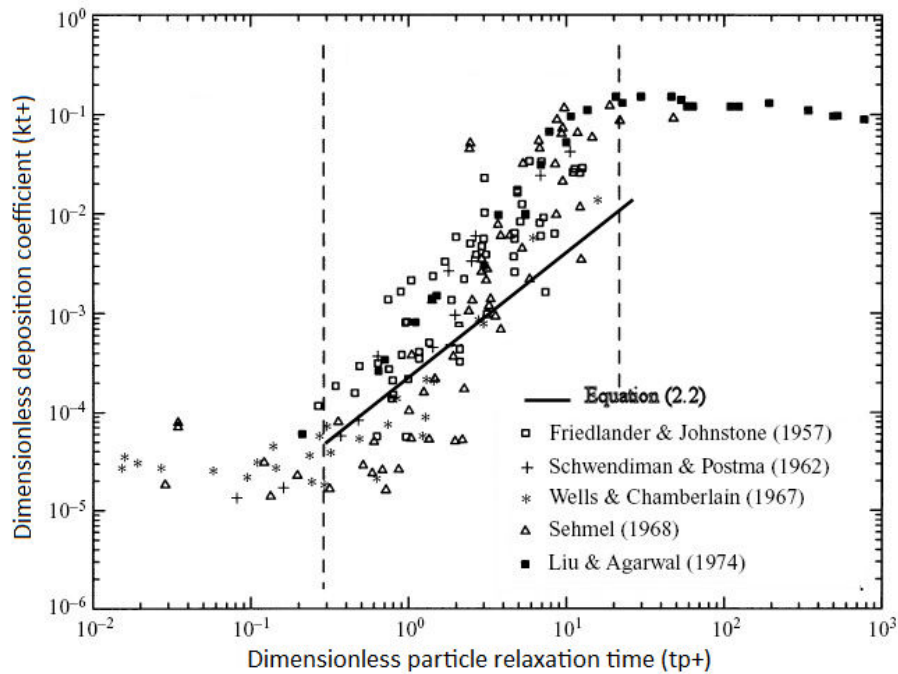


Figure 2.1 Summary of experimental data on particle deposition from turbulent pipe flow, adapted from Young and Leeming [18]

Gravitational settling becomes important for larger particles with $t_p^+ \geq 1$. The deposition coefficient, k_t , from gravitational settling then becomes equal to the particle terminal velocity, V_t . A summary of experimental data on particle deposition from turbulent pipe flow is given in Fig. 2.1 (from Young and Leeming [18]).

The above considerations are related to the transport of particles to the surface. If perfect sticking is assumed, the particle transport flux becomes equal to the particle deposition rate and vice versa. Particles can also be re-entrained into the gas stream (Epstein [12]). This phenomenon can happen with solid particles (Vincent and Humphries [19]), but in the case of organic liquid droplets deposited on hydrophilic surfaces, with low contact angles, it is reasonable to assume that re-entrainment does not occur.

2.2. Particle deposition from the flow around bluff bodies and surfaces

Mechanisms of deposition on solid surfaces from the flow normal to the surface are encountered in filtration and membrane operations. They also govern the collection of small droplets or particles in wet scrubbers, the deposition of super-cooled water drops on the wings of aircrafts (aircraft icing), and the build-up of deposits in cyclones and other process equipment.

An important parameter used to describe deposition on bodies from normal flows is the collection efficiency or *capture efficiency*. It is defined as the fraction of particles that are approaching the collector in the region defined by the projected area of the collector, that are ultimately deposited on the collector surface,

$$E = \frac{\text{Mass of particles from the projected area deposited on the body}}{\text{Mass of particles in the projected area approaching the body}} \quad (2.7)$$

The *deposition coefficient*, k_d , or *deposition velocity*, can be obtained by multiplying the capture efficiency, E , with the superficial velocity, U ,

$$k_d = E \cdot U \quad (2.8)$$

The deposition rate, r_d , is then obtained by multiplying the deposition coefficient, surface area, A , and concentration, c_b ,

$$r_d = k_d \cdot c_b \cdot A \quad (2.9)$$

As described by Hinds [20] and Friedlander [21], the main collection mechanisms that govern deposition from a normal flow are: interception, inertial impaction, diffusion, gravitational settling, electrostatic attraction and thermal forces. However, all these mechanisms rarely occur simultaneously – usually one or two mechanisms dominate the deposition process.

Collection by *interception* occurs when a particle follows a gas streamline that is within one particle radius from the body. A particle will be captured because of its size; the larger the particle, the greater the possibility for interception. This is the only mechanism that is not a result of a particle departing from its original gas streamline. The main parameter that controls interception is the ratio of the particle, D_p , and body diameters, D_c , i.e., $R_I = D_p / D_c$.

Inertial impaction occurs when particles, because of their inertia, are unable to adjust to the change in direction of the flow in the vicinity of the body. Their path starts to deviate from the fluid streamlines, and if the inertia is sufficiently large, particles can reach the surface. The main parameter that controls inertial impaction is the Stokes number, defined as a ratio of particle stopping distance, S_p , and the diameter of the body,

$$St = \frac{S_p}{D_c} = \frac{t_p U}{D_c} \quad (2.10)$$

In the *diffusion regime*, Brownian motion of small particles causes deviation of particles from the fluid streamlines, and particles can reach the surface. Diffusion depends on the flow characteristics, and therefore the Brownian diffusion coefficient (Eq. (2.1)) should be used in empirical correlations for mass transfer to obtain the deposition coefficient.

Gravitational settling can increase the capture efficiency if the flow is in the direction of gravity, or decrease the capture efficiency if it is in the opposite direction. It is important for larger particles only ($t_p^+ > 1$).

Electrostatic deposition can be important, but it requires knowing the charge of the collector and the particles. *Thermal forces*, which include *thermophoresis* (migration of particles down a temperature gradient close to the surface) and the *thermoelectric effect* (heat flux induced thermoelectric voltage in the adjacent coolant stream), can be important, but only when temperature gradients exist.

For deposition onto body and surface collectors normal to the flow, we can distinguish between the deposition on the upstream (front) side, and deposition on the downstream (back) side, since each side is characterized by a different flow field.

2.2.1. Upstream (front) side

In the literature, it is mainly the inertial impaction mechanism on the upstream (front) surface of single elements that has been studied, both theoretically and experimentally. Early work on the theory of inertial impaction was done by Albrecht [22], Sell [23], Langmuir and Blodgett [24] and Landhal and Herrmann [25]. Their results differed to some degree, depending on the flow approximation, position where the particles were injected, and number of particles, but the results of Langmuir and Blodgett were mainly consistent with the results obtained later on. Early experimental measurements by Landhal and Herman [25] and Sell [23], due to the complexity of the phenomena involved, were not successful in separating inertial effects from the diffusion and interception effects. However, results on inertial impaction obtained by Ranz and Wong [26], Wong et al. [27] and May and Clifford [28], could be considered correct. Table 2.1 summarizes the main theoretical and experimental results on inertial impaction.

It is worth noting that, according to the theoretical predictions from the literature [30], disks showed the highest capture efficiencies among all simple geometries (ribbon, sphere, cylinder). Also, the ideal flow approximation seemed to be a satisfactory description of the flow in front of the body, in all cases. In the body of experimental data, there are discrepancies among the results, depending on whether particles or droplets are used, and how the flow was oriented. In order to explain experimental capture efficiencies lower than theoretical predictions, Wong et al. [27] suggested that viscous forces should decrease capture efficiencies. Golovin and Putnam [30] suggested the same, but for targets of the order of few centimetres in size (1–2 inches), viscosity effects

should be negligible if $Re_{target} > 100$. The results of May and Clifford are just slightly below the potential flow predictions for horizontal flow. This is probably because the flow was oriented upward, with gravity acting in the opposite direction to the flow, suggesting that gravity could be responsible (remark of Vincent and Humphries [19]), and not the viscous forces.

Experimental results from the literature, along with a theoretical prediction of inertial impaction on disks, are given in Figure 2.2. Calculations and experimental data are given for horizontal flow (except May and Clifford [28], upward flow). It can be seen that the capture efficiencies can be presented as a unique function of the Stokes number. As the Stokes number is increased, particles possess more inertia, and are unable to closely follow the fluid streamlines that go around the body. As a result, particles impact the surface and deposit.

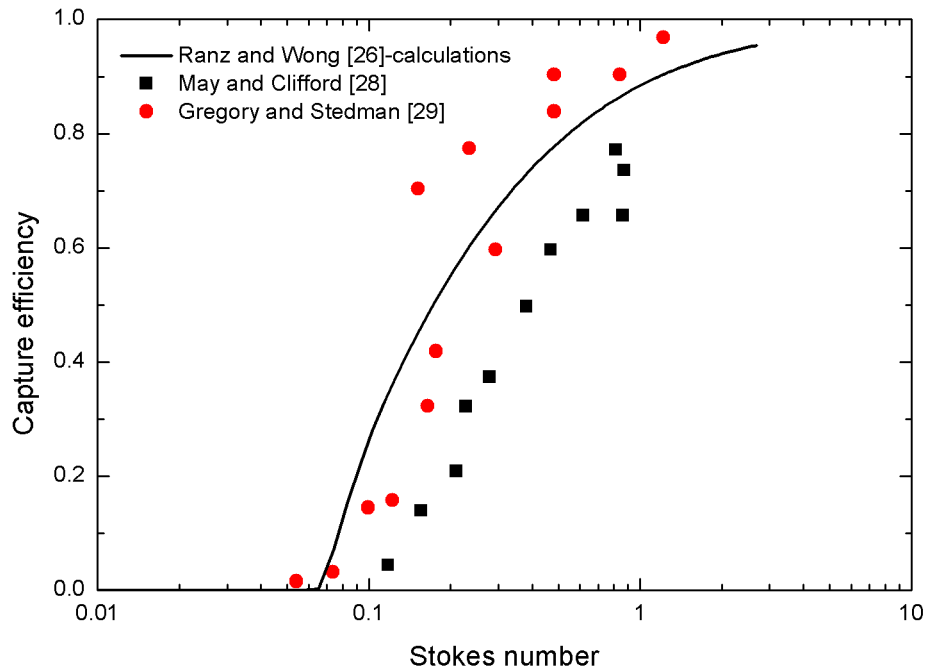


Figure 2.2 Experimental and theoretical data on inertial deposition onto front surfaces of disks

Table 2.1 Summary of experimental data and simple theoretical treatments of inertial impaction on the front side of bluff bodies

Authors	Theory		Experiments		
	Shape	Simulation	Shape	Materials (solid particles/droplets)	Measurements
Langmuir and Blodgett [24]	Cylinder, Sphere, Ribbon	Potential flow, no gravity, non-Stokesian drag force	–	–	–
Ranz and Wong [26]	Disk, Ribbon	Potential flow, no gravity, Stokes drag force	Cylinder, Sphere	No indications on the flow orientation. Nearly uniform 0.3–1.4 micron droplets of concentrated sulphuric acid (aerosol condensation generator). Collectors: 3-mil platinum wires and 0.9 mm platinum sphere	Droplet size not measured, but controlled by changing operating conditions of the aerosol generator. Weight of deposits measured after the experiment.
Gregory and Stedman [29]	–	–	Disks, Cylinders, Stripes	Horizontal flow. Lycopodium spores, about 28 micron diameter. Velocity: 0.5–9.5 m/s	Direct counting of deposited spores under the microscope
Wong et al. [27]	Cylinders	Potential flow, no gravity, Stokes drag force	Cylinders	No indications on the flow orientation. 0.6–1.4 micron uniform droplets, concentrated sulphuric acid (homogeneous aerosol generator). Collectors: 29–106 micron platinum wires. Velocity: 4–50 m/s, Reynolds number: 13–330	Droplet size not measured, but controlled by changing aerosol generator operating conditions. Weight measured after the experiment.
Golovin and Putnam [30], review article	Cylinders, Spheres, Ribbon, Airfoils at different angles	Potential flow theories, no gravity, Stokes drag force	Cylinders	Reviewed experimental results for cylinders: Gregory and Stedman (1953), Ranz and Wong (1952), Ranz, Wong and Johnstone (1954), Amelin and Belyakov (1956)	–
May and Clifford [28]	–	–	Disks, Cylinders, Spheres, Ribbons	Upward flow. Uniform dibutyl phthalate droplets 20, 30, 40 microns in diameter (aerosol spinning top generator). Velocity: 2.2–6.2 m/s in the 20×20 cm wind tunnel. Targets: 0.1–2.9 cm (disks: 0.154, 0.480, 0.995, 1.431, 2.875cm). Reynolds: 165–8500.	Droplets size measured by magnesium oxide method. No indications on measurements of the weight of deposits.
Noll and Pilat [31]	Ribbon, Half-body	Potential flow, no gravity, non-Stokesian drag force	Ribbon, Half-body	Flow orientation is not evident. Size distribution of the atmospheric aerosol, with particles larger than 1 micron.	Aerosol size distribution measured in the Atmospheric giant particle inertial impactor.
Vincent and Humphries [19]	–	–	Disks	Horizontal flow. Size distribution of dusts. 5 cm diameter disk.	10 times lower efficiencies. Close to the rim there was no dust deposits (bounced off or re-entrained).

Although it does affect capture efficiencies, gravity was often not considered important, and in most cases it was not explicitly stated if the experiments were performed with horizontal, upward or downward flow. From the description of the experimental procedures and the pictures of the experimental setup, it seems that only the experiments of May and Clifford were performed in upward flow, and all others in horizontal flow. In their calculations, Tsai and Liang [32] studied inertial effects along with gravity from the axisymmetric stagnation point flow approximation, but the presented results were for the gravity in the flow direction only. Also, experimental results were available only for small blockage ratio ($Br \approx 0.05$, May and Clifford [28]), where the effect of column walls or other neighbour elements, have a negligible effect on the flow field and deposition.

Experimental investigation of deposition due to convective diffusion and inertial mechanisms from turbulent flow onto normal surfaces has not been reported in the past, to the best of our knowledge. These deposition mechanisms lead to small amounts of deposits, compared to other mechanisms encountered in normal flow (inertia, gravity or interception). Successful separation of these mechanisms would require working with small droplets (a few microns), flowing over targets in the range of few centimeters. Removal of small droplets was of primary interest in fiber filter technology and was therefore mainly studied for the flow over small fibers (<100 microns), where inertia and interception are the dominating mechanisms.

2.2.2. Downstream (back) side

Deposition on the downstream (back) side of bluff bodies did not attract much attention of researchers in the past; probably because in the majority of applications, the upstream side collected significantly more deposits. Also, the imprecisely defined turbulent wake behind the disk did not allow theoretical treatment, and deposition could be investigated only experimentally.

Experimental results on the downstream surface were reported by Amelin and Belyakov [33], who investigated capture efficiencies of the front and back sides of cylinders. As explained by Golovin and Putnam [30], their results showed a linear increase with increased Stokes number (i.e., due to increased velocity). However, the results could not be considered reliable, since their lowest capture efficiencies were of

order 10^{-6} , while just due to the interception, capture efficiencies should be at least 10^{-4} . Yeomans et al. [34] investigated deposition of DDT solutions on the front and back surfaces of glass discs and leaves in still and moving air. They found that for small particles, deposition on the downstream side exceeded deposition on the upstream side. As the Stokes number was increased (by increasing the drop size), capture efficiencies first increased. At about a Stokes number of 0.06 (calculated from $VMD=15$ micron, at $U=3.6$ m/s), the capture efficiencies started decreasing steadily toward zero. At this value, the amount of deposits on the upstream and downstream sides was similar.

Goldshmid and Calvert [35], measured deposition of small particles (0.8–2.8 microns) on oscillating drops and observed that for particles below 1 micron in size, capture efficiencies suddenly increased. They tried to explain this by claiming that the deposition takes place in the vortex behind the disk. They employed a simple model based on inertial deposition from the vortex (centrifugal force of particles), which was able to qualitatively explain the results.

Vincent and Humphries [19] measured capture efficiencies of dusts onto the front and back surfaces of disks. For the back side, their results showed a decreasing trend with velocity and increasing trend with particle size. The results also showed that the back side capture efficiencies could not be represented solely as a function of the Stokes number. In trying to explain the mechanisms of deposition, they did not consider inertial impaction or gravity, but mentioned turbulent diffusion, Brownian diffusion and electrostatic forces.

Again, in none of the works mentioned above was gravity considered important enough to be mentioned how experiments were performed, and whether or not it could have had an effect on deposition. Table 2.2 summarizes the main results on downstream deposition.

Table 2.2 Summary of experimental investigations for the downstream (back) side of bluff bodies

Authors	Shapes	Materials	Measurements
Amelin and Belyakov [33]	Cylinders	n/a	n/a
Yeomans et al. [34]	Glass, wire cloth, filter paper and leaf <i>disks</i> (4.1–15 cm in diameter)	Horizontal flow in the 18m long wind tunnel. Droplets of DDT in petroleum (VMD: 8.4 – 33.0 microns) via La Mer-Sinclair homogeneous aerosol generator. Velocities: 3.2 to 25.6 km/h.	Weight of DDT deposits at the end of experiment, counting dead mosquitoes, measuring median diameter
Goldshmid and Calvert [35]	Oscillating drops	La Mer-Sinclair homogeneous aerosol generator. Drops of formamide, hexadecane, water and glycerol. Polystyrene particles and sulfur droplets, 0.8–2.8 microns in size.	Counting of polystyrene particles and weighing of sulfur deposits
Vincent and Humphries [19]	Metallic <i>disks</i>	Horizontal flow. Graded dusts of brown aloxite, size distribution with median diameter 3.0, 6.5, 13.0 and 17.0 microns. Disks 2.0, 2.8, 5.0 and 10.0 cm diameter.	n/a

In summary, the inertial deposition onto the upstream side of bluff bodies was investigated mainly with success: theoretically, using the inviscid flow approximation, and experimentally too, although discrepancies between the reported results exist. In all investigations, the flow orientation was not considered important and the effect of gravity was not included into the calculations (except Tsai and Liang [32]). In addition, in the investigations of particle deposition on disks, only the Stokes drag force on particles was used.

For the downstream side, there has been no computational treatment of the deposition from the wake (except by Lakghomi [36]), and the mechanisms of deposition were not understood clearly. The experimental results also showed some discrepancies; and to the best of our knowledge, no investigation on the deposition from an upward flow with droplets in the aerosol has been conducted. The following section (Section 2.3) discusses distribution of deposits along the coupon radius.

2.3. Distribution of deposits along the coupon radius

In order to predict whether some areas of packing elements in the scrubber section of the Fluid Coker would foul more rapidly and potentially become a bottleneck for the

whole scrubber, and therefore the whole reactor, the mass and size distribution of the deposits on the disk surface had to be determined.

Gregory and Stedman [29] reported higher concentrations of *Lycopodium spore* deposits at the edges of the front side of disks. This is contrary to what they observed for cylinders, in which case there were more deposits in the centre. Noll and Pilat [31] measured local capture efficiencies on the front side of ribbons and found that the pattern is similar to that on disks: more deposits were found close to the ribbon edge. These observations were explained with an inertial deposition model, which predicted more deposits toward the edge of the ribbon. Vincent and Humphries [19] noted that on the front surface of disks, deposits were concentrated close to the centre. However, their capture efficiencies were as much as 10 times below theoretical predictions. Since they worked with solid particles (aloxite dusts), they explained the discrepancies by the probable re-entrainment of dusts particles, and therefore, their results for the distribution of deposits cannot be considered reliable.

To summarize, data on the distribution of droplet deposits on the upstream sides of disks are not available in the literature. Also, distribution of deposits on the downstream side of surfaces or body collectors of any shape, to the best of our knowledge, has not been reported. This justifies our intention to determine the distribution of deposits along the radius of the disk.

2.4. Contact angle effect

The majority of the prior work on deposition was focused on particle transport to the surface, probably because it was considered more important in the fouling process. Two other factors that can affect the fouling process are droplet sticking and droplet re-entrainment. In our case, it is reasonable to assume that the re-entrainment of liquid droplets deposited on the surface of the disk does not occur; these phenomena are more common for solid particles. The remaining important phenomenon is sticking, and how it can be influenced. To explain sticking, we start by explaining the wetting and contact angles.

2.4.1 Wetting and contact angles

Wetting (or *wettability*) represents the ability of a liquid to maintain contact with a solid surface, which is the result of intermolecular forces of the two phases in contact. The degree of wetting is determined by the equilibrium of adhesive forces between the solid and the liquid, and cohesive forces within the liquid. If the adhesive forces are stronger, the degree of wetting will be higher.

Contact angle represents a quantitative measure of wettability, and the relative strength of adhesive and cohesive forces. It is the angle, θ , between the tangent lines of the liquid-vapour and the solid-vapour interfaces, as presented in Fig. 2.3.

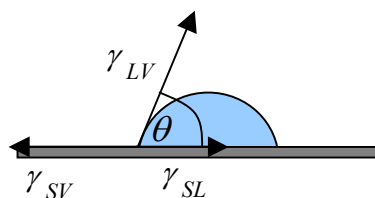


Figure 2.3 Schematic representation of the surface tension forces acting on a droplet deposited on the surface

From a force balance along the three-phase interface, the following relation can be devised (Young's equation): $\gamma_{SV} - \gamma_{SL} = \gamma_{LV} \cos(\theta)$, where γ_{SV} , γ_{SL} , γ_{LV} are the surface tensions on the solid-vapour, solid-liquid and liquid-vapour interface respectively. This equation is often approximated as $\gamma_S - \gamma_{SL} = \gamma_L \cos(\theta)$, where γ_S and γ_L are the surface tensions of the solid and liquid.

The *surface tension* of liquid represents the energy required for a unit increase in area of the liquid-gas interface. Surface tensions of solids have the same meaning. Usually, they are referred to as *surface energy*. Exact measurements are difficult, and according to Marere and Douillard [37], currently assumed values for surface energies of solids are 10–72 mJ/m² for low energy solids (e.g. polymers, carbons, and sulfurs), 72–200 mJ/m² for middle energy surfaces (e.g. clays and clay minerals, silicas, quartz) and 200–2000 mJ/m² for high energy solids (e.g. metals) [37]. Surface tensions of liquids

at 20°C vary from 20–75 mJ/m²; the exception is mercury with surface tension of 425 mJ/m². Table 2.3 summarizes possible combinations of liquid-solids interactions and the relation with contact angles and wettability.

Table 2.3 Degree of wetting explained in terms of solid-liquid and liquid-liquid interaction

Contact angle	Degree of wetting	Strength of	
		S/L interactions	L/L interactions
$\theta = 0^\circ$	Perfect wetting	Strong	Weak
$0^\circ < \theta \leq 90^\circ$	High wettability	Strong Weak	Strong Weak
$90^\circ < \theta < 180^\circ$	Low wettability	Weak	Strong
$\theta = 180^\circ$	Perfect non-wetting	Weak	Strong

From Table 2.3, it can be seen that low wettability can be achieved with strong liquid-liquid interactions and weak solid-liquid interactions. Strong L/L interactions are characterized by high surface tension of the liquid, and weak solid-liquid interactions are usually result of low surface energies of solids (the majority of high surface energy solids wet all liquids, i.e. metals, while low surface energy solids give low wetting, i.e. Teflon). The following table shows contact angles of water at 20°C ($\gamma=73$ mJ/m²), with different surface energy solids [38].

Table 2.4 Contact angles of water at 20°C with solids of different surface energies [38]

Material	Surface energy (mJ/m ²)	Contact angle (°)
Clean glass	73	0
Ordinary glass	70	20
Platinum	62	40
Anodized aluminium	50	60
Polymethyl-methacrylate	41	74
Nylon	38	79
Polyethylene	33	96
Polypropylene	26	108
Paraffin	19	110
Teflon	18	112

From this table, we can see that as the surface energy is decreased, contact angles are increased. The role of contact angles in droplet sticking or rebounding is explained in the next section.

2.4.2. Impact of droplets on the solid surface (sticking vs. rebounding)

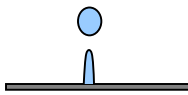
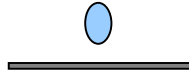
The phenomena governing liquid impacts on solid surfaces are quite complex, and more complicated than those encountered on wetted surfaces. The reason for the additional complexity is the influence of surface texture, i.e. wettability and surface roughness (Yarin [39]). The main types of behaviour when a droplet impacts a dry solid surface (Table 2.5) can be described as follows [39, 40].

a. Deposition. The droplet spreads upon impact and stays deposited on the surface. This mostly occurs with hydrophilic (and oleophilic) surfaces ($\theta < 90^\circ$), but it can also happen with hydrophobic (and oleophobic) surfaces ($\theta > 90^\circ$). For hydrophobic surfaces, it occurs when force that is acting to remove the droplet from the surface is sufficiently small, i.e. droplet deposition velocity is so small that there is no bouncing and the droplet stays on the surface; or, the gravity force on the droplet resting on a slightly inclined hydrophobic surface is not sufficient to cause sliding.

b. Splashing (prompt splash or corona splash). An increased impact velocity on a hydrophilic rough surface causes tiny droplets to detach from the edge of the lamella (*prompt splash*), and if the surface tension of the liquid is reduced, lamella are able to detach from the wall (*corona splash*). If the impact velocity is high enough, splashing or breakup can also occur on hydrophobic and superhydrophobic surfaces ($\theta > 150^\circ$).

c. Rebounding. Rebounding happens most often on hydrophobic surfaces, although according to the simulations of Khatavkar [41], partial rebounding can occur on hydrophilic surfaces also. Rebounding follows retraction of a droplet from the elongated state, where its initial kinetic energy is transformed into the potential energy of surface tension (and partly dissipated inside the droplet via viscous dissipation). If, in retracting, the droplet-surface interactions are strong (hydrophilic surface or hydrophobic surface), and viscous dissipation is present, only partial rebounding can occur. However, if the surface is superhydrophobic, droplet-surface interactions are negligible, and the droplet can fully rebound. This can happen only if viscous dissipation is not significant: e.g. it is unlikely that a drop of honey would rebound from any surface. In addition, advancing and receding contact angles (θ_{adv} and θ_{rec}) should be similar, in order to avoid contact angle hysteresis as a significant source of energy dissipation.

Table 2.5 Possible outcomes of droplet impact on a solid surface

Deposition (drop oscillates a little)	Prompt splash	Corona splash	Partial rebounding	Complete rebounding
				

To reduce fouling, we are interested in *partial* or *complete rebounding*. From experimental observations, it is known that complete rebounding can occur only on high contact angle surfaces ($\theta > 150^\circ$), classified as superhydrophobic surfaces [42, 43, 44]. In nature, examples are the surfaces of the lotus leaf (*Nelumbo Nucifera*), or bird feathers. In addition to having a hydrophobic waxy layer, their surface is enhanced with two levels of roughness on the microscale. The first level consists of 10–20 micron size bumps that do not allow large droplets to penetrate between them. The second level of roughness is made of below micron-size hairs, densely packed all over the surface. Droplets sitting on such surfaces are found in the so-called Cassie state: pockets of air remain below the droplets, and apparent contact angles between the liquid and the surface are usually greater than 150° .

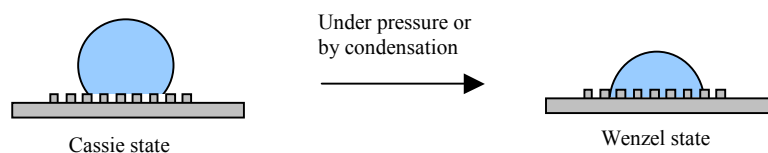


Figure 2.4 Droplet on a surface in the Cassie (metastable) state, showing superhydrophobic properties, and in the Wenzel (stable) state, wetting the surface

However, if exposed to increased pressures (e.g. by submerging at certain depths under the water), these surfaces could lose their properties and undergo transition into the Wenzel state, where droplets actually wet the surface. Indeed, recent experiments showed that the surface of the lotus leaf is covered with a hydrophilic (not hydrophobic) waxy layer ($\theta = 74^\circ$), and that it loses its superhydrophobic properties if under pressure, or if condensation occurs [45, 46]. In addition, pressure from the droplet impact can cause penetration of water into asperities and wetting of the surface (Wenzel state).

A good review of possible outcomes of drop impact on superhydrophobic surfaces, depending on the impact velocity and Wenzel roughness is given by Rioboo et al. [47]. Their experiments also showed that droplets below 0.1 mm, in the range of impact velocities from 0.1 to 10 m/s, would rebound or stay deposited on the surface. If droplets stayed deposited on the surface, they were in the Cassie state and could be easily removed. Richard and Quere [44] investigated the bouncing of water drops from a superhydrophobic surface with a contact angle of 170° , and noted perfect droplet bouncing with the coefficient of restitution close to 0.9. Bouncing and splashing of droplets on 150° surface was investigated also by Durickovic and Varland [44]. Wang et al. [48] investigated rebounding of water drops from carbon nanotube arrays and observed that for contact angles of 163° , the droplets would bounce off several times, while for contact angles of 140° , they remained pinned to the surface.

Bergeron [69], in his popular article on deposition of droplets on the leaves of plants in agricultural applications, explained that sticking or rebounding is governed by inertial, viscous and capillary forces of the drop upon the impact. One way to increase deposition is to reduce the surface tension of the liquid or increase its viscosity; for reducing deposition, the opposite holds. Therefore, in order to promote droplet bouncing, one could:

- Increase contact angle, by using low surface energy solids (e.g. Teflon), to achieve partial rebounding.
- Increase contact angle, by using superhydrophobic surfaces ($\theta > 150^\circ$), to achieve complete rebounding.

In addition, one could promote rebounding by:

- Decreasing the viscosity of the liquid, so that the droplet upon impact does not lose energy via viscous dissipation, and has more energy to bounce off.
- Increasing the surface tension of the liquid, in order to increase the contact angle and decrease the wettability.

Since the superoleophobic surfaces with high contact angles look as the most promising for our application, they are discussed in more details in the next section (Section 2.3.4).

2.4.3. Superoleophobicity

Recently, a number of authors have reported that they have synthesised surfaces which manifest superhydrophobicity and superoleophobicity at the same time. The first to report super-oil repellent surfaces were Tsujii et al. [49], who coated fractal structures on an oxidized aluminum plate surface with the trifluoromethyl groups of fluorinated monoalkylphosphates. They obtained high contact angles; for rapeseed oil 150° , and for octane 120° . Tuteja et al. [50,51] described designing parameters for such surfaces, and explained that for high contact angles of low surface tension oils, such as decane (23.8 mN/m) and octane (21.6 mN/m), a surface energy of a smooth solid of the order of 5 mN/m was needed. They synthesised a new class of hydrophobic fluoroPOSS molecules (Fluorinated Polyhedral Oligomeric Silsesquioxanes), to cover the roughened surface. Advancing and receding contact angles were 163° and 145° respectively. Wu et al. [52] treated alumina nanowire forests with perfluorocompounds and obtained contact angles higher than 150° for different oils (155.6° for crude oil, 150.4° for silicone oil).

High contact angles of oils make them potentially useful for application in causing the rebounding of oil droplets in the scrubber of the coker reactor. However, since all these surfaces are treated with organic compounds (fluoro-groups, silanes) with relatively low melting points, their application at high temperatures above 300°C is questionable. Fractal surfaces of Teflon (melting point 327°C) may provide better performance. Recently, Cao et al. [70] reported superhydrophobic surfaces (water contact angle $159 \pm 2^\circ$) produced by packing flowerlike hematite particles which are intrinsically hydrophilic. The largest asperities on the surface seemed to be in the order of 1 micron, and such surfaces did not lose their properties after heating in air at 800°C for 10 hours ($\theta=158 \pm 2^\circ$). However, they did not report tests with oils.

In the case of the scrubber section of the coker reactor, it seems that only complete rebounding could be considered as an option. Partial rebounding would leave some amount of deposits on the surface, which would eventually form a monolayer of coke deposits and the repellent surface properties would diminish. However, superhydrophobic surfaces have also 'self-cleaning' properties. Lotus leaves, feathers of birds, etc. have the property of using the water to collect all the dirt (i.e. small particles)

from their surface, while rolling down the surface. In that sense, even partial rebounding of bitumen droplets from superhydrophobic surfaces could be satisfactory. If the wash-oil that is poured from the top doesn't wet the surface, it would roll off the surface, collecting deposited bitumen droplets. Still, many practical questions remain,

- How long could superoleophobic surface be maintained clean, i.e. whether small bitumen droplets would deposit inside the microstructures so that they could not be reached and picked up by the liquid flowing down? How small should asperities on the surface be, to prevent that from happening?
- How would superhydrophobic surfaces behave at high temperatures, would they be stable, without sintering?
- Would the metastable Cassie state be diminished if the droplet impacting the surface possesses sufficient pressure to penetrate inside the pores? Is the wash-oil sprayed from the top more likely to do so?
- Does the condensation of vapours in the scrubber section occur? If so, surfaces would most probably lose the feature of superoleophobicity.

To summarize, for complete rebounding, superhydrophobic and superoleophobic surfaces, with contact angles higher than 150° are required. To repel oil droplets, in addition to the fractal structure of surface roughness, low surface energy materials are needed. Since such surfaces are not commercially available yet, we decided to test surfaces with contact angles in the range that could be obtained (20 – 94°) and see if partial rebounding [41] could reduce deposition rates. Goldshmid and Calvert [35], who investigated the collection of polystyrene and sulphur particles from aerosols onto supported liquid drops (water, glycerol, formamide, phenol), showed that with an increased contact angle in the range from 0° to 87° , there is “definite effect of interfacial tension on the collection efficiency”. These results also justify our attempts to investigate the contact angle effect in a similar range.

Chapter 3. Modeling

The main focus of this work was an experimental investigation of the transport and deposition of droplets. Simulation of the deposition phenomena would require knowing the velocity field in front of the disk, and the velocity field in the vortex behind the disk. These types of problems are nowadays usually tackled using Computational Fluid Dynamics (CFD), and this was the objective of a separate thesis work on this project (Lakghomi [36]). However, in order to at least qualitatively explain the obtained results, simple models that describe the flow field around a disk were used. For the upstream side, inviscid flow approximations have been successfully used in the past [24, 26, 27, 31]. Also, in order to estimate deposition rate on a dry surface of different materials, a model for the change of the surface coverage of the disk during deposition was developed. To compare the results of the room temperature studies with the data obtained in the Hot Unit (Song [52]), the effect of reaction of heavy hydrocarbons at elevated temperatures was modeled as well. These models were used in Section 5.4 and Chapter 6, to explain the experimental results.

3.1. Particle deposition on the upstream and downstream side

In the work of Subudhi [9], fouling in the scrubber section of the Fluid Coker was modeled as deposition from a turbulent flow parallel to the surface of the packing elements. Although the flow around bluff bodies, such as circular disks, is different from the flow over horizontal surfaces, in the vicinity of the disk surface, flow can be regarded as parallel to the surface. Although this may not be a good approximation of the flow around the small objects usually used in inertial impaction experiments (0.1–1 mm), it should be an acceptable approximation for the 5 cm diameter disks used in this work. This view is supported by the results of the flow field obtained from CFD simulations [36], but also from the simple potential flow field approximation [26, 31]. Experimental observations of the aerosol flow in the vicinity of the coupon surface by the means of shadowgraphy technique (Section 4.3.3), confirm this view. Furthermore, aside from inertial impaction, the concept of ‘eddy impaction’ (from the parallel flow), for deposition from a normal flow over cylinders, was used by Lokare et al. [53]. Therefore,

the theories of particle transport from parallel flow should also apply to some extent to this case of the normal flow.

In the case of normal flow, as stated in Chapter 2, rarely do all mechanisms of deposition occur simultaneously. When the diameter of the body is significantly larger than the diameter of the approaching particle, $R_f \ll 1$, interception can be neglected [20]. This is the case in our study, where the parameter R_f is in the order of 10^{-3} (5 cm disk and 1–100 micron droplets). If electrostatic charge on the disks is neglected, and under the assumption that the produced aerosol droplets are free of charge, electrostatic forces can also be neglected. Since we are concerned with isothermal cases (in both the Cold Unit and the Hot Unit), thermal forces are excluded from consideration. Therefore, the main mechanisms of deposition on the surface of a disk from the upward flowing aerosol (schematically shown in Fig. 3.1), can be summarized as in Table 3.1. Close to the surface, flow can be roughly considered parallel on both sides. Relevant mechanisms of deposition are presented in Fig. 3.1 (inertial impaction, gravity, convective diffusion, eddy impaction).

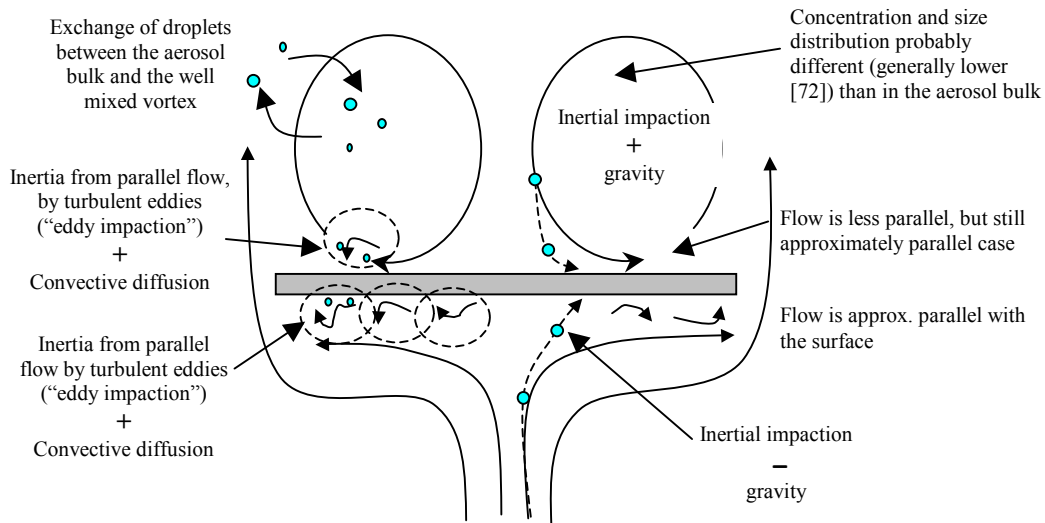


Figure 3.1 Schematic representation of the flow field around a disk, with particle transport mechanisms

Table 3.1 Summary of mechanisms of deposition on a circular disk from an upward flow

Upstream (front) side		Downstream (back) side	
Normal flow	Parallel flow	From the vortex	Parallel flow
Inertial impaction	Convective diffusion*	Inertial impaction	Convective diffusion*
Gravity in negative direction (decreases deposition)	Inertia due to turbulence (“eddy impaction”)	Gravity in positive direction (increases deposition)	Inertia due to turbulence (“eddy impaction”)

* Convective diffusion is categorized under parallel flow. However, the mass transfer coefficient is estimated from mass transfer correlations obtained for flow that is normal to disks [57].

3.2. Gas phase flow

To describe the motion of particles, the first step is to describe the flow field around the disk.

3.2.1. Continuity and momentum conservation equations

The flow of the gas phase is described by mass, momentum and energy conservation equations. Since experiments are performed at isothermal conditions, the energy equation can be omitted [54]. Therefore,

$$\text{Continuity: } \frac{\partial \rho}{\partial t} + \nabla \cdot \rho \vec{v} = 0 \quad (3.1)$$

$$\text{Momentum: } \rho \left(\frac{\partial \vec{v}}{\partial t} + \vec{v} \cdot \nabla \vec{v} \right) = -\nabla P + \mu \nabla^2 \vec{v} + \vec{F} \quad (3.2)$$

For a flow which is symmetric around the x -axis (axisymmetric flow) in cylindrical coordinates, the θ -direction can be neglected. The steady-state equations are then,

$$\frac{1}{r} \frac{\partial}{\partial r} (r v_r) + \frac{\partial v_x}{\partial x} = 0 \quad (3.3)$$

$$x: \rho \left(v_r \frac{\partial v_x}{\partial r} + v_x \frac{\partial v_x}{\partial x} \right) = -\frac{\partial p}{\partial x} + \mu \cdot \left[\frac{1}{r} \frac{\partial}{\partial r} \left(r \frac{\partial v_x}{\partial r} \right) + \frac{\partial^2 v_x}{\partial x^2} \right] + \rho g_x \quad (3.4)$$

$$r: \rho \left(v_r \frac{\partial v_r}{\partial r} + v_x \frac{\partial v_r}{\partial x} \right) = -\frac{\partial p}{\partial r} + \mu \cdot \left[\frac{1}{r} \frac{\partial}{\partial r} \left(r \frac{\partial v_r}{\partial r} \right) + \frac{\partial^2 v_r}{\partial x^2} \right] + \rho g_r \quad (3.5)$$

These are second-order nonlinear partial differential equations. They are, at present, usually solved using CFD, which also employs turbulence models to describe the flows at high Reynolds numbers. For the case of an ideal fluid (inviscid fluid, flow is characterized by irrotational motion), the equations of the flow field around the disk can be simplified to yield the equations of potential flow. This approach had been found useful in prior work (Table 2.1, Chapter 2), and was used in this study.

3.2.2. Potential flow approximation

Potential flow results when viscous forces are neglected, and is characterized by an irrotational velocity field. This approximation is valid in many cases of external flow, except very close to a solid boundary, where the action of viscosity is important, and in the wake region of a solid obstacle where instabilities and turbulence can occur [55]. In general, this approximation should be valid for high Reynolds numbers, when the ratio of inertial to viscous forces is sufficiently large ($Re > 100$, [30]). In deriving the velocity field equations, the flow of the gas is considered incompressible and the effect of gravity on the flow field is also neglected. After solving Eqs. (3.3)–(3.5), the velocity field components, are given by [26, 31],

$$\bar{v}_x = -2\bar{x} \quad (3.6.a)$$

$$\bar{v}_r = \bar{r} \quad (3.6.b)$$

where new non-dimensional variables are used: dimensionless axial and radial positions,

$$\bar{x} = \frac{x}{R_c} \text{ and } \bar{r} = \frac{r}{R_c}, \text{ and dimensionless axial and radial velocities, } \bar{v}_x = \frac{v_x}{v_0} \text{ and } \bar{v}_r = \frac{v_r}{v_0}.$$

Equations (3.6a,b) are derived neglecting the effects of column walls around the disk, and are valid for the region in front of the disk only. Salmanzadeh et al. [56] showed that capture efficiencies on the front face of a rectangular obstruction in a duct flow increased by 10–15% with the increase in the blockage ratio ($Br=A/A_{column}$) from 0.1 to 0.5. Therefore, it may be expected that this flow field, which does not consider the presence of column walls, somewhat underestimates deposition on the disk inside the column ($Br=0.45$).

3.2.3. Potential flow with a viscous sublayer

The flow field close to the coupon surface plays an important role in determining if the particle will reach the surface, especially for particles with smaller inertia. Higher radial velocities will sweep particles away from the surface, while lower radial velocities, occurring in the viscous sublayer, should allow more particles to reach the surface. To investigate the validity of the inviscid flow approximation, an attempt is made to calculate deposition with a viscous sublayer, added to the free-stream inviscid flow. A 5 mm thick viscous sublayer that has a velocity linearly increasing from $\bar{v}_r = 0$ at the coupon surface, to $\bar{v}_r = \bar{r}$ at 5 mm from the coupon, was added. From the linear velocity gradient close to the wall, and the free-stream velocity, the thickness of the boundary layer was estimated to be: 6.5 mm at 0.2 m/s, 3.8 mm at 0.4 m/s, 1.8 mm at 1 m/s and 1.2 mm at 1.6 m/s. The value of 5 mm, somewhat above most of the above estimated values, was chosen to see if it would yield a noticeable effect. Although this is a simplified model, it should indicate the sensitivity of the results to the excluded boundary layer.

$$\bar{v}_r = \begin{cases} \bar{r}, & \bar{x} < -0.2 \\ \frac{\bar{r}}{-0.2} \cdot \bar{x}, & -0.2 < \bar{x} < 0 \end{cases} \quad (3.7a,b)$$

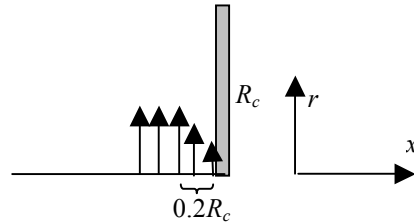


Figure 3.2 Schematics of the patched viscous sublayer, linearly increasing from $\bar{v}_r = 0$ at $\bar{x} = 0$, to $\bar{v}_r = \bar{r}$ at $\bar{x} = -0.2$

3.3. Inertial impaction mechanism

Calculation of the trajectory of droplets in the flow field requires that particle motion be described. Although the model for inertial deposition on a circular disk from potential flow was presented by Ranz and Wong [26], it was concerned with horizontal flows, and hence the effect of gravity was not included. Also, in order to obtain linear

equations that could be solved analytically, they used the Stokes drag force on the particles.

Since we are concerned with the upward flow of an aerosol, the model should include the effect of gravity. To represent the drag force on larger particles more faithfully, it was also desirable to include a non-Stokesian drag force in the calculations. The results of simulations for the upward flow captured some interesting characteristics of inertial impaction. Also, it turned out that with gravity in the downward direction, the same model was capable of explaining the trends of deposition on the downstream side (Chapter 5). The detailed inertial particle deposition model with its solution procedure (analytical and numerical) is described in *Appendix C*. Here, only the most important steps are presented.

The equation of particle motion in vector notation, in the presence of gravity, under the assumption of Stokes drag force on the particle is given by [26],

$$\frac{d(m\vec{u})}{dt} = 3\pi\mu D_p (\vec{v} - \vec{u}) + m\vec{g} \quad (3.8)$$

where u is particle velocity, v is fluid velocity, and mg is the gravity force. If the vector notation is removed, and the gravity force is retained, for each component we can write,

$$x: \frac{d(mu_x)}{dt} = 3\pi\mu D_p (v_x - u_x) + pmg \quad (3.9a)$$

$$r: \frac{d(mu_r)}{dt} = 3\pi\mu D_p (v_r - u_r) \quad (3.9b)$$

where parameter $p \in \{-1, 0, 1\}$ denotes the orientation of the gravity field. After introducing dimensionless variables, the following equations are obtained,

$$x: 2St \frac{d^2 \bar{x}}{d\bar{t}^2} + \frac{d\bar{x}}{d\bar{t}} - \bar{v}_x - p \frac{t_p g}{v_0} = 0 \quad (3.10a)$$

$$r: 2St \frac{d^2 \bar{r}}{d\bar{t}^2} + \frac{d\bar{r}}{d\bar{t}} - \bar{v}_r = 0. \quad (3.10b)$$

Here, t_p is the particle relaxation time, $t_p = \frac{\rho_p D_p^2}{18\mu_a}$, and St is the Stokes number

$St = \frac{t_p v_0}{2R_c}$. If the equations of the flow field derived from the potential flow

approximation are used (Eqs. (3.7a,b)), and the solution procedure described in detail in *Appendix C* is followed, the following expression for the capture efficiencies can be obtained,

$$E = \left(\frac{z_2 - z_1}{z_2 e^{z_1 \bar{t}'} - z_1 e^{z_2 \bar{t}'}} \right)^2 \quad (3.11)$$

where z_1 and z_2 are solutions of the characteristic equation $z_{1,2} = \frac{-1 \pm \sqrt{1-16St}}{4St}$ (Eq.

(C.13)), and \bar{t}' is the time needed for particle to reach the coupon surface (Eq. (C.32)).

When gravity is involved, \bar{t}' must be calculated numerically, by solving Eq. (C.37). Also, if the non-Stokesian drag force is used, Eqs. (3.10a,b) are nonlinear, and must be solved numerically.

It should be mentioned that Eqs.(3.9a,b) are not strictly valid for horizontal flow, since the problem is not axisymmetric anymore due to the presence of gravity. However, in the case of fine droplets with small terminal velocities, gravity can be neglected and the approximation expressed by Eqs. (3.9a,b) should be satisfactory.

Distribution of deposits along the coupon radius predicted by this model can be deduced from the following equation (also derived in *Appendix C*),

$$\bar{r}(\bar{r}_0) = \bar{r}_0 \left(\frac{z_2}{z_2 - z_1} \right) e^{z_1 \bar{t}'} + \bar{r}_0 \left(\frac{z_1}{z_1 - z_2} \right) e^{z_2 \bar{t}'} = const \cdot \bar{r}_0 \quad (3.12)$$

where \bar{r}_0 is the initial radial position of the particle where it is injected. The equation states that the final position of the particle on the disk is linear function of its initial radial position. This indicates that deposits should be uniformly distributed along the coupon radius.

3.4. Particle transport due to turbulence

Since deposition from the normal flow also occurs from the flow parallel to the surface (Table 2.1, Fig. 3.1), a description of the latter deposition phenomena was attempted with the models described below.

3.4.1. Particle transport due to convective diffusion

As already stated in Chapter 2, in the diffusion regime, submicron and micron-size droplets are carried to the surface by Brownian diffusion through the boundary layer. The transport coefficients can then be obtained from the relevant empirical correlations or theoretically developed equations for forced convection mass transfer [12]. Empirical correlations for forced convection mass transfer from circular disks are given by Beg [57], who investigated sublimation of naphthalene from 5 cm disks into air. Mass transfer from the front side of a disk can be described by the following equation,

$$Sh = 0.67(Re)^{0.54} (Sc)^{1/3} \quad (3.13)$$

and from the back side with,

$$Sh = 0.532(Re)^{0.60} (Sc)^{1/3} - 0.67(Re)^{0.54} (Sc)^{1/3} \quad (3.14)$$

for Reynolds numbers in the range $270 < Re < 34900$, and a Schmidt number of 1.75. If we use values for the Brownian diffusivity of droplets in the Schmidt ($Sc = \nu_a/D$) and Sherwood ($Sh = k_t/D$) numbers, we can estimate deposition coefficients (k_t) for different droplet sizes at different Reynolds numbers.

3.4.2. Particle transport due to turbulent diffusion in the inertial regime

In addition to convective diffusion, when the flow is turbulent, particles can be deposited by inertia. If we can assume a parallel flow to the surface (Fig. 3.1), and if the particles are sufficiently large ($t_p^+ > 0.2$), turbulent eddies give them some transverse free-flight velocity, which enables particles to travel through the viscous sublayer (Fig. 3.1). This assumption holds true more for the upstream side than for the downstream side, because of the nicely defined flow field in front of the coupon, and imprecisely defined turbulent wake behind the coupon (Fig. 3.1). Correlations for deposition from turbulent

flow in the inertia regime, given in Chapter 2 (Eqs. (2.2), (2.6a,b)), were used for this purpose.

3.5. Surface coverage

In order to investigate the effect of the contact angle on deposition, surfaces of disks had to be kept dry somehow, so that deposition does not take place on the liquid layer. One possibility was to use Vycor[®] porous glass disks (pore diameter 0.4 microns), that would absorb the liquid film from the surface by capillary forces. To keep the surface dry, the rate of absorption should be faster than the deposition rate. Calculations of the rate of absorption, using the Washburn equation, showed that this process would not be sufficiently fast; larger capillaries in the material, or a less viscous liquid were needed.

The other possibility was to perform short experiments (10–120 sec.), where deposition would still take place on a dry surface. In order to estimate deposition rates on a dry and irrigated surface from experimental data, this approach required a proper model. This is for the reason that low amounts of deposits were expected from such short experiments (1–3 mg), and a scatter in the experimental data was anticipated.

3.5.1. Deposition model

The deposition rate on a disk surface, partly covered with liquid, can be written as,

$$r_d = r_{d,1} \cdot (1 - y) + r_{d,2} \cdot y \quad (3.15)$$

where $r_{d,1}$ is the deposition rate on a dry surface and $r_{d,2}$ is the deposition rate on a wet surface. Surface coverage y , is defined as the ratio of the surface area covered with liquid and the total surface area, $y = \frac{A_{wet}}{A}$. If we assume that deposition on the wet surface does not increase surface coverage (a small droplet will be ‘eaten’ by a liquid deposit without spreading too much), the decrease in a dry surface area can be written as a first-order process,

$$\frac{dA_{dry}}{dt} = -k_s \cdot A_{dry} \quad (3.16)$$

The deposition constant, k_s , is equal to $\frac{r_{d,1}}{m_s \cdot A}$, where m_s is specific mass (kg/m^2) of a droplet sitting on a surface,

$$m_s = \frac{\frac{D_p^3 \pi}{6} \cdot \rho_p}{\frac{D_p^2 \pi}{4}} = \frac{2}{3} D_p \cdot \rho_p \cdot (k(\theta))^2 \quad (3.17)$$

Here, D_p is the diameter of a droplet in the aerosol, $D_p' = k(\theta) \cdot D_p$ is the diameter of a droplet on the surface, and $k(\theta)$ is the correction factor derived in *Appendix C*. Using the definition of the surface coverage, and replacing A_{dry} with $A - A_{wet}$, Eq. (3.16) becomes,

$$\frac{dy}{dt} = k_s \cdot (1 - y) \quad (3.18)$$

After integration of Eq. (3.18) we get,

$$y(t) = 1 - e^{-\frac{r_{d,1} \cdot t}{A \cdot m_s}} \quad (3.19)$$

Equation (3.15) then finally becomes,

$$r_d(t) = (r_{d,1} - r_{d,2}) \cdot e^{-\frac{r_{d,1} \cdot t}{A \cdot m_s}} + r_{d,2} \quad (3.20)$$

For a size distribution of droplets, specific mass m_s to be used in Eq. (3.20) is calculated according to:

$$m_s = \sum_{i=1}^n \frac{2}{3} \rho_p \cdot (k(\theta))^2 \cdot (D_{p,i} V_{i,downstream}) \quad (3.21)$$

where $D_{p,i}$ is the maximum diameter of the class i of the distribution in the aerosol, having relative volume frequency on the downstream side of the coupon, $V_{i,downstream}$.

3.5.2. Estimation of deposition rates

Deposition rates from individual experiments are calculated from the mass of deposits at the end of each experiment i ,

$$r_{d,i}^{\text{exp}} = \frac{m(\tau_i) - m(0)}{\tau_i} \quad (3.22)$$

where τ_i is duration of the experiment i , $m(0)$ and $m(\tau_i)$ denote the masses of the deposits at the beginning and end of the experiment, and $r_{d,i}^{\text{exp}}$ is the deposition rate calculated from experimental data. This deposition rate represents the integral of all deposition rates during the experiment and is given by,

$$r_{d,i}^{\text{exp}} = \frac{\int_0^{\tau_i} r_d(t) dt}{\tau_i} \quad (3.23)$$

Integral deposition rate at the end of experiment predicted by the model, $r_{d,i}^{\text{int}}$, is obtained by integrating Eq. (3.20) from 0 to τ_i . This gives,

$$r_{d,i}^{\text{int}} = \frac{A \cdot m_s}{\tau_i} \cdot \left(1 - \frac{r_{d,2}}{r_{d,1}}\right) \cdot \left(1 - e^{-\frac{r_{d,1}}{A \cdot m_s} \tau_i}\right) + r_{d,2} \quad (3.24)$$

To estimate $r_{d,1}$ and $r_{d,2}$ from experimental data, sum of squares of relative errors between deposition rates from experiments (Eq. (3.22)) and from the model predictions (Eq. (3.24)) was minimized. The objective function also included weights to account for the variability in measurements. The parameter estimation problem can be finally stated as,

$$\underset{r_{d,1}, r_{d,2}}{\text{Minimize}} \sum_{i=1}^n \left(\frac{r_{d,i}^{\text{exp}} - r_{d,i}^{\text{int}}}{r_{d,i}^{\text{exp}}} \right)^2 \cdot \frac{r_{d,i}^{\text{exp}} \cdot \tau_i}{\underbrace{\max(r_{d,i}^{\text{exp}} \cdot \tau_i)}_{\text{weights}}} \quad (3.25)$$

3.6. Deposition coefficients

Deposition coefficients and capture efficiencies calculated from Eqs. (2.7) and (2.8) are valid only for monosize aerosols, or for the particular aerosol drop size distribution used in the experiment (as was the case in this study). Since drop size distributions on the disk surface and in the aerosol were measured, it was possible to calculate the deposition coefficients for each droplet size. Knowing the deposition coefficients for each droplet size and velocity gives more generality to the obtained

results, since deposition rates for any size distribution at a given velocity can then be easily calculated. For the upstream side, we can write,

$$k_{i,upstream} = \frac{r_d \cdot V_{i,upstream}}{A \cdot c_b \cdot V_{i,aerosol}} \quad (3.26)$$

$$E_{i,upstream} = \frac{r_d \cdot V_{i,upstream}}{A \cdot c_b \cdot V_{i,aerosol}} \frac{1}{U} = \frac{k_{i,upstream}}{U} \quad (3.27)$$

where $k_{i,upstream}$ is the deposition coefficient of the droplet class i for the upstream side, $V_{i,upstream}$ is the volume relative frequency of the droplet class i on the upstream side of the coupon, and $V_{i,aerosol}$ is the volume relative frequency of the droplet class i in the aerosol. In Eq. (3.27), $E_{i,upstream}$ is capture efficiency of the droplet class i for the upstream side, and U is the gas velocity. The same equations (only with index ‘downstream’) are valid for the downstream side too.

3.7. Droplet size distribution fitting

To fit the size distribution of droplets in the aerosol produced by atomization, usually a two-parameter log-normal probability density function is employed [77]. This ‘skewed’ distribution is widely encountered in nature [78]. In our case, generated size distribution of droplets (presumably log-normal) was affected by deposition of droplets from the outer part of the spray cone on the column walls around the nozzle, and by removal of large droplets in the elbows (see Section 4.1.1.1). Therefore, it is possible that the size distribution of droplets that remain in the aerosol is a modified log-normal distribution, which can not be fitted satisfactorily by adjusting the two parameters only. To allow for a proper fitting, a standard log-normal probability density function was extended with two additional parameters (a_1 and a_3):

$$f_x(x, \mathbf{a}) = \frac{a_1}{a_4 \sqrt{2\pi}(x - a_2)} \exp\left[-\frac{(\ln(x - a_2) - a_3)^2}{2a_4^2}\right] \quad (3.28)$$

where x represents the independent variable, and \mathbf{a} is the vector of four parameters (a_1, a_2, a_3, a_4) to be determined by fitting. In the fitting procedure, a sum of squares of

differences between the model predictions and experimental measurements (2-norm) was minimized (function *f2lognormalpdf.m* in *Appendix D*),

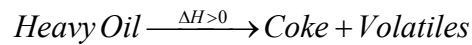
$$\text{Minimize}_a \sum_{i=1}^{i_{\max}} \left(f_x(D_{p,i}, \mathbf{a}) - V_{i,\text{aerosol}} \right)^2 \quad (3.29)$$

It proved that in our case, more meaningful fitting of the experimental data was obtained by setting the first parameter $a_1=1$. Therefore, only parameters a_2, a_3, a_4 were reported in the tables presented in *Appendix E*.

3.8. Reaction

In order to compare results of the room temperature studies with the data obtained in the Hot Unit (Song [52]), the effect of reaction of heavy hydrocarbons at elevated temperatures had to be considered and required modeling.

In the high temperature unit experiments, deposits of heavy oil droplets were exposed to temperatures from 295°C to 425°C. At these temperatures, heavy oil undergoes thermal decomposition into volatile fractions and coke,



Volatiles evaporate from the coupon surface and can reduce the observed deposition rate (or accumulation rate). Droplets deposited at the beginning of the experiment have more time to react than droplets deposited later on. Therefore, the rate of reaction during the experiment is changing. Deposits on the coupon can be represented as a series of thin layers, as in Fig. 3.3, with the first layer being deposited at the start of experiment, and the last layer n being deposited at the end.

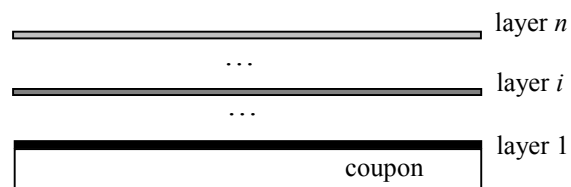


Figure 3.3 Schematic representation of the discrete amounts of deposits on the coupon surface. Layer 1 had more time to react than layer n and release more volatiles

Assuming a first-order decomposition reaction of heavy oils (Yue et al. [58]), the weight loss from the i -th layer (Fig. 3.3) can be written as,

$$\frac{dm_i}{dt} = -k_r \cdot (m_i - m_{i,f}) \quad (3.30)$$

where k_r is the first-order reaction constant, and $m_{i,f}$ is the mass of the layer i at the end of reaction ($t=\infty$). After integration and differentiation of Eq. (3.30) we get,

$$\frac{dm_i}{dt} = -k_r \cdot (m_{i,0} - m_{i,f}) \cdot e^{-k_r \cdot (t-t_i)} \quad (3.31)$$

where $m_{i,0}$ is the mass of the freshly deposited layer, and t_i is the moment of deposition of the layer i . The accumulation (fouling) rate is then the sum of the deposition rate r_d , and the weight loss rates from all n layers (assuming no restriction due to overlying layers),

$$\frac{dm}{dt} = r_d + \sum_{i=1}^n \left(\frac{dm_i}{dt} \right) \quad (3.32)$$

Substituting Eq. (3.31) into Eq. (3.32), along with $m_{i,f} = m_{i,0} \cdot MCR$, results in,

$$\frac{dm}{dt} = r_d - k_r \cdot (1 - MCR) \cdot \sum_{i=1}^n m_{i,0} \cdot e^{-k_r \cdot (t_n - t_i)} \quad (3.33)$$

In the previous equation MCR stands for Micro Carbon Residue, which is a measure of potential coke yield from a given feedstock, obtained by heating the sample under prescribed conditions of time and temperature (Yue et al. [58]).

The right hand side of Eq. (3.31) is equivalent to $r_d - k_r \cdot (1 - MCR) \cdot \sum_{i=1}^n m_{i,0} \cdot e^{-k_r \cdot t_i}$. The sum can be replaced by the integral, and since $m_{i,0} = r_d \cdot (t_{i+1} - t_i)$, it is also $dm_{i,0} = r_d \cdot dt$. This yields,

$$\frac{dm}{dt} = r_d \cdot \left(1 - k_r \cdot (1 - MCR) \cdot \int_0^t e^{-k_r \cdot t} dt \right) \quad (3.34)$$

After integration, the accumulation rate is finally given by,

$$\frac{dm}{dt} = r_d \cdot (MCR + (1 - MCR) \cdot e^{-k_r t}) \quad (3.35)$$

and the weight of deposits as a function of time is,

$$m(t) = r_d \cdot \left(MCR \cdot t + \frac{1 - MCR}{k_r} \cdot (1 - e^{-k_r t}) \right) \quad (3.36)$$

In the paper of Yue et al. [58], the yield of volatiles from the decomposition of Athabasca pitch is described as $\frac{dV}{dt} = k \cdot (V^* - V) = k \cdot (1 - MCR - V)$. This form is essentially equivalent to Eq. (3.30), with the constant k being equal to k_r . For the first-order reaction constant, $k_r = k_{r,0} \cdot \exp(-E_a / RT)$, the pre-exponential factor and activation energy values (adopted from Yue et al. [58]) are $k_{r,0} = 1.2334 \cdot 10^{13} \text{ min}^{-1}$ and $E_a = 197.5 \text{ kJ/mol}$. Table 3.2 shows limiting cases for the effect of reaction over time.

Table 3.2 Accumulation rate and mass of deposits as a function of time

	t	$t = 0$	$t = \infty$
Accumulation rate	$r_d \cdot [MCR + (1 - MCR) \cdot e^{-k_r t}]$	r_d	$r_d \cdot MCR$
Mass of deposits	$r_d \cdot \left[MCR \cdot t + \frac{(1 - MCR)}{k_r} \cdot (1 - e^{-k_r t}) \right]$	0	$r_d \cdot MCR \cdot t$

To compare the results from room temperature and high temperature units, size distribution of droplets in the Hot Unit experiments had to be known. The following section (Section 3.9) describes how this size distribution was estimated.

3.9. Drop size estimation in the Hot Unit

In order to obtain high temperatures (up to 425°C) in the Hot Unit, heating elements were required to be placed around and along the whole chamber length (Fig. 4.2). With the heating elements in place, setting up a shadowgraphy system, that would look inside the chamber interior, and measure the droplet size distribution, presented a difficulty. It was also estimated that, due to the high temperature difference between the chamber interior and the environment, condensation of vapours from the chamber would

occur on the inner side of glass slides (Fig. 4.17), and block the camera view field. This essentially eliminates the possibility of proper measurements of the droplet size distribution. The shadowgraphy system was therefore used only on the Cold Unit. In the Hot Unit experiments, size distribution was estimated with the aid of an empirical correlation (Eq. (3.37)), and shadowgraphy measurements performed in the Cold Unit (using the Hot Unit nozzle).

Firstly, the droplet size distribution at a few common gas and liquid flow rates to the nozzle (of the Hot Unit experiments), using the Hot Unit nozzle and air and water as fluids, was measured with the shadowgraphy technique in the Cold Unit. Then, the empirical correlation for twin fluid atomizers [59] was used to calculate the volume median diameter (Eq. (3.37)) of the size distribution, for the same operating conditions. By comparing the measured and calculated volume median diameters in the Cold Unit, a correction factor was obtained. This factor indicates how many times the true (measured) volume median diameter is larger or smaller than the diameter predicted by the correlation (due to the reasons discussed below). The correction factor was then used to correct volume median diameters predicted by the correlation at high temperature conditions, and estimate the ‘true’ value, which would most probably be measured with shadowgraphy.

The volume median diameter, VMD , can be calculated from the following empirical equation (Wigg [59]),

$$VMD = 200 \cdot N \cdot \left[1 + 2.5 \cdot \left(\frac{\dot{M}_l}{\dot{M}_g} \right)^{0.6} \cdot \dot{M}_l^{0.1} \right] \quad (3.37)$$

$$N = \nu_l^{0.5} \cdot \dot{M}_l^{0.1} \cdot \left(1 + \frac{\dot{M}_l}{\dot{M}_g} \right)^{0.5} \cdot h^{0.1} \cdot \sigma_l^{0.2} \cdot \rho_g^{-0.3} \cdot (V_g - V_l)^{-1}$$

valid for a wide range of parameters. Lower limit of the volume median diameter data correlated with this equation is about 10 microns [59]. Symbols in the Eq. (3.37) are explained in the Nomenclature, along with the appropriate units that should be used. Approximations used to estimate missing parameters in this equation are as follows,

- The surface tension of 5% and 10% MEHR in Voltesso is assumed to be 49 mN/m, as for pure Voltesso [71]. Voltesso is a mixture of volatile oil, while MEHR stands for a mixture of heavy hydrocarbon materials. The critical temperature of Voltesso (IBP=218°C, FBP=420°C) is estimated to be about 500°C, from comparison of boiling points and critical temperatures of n-paraffins given in [60]. Surface tension dependence on temperature can be approximated from the following linear equation,

$$\sigma_l(T) = \frac{(0 - \sigma_{l,0})}{(T_c - T_0)} \cdot (T - T_0) + \sigma_{l,0} \quad (3.38)$$

According to Eq. (3.37), the volume median diameter is not very sensitive to surface tension ($VMD \sim \sigma_l^{0.2}$), and therefore these assumptions are acceptable.

- The temperature of the liquid in the nozzle, which affects liquid and gas properties, is calculated from the heat balance equation, assuming ideal mixing of nitrogen and oil in the nozzle,

$$T = \frac{\dot{M}_{N_2} C_{p,N_2} T_{N_2} + \dot{M}_{oil} C_{p,oil} T_{oil}}{\dot{M}_{N_2} C_{p,N_2} + \dot{M}_{oil} C_{p,oil}} \quad (3.39)$$

The temperature of oil in the nozzle was taken to be 100°C, at which $C_{p,oil} = 2.1 \text{ kJ}/(\text{kgK})$ and $C_{p,N_2} = 1.05 \text{ kJ}/(\text{kgK})$ [52]. The resulting nozzle temperatures varied between 170°C and 215°C for all runs.

- There is no evaporation of the liquid in the nozzle itself, and thus no increase in the gas flow rate. This seems a valid assumption, since the maximal estimated temperature in the nozzle (215°C) is just below the Voltesso's initial boiling point (218°C).
- The velocities of gas, V_g , and liquid, V_l , are calculated from their flow rates through the nozzle orifice, at the nozzle temperature and pressure. Although it is not stated clearly how these velocities should be calculated, the same method was used for obtaining the correction factor from the Cold Unit experiments and in subsequent drop size estimation in the Hot Unit. Therefore, the choice for calculating the correction factor should have no effect on the estimated volume median diameter.

- The viscosities of oils at a given temperature are obtained by extrapolating available experimental data for 5% and 10% MEBR (Hot Unit Progress Report, Feb 27th, 2009) in the temperature range 30–150°C using the equation,

$$\mu_{oil} = 1000 \cdot 10^{\left(-3 + \frac{69.06 \cdot e^{-0.0126 \cdot T}}{26.9}\right)} \quad (3.40)$$

where T is in (°C) and μ_{oil} is in (cP). The extrapolated curve followed the same trend as that of the experimental data, and Eq. (3.40) is believed to be a good approximation. Estimated viscosities were in the range 1.3–1.8 cP.

- The percentage of oil as droplets after evaporation is taken from the Hot Unit data obtained from HYSYS predictions [52].

The drop size distribution was estimated according to the following procedure,

1. The Hot Unit nozzle was placed in the Cold Unit and size distribution for nine Hot Unit run settings, with the air and water as fluids, was measured with shadowgraphy method (run numbers: S-5, S-17, S-18, S-19, S-20, S-21, S-27, S-34, S-36) [52].
2. The empirical correlation (Eq. (3.37)) was used to estimate volume median diameter for these experiments, using the physical properties of air and water.
3. The measured volume median diameter was about 4–5 times lower than the volume median diameter predicted by the correlation, leading to correction factors of 0.25 (at liquid flow rate 10 ml/min) and 0.17 (at the liquid flow rate 20 ml/min). The measured droplet sizes are lower than predicted by the correlation, most likely due to the impaction of large droplets from the spray cone, on the column walls close to the nozzle. The smaller correction factor at the higher liquid flow rate (0.17 vs. 0.25) is probably due to the fact that, although larger droplets were generated, all droplets above some ‘critical drop diameter’ impacted column walls. Therefore, the aerosol was left only with fine droplets, which resulted in larger discrepancy between predicted and measured values and the smaller correction factor. The other reason could be the ambiguous use of the characteristic dimension ‘ h ’ in the correlation, since it is not clearly stated how this value should be chosen [59].

4. To estimate droplet diameters in the Hot Unit, estimated volume median diameters at Hot Unit conditions (at a different temperature, with different oil and gas properties, e.g. Eq. (3.40)) were multiplied by the correction factor 0.25 when the oil flow rate was 10 ml/min, and by 0.17 when the flow rate was 20 ml/min.
5. The final volume median diameter of the size distribution after evaporation was calculated from the fraction of oil that remained in the liquid phase, from the HYSYS predictions [52].
6. A log-normal size distribution, with the volume median diameter as calculated in point 5, was generated and used in further calculations.

Chapter 4. Experimental Study

4.1. Cold Unit apparatus

In order to experimentally investigate the deposition of droplets from an aerosol at room temperature, the Cold Unit apparatus, with its measurement and data acquisition systems, was designed and built (by the author). The Unit consisted of a 180 cm high glass column, 7.5 cm inside diameter, in which the 5 cm diameter circular coupon was placed 55 cm below the top of the column (Fig. 4.1). The coupon was attached to a 1.6 mm diameter st. steel rod connected to a load cell, which was positioned 10 cm above the column.

The aerosol was generated in a two-fluid nozzle, using air and a 50% wt. aqueous sugar solution or tri-ethylene glycol. Before entering the vertical column, the aerosol passed through two short sections (45 cm and 30 cm) connected with 90° and 45° elbows, in order to remove large droplets (>100 microns). Since the atomizer was placed in the 7.5 cm diameter column, droplets from the outer part of the spray cone deposited on the column walls, creating a liquid film. This liquid was continuously drained and collected below the column as a washdown stream. The concentration of droplets in the aerosol was then determined as the difference between the flow rate of liquid to the nozzle and the washdown flow rate (Section 4.3.1), divided by the volumetric flow of the air.

The aerosol droplet size distribution was measured with a shadowgraphy system, installed in the middle section of the column. For this purpose, the flow of aerosol had to be momentarily stopped (Section 4.3.3). The exit from the column was placed about 45 cm above the coupon, which was high enough behind the coupon, not to disturb the flow.

The droplet size distribution was changed by changing the flow rate of liquid to the nozzle, at a constant air flow rate. The volume median diameter of the distribution varied between 3.9 and 7.5 microns. The velocity in the column was changed by adding secondary air to the column. This was done at constant air and liquid flow rates to the nozzle, in order to keep the size distribution constant. The range of superficial velocities covered was from 0.05 to 1.5 m/s. The complete Cold Unit operating procedure is given in *Appendix A*.

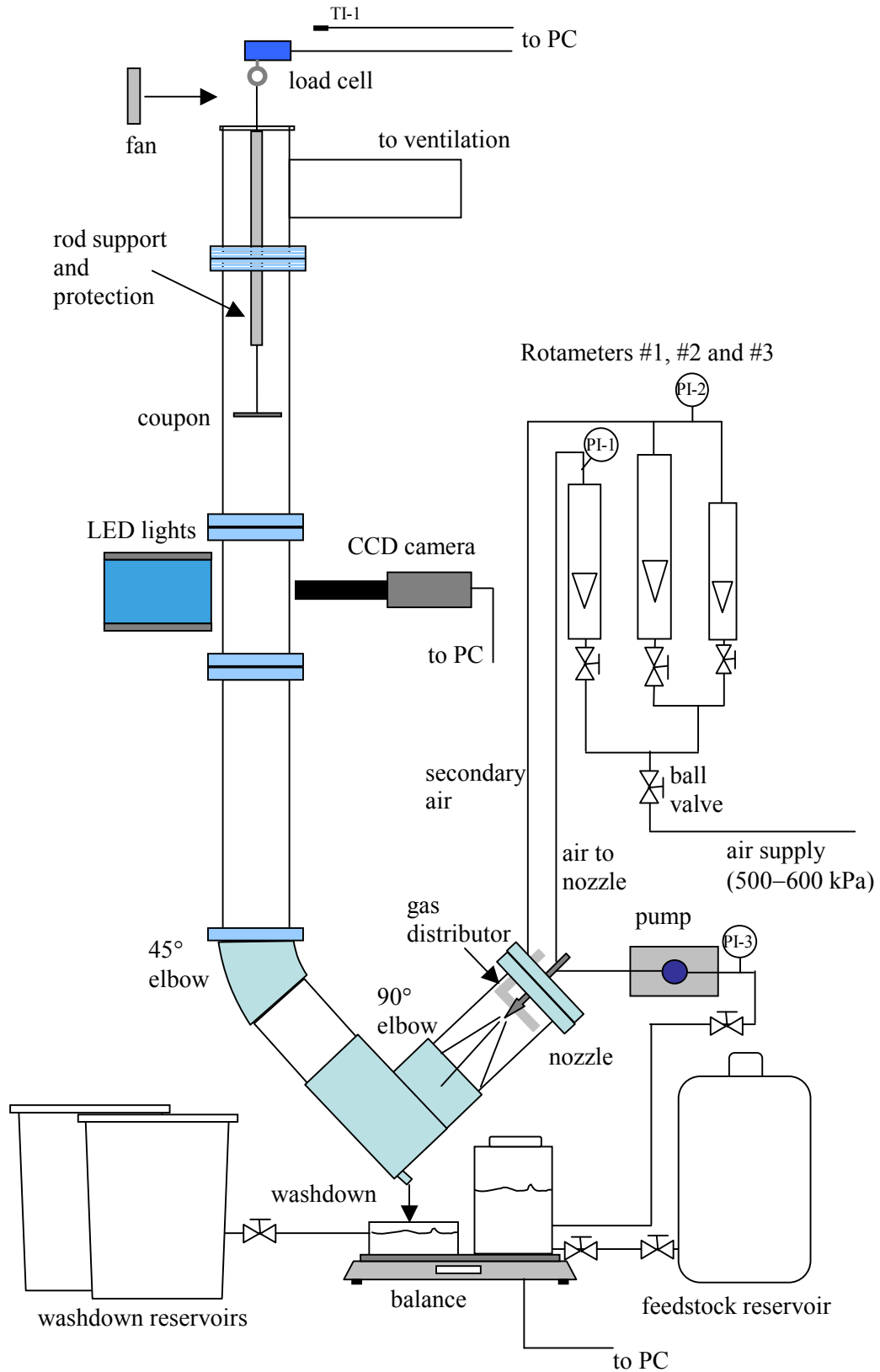


Figure 4.1 Schematic of the Cold Unit apparatus

4.1.1. Cold Unit details

4.1.1.1. Cold Unit Setup #1 and Setup #2

Initially, the Cold Unit nozzle was positioned below the column. At velocities about 0.8 m/s and higher, large droplets from the aerosol (100 microns and larger) were depositing on the coupon upstream surface, controlling the deposition rate. Although the gas velocity profile close to the coupon was well developed (according to CFD simulations [36]), droplets reaching the coupon did not have uniform velocities. The main reason for large droplets having higher velocities is that the air exiting the nozzle orifice at about 100 m/s transferred momentum to the droplets. This momentum dissipated faster for smaller droplets, because of their smaller particle relaxation time, but the large droplets retained their momentum longer, eventually reaching the coupon surface. Velocities of these large droplets were significantly higher than the aerosol bulk velocity.

To remove large droplets, one 45 cm long PVC column section with a 90° elbow was added to the bottom of the column. Although it was successful in droplet removal, it was not suitable for continuous draining of the washdown liquid and proper measurement of the aerosol concentration. The 90° elbow was replaced with a 45° elbow (Fig. 4.2), but draining issues persisted. Secondary air from the gas distributor exerted drag force on the liquid film, preventing it from flowing down, which eventually resulted in air from the nozzle bubbling through liquid.

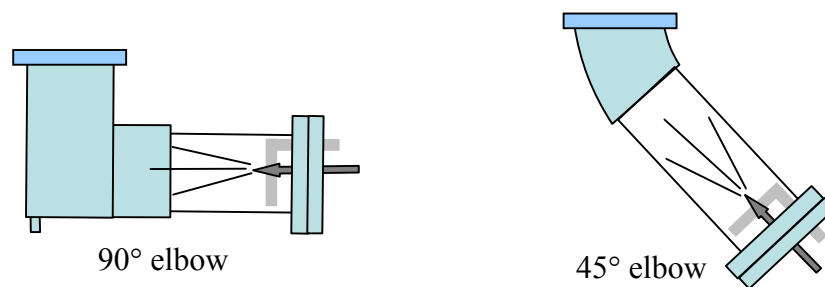


Figure 4.2 90° and 45° elbows used for removal of large droplets

Finally, a solution was obtained by installing one column section with the 90° elbow, followed by a second section with a 45° elbow, as shown in Figs. 4.1 and 4.3 (Setup #1). Draining of the liquid from the column was stable, since the air from the gas distributor helped the flow of the liquid film from the column walls.

For the experiments with the Hot Unit nozzle, the nozzle was installed at the bottom of the column (Setup #2, Fig. 4.3). It worked sufficiently well in terms of draining, although the upstream side of the coupon was still collecting large droplets for the reasons mentioned above. Upstream results from these experiments were disregarded, and only results from the downstream deposition were used (Section 5.1.2.2).

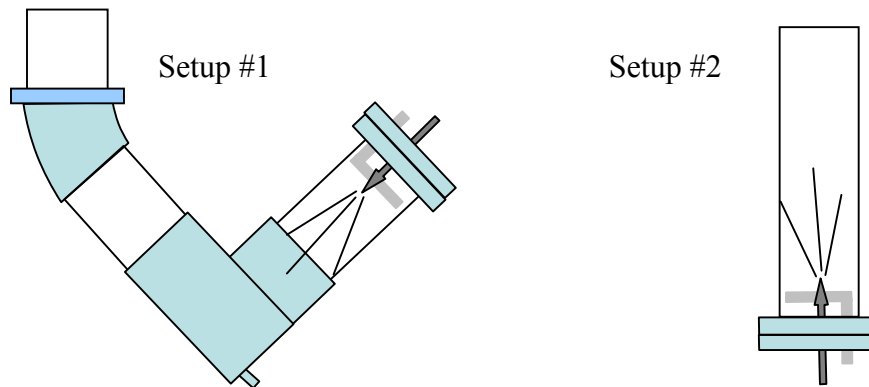


Figure 4.3 Cold Unit Setup #1 and Setup #2, used in the experiments. Setup #1 was used with the Cold Unit nozzle and the nozzle from Spraying Systems Co., while Setup #2 was used for the experiments with the Hot Unit nozzle

4.1.1.2. Atomizers

Two atomizers (nozzles) were used in the experiments: the Cold Unit nozzle and the Hot Unit nozzle. A third atomizer (Quick Mist, from Spraying Systems Co.) was used for shadowgraphy validation only. The details of all three nozzles are given in Figs. 4.4–4.6.

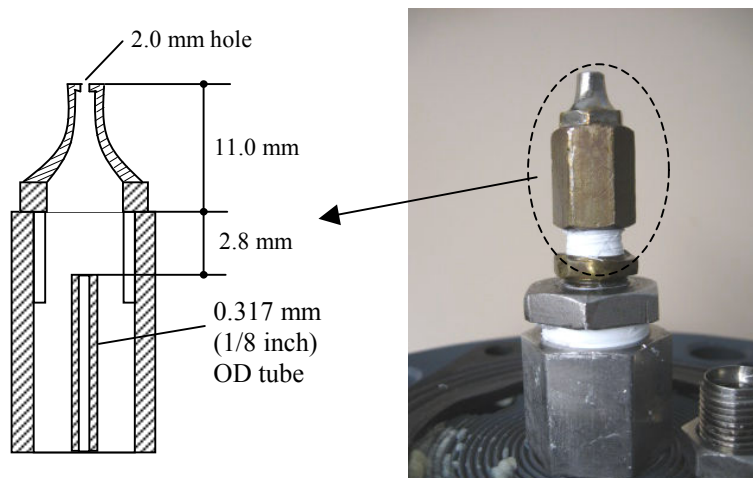


Figure 4.4 Cold Unit nozzle, used in the setup with elbows (Setup #1)

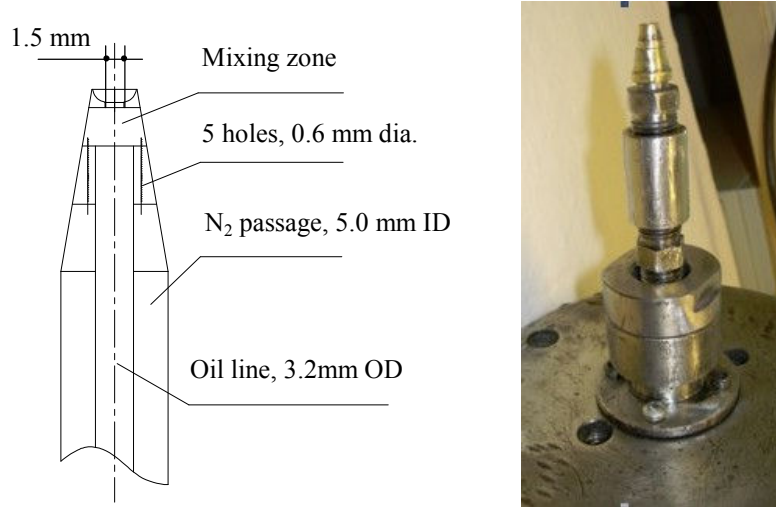


Figure 4.5 Hot Unit nozzle, used in the position below the column (Setup #2)

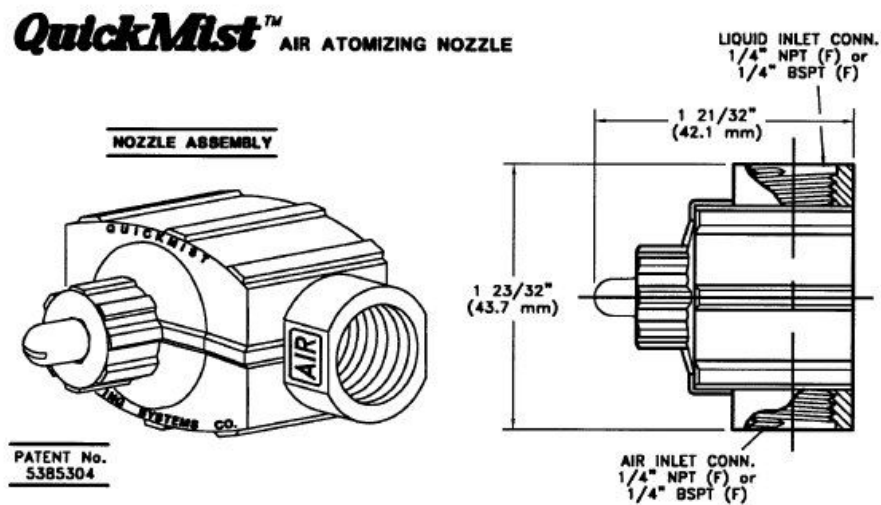


Figure 4.6 1/4QMJ + SUQR220B QuickMist™ nozzle, used in experiments for shadowgraphy validation

4.1.2.3. Gas distributor

In order to evenly introduce secondary air in the column, a gas distributor made of 9.52 mm (3/8 inch) OD stainless steel tube, was placed around the nozzle. Fifteen 2.3 mm holes, evenly spaced, were drilled along the perimeter of the distributor (Fig. 4.7).

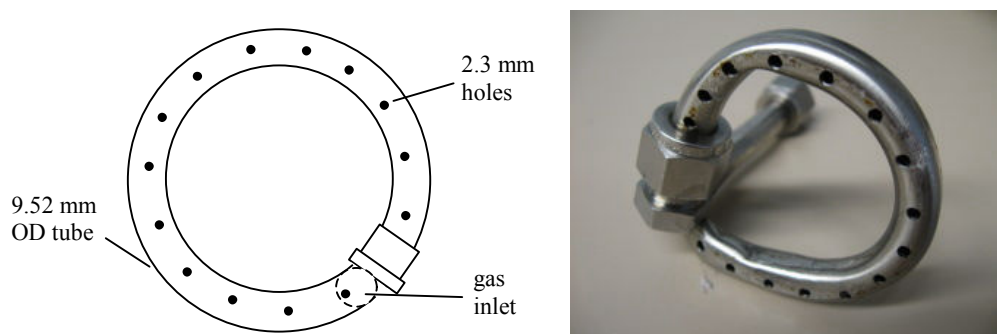


Figure 4.7 Drawing and the picture of the gas distributor in the Cold Unit

At first, the gas distributor was positioned at the bottom of the column, while the nozzle was installed as in Setup #1. This was done in order to change the concentration of the aerosol in a controlled manner: by diluting the aerosol with the known flow rate of pure air that would mix with the aerosol. This arrangement did not work well since the turbulence created by introduced secondary air caused significant deposition of droplets on the column walls. The distributor was then placed close to the nozzle, and the concentration of droplets in the aerosol was measured at each operating condition.

4.1.2.4. Other settings

The exit pipe from the column was placed 15–20 cm away from the ventilation suction. This was done to eliminate significant fluctuations of the load cell readings (max. ± 300 mg), caused by variations in the ventilation pressure. If the pressure drop downstream of the column was significant, and the column operated at pressures higher than atmospheric, variations in the ventilation pressure would not cause significant fluctuation in the load cell readings.

Close to the load cell, a small computer fan (50 W) was installed in order to blow away droplets passing through the clearance between the rod and the cap (Fig. 4.8). It was determined that, at velocities higher than 1 m/s, these aerosol droplets were depositing in the load cell, causing permanent load cell failures.

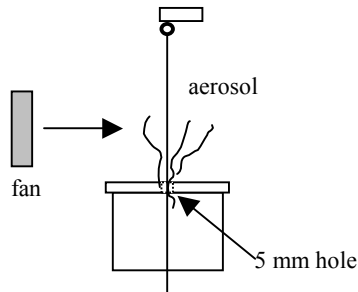


Figure 4.8 Fan positioned close to the load cell to remove aerosol droplets causing load cell failures

Oscillations of the rod at higher velocities (>1 m/s) were reduced with a support that constrained the motion of the coupon. The rod was also protected from deposition by a 2.5 cm diameter plastic pipe, placed around it (Fig. 4.9). The plastic pipe ended about 15 cm before the coupon, to avoid disturbing the flow field of the wake behind the coupon (Fig. 4.1).

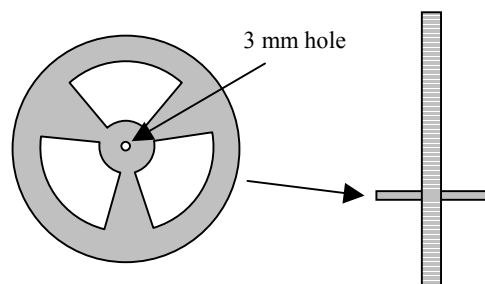


Figure 4.9 Motion constraint and deposition protection, installed to reduce oscillations of the coupon and prevent formation of deposits on the rod

Proper measurements of the difference between the liquid to the nozzle and the washdown flowrate required that the feedstock and washdown reservoirs were disconnected from the reservoirs on the balance. Therefore, they were attached only when the concentration measurements were finished (usually after 1 hour). The complete Cold Unit operating procedure is given in *Appendix A*.

4.2. Hot Unit apparatus

To investigate deposition at high temperatures with the mixtures of heavy hydrocarbons, the Hot Unit experimental apparatus was used (Fig. 4.10). The experiments were performed by Dr. J. Song [52].

In the Hot Unit apparatus, the coupon was placed in the middle of the upper section of the 1 m high and 7.5 cm diameter spray chamber, heated with external heaters. A mixture of MEBR and Voltesso was pumped from the heated oil tank to the nozzle, positioned below the chamber, and sprayed with a flow of nitrogen. Temperature in the unit was varied from 295°C to 425°C; 5% and 10% wt. concentrations of MEBR in Voltesso were used. The velocity was varied from 0.25 to 0.92 m/s.

Deposition rates were measured via a load cell placed in a chamber above the unit, protected from overheating by a flow of cold nitrogen into the chamber. The remaining aerosol was sent to the Condenser where it was cooled down. Part of the oil was captured in the Oil Trap. The remaining fine droplets in the aerosol were partially removed in the Demister, stuffed with steel wool. The aerosol was then treated in a Scrubber with a solution of sodium hydroxide, to remove sulphur components. The remaining aerosol was combusted in the afterburner.

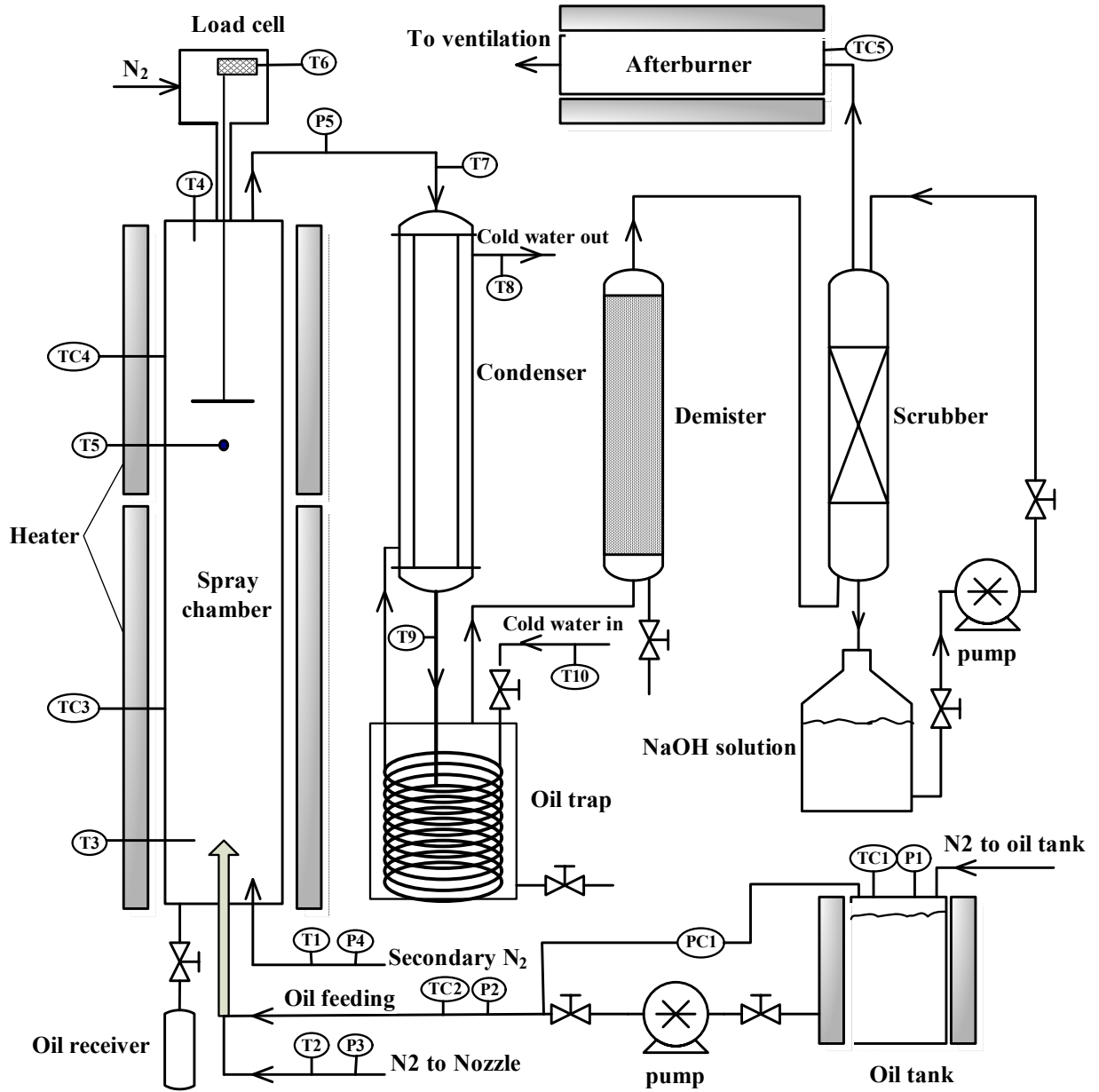


Figure 4.10 Process flow sheet diagram of the Hot Unit Apparatus [52]

4.3. Measurement techniques

The following variables in the Cold Unit experiments were measured: liquid flow to the nozzle, washdown liquid flow, velocity of the aerosol, droplet size distribution in the aerosol, droplet size distribution of deposits on the coupon, deposition rate, and contact angles of droplets on the coupon. All measurement techniques employed in measuring these variables are described in the sections that follow.

4.3.1 Liquid flow and aerosol concentration measurements

4.3.1.1. Measurements of the liquid flow to the nozzle

For pumping liquid to the nozzle, a gear pump was used (Fig. 4.11), since it provided flow without pulsations, while being able to deliver liquid at differential pressures up to 700 kPa (100 psi). The scale on the console drive was labelled and the pump was calibrated with and without differential pressure. The desired flow rate was then obtained by setting the position on the console drive. Details of the pump calibration are given in *Appendix B*.

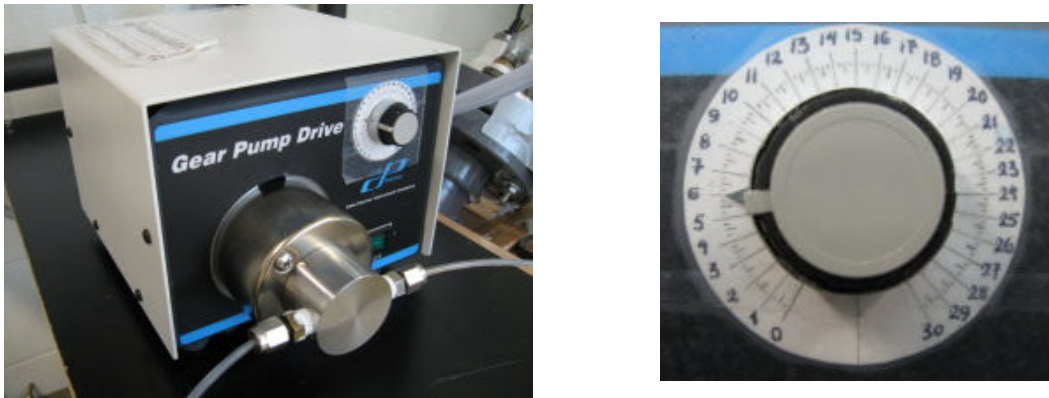


Figure 4.11 Picture of the RK-75211-10 Cole Parmer Console Drive and RK-07002-27 Micropump[®] A-mount Suction Shoe Pump Head with its scale

4.3.1.2. Measurements of the liquid flow to the aerosol

The concentration of droplets in the aerosol bulk, c_b , can be calculated as,

$$c_b = \frac{F_l}{U \cdot A_{column}} \quad (4.1)$$

where F_l represents the droplet flow rate of the aerosol (g/s), U is the superficial velocity of the gas in the column (m/s) and A_{column} is the column cross-sectional area (m²). If the aerosol droplet concentration is known, the deposition coefficient, k_d , can be calculated from the measured deposition rate r_d ,

$$k_d = \frac{r_d}{c_b \cdot A} \quad (4.2)$$

Therefore, it was necessary to measure the flow of liquid to the aerosol, F_l . Since the aerosol was generated in the relatively small diameter column (7.5 cm), as mentioned before, droplets close to the edge of the spray cone impacted the column walls, creating a film of liquid. The liquid film formed a washdown stream drained below the column and collected in a separate tank (Fig. 4.12). The droplet flow rate of the aerosol was measured as a difference between the flow of liquid to the nozzle and the washdown liquid. The mass flow rate of the liquid to the aerosol, F_l , was estimated from the slope of the weight loss curve, and recalculated as the liquid volume flow. Figs. 4.13 and 4.14 show logs of droplet flow for two different Cold Unit arrangements (Setup #1 and #2, Fig. 4.3).

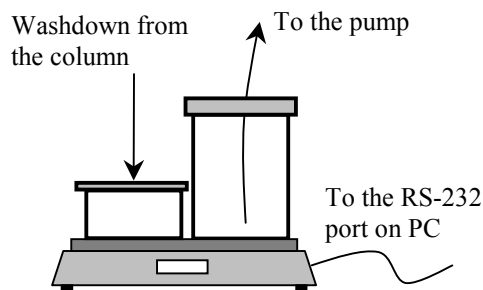


Figure 4.12 Schematic representation of the tank with the liquid that is pumped to the nozzle (4 liter), and the tank for collecting the washdown (2.5 liter), placed on the balance

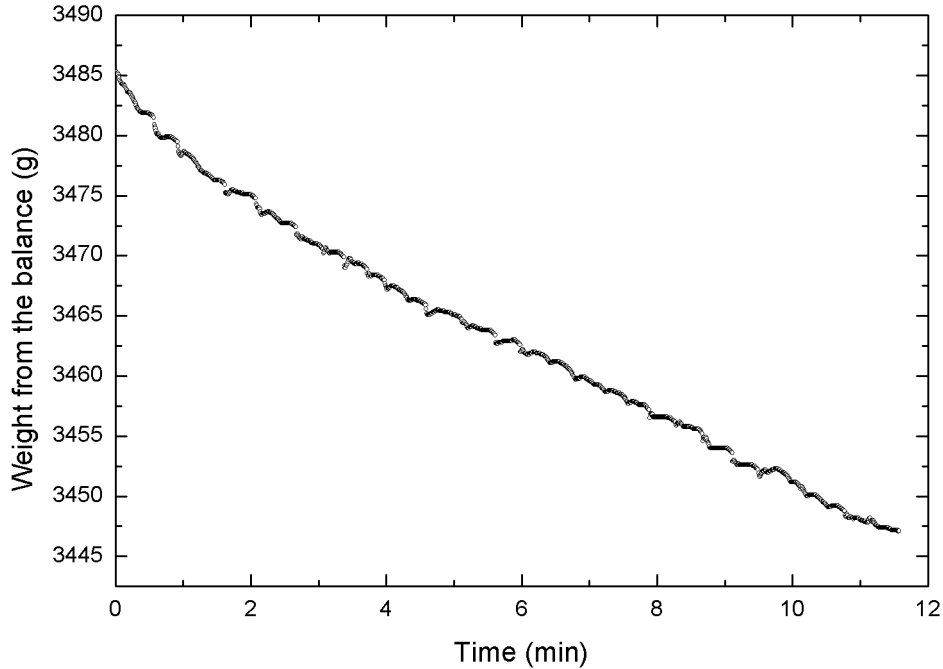


Figure 4.13 Log of the liquid flow to the aerosol for Run 28 (Cold Unit at 1 m/s, Setup #1, Figure 4.3). Short experiments and the presence of elbows reduce accuracy of droplet flow measurements.

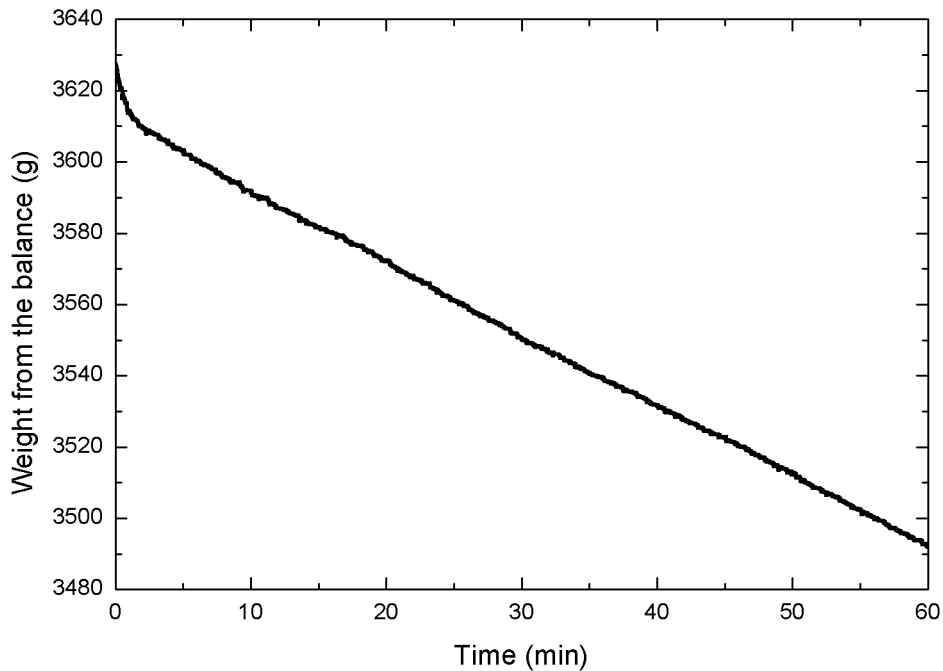


Figure 4.14 Log of the liquid flow to the aerosol for Run 53 (Cold Unit at 1 m/s, Setup #2, Figure 4.3). Straight line from long experiment results in droplet flow measurement accuracy higher than 1%.

As can be noted from the figures, the slopes of the curves are significantly higher (from 2–8 times) during the first several minutes, depending on the experimental conditions. This is due to the transient period needed to establish a steady flow of washdown liquid. This effect is more pronounced in experiments performed with the Cold Unit arrangement with elbows, since it takes more time for the liquid film to form in the two PVC elbow sections.

The variability of liquid flow measurements was determined in separate experiments, and the results are given in Table 4.1. The tests lasted from 15 to 20 minutes, with 2–3 minute pauses in between. The liquid flow was estimated by a linear interpolation of all the data, excluding the 2–5 minute transient period at the beginning.

Table 4.1 Variability in liquid flow rate measurements (g/min), with aqueous sugar solution and tri-ethylene glycol, at different superficial velocities (Setup #1, Fig. 4.3)

Velocity Test #	50% aqueous sugar solution			Tri-ethylene glycol		
	0.43 m/s (Run 4)	0.87 m/s (Run 7)	1.37 m/s (Run 11)	0.44 m/s (Run 14)	0.87 m/s (Run 17)	1.42 m/s (Run 19)
1	2.08	4.75	7.19	1.57	3.12	3.65
2	1.99	4.43	6.56	1.63	2.58	3.88
3	1.86	4.18	6.66		2.83	4.64
4	2.03	4.09	6.92		3.65	4.74
St. dev.	4.7%	3.9%	4.1%	2.6%	15.1%	12.9%

The accuracy of the droplet flow measurements for the Setup #1 could have been improved by performing longer experiments, for more than 30 minutes. However, safe recovery from the column, of the coupon its adhering liquid deposits, without danger of losing any, set a limit of about 200–300 mg of deposits on the upstream side. At velocities higher than about 0.8 m/s, this limit is reached in about 10–15 minutes. This was the main constraint for keeping the experiment durations below 15 minutes. For the Setup #2, the variability is estimated to be not more than 1%, except at very low gas velocities (<0.1 m/s) when the flow of liquid to the aerosol was quite low (0.1–0.5 g/min) and the error somewhat larger (1–2%).

4.3.2. Velocity measurements

The velocity in the column, U , was calculated from the flow of air to the nozzle, $F_{a,nozzle}$ (m^3/s), and the flow of secondary air, $F_{a,secondary}$ (m^3/s), measured by means of rotameters,

$$U = U_{nozzle} + U_{secondary} = \frac{F_{a,nozzle}}{A_{column}} \cdot \frac{P_{nozzle}}{P_{atm}} + \frac{F_{a,secondary}}{A_{column}} \cdot \frac{P_{secondary}}{P_{atm}} \quad (4.3)$$

where P_{nozzle} is the pressure in the nozzle and $P_{secondary}$ is the pressure in the gas distributor. The velocity from the nozzle varied from 0.1–0.6 m/s, with a pressure in the range of 100–500 kPa, depending on the nozzle type. The velocity of the secondary air varied in the range 0–1 m/s, with a pressure from 100–200 kPa, depending on the gas distributor type. Details on the rotameter calibrations are given in *Appendix B*.

4.3.3. Shadowgraphy measurements of aerosol drop size distribution

To measure size distribution of droplets in the aerosol, a shadowgraphy technique was selected. Shadowgraphy is an imaging technique that is used to visualize particles (e.g., solid particles, gas bubbles, liquid droplets) based on imaging with pulsed backlight illumination. For transparent particles, shadowgraphy utilizes difference in the index of refraction between the dispersed phase and the surrounding medium [61]. The direction of light rays that leave a dispersed phase is different than the direction of the same rays that enter, which makes the object non-transparent (Fig. 4.15).

4.3.3.1. Shadowgraphy setup

The shadowgraphy system that was used in this work is schematically presented in Fig. 4.1. The LED lights were placed opposite to the camera, with its axis aligned with the camera axis. This way, the light rays that pass through the column and a 20 cm long lens could reach the camera chip. A synchronization signal for the lights is sent from the camera, and the camera shutter was controlled from the software on the computer.

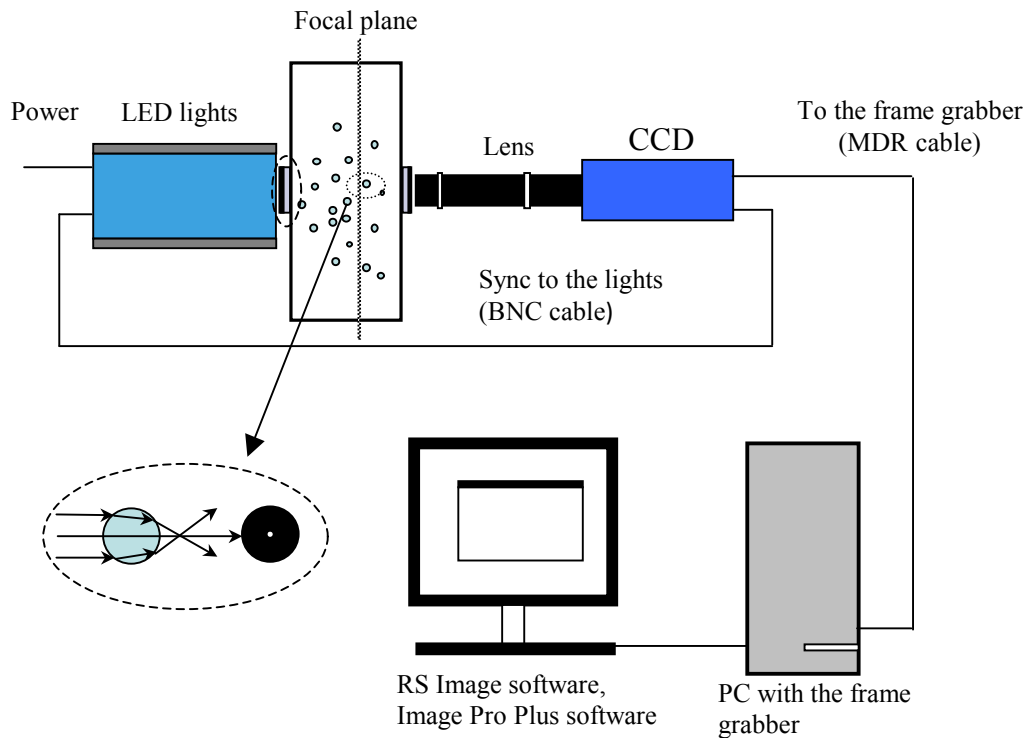


Figure 4.15 Schematic representation of the Shadowgraphy system used on the Cold Unit and the path of light rays entering and leaving the droplet

This shadowgraphy system was designed and assembled (by the author); it was made partly from components existing in the lab (Fig. 4.16).

- Lights were 19-LED Constellation Lights, with collimated light beams, from IDT Inc. (San Jose, CA, 6024 Silver Creek Valley Rd.). The power of the lights was 130 W, with an illuminance of 60,000 lux at 1 foot distance.
- Camera was 36-bit Cool Snap cf Color Camera, 1392×1040 with 4.65 micron pixels, from Photometric (Tucson, AZ, 3440 E. Britannia Dr.).
- Lenses were OPTEM Zoom 70 XL long distant lenses with maximum 14× magnification, from QIOPTIQ (La Verne, CA, 1318 Palomares Ave.). They were mounted on the camera via a C-mounts.
- Software used to control the camera and take images was RS Image 1.9.2 from Photometrics, while image analysis was performed in Image Pro Plus 5.0.1.

Similar systems are also commercially available from La Vision (\$35,000) and Dantec Dynamics (\$60,000).

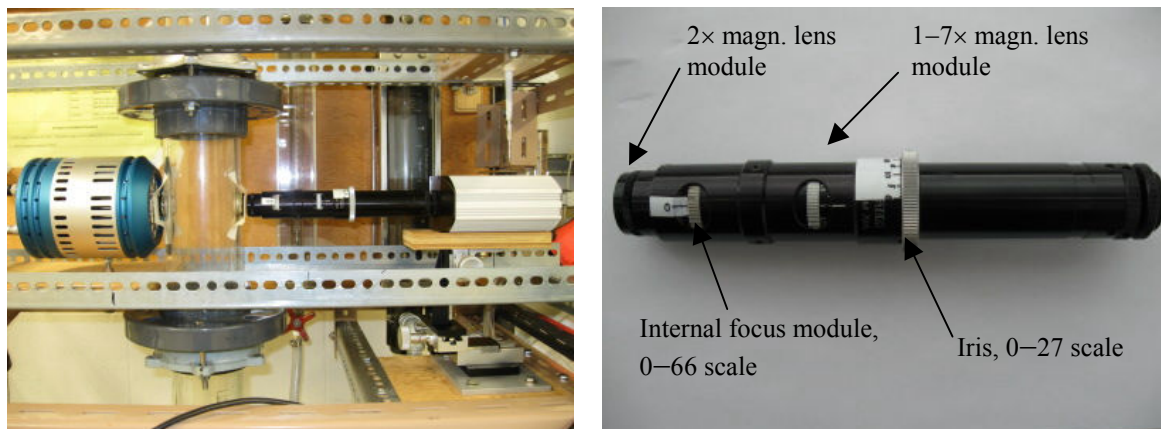


Figure 4.16 Pictures of the Shadowgraphy system installed on the Cold Unit and details of the Optem ZOOM XL long distant lenses

In order to maximize the intensity of light and use the shortest possible exposure, the camera and lights were placed right next to the column. The camera was mounted on an Edmund Optics XYZ moving stage (60 mm travel in X and Y, 40 mm in Z direction, Fig. 4.3). With the additional 2× magnification mounted on the basic lens, the focal plane was 35 mm away from the lens tip, or 25 mm inside the column (at one third of the column diameter). Since the curvature of the glass column did not allow taking undistorted images of droplets, an acrylic column section was used instead, with two 2.5 cm (1 inch) circular openings, opposite each other, cut into the column. Acrylic tube pieces with rubber gaskets on the outer side were inserted in the openings and glued to the column. Flat microscopic glass slides were then put on top of the gaskets and attached to the column with tape. This setup prevented aerosol leaking and also allowed easy removal of the glass slides for cleaning (Fig. 4.17).

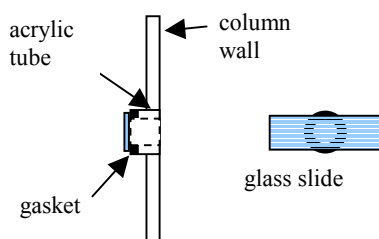


Figure 4.17 Schematic of the solution for eliminating glass curvature

4.3.3.2 Aerosol Sampling

Aerosol measurements frequently require that an aerosol sample be conveyed to a measurement device by withdrawing a sample from its environment and transporting it to the device [20, 62]. Ideally, sampling at the inlet of the sampler would be isokinetic, with no deposition or settling in the sample transport system. In the present case, the shadowgraphy system was pointed directly into the environment, and therefore no sampling systems were required. Because the aerosol was moving (Fig. 4.18), in order to get sharp shadow images of droplets, short exposures were needed.

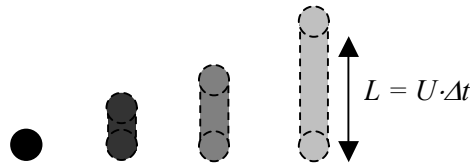


Figure 4.18 Schematic representation of the shape and intensity of droplet shadows captured at constant aerosol velocity and increased exposure. Sharpness of the images also decreases with a decrease in shadow intensity.

If we define blurriness, B , as a ratio of the droplet path, L , (traveled at velocity U during exposure time Δt) and its diameter, D_p ,

$$B = \frac{L}{D_p} = \frac{U \cdot \Delta t}{D_p} \quad (4.4)$$

exposures that will yield a given blurriness can be easily calculated (Table 4.2).

Table 4.2 Exposures (in microseconds) needed for 50% blurriness of different drop diameters and different velocities

$D_p(\mu\text{m})$ $U(\text{m/s})$	1	5	10	20	30	50	100
0.1	5	25	50	100	150	250	500
0.5	1	5	10	20	30	50	100
1.0	0.5	2.5	5	10	15	25	50
1.5	0.33	1.67	3.33	6.67	10.00	16.67	33.33

We can see that even at 50% blurriness and 1 m/s, the required exposures are on the order of few microseconds. The lowest possible exposure at the maximum light intensity that produced images bright enough to be analyzed was about 100 microseconds. This was

too long to capture acceptably sharp images of droplets, and the droplets had to be slowed down somehow. The solution was to stop the flow and capture the images shortly after the flow was stopped.

Firstly, the supply of air to the nozzle and gas distributor was shut off, by closing the ball valve shown in Fig. 4.1. Aerosol droplets continued moving upward under their inertia, then stopped, and started falling down slowly under the effect of gravity. To wait for the droplets to slow down, image recording was started 5 seconds after the flow was stopped. In about 14 seconds, 130 images were recorded in a frame sequence. The same procedure was repeated 10 times. Two consecutive frame sequences of 130 images were joined together to form a sequence of 260 images. This is what is referred to as one sample throughout this text.

To investigate the effect of the waiting period (5 seconds) on the sampling procedure, size distributions from images taken right after the flow is stopped, and 5 seconds after the flow is stopped were compared. From Table 4.3, this difference is within the sampling error (standard deviation 0.5 microns, Table 4.8). Corrected values for the number of droplets, volume of droplets, volume median diameter and maximum diameter are based on the border and depth of field corrections described in Section 4.3.3.7. The corrected values for the number of droplets are about $\frac{78115}{9667} < 10$ times the uncorrected values, primarily because of the depth of field correction.

Table 4.3 Comparison of the volume median diameter measured right after the flow is stopped and 5 seconds after the flow is stopped, at 6× magnification and 110 microseconds exposure. Velocity 1 m/s, liquid flow to nozzle 40 ml/min.

	Immediately after the flow is stopped		5 sec. after the flow is stopped	
	measured	corrected	measured	corrected
No. of droplets	9667	78115	10365	72170
$D_{V,50}$ (μm)	8.3	5.5	7.9	5.5
D_{max} (μm)	29	29	25	25

To investigate the effect of stopping the flow on the sampling process, the new Cold Unit nozzle (*Quick Mist*, Fig. 4.5) was placed below the column and set to produce large droplets (air velocity 0.15 m/s, liquid flow 90 ml/min). Because of the low velocity

and large droplet sizes in the aerosol, a $2\times$ magnification and a 60 microseconds exposure could be used. The comparison is presented in Table 4.4.

Table 4.4 Comparison of the volume mean diameter measured 5 seconds after the flow is stopped and when the aerosol flows upward.

	In the flow		5 sec. after the flow is stopped	
	measured	corrected	measured	corrected
No. of droplets	27959	330352	28508	297269
Volume of droplets (mm^3)	0.033	0.142	0.028	0.116
$D_{V,50}$ (μm)	33.8	13.6	29.2	12.7
D_{max} (μm)	92	92	80	80

Again, the volume median diameter in the aerosol flow is somewhat larger than when the flow is stopped (both measured and corrected values). The observed difference could be within the experimental error (standard deviation is about 0.5 micron, Table 4.8), but it is possible that the difference exists. To explain this, we consider a disappearing of larger aerosol droplets from the camera view field by gravitational settling. Table 4.5 shows the terminal velocities of tri-ethylene glycol droplets in air at room temperature as calculated using a non-Stokesian drag force. Also it shows the time needed for the droplets to fall down and vanish from the 80 cm high column segment above the shadowgraphy section.

Table 4.5 Terminal velocities of tri-ethylene glycol in air at room temperature and the time needed to travel 80 cm in free fall

D_p (μm)	1	10	20	30	40	50	60	70	80	90	100
V_t (cm/s)	0.00	0.34	1.35	3.04	5.40	8.44	12.15	16.54	21.60	27.34	33.75
Time (s)	23705.1	237.1	59.3	26.3	14.8	9.5	6.6	4.8	3.7	2.9	2.4

Based on Table 4.5, it seems that only droplets below 40 microns would be fully recorded during the first 19 (=5+14) seconds after the flow is stopped. However, since at $6\times$ magnification, the volume of 5 samples is quite small (about 1 mm^3 for $10 \mu\text{m}$ droplet), and the diameter of the largest recorded droplet is not higher than 35 microns (Table E.1), the settling of droplets does not affect the droplet size distribution measured at $6\times$ magnification. The data from Table 4.3 support this conclusion to a certain degree. Therefore, the sampling procedure described above (flow stopped, images taken after 5 seconds) was accepted and used further on.

4.3.3.3. *Hardware and Software settings*

The parameters in the shadowgraphy hardware and software were determined and set as described in the following sections (Sections *a* and *b*).

a. Shadowgraphy hardware settings

Iris on the long distant lenses was completely open (scale 27) to maximize the light intensity and enable using the shortest possible exposure.

Internal focus module scale was set at the middle of the scale, at 33. The recorded droplet size distribution did not change with the change in the position in the internal focus.

Magnification. To select the optimal magnification of the lens considering all the constraints of the shadowgraphy hardware, software and process parameters, the following procedure was followed. From the experimental results (chapter 5) it is known that droplets below 1–2 microns do not contribute significantly to the deposition rates. Also, when the diameter of the droplet is close to the wavelength of visible light (400–700 nm), light diffraction occurs and the images of droplets obtained with shadowgraphy become blurry. The manufacturers of commercially available shadowgraphy systems also claim that the lower limit for proper measurements of particle size is about 2 microns [63]. Therefore, it was not possible (and also not too important in our case) to measure droplets smaller than 1-2 microns accurately.

From Fig. 4.21, at 6× magnification, a 2 micron particle is represented by a square made of 4×4 pixels. Although it is desirable to have more pixels representing the smallest particle, increased magnification decreases the XY view field, and also reduces the depth of focus. Reduced depth of focus results in a decreased depth of field, with fewer particles being recorded, which further increases the number of images required for analysis and the number of samples needed to be taken above practical limit. In addition, magnifications larger than 6× magnification require a higher light intensity or longer exposures than currently used. However, maximum possible light intensity was already used (LED lights at full power, iris open to maximum), and longer exposures than currently used (110 μs), resulted in blurry and low-contrast droplet shadows (see section

b), which caused improper droplet identification. Considering all the constraints, 6× magnification (at 110 μs exposure) represented the upper limit. Magnification below 6× would increase the number of droplets recorded, but droplets larger than 2–3 microns would be improperly identified. Therefore, 6× magnification was considered to be the optimal choice. Table 4.6 summarizes the main shadowgraphy hardware settings, discussed in this section.

Table 4.6 Main shadowgraphy hardware settings

Iris	27 (maximum)
Internal focus	33
Magnification	6× (2×3)*

* 3× zoom, plus 2× magnification lens

b. RS Image software settings

Shadowgraphy images were recorded using RS Image 1.9.2 software. To enable acquisition of images clear enough for droplet identification, the exposure had to be set to not less than 60 microseconds. Since the concentration of the aerosol varied from 4–10 mg/m³, with volume median diameter from 3.9–7.5 microns, light transmittance of the aerosol also varied. Denser aerosols with smaller particles required longer exposures to obtain proper images. Therefore, the exposure was set to the value that was appropriate for the most dense aerosol, that is to 110 microseconds. The main RS Image software settings are given in Table 4.7.

Table 4.7 Main RS Image software settings

Exposure Type	Normal
Exposure Mode	Times
Manual Exposure	110 μs

4.3.3.4. Sample size

To obtain a meaningful size distribution of droplets in the aerosol, a sufficient number of droplets had to be recorded. In the initial stages of experimentation, when the image analysis procedure was not automated (*Appendix D*), a sample contained 260 images. Later on, the number was increased to 5 samples, each consisting of 260 images.

Table 4.8 shows the effect of sample size on the volume median diameter, and its standard deviation.

Table 4.8 Effect of sample size on measured volume median diameter (Run 33)

Sample	$D_{V,50}$ (μm)	Joined samples	$D_{V,50}$ (μm)	$S_{D_{V,50}}$ (μm)	$\bar{D}_{V,50}$ (μm)	$S_{\bar{D}_{V,50}}$ (μm)
1	11.0	1	11.02			
2	12.4	1 to 2	11.77	0.98	11.72	0.70
3	10.7	1 to 3	11.43	0.90	11.39	0.52
4	10.0	1 to 4	10.97	1.02	11.03	0.51
5	10.4	1 to 5	10.85	0.92	10.91	0.41
6	8.5	1 to 6	10.49	1.29	10.51	0.52
7	12.5	1 to 7	10.72	1.38	10.79	0.52
8	11.3	1 to 8	10.79	1.29	10.85	0.46
9	12.0	1 to 9	10.92	1.27	10.98	0.42
10	10.4	1 to 10	10.87	1.22	10.92	0.38

From the results in Table 4.3, it was decided that a sufficient number of samples would be 5, after which the volume median diameter showed little change.

4.3.3.5. Image processing and image segmentation settings

Image segmentation refers to the process of partitioning a digital image into multiple segments (sets of pixels). Image segmentation is typically used to locate objects and boundaries (lines, curves, etc.) in images. In this case, the objects were shadow images of droplets in the aerosol. To identify object boundaries, commercial shadowgraphy systems (such as La Vision's ParticleMaster Shadow software [63]) use a thresholding segmentation algorithm, applied to grey-scale images. In this work, the Image Pro Plus software was used, and color images of the aerosol were recorded. Therefore, image segmentation was performed using a segmentation technique implemented in the Image Pro Plus, i.e. based on the histogram ranges for the red, green and blue component of images. For this step, valid histogram ranges had to be specified, as described below.

Before segmentation, the images were pre-processed to even out background color variations and remove the noise in the images. Images were filtered with a *Bright Flatten* filter, with a 15 pixel strength. It was applied in two passes, and proved to be sufficient in removing background noise. This eliminated the need for background

subtraction. Image segmentation was based on the histogram ranges of the red, green and blue components of the images. Investigation of the identification process led to the following choices for the red, green and blue ranges: Red: 0–255, Green: 0–200, Blue: 0–255. Shadowgraphy verification, described in Section 4.3.3.8, confirms the validity of this choice. Important image analysis options also included a *Convex Hull* feature for the shadowgraphy of the aerosol droplets. The results reported include the surface area, as well as the minimum, mean and maximum droplet diameter. The size distribution of the aerosol was based on the minimum droplet diameter.

4.3.3.6. Calibrations

Calibrations of the shadowgraphy system used in this work included: (a) calibration of the camera view field, (b) calibration of the internal focus module and (c) depth of field calibration.

a. Camera view field calibration

In order to properly size particles observed with shadowgraphy and under the microscope (Section 4.3.4), the camera view field had to be calibrated (Figure 4.19).

The view field was calibrated using an Objective Micrometer MA285 glass slide, with a 1 mm scale and 0.01 mm divisions. The slide was attached to the side opening of the column (Fig. 4.18), and observed under different magnifications. The same micrometer slide was used to calibrate images from the OLYMPUS BX41 microscope.

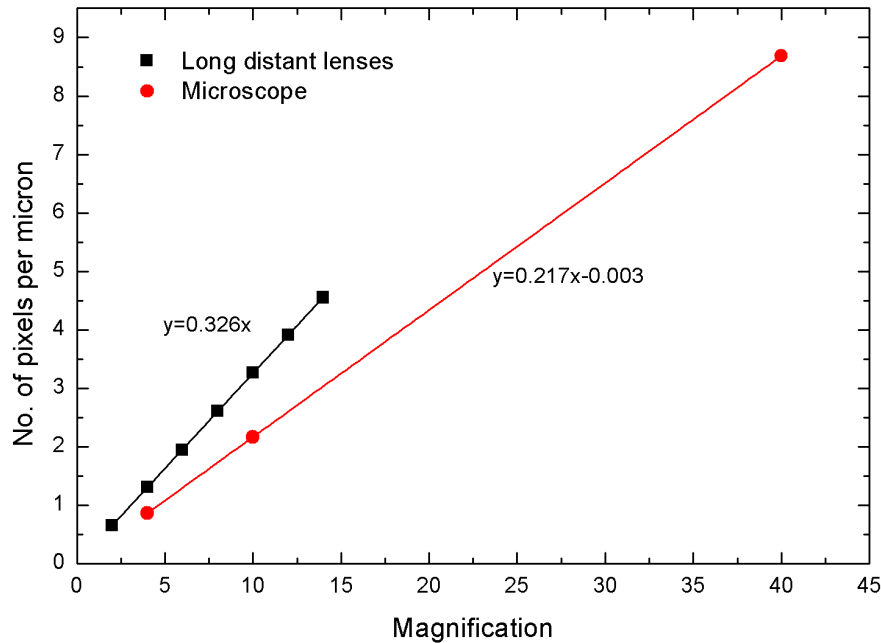


Figure 4.19 Calibration lines of ‘Cool Snap Pro cf camera + OPTEM Zoom 70 XL lens’ and ‘Cool Snap Pro cf camera + OLYMPUS BX41 Microscope’ systems

b. Calibration of the Internal focus module

The depth of the view field for a given drop diameter (section *c*) was determined with the help of the OPTEM Zoom internal focus module (Figs. 4.16, 4.20). The scale on this module (0–66) was calibrated in the following manner. First, the Objective Micrometer was attached to the side opening of the column and the camera was focused on the slide. The camera was then moved in the X-direction and the internal focus was adjusted in order to bring the focus back on the Micrometer slide (Fig. 4.20). The micrometer on the X-axis of the XYZ stage was then used to measure the displacement of the camera. This procedure was repeated at several points and for each data point, the camera displacement and internal focus position were recorded. This was performed at every magnification.

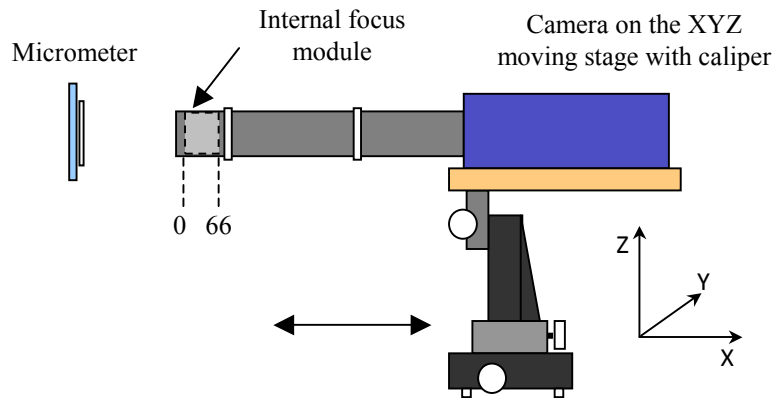


Figure 4.20 Camera on the moving stage for the Internal focus module calibration

Figure 4.21 shows the estimation of the slope from 12 measured points at 6 \times magnification (6 points from moving the stage in the positive X-direction and 6 points from going backwards in the negative X-direction). The slopes at all other magnifications (1–4 \times , 8–12 \times) were estimated from 3 points, by moving the camera in one direction only. The results are given in Table 4.9.

Table 4.9 Internal focus module calibration at different magnifications

Magnification (\times)	2	4	6	8	10	12	14
Microns per 1 scale	37	36.4	35.1	33.9	34.5	34.2	34.9

The results show that the change in focus is independent of the magnification; one scale division shifts focus by about 0.35 mm.

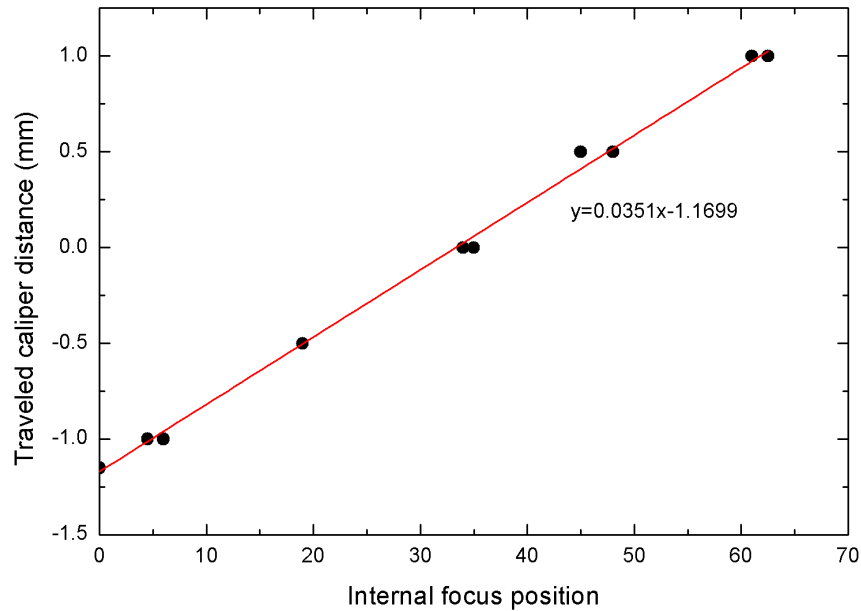


Figure 4.21 Traveled camera distance in X-direction vs. internal focus module position, required to bring the Objective Micrometer back in focus, 6 \times magnification

c. Depth of Field Calibration

The depth of field, as presented in Fig. 4.22, represents the length of the view field in the X-direction (Fig. 4.20), where particles are seen by the camera. It is a function of the particle diameter; for smaller particles, the depth of field will be smaller, for larger particles, the depth of field is larger.

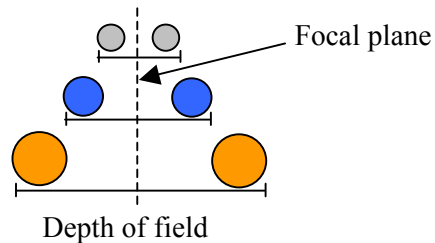


Figure 4.22 Schematic representation of the depth of field. For larger particles, depth of field is larger

To calibrate the depth of field, fine solid particles were deposited on a microscopic glass slide using a paintbrush, and the excess deposits were removed by blowing air on the slide. Spherical glass beads from Potter Industries Inc. (Spherglass 6000A, $D_{V,50} = 7.0\mu\text{m}$) were used for particles in the range 3–16 microns, while 20

micron Polyamid seeding particles (Dantec Dynamics Ltd.) provided particles larger than 20 microns. The slide was then fixed on the column openings (as in Fig. 4.20). The camera focus was then changed in 0.035 mm steps, using the internal focus on the lenses. For the smallest particle (3 micron), this step was 50% smaller (0.0175 mm). Images were then analyzed in Image Pro Plus with settings given in Table 4.10. From the X-positions of the particle when it entered the view field and was identified, and from its position when it was lost from the view field, the depth of the field was calculated. This procedure is somewhat different from the depth of field determination implemented in the commercial shadowgraphy software [63], where a criteria based on the color gradient at the edge of the object is used. There, the particle is removed from counting if the gradient on its edge is below a certain value, meaning that the image is too blurry, and that the particle is too far from the focus.

Table 4.10 Main settings for the image segmentation

Option	Setting
Histogram range	Red (0–255), Green (0–200), Blue (0–255)
Convex Hull	Yes
Analysis based on	D_{\min}

All images were recorded at 6× magnification. An enhancement filter was applied to all images (Flatten, Bright, 15 pixel strength, 2 passes) in order to even out the background variations. Figure 4.23 shows in-focus images of glass beads and Polyamid particles, used for the depth of field calibration.

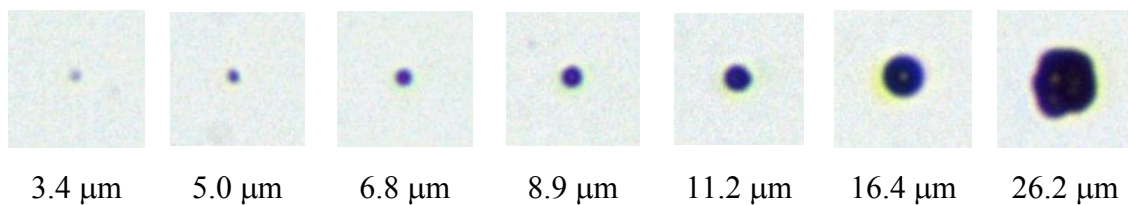


Figure 4.23 Glass beads (3.4–16.6 μm) and Polyamid particle (26.2 μm) in the focus, used for depth of field calibration; 6× magnification

The measured depth of field for different drop diameters is shown in Fig. 4.24. The data points were fitted with a linear function that goes through the origin, since it is known that the depth of field is a linear function of particle diameter [63, 64].

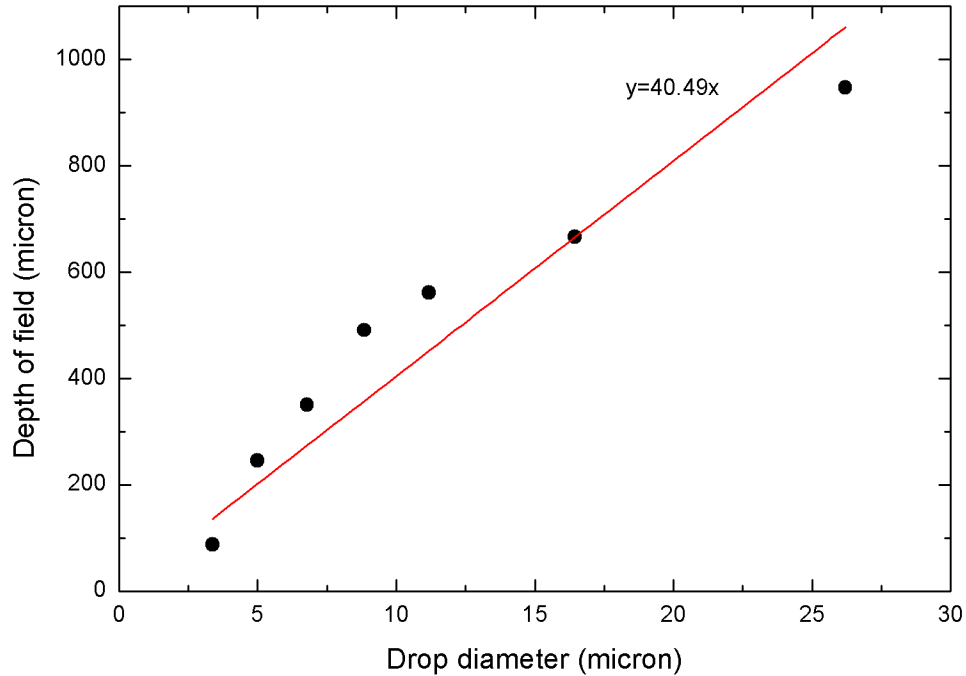


Figure 4.24 Depth of field for the shadowgraphy system, determined using Image Pro Plus settings given in Table 4.10

It is believed that the glass beads are faithful representation of tri-ethylene glycol spherical droplets in the aerosol since the refractive index of tri-ethylene glycol is 1.46 – very close to the refractive index of glass (1.46–Pyrex glass, 1.52–Crown glass).

4.3.3.7. Corrections

Since different particle sizes have different depths of field, and a different probability of being captured in the XY view field, it is necessary to introduce corrections in the measured particle size distribution.

a. Border correction

Larger particles have a lower probability of being inside the XY view field than smaller particles (Fig. 4.22). Hence, the following border correction must be applied [63],

$$P_{i, \text{Border}} = \frac{(W - D_{p,i})(H - D_{p,i})}{W \cdot H} \quad (4.5)$$

where $p_{i,Border}$ is the probability of a particle being detected inside the window, W is the window width, H is the window height and $D_{p,i}$ is the particle diameter (in the class i). This correction assumes that particles on the border of the image are not counted.

Table 4.11 Detection probability for different particle sizes, at 6× magnification ($W=718$ μm , $H=536$ μm)

$D_{p,i}$ (μm)	1	5	10	20	30	50	100
$p_{i,border}$	0.997	0.984	0.968	0.936	0.905	0.844	0.7

b. Depth of field correction

The depth of field correction increases the relative weighting of smaller particles. The detection probability, $p_{i,DOF}$, can be written in the following form [63],

$$p_{i,DOF} = \frac{D_{p,i}}{D_{p,reference}} \quad (4.6)$$

where $D_{p,reference}$ is the reference diameter, usually set to the largest diameter measured, in order to keep probabilities smaller than 1. The value of the reference diameter is not relevant, as long as the depth of field is linearly dependent on the particle diameter. Including the border correction, the total probability of detection is calculated as,

$$p_i = p_{i,Border} \cdot p_{i,DOF} \quad (4.7)$$

The statistically corrected number of particles N' is then given by,

$$N' = \sum_{i=1}^{i_{\max}} \frac{1}{p_i} \cdot N_i \quad (4.8)$$

4.3.3.8. Shadowgraphy verification

The shadowgraphy technique used in this study employed an image segmentation algorithm based on the histogram range values of the red, green and blue color components. According to the depth of field criteria employed, a droplet is counted as ‘in focus’ as long as it is seen in the view field. Since this method is somewhat different from the ones employed in the commercial systems, the shadowgraphy technique had to be

verified with a known size distribution of particles, that would behave like a real aerosol. For this purpose, the following procedure was devised and followed.

Glass beads with $D_{V,50}=7.0\ \mu\text{m}$ from Potter Industries Inc. were deposited on the glass slide and attached to the column (Fig. 4.25). The camera was traversed in the Y-direction using the moving stage and 120 images were taken in each image series sample. During 12 seconds, the camera was moved 16 mm at a velocity about 1.33 mm/s. Then, the camera was moved from the focus for one scale (0.035 mm) and a new series of images was taken. This procedure was repeated in both the negative and positive X-directions until the glass beads became too far from the focal plane to be identified by the software. Series of images obtained in this manner emulated a real aerosol, by having the droplets of known size in and out of focus.

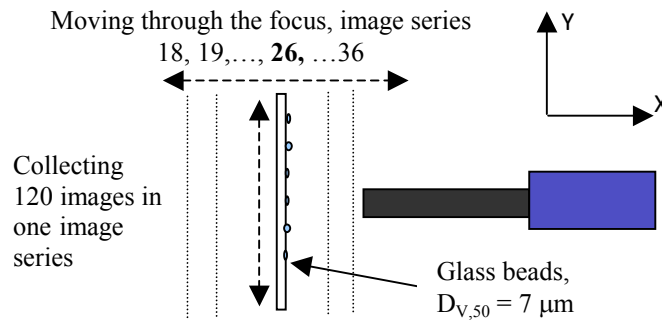


Figure 4.25 Verification of shadowgraphy with glass beads on the microscopic glass slide

The data from this experiment are given in Table 4.12. It can be seen that, at focus position 26, the volume median diameter is 7.1 micron and very close to the one specified by the manufacturer. This agreement verified that in-focus images are identified properly. Also, the corrected volume median diameter is 7.3 microns, which is very close to the 7.1 micron measured in the focus. Therefore, it was concluded that the applied border and depth of field corrections are valid, and could be used in the measurement process.

Table 4.12 Glass beads in different focus position, captured and analyzed with shadowgraphy

Focus position	Number of image series	Number of glass beads	$D_{V,50}$ (μm)	Number of glass beads, corrected	$D_{V,50}$ (μm), corrected
26	1	17467	7.1	17467	
25–27	3	45966	7.4	223854	5.8
24–28	5	60139	8.4	318911	6.4
23–29	7	67095	9.1	352819	6.8
22–30	9	71104	9.6	372716	7
21–31	11	73674	9.9	385656	7.2
20–32	13	74850	10	391464	7.3
19–33	15	75683	10.1	395894	7.3
18–34	17	76190	10.1	399054	7.3
18–36	19	76491	10.1	401082	7.3

4.3.3.9. Summary procedure

The procedure used for measuring droplet size distribution in the aerosol, using shadowgraphy technique, can be summarized as follows.

Before each run, shadowgraphy was used to record images at the operating conditions for that run. The atomizer was put into operation, and 10–15 seconds after the atomizer startup (but before the experiment was performed), the supply of air and liquid to the nozzle was cut off. After 5 seconds, image acquisition was started.

After taking images of two samples at velocities 0–0.6 m/s, and one sample at velocities 0.8–1.4 m/s, the glass slides were removed and cleaned. Deposition on the glass slides was quite intense at higher velocities and if this procedure was not followed, low contrast images were obtained, which introduced errors in the sampling process. After five samples of 260 images were recorded, the images were analyzed in Image Pro Plus (*Appendix D*), and the results of individual droplet sizes are further processed using the MATLAB script *shadow.m* (*Appendix D*), to give a size distribution and characteristic diameters.

4.3.3.10. Suggestions for improvements

For future work, the performance of the shadowgraphy system could be improved by implementing the following changes:

- Adopt an improved segmentation algorithm that segments droplets based on the color gradient on their edge, such as the one implemented in LaVision's ParticleMaster Shadow software [63]. This would allow the droplets far away from the focus, which are identified as somewhat smaller objects, to be eliminated from counting.
- Using a stronger light source, such as PalFlash 501 (The COOKE Corporation), would provide enough light for low exposures, down to few microseconds, which would in turn enable freezing small aerosol droplets at velocities up to 1.5 m/s. This way, the droplet size distribution and the concentration of droplets at any point in the aerosol (e.g., in front of the coupon, in the vortex behind the coupon) could be measured.
- Long distance lenses of better quality (with higher resolving power), such as the lenses used on the OLYMPUS microscope, would improve accuracy by increasing the sharpness of the droplet images.
- Using an 8-bit camera that would produce grey-scale images would be beneficial, since it would improve the white balance issues.

4.3.4. Coupon drop size distribution measurements

In order to determine deposition coefficients and capture efficiencies for each droplet size, the drop size distribution on each coupon had to be measured. Hence, the following technique was developed and used.

For these measurements, the coupon deposits had to be observed under a microscope, and therefore, a transparent coupon was used. Based on the results of the interfacial tension effect, droplet rebounding should occur only at very high contact angles ($\theta > 150^\circ$). This means that at low contact angles, perfect sticking can be assumed, and the size distributions of droplets on the glass ($\theta=20^\circ$) and stainless steel ($\theta=50^\circ$)

coupon should be the same. Therefore, a glass coupon can be used to determine size distribution of deposits on a stainless steel coupon.

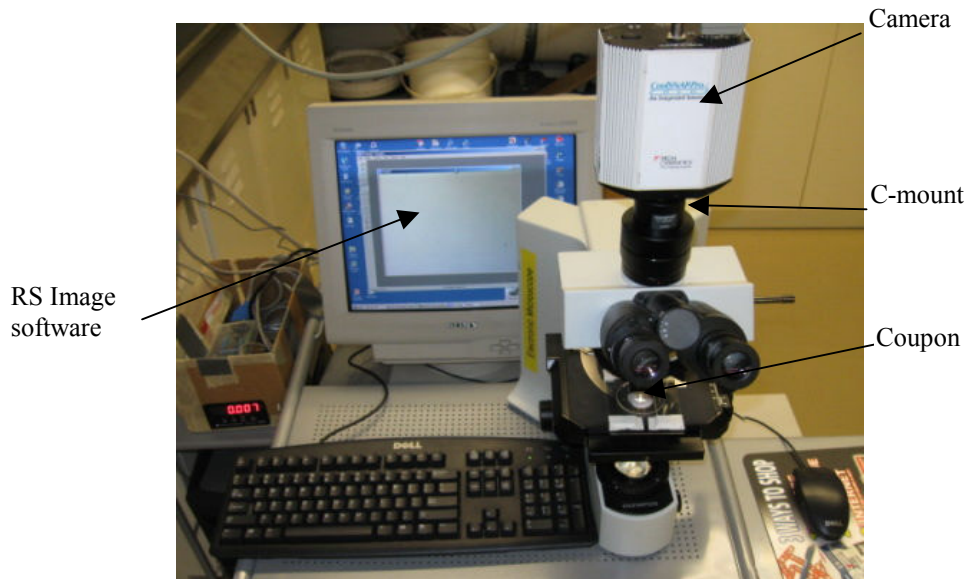


Figure 4.26 Picture of the Microscope and Camera setup, used for recording images of coupon deposits

For each Cold Unit experiment, a short deposition experiment with the 5 cm (2 inch) glass coupon, under identical operating conditions was performed. A Cool Snap Pro *cf* camera was attached to the OLYMPUS microscope via a C-mount, and deposit images were taken by means of the RS Image software (Fig. 4.26). Although droplets on the surface were not full spheres but spherical caps, the shadowgraphy effect applied to a certain degree (Fig. 4.30) and enabled identification of the droplets. The procedure consisted of: deposition on the glass coupon in the column (sampling), taking images of deposits under the microscope, analysis of images in Image Pro Plus software and drop size distribution analysis using the Matlab scripts *shadow.m* and *coupon.m* (Appendix D).

4.3.4.1. Deposition (sampling)

Firstly, a 4 mm long joint made of 3.175 mm (1/8 inch) diameter acrylic rod was cut and a hole was drilled in it. The hole was threaded with a 1.58 mm (1/16 inch) thread, to enable attachment of the rod. Then, the joint was glued to the glass coupon (Fig. 4.27).

The experiment was started and after 15–20 seconds of atomization when the flow seemed stable, the coupon was inserted in the column by hand, 15 cm below the

exit, and held by hand normal to the aerosol flow during deposition. It is estimated that this distance was enough not to affect the vortex behind the coupon.

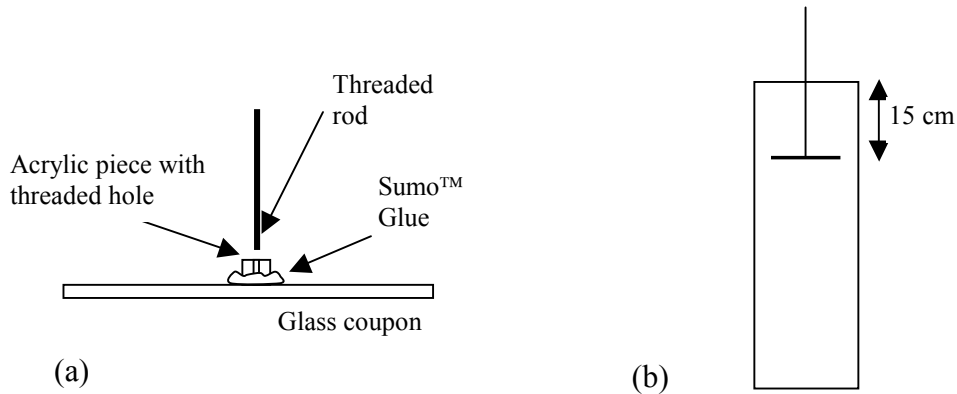


Figure 4.27 Schematic representation of: (a) glass coupon used for deposit size distribution analysis and (b) placement of the coupon in the column

Since these sampling experiments had to be quite short in order to avoid coalescence of droplets on the surface (10–15 seconds), variability in the sampling process could be considerable. The main sources of sampling errors could be during the period of placing the coupon in the column (approximately 1 second) and during the period of taking the coupon out from the column (also around 1 second).

4.3.4.2. Recording images along the coupon radius

Images of droplet deposits were taken starting from the coupon centre and moving the coupon on the microscope stage toward the coupon edge (Fig. 4.28). In about 12 seconds, 120 consecutive images of deposits were taken and saved into a file as a frame sequence. The microscope stage was moved, by turning the wheel on the stage micrometer, at a speed that the coupon traveled for 2.5 cm, in about 12 seconds. The time was counted, and the last image in the sequence was taken when the camera view field was at the coupon edge. If the timing was not right, sampling was repeated. Four samples along the coupon radius were taken. When there were deposits on both the upstream and downstream surfaces, sampling was done for each case, since placing the coupon on the stage removed part of deposits from the surface touching the stage.

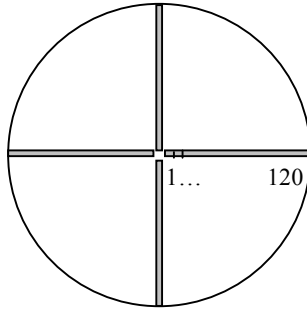


Figure 4.28 Locations of coupon deposit samples taken from the upstream and downstream side. First image starts at the coupon centre, last image is taken at the coupon edge.

Droplet deposits on the upstream side were observed under $4\times$ magnification, while droplets on the downstream side were observed with $10\times$ magnification. For taking images of the upstream side, the coupon was placed on the additional stage made of glass slides, to allow placing the coupon in the horizontal plane (Fig. 4.29).

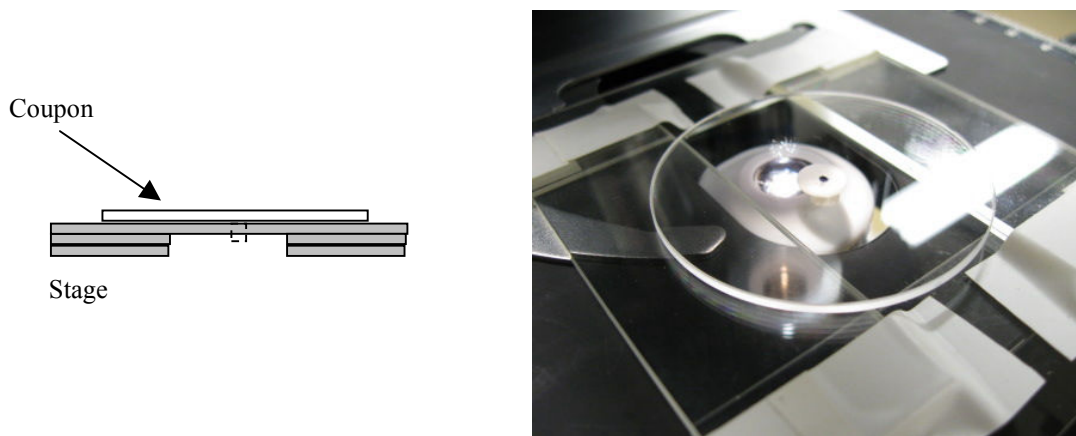


Figure 4.29 Supporting stage made of glass slides

4.3.4.3. Image Analysis in Image Pro Plus

As can be seen schematically from Fig. 4.30, light rays that pass through the central part of deposited droplets do not deviate significantly from their original path. However, light rays close to the coupon edge, where curvature of the gas-liquid interface is more pronounced, bend more and produce shadow-like images.

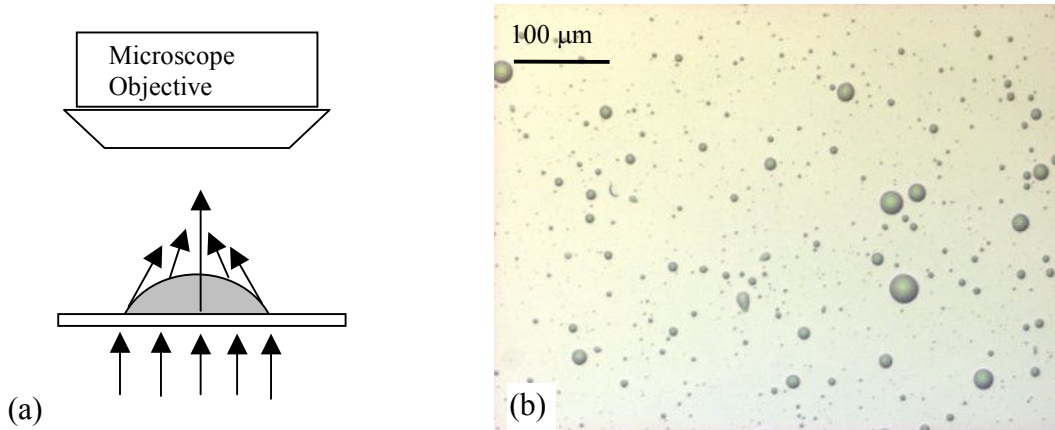


Figure 4.30 Schematic representation of (a) light rays that pass through the spherical cap and (b) one example of deposits on the downstream side, Run 56

From 120 images of deposits, only 30 images were analyzed (every fourth). This means that each image covers 1.6 mm along the coupon radius at 4× magnification, and 0.64 mm at 10× magnification, while only 0.83 mm ($=25.4/30$ mm) contains a new information. This means that at 4× magnification, the number of different droplets that were analyzed is about two times smaller than the reported number.

The images were first enhanced by applying the ‘*Flatten*’ filter, with a 15 pixel strength, in two passes, to equalize background variations. Object identification was based on the histogram range values R(0–255), G(0–200), B(0–255), as used in the shadowgraphy measurements. Some settings for the upstream deposit image analysis are given in Table 4.13.

Table 4.13 Relevant environment settings in the Image Pro Plus for coupon deposit analysis (1–set, 0–not set)

	Convex Hull	Fill Holes	Clean Border
Upstream	1	1	1
Downstream	0	1	1

The difference in the settings is in the *Convex Hull* property. It is used in the case of upstream deposits where droplets are quite large, and where in about 10–20% cases, the droplet borders were not sufficiently dark for proper droplet identification (Fig. 4.31). On

the downstream side, there was no need for using this option since the droplets were smaller and sufficiently dark.

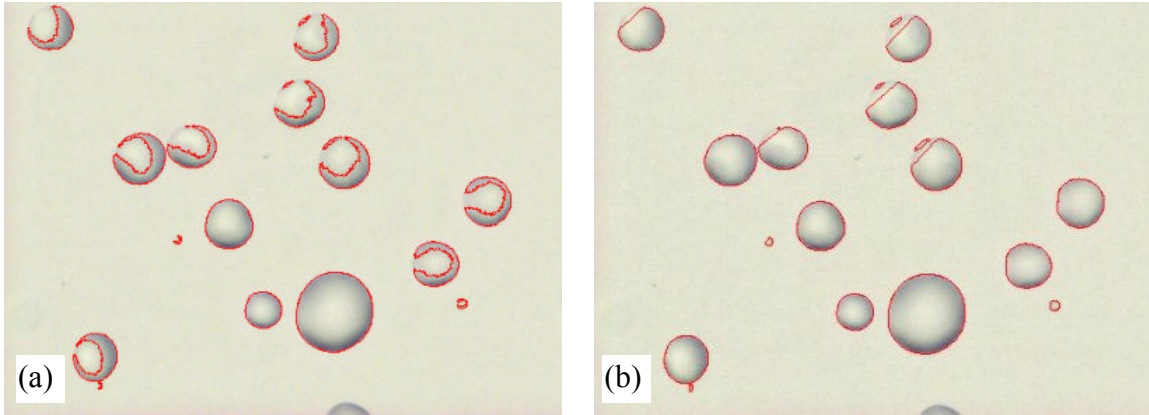


Figure 4.31 Identified droplets on the upstream surface, with (a) *Convex Hull=0* and (b) *Convex Hull=1* option. In the second case, measured diameter is much closer to the real diameter of droplets.

Size distribution analysis in MATLAB was performed using the scripts *shadow.m* and *coupon.m* (*Appendix D*). The reported results were based on the mean droplet diameter. This is logical since the mean drop diameter is most representative of the mean droplet diameters on the surface, which combined with the mean contact angle gives the best estimate of the drop diameter in the aerosol. To account for the spreading of spherical droplets on the surface, correction factor derived in *Appendix C* was used.

4.3.5. Deposition rate measurements

In order to monitor potential changes in deposition rates over time (deposition on a dry coupon, thin, and thick layer of deposits), the weight of deposit on the coupon was monitored during the whole experiment, using the load cell. In addition, the weight of the deposit was measured at the end of experiments using an analytical balance.

4.3.5.1. Load cell measurements

The load cell, GSO-50, with a DPM-3 data logger from Transducer Techniques, with 1 mg precision was used for the experiments. The load cell was mounted above the column, on a 20×20 cm square wood panel, and covered with plastic protection. The system for connecting the load cell with the rod attached to the coupon is shown in Fig.

4.32. This was needed in order to avoid a stiff connection of the rod with the load cell that, would lead to incorrect measurements. Although the load cell was calibrated by the manufacturer, it was also calibrated in the laboratory, when installed on the Cold Unit. The details are given in *Appendix B*.

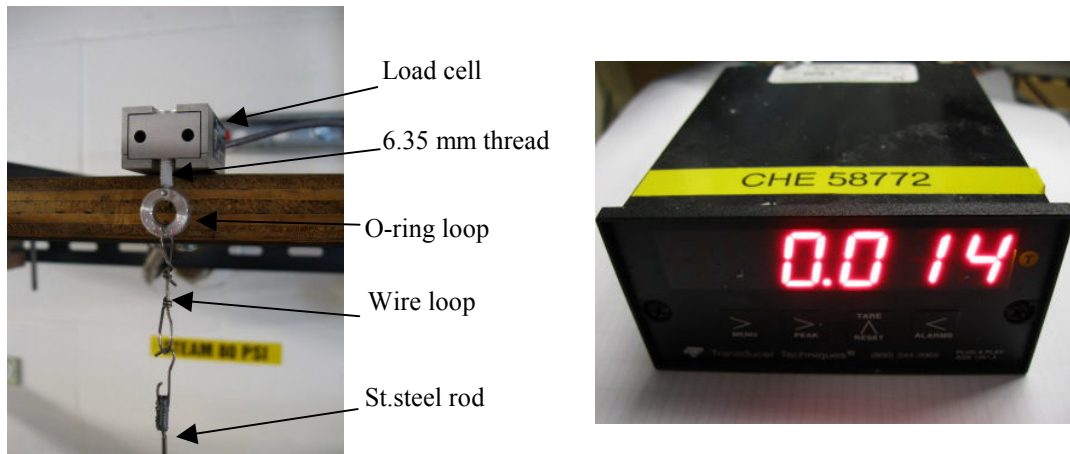


Figure 4.32 GSO-50 load cell and DPM-3 data logger from Transducer Techniques

The load cell was operated in the following manner. When the coupon is attached to the load cell, a certain amount of time is needed for the load cell to respond to the step change and reach equilibrium. For the new load cell, this time is about 10 minutes; but as the load cell is used more its response becomes slower, up to 45–60 minutes (Fig. 4.33). After the air is introduced and the drag force on the coupon reduces its weight, at high velocities and with a used load cell, some time is required for the response to settle down (2–3 minutes). After that, the liquid is introduced and the deposition starts. The deposition rate curve shows that the deposition rate is generally constant during the whole experiment. This enables deposition rates to be estimated from the mass of deposits at the end of the experiment.

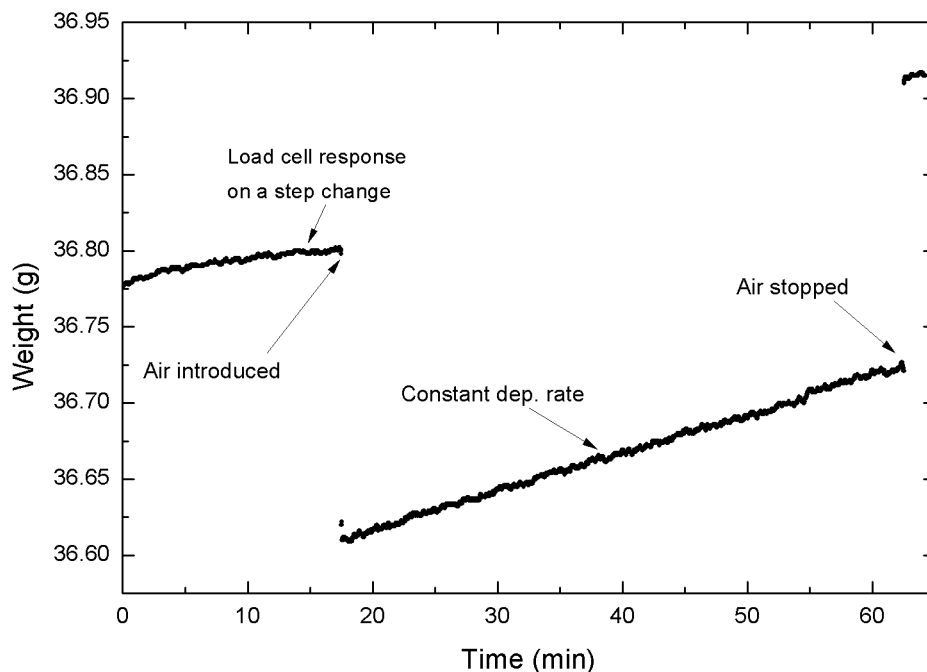


Figure 4.33 Typical response of the load cell, Run 15

From the deposition curve (Fig. 4.33), it can be also noted that the deposition rates are slightly higher at the beginning than later on; this is most certainly due to the continuing effect of the initial load cell response on the attached coupon. At velocities larger than 1 m/s, fluctuation and noise are greater, such that at 1.3 m/s, estimation of deposition rates from the graph is quite unreliable.

4.3.5.2. Analytical balance measurements

The mass of deposits was measured at the end of each experiment on the analytical balance (AND GR-200) with 0.1 mg precision. Once the aqueous sugar solution was replaced by tri-ethylene glycol, there was no evaporation and loss of weight of the deposits after the experiment. Therefore, the analytical balance measurements are considered more accurate than the load cell measurements, and were used to calculate the deposition rates. Also, the amounts of deposits on the rod, upstream and downstream sides could be measured separately on the analytical balance, results that were not possible to obtain from the load cell readings alone.

4.3.6. Contact angle measurements

Contact angles between the liquid and the solid surface were measured using the sessile drop method [65, 66]. The drops were dispensed on the coupon surface and observed from the side with a camera (Fig. 4.34). The shadowgraphy system was adapted for this purpose by putting the adjustable stage between the camera and the light source on which the coupon was placed. The stage was adjusted using fine screws to position the coupon in the horizontal plane. The droplet images were recorded using the Image Pro Plus software and the contact angles were then determined by image analysis using the FTA 32 software.

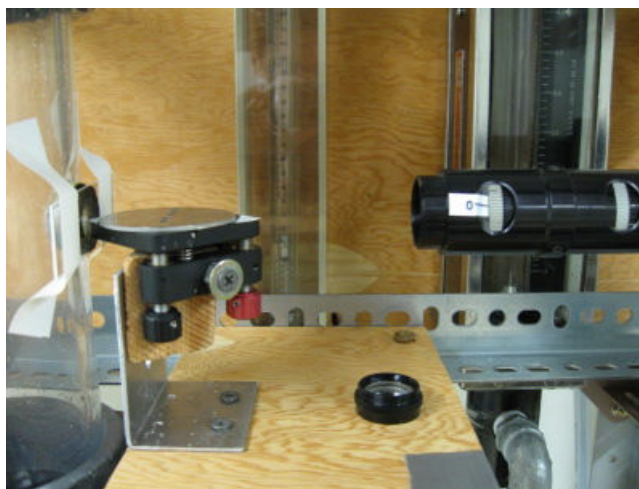


Figure 4.34 Photo of the sessile drop measurement system. Lenses are at 1 \times magnification, 90 cm away from the drops

4.3.6.1. Measurement procedure

The surface of the coupon was first cleaned with water and dried. The coupon was placed on the camera mounted on the moving stage (Fig. 4.35a) with a micropipette fixed above. The camera was then lifted toward the micropipette, and when the coupon touched the drop pending from the pipette tip, it was slowly pulled back down. This was important in order to eliminate variability due to the way that drop is applied to the surface [65]. The droplet volume was 2 microliters, which should be enough for proper contact angle measurements [67]. The next drop was deposited in the same manner, 3–4 mm adjacent to the previous one by moving the camera in the Y-direction. This created a series of drops that lie in a line. The coupon was then placed on the stage (Fig. 4.35b) so

that the droplets were positioned in the focal plane of the camera. Bounded with strips, the coupon was moved in the Y-direction and images of the droplets were recorded.

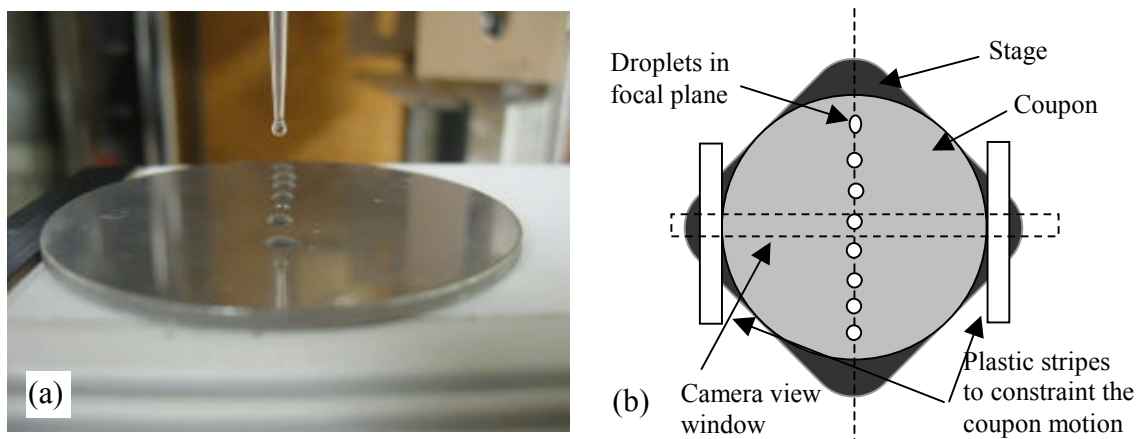


Figure 4.35 (a) Coupon on the camera when droplets are deposited from the pipette, and (b) schematics of the coupon on the stage as in Fig. 4.34

Although the pendant drop method is generally more accurate [65], it requires that needles used for dispensing the liquid be made of the materials in question (st. steel, graphite, Teflon etc.) which was not suitable for this work. Contact angles were measured 1–2 minutes after the droplets were deposited on the coupon, when it is assumed that equilibrium was reached (there is only a small difference between the values in the second and third column of the Table 4.14).

4.3.6.2. Accuracy of contact angle measurements

Sessile drop measurements of contact angles assume a spherical shape of the droplet, and a circular contact line with the surface [65]. In reality, irregularities in surface roughness and impurities cause a noncircular wetting line, which results in variability in the measured contact angles. Repeated measurements are the only way to estimate the true value [68]. The variability in contact angle measurements of tri-ethylene glycol droplets on the stainless steel coupon surface is presented in Table 4.14. In this particular case, results obtained from 4–7 repeated measurements yield a relative error (standard deviation of the arithmetic average) of about 1.4–1.6%. The estimated true value of the contact angle is $\theta_{avg}=48.9 \pm 1.6^\circ$ (95.5% confidence interval).

Table 4.14 Variability in contact angle measurements using the sessile drop method

Drop #	Contact angle (°)	Contact angle after 1 hour (°)	Average contact angle, from the drop #1	Standard deviation starting from the drop #1 (°)	Standard deviation of the average contact angle (°)	Relative error (%)
1	47.0	47.6	47.0			
2	49.4	48.3	48.2	1.7	1.2	2.4
3	45.9	45.0	47.4	1.8	1.0	2.3
4	47.6	46.6	47.5	1.5	0.7	1.5
5	49.5	49.0	47.9	1.6	0.7	1.4
6	51.3	50.3	48.5	2.0	0.8	1.6
7	51.6	50.4	48.9	2.2	0.8	1.6

Images of tri-ethylene glycol (TEG) droplets on different surfaces are shown in Fig. 4.36. The exposure that was used to record images of droplets in Image Pro Plus was 100 milliseconds at $1\times$ magnification, a value that should be kept constant to obtain consistent results.

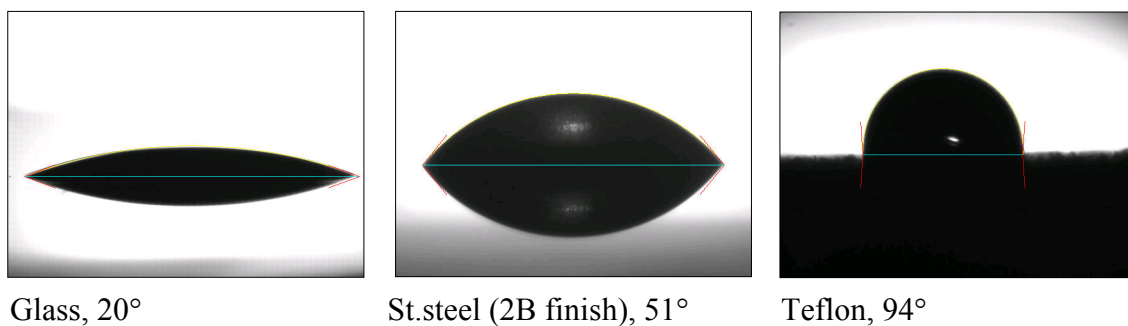


Figure 4.36 Images of TEG droplets on different surfaces, recorded with Image Pro Plus

Chapter 5. Results and Discussions

In order to investigate the effect of velocity and droplet size on the deposition rate, four sets of experiments were performed. The *first* and *second sets* of experiments investigated the effect of velocity at an (almost) constant droplet size distribution. Aqueous sugar solution of concentration 50% (Section 5.1.1), and triethylene glycol (Section 5.1.2), with Setup #1 (Fig. 4.3) were used. The second set of experiments was performed using triethylene glycol, to eliminate issues encountered with the sugar solution, as described below.

The *third set* of experiments was performed using the Hot Unit nozzle (Fig. 4.5) in the Cold Unit (Setup #2, Fig. 4.3) and investigated the effect of velocity on *downstream* deposition only (Section 5.1.2.2). This was done in order to provide more accurate results, from which downstream deposition coefficients for each drop size at a given velocity could be calculated (Section 5.3).

The *fourth set* of experiments investigated the effect of droplet size distribution, at constant aerosol velocity ($U=1$ m/s), using triethylene glycol (Section 5.2). The Cold Unit nozzle and Setup #1 were used. These experiments were performed in order to gain insights about the behaviour of the system when the drop size distribution is varied.

In the next step, models developed in Chapter 3 were used to simulate deposition and compare the results of simulations with the experimental data (Sections 5.4, 5.5).

The morphology and distribution of deposits on the coupon surface were also studied and the results are presented in Section 5.6.

Finally, to investigate the effect of contact angle on deposition rates, short experiments on dry and partly wet disk surfaces (glass, stainless steel and Teflon), using triethylene glycol were performed. The results are presented in Section 5.7.

Recall that deposition rates, deposition coefficients and capture efficiencies were introduced in Section 2.2 (Eqs. (2.7)–(2.9)). The deposition rate can represent the rate of fouling at a given aerosol concentration. The deposition coefficients are independent of the aerosol concentration, and can be viewed as a direct measure of the deposition rates. Capture efficiencies represent the measure of the aerosol removal by deposition: higher

capture efficiencies mean a lower concentration of droplets in the aerosol leaving the unit and higher product purity. Therefore, to minimize fouling, one should operate at the minimum deposition coefficients, but to maximize droplet removal (and product purity), one should operate at the highest capture efficiencies. The effects of the investigated factors on capture efficiencies and deposition coefficients are presented in the following sections.

5.1. Effect of velocity

The velocity of the aerosol was varied by adding secondary air, using a gas distributor placed around the nozzle. In order to keep the drop size distribution constant, the flow of air to the nozzle was kept constant. However, the addition of secondary air changed the size distribution to a certain degree, and the effect of velocity should be considered bearing in mind the change in the volume median diameter.

Total deposition coefficients were calculated by dividing mass deposition rates by the droplet concentration and the surface area of the coupon, while capture efficiencies were obtained by dividing the deposition coefficients by the velocity (as already mentioned in Section 2.2, Eqs. (2.7), (2.8)).

5.1.1. Effect of velocity with 50% sugar solution

In the first set of experiments, a 50% wt. aqueous sugar solution was used. This solution was chosen because of its stickiness and moderate viscosity (0.015 Pa·s at 20°C), which is not too high to make atomization difficult. It was easy to handle and did not require treatment of the aerosol leaving the Cold Unit. The experiments were performed using the Cold Unit nozzle (Fig. 4.4) and Setup #1 (Fig. 4.3). The experimental results showed low reproducibility (standard deviation was 54%) that was attributed to the evaporation of water from the deposits on the coupon surface. Evaporation took place during the experiments (humidity in the column was not controlled and varied between 5–30%), and after the experiments, during measurements on the analytical balance.

In order to reduce the variability in measuring the deposition rates, saturation of the air in the column was attempted in several ways. The ‘air to the nozzle’ stream (Fig. 4.1) was humidified using the following designs: spray column, bubble column, bubble

column with packing, and bubble column with packing and heated water. Saturated air in the column was not obtained in any of these cases. It can be shown from calculations that even if the air before the nozzle is saturated, after it expands from 300–400 kPa (nozzle pressure) to 101.3 kPa (atmospheric pressure in the column), the relative humidity in the column cannot be higher than about 30%. Therefore, in the subsequent work, the aqueous sugar solution was replaced by *triethylene glycol*, due to its low vapour pressure (0.02 Pa at 20°C), and ease of handling. A comparison of the relevant physical properties of a 50% aqueous sugar solution and triethylene glycol is given in Table 5.1.

Table 5.1 Properties of 50% aqueous sugar solution and triethylene glycol at 20°C

Property	50% wt. aq. sugar solution	Triethylene glycol
Density (kg/m ³)	1230	1127
Dynamic viscosity (Pa·s)	0.015	0.049
Surface tension (mN/m)	78	45
Vapour pressure (Pa)	2200	0.02

5.1.2. Effect of velocity with triethylene glycol

Experiments with triethylene glycol were performed in the same manner as with the 50% aqueous sugar solution. The air and liquid flows to the nozzle were kept constant, and the velocity was changed by adding secondary air, via the gas distributor placed around the nozzle. Two sets of experiments were performed: one using the Cold Unit nozzle and Setup #1, and the other using the Hot Unit nozzle and Setup #2.

5.1.2.1. Cold Unit nozzle, Setup #1

Since deposition coefficients and capture efficiencies are calculated from measured aerosol concentrations (and deposition rates), the accuracy of the aerosol concentration measurements with the Cold Unit Setup #1 (Fig. 4.3) is discussed first.

The aerosol concentrations calculated from washdown and shadowgraphy measurements are presented in Fig. 5.1. It can be noted that the trends of the data obtained from these two measurement techniques are similar, but the concentration from shadowgraphy measurements is lower (by a factor of 1.5–2) than the concentration obtained from washdown measurements. This is most probably because a portion of the large droplets, which significantly contribute to the droplet mass concentration in the

aerosol, deposits in the elbows and is not measured by shadowgraphy (correct measurement). These droplets may stay deposited on the column walls and do not form part of the washdown stream, which causes an increase in the measured concentrations (incorrect measurement). The difference is more pronounced at higher velocities, where the removal of larger droplets is more pronounced. Therefore, for the Cold Unit Setup #1 (Cold Unit nozzle, 90° and 45° elbows), the better measurement method is *shadowgraphy*. The concentrations measured by shadowgraphy were therefore considered more reliable, and, consequently, were used in the calculation of deposition coefficients and capture efficiencies. For the Hot Unit nozzle and Setup #2, the washdown and shadowgraphy measurements of concentration match more closely (Fig. 5.4, pg. 95).

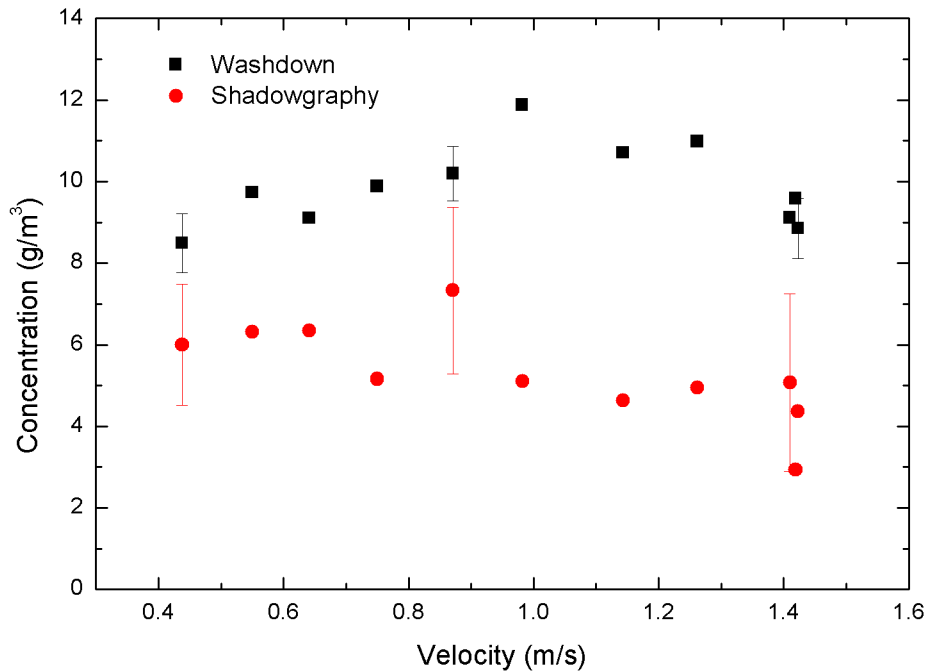


Figure 5.1 Aerosol concentration vs. velocity for Cold Unit nozzle and Setup #1 experiments, calculated from washdown and shadowgraphy measurements of concentration, for triethylene glycol. 95% confidence intervals are estimated from three repeated experiments

One would expect that as more secondary air was added, the aerosol would be diluted and the concentration would show a systematic reduction. However, since the secondary air was introduced from the gas distributor that was placed around the nozzle,

injected air increased the drag force on the droplets from the spray in the axial direction, thereby reducing impaction on the column walls. As the velocity was increased, less washdown was formed, resulting in an increased flow of droplets to the aerosol. Interestingly, the droplet flow to the aerosol increased linearly with the velocity, and as a result the aerosol concentration did not change significantly over the entire range of velocities.

a. Upstream side

The effect of velocity on the upstream deposition rates was investigated in the range of $U=0.44\text{--}1.44$ m/s. At velocities below about $U=0.55$ m/s, there were no deposits on the upstream side. Above $U=0.55$ m/s, deposition rates increased almost linearly from 0 to 1390 mg/hr, as given in Table E.1.

The effect of velocity on capture efficiencies and deposition coefficients for the upstream side is presented in Fig. 5.2. The capture efficiencies show a steady increase with velocity, starting from $E=0$ at about $U=0.55$ m/s, to $E=0.03$ at $U=1.25$ m/s. At velocities above $U=1.25$ m/s, the capture efficiencies decrease, although this difference could be within the experimental error. If the decrease in capture efficiencies exists, the only explanation could be the removal of large droplets (due to higher superficial velocities) in the elbows. If the size distribution of droplets wasn't reduced in this manner, there would be no other reason for the capture efficiencies to decrease. The deposition coefficients, obtained by multiplying capture efficiencies with velocity, show a similar increasing trend. The volume median diameter slightly decreased with velocity from 6.5 microns to about 6.0 microns, as a result of inertial deposition of larger droplets in the elbows.

The observed increase in capture efficiencies with velocity is expected: according to the mechanism of inertial impaction, capture efficiencies increase with the Stokes number, which is a linear function of velocity ($St = t_p U / D_c$). However, a proper quantitative comparison is limited to monosize droplets, where Stokes numbers can be calculated. This was done in Section 5.5, where the measured size distribution of droplets in the aerosol and on the coupon were used to calculate the capture efficiencies and deposition coefficients for each drop size.

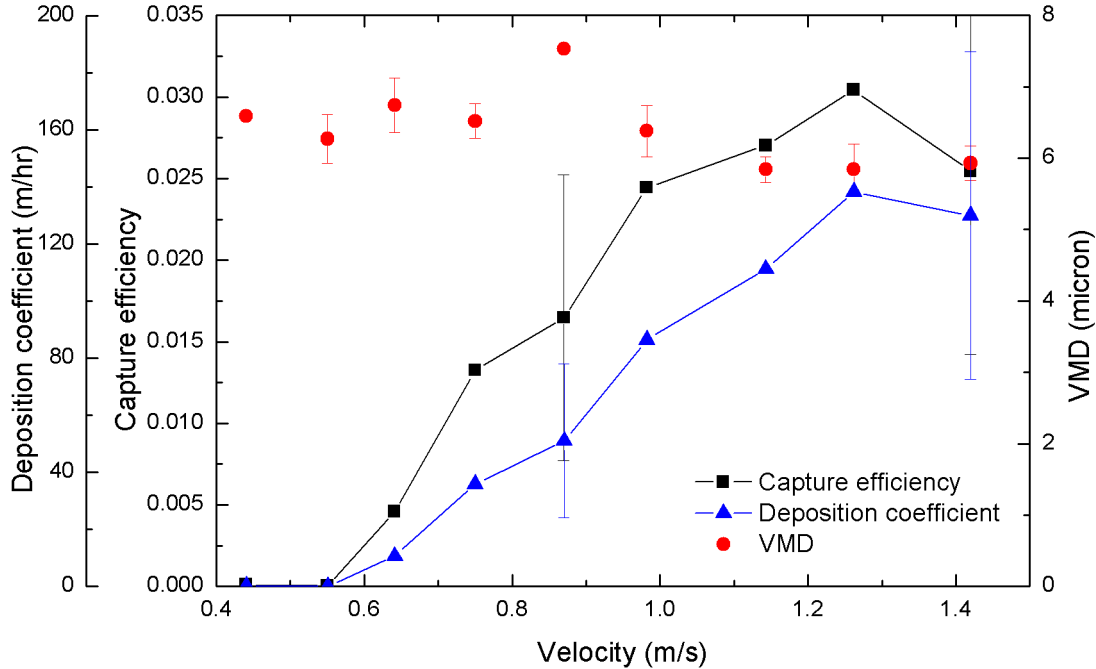


Figure 5.2 Upstream side capture efficiencies, deposition coefficients and volume median diameter vs. velocity. 95% confidence intervals are estimated from three repeated experiments

b. Downstream side

Deposition rates on the downstream side were significantly lower than deposition rates on the upstream side; they varied from 80.9 mg/hr at $U=0.64$ m/s to about 152 mg/hr at $U=1.26$ m/s (Table E.1).

The effect of velocity on capture efficiencies and deposition coefficients for the downstream side is presented in Fig. 5.3. The capture efficiencies decrease with velocity in the range $U=0.44$ – 0.64 m/s. After $U=0.64$ m/s, although the variability in the data is significant, the capture efficiencies show little change and remain almost constant ($E \approx 0.0035$). As a result of almost constant capture efficiencies, the deposition coefficients show a steady increase with velocity. The trend of the data presented in Fig. 5.3 could be explained satisfactorily with the inertial impaction mechanism and gravity in the flow direction, as will be shown in Sections 5.4 and 5.5.

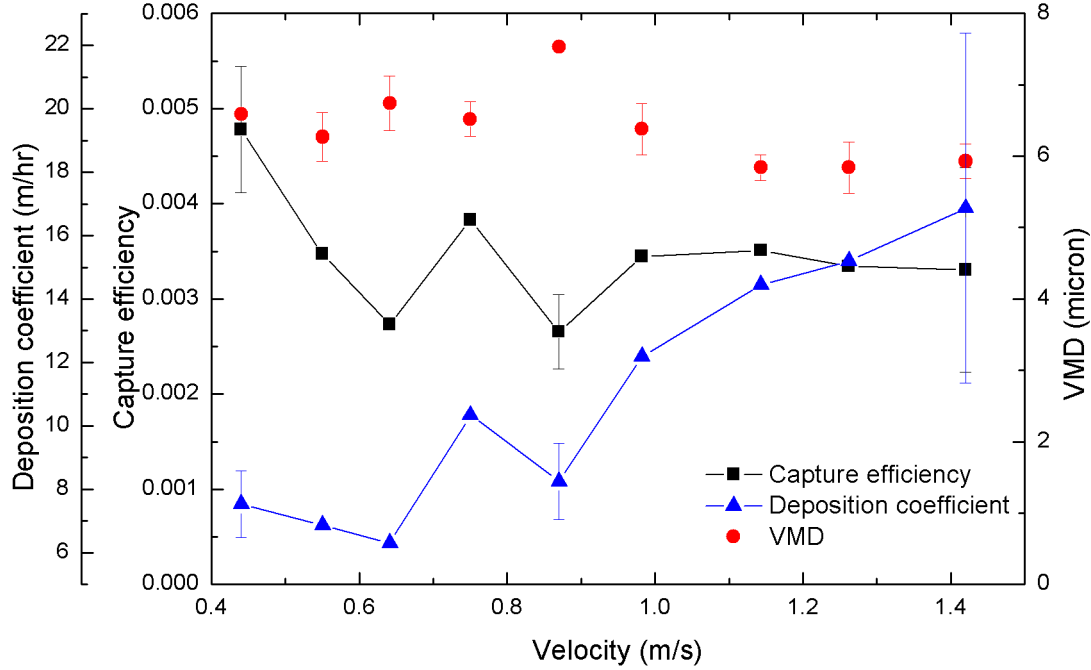


Figure 5.3 Downstream side capture efficiencies, deposition coefficients and volume median diameter vs. velocity. 95% confidence intervals are estimated from three repeated experiments

In summary,

1. Increasing the velocity increased the capture efficiencies on the upstream side of the coupon, in accordance with the theory of inertial impaction. A quantitative comparison with theoretical predictions is possible only for each drop size, and is presented in Section 5.5.1.

2. For the downstream side, an initial decrease with velocity was followed by a region of constant capture efficiencies. The deposition coefficients showed a minimum between $U=0.4$ m/s and $U=0.7$ m/s. The downstream capture efficiencies were up to 10 times lower than the capture efficiencies for the upstream side.

5.1.2.2. Hot Unit nozzle, Setup #2

From the experiments performed in the Hot Unit [52], there were little or no deposits on the upstream side (even at $U=0.92$ m/s), which suggested that the Hot Unit nozzle produced very fine droplets, carried with the aerosol. The drop size distribution from this nozzle is similar to the distribution that is estimated to be in the scrubber section of the Fluid Coker (<11 microns, [8]). Therefore, the Hot Unit nozzle was used in the next set of experiments.

Recall that Setup #2 (Fig. 4.2) had the nozzle spraying upward in a straight cylindrical section. This arrangement caused uncontrolled deposition of large droplets entrained in the aerosol from the bottom of the column on the upstream side, at velocities $U > 0.7$ m/s. This is the reason why elbows were installed initially. Therefore, although the results on upstream deposition are presented in Table E.2, they could not be considered reliable, and are not discussed below.

As already mentioned (Section 5.1.2.1), the validity of the aerosol concentration measurements is an important factor in calculating the deposition coefficients and capture efficiencies. While shadowgraphy measurements are considered to be more accurate than washdown measurements, Figure 5.1 shows that the shadowgraphy measurements are less precise (have greater scatter) than the washdown measurements. For the Hot Unit nozzle and Setup #2, the results from the two measurement methods match closely for two reasons: (1) the size of the shadowgraphy sample is increased 5 times while the variability is reduced, and (2) washdown issues (deposition of droplets in elbows) do not persist with Setup #2 anymore, hence, accuracy is improved. Since the washdown measurements showed less scatter (Fig. 5.4), they were used in the calculation of downstream deposition coefficients and capture efficiencies (Section 5.3).

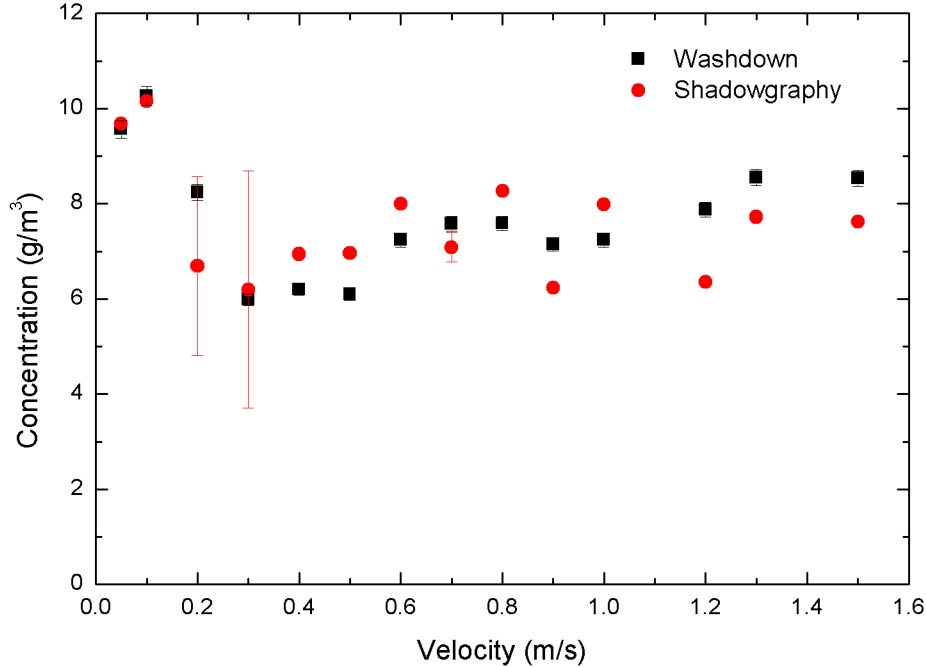


Figure 5.4 Aerosol concentration vs. velocity, for Hot Unit nozzle and Setup #2 experiments, calculated from washdown and shadowgraphy measurements of concentration. 95% confidence intervals calculated from two repeated experiments

In these experiments, the deposition rates on the downstream side varied between 30.5 mg/hr at $U=0.5$ m/s, and 123.9 mg/hr at $U=1.5$ m/s (Table E.2). The volume median diameter was almost constant over the whole range of velocities (4.9–5.4 microns), with the exception of the first point, when the flow of air to the nozzle was quite low and the nozzle produced large droplets. Capture efficiencies and deposition coefficients vs. velocity are presented in Fig. 5.5.

The capture efficiencies showed an exponential-like decrease from about 1.5% at $U=0.05$ m/s to about 0.1% at $U=0.7$ m/s. In the range from 0.7 m/s to about 1 m/s, the capture efficiencies remained constant, and at $U>1$ m/s they showed a slight increase. One might expect that as the velocity is decreased below 0.05 m/s, the capture efficiencies would approach one. This would be the case for the coupon side facing a fresh stream of slow aerosol that flows in the downward direction (gravitational settling would be approached). For upward flow, the capture efficiencies would probably still increase as the velocity is reduced below 0.05 m/s, but only up to the point when the flow becomes too slow to transport droplets in the upward direction. Deposition coefficients showed a

minimum at about 0.6 m/s, indicating that the minimum deposition (fouling) rate could be expected at that velocity. It can be noted that the observed trends are in accordance with the trends obtained in Section 5.1.2.1.b, when the Cold Unit nozzle and Setup #1 were used. These results can also be explained by the inertial impaction mechanism along with gravity in the flow direction (Sections 5.4, 5.5).

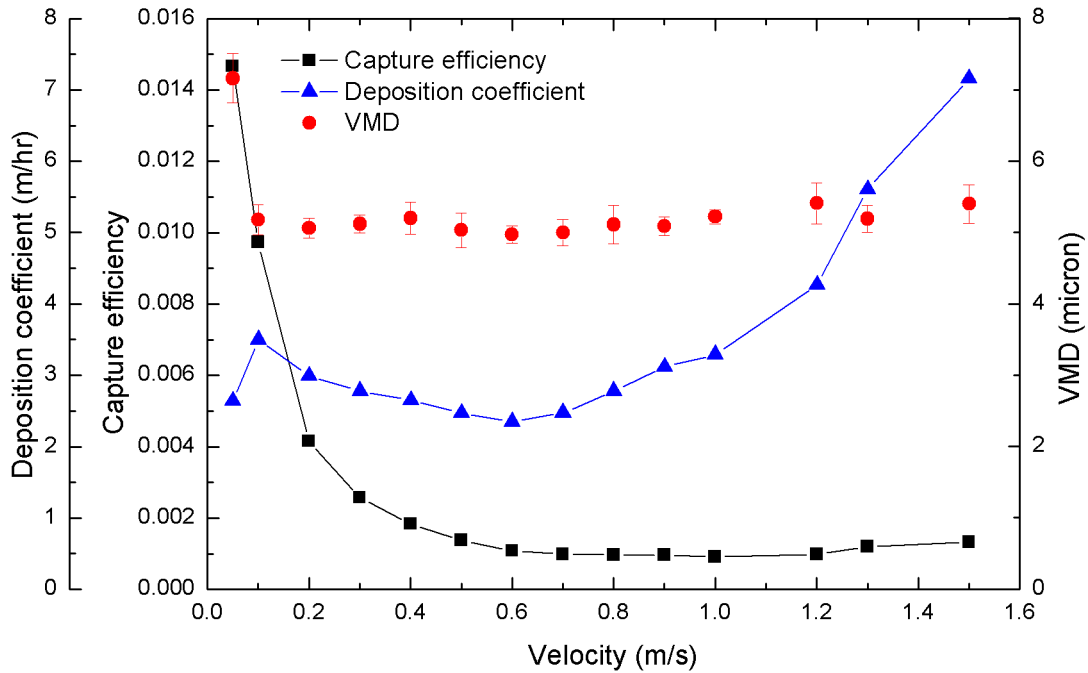


Figure 5.5 Downstream side capture efficiencies, deposition coefficients and volume median diameter vs. velocity

In summary,

1. The downstream side capture efficiencies showed an exponential-like decrease to a minimum value of 0.0009 (<0.1%) at $U=1.0$ m/s. The deposition coefficients showed a minimum ($k_d=2.35$ m/hr) at about $U=0.6$ m/s.

2. In addition, the observed trends were in accordance with the results obtained for the downstream side using the Cold Unit nozzle and Setup #1 (Fig. 5.3).

5.2. Effect of droplet size distribution, Cold Unit nozzle, Setup #1

To investigate the effect of the droplet size distribution (quantified by its volume median diameter) on deposition, the liquid flow to the nozzle was varied from 7.2 ml/min to 95 ml/min, while the air flow rate to the nozzle was kept constant. As the liquid flow was increased, the volume median diameter increased from 3.9 to about 7.5 microns. Qualitatively speaking, this change is in accordance with the empirical correlation for twin-fluid atomizers (Eq. (3.37)). The resulting velocity in the column from the air flow rate to the nozzle was $U_{nozzle} = 0.43$ m/s, and the total velocity was kept at $U_{total} = 1$ m/s.

5.2.1. Upstream side

Deposition rates on the upstream side varied from 12.3 mg/hr for the smallest size distribution of droplets (VMD=3.9 microns), to about 1380 mg/hr for the largest size distribution. As the liquid flow rate was increased, the concentration increased almost linearly from 1.1 g/m³ to 5.54 g/m³ (Table E.3). The capture efficiencies and deposition coefficients for the upstream side are presented in Fig. 5.6.

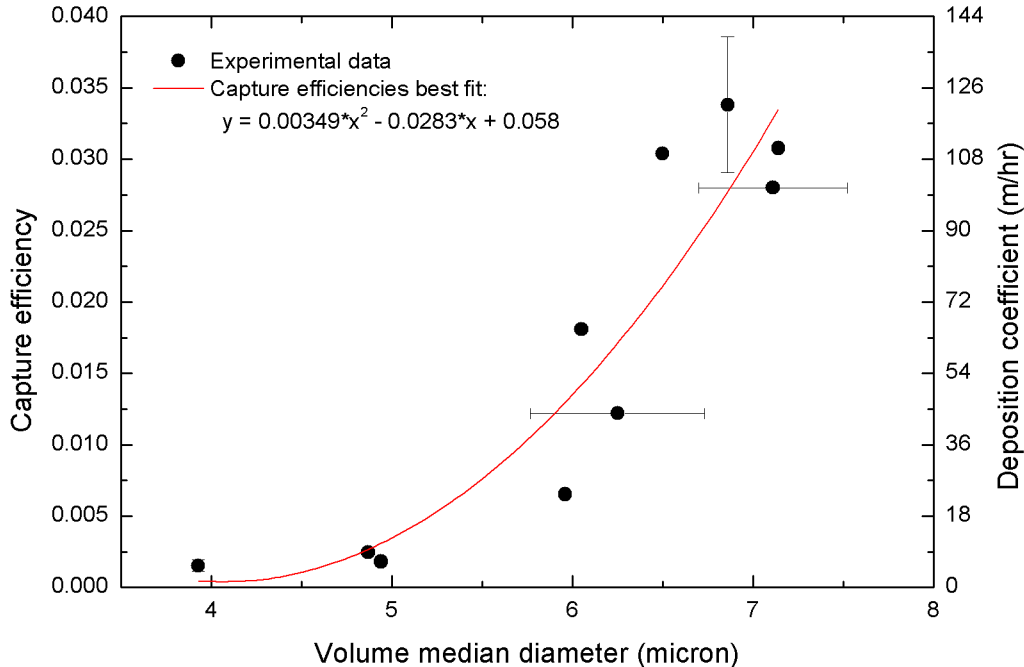


Figure 5.6 Capture efficiency and deposition coefficient for the upstream side vs. volume median diameter, at $U = 1$ m/s. 95% confidence interval were estimated from three repeated experiments

From Figure 5.6, it can be seen that increasing the volume median diameter caused a major increase in capture efficiencies (and deposition coefficients). Increasing the median diameter from 5 to 7 microns resulted in an increase in capture efficiencies of more than an order of magnitude. These results are logical, because as the volume median diameter is increased, the concentration of large droplets in the aerosol is increased. This means that there were more droplets with a larger Stokes numbers present in the aerosol, which according to the theory of inertial impaction, increased the total capture efficiency.

5.2.2. Downstream side

As the volume median diameter was increased, the deposition rates on the downstream side increased from 10.5 mg/hr to 137 mg/hr (Table E.3). The capture efficiencies and deposition coefficients for the downstream side are given in Fig. 5.7.

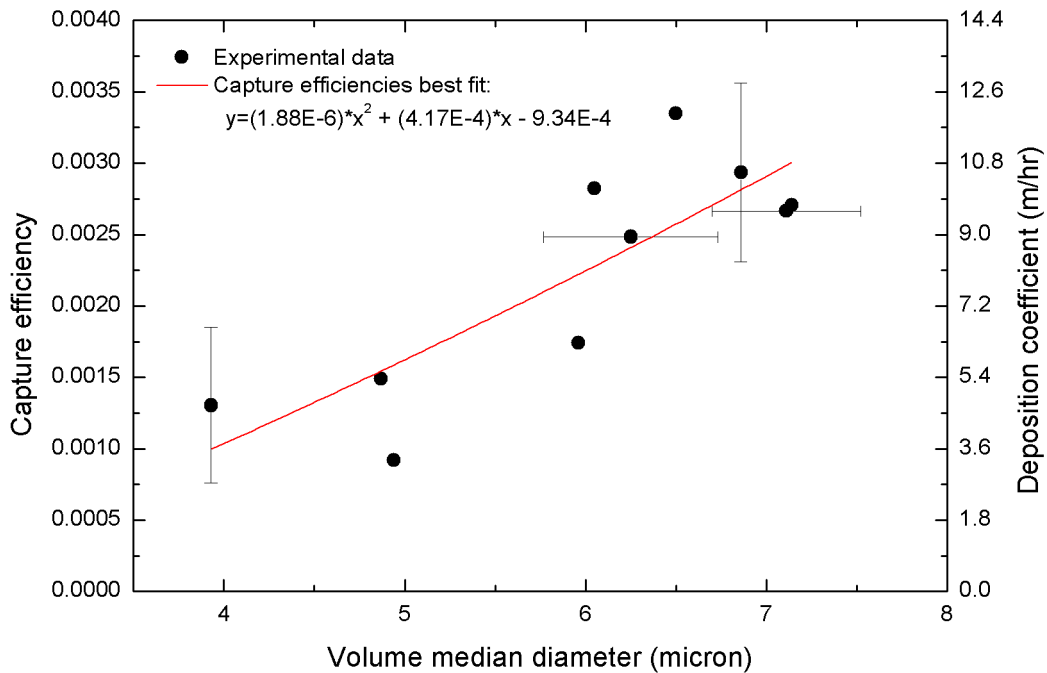


Figure 5.7 Capture efficiency and deposition coefficient for the downstream side vs. volume median diameter, at $U = 1$ m/s. 95% confidence intervals were estimated from three repeated experiments

From Fig. 5.7, it can be noted that capture efficiencies show a slight but definite increase with the volume median diameter. The increase in capture efficiencies with drop diameter can be explained by the increased Stokes number, which according to the theory of

inertial impaction and gravity in the flow direction, increases capture efficiencies (Sections 5.4 and 5.5). The solid lines in Fig. 5.6 and Fig. 5.7 represent the best-fit polynomial curves, which can be used for calculating the change in capture efficiencies, depending on the volume median diameter of the size distribution.

5.3. Calculation of capture efficiencies and deposition coefficients for individual drop sizes from experimental results

From their experiments of deposition on the front and back surfaces of disks, Vincent and Humphries [19] concluded that although difficult to interpret, meaningful experiments could be carried out using polydisperse dusts. Polydispersity almost always characterizes natural or ‘real’ systems, and there are many phenomena that are not revealed when working with monodisperse systems. For this reason, in this section, the effects of the size distributions of the droplets in the aerosol and on the coupon were investigated.

Therefore, to obtain more general results and draw meaningful conclusions that could be explained quantitatively from a theoretical point of view, the calculation of deposition coefficients and capture efficiencies for each drop size at a given velocity was carried out. This was done by the use of Eq. (3.26) and Eq. (3.27). Since measurements of deposition rates and aerosol concentration are believed to be sufficiently accurate, proper determination of the size distributions on the coupon and in the aerosol proved to be important for the validity of results. Images of the deposits on the upstream and downstream glass coupon surfaces for Run 26 are given in Fig. 5.8.

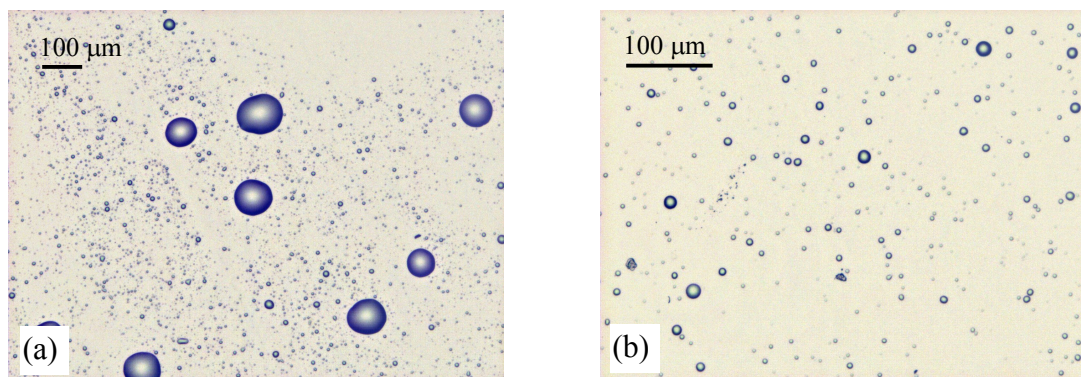


Figure 5.8 Images of triethylene glycol deposits on the (a) upstream and (b) downstream surface of the glass coupon, Run 26

The size distributions of droplets in the bulk aerosol, and on the upstream and downstream surfaces of the coupon, for Run 26, are given in Fig. 5.9.

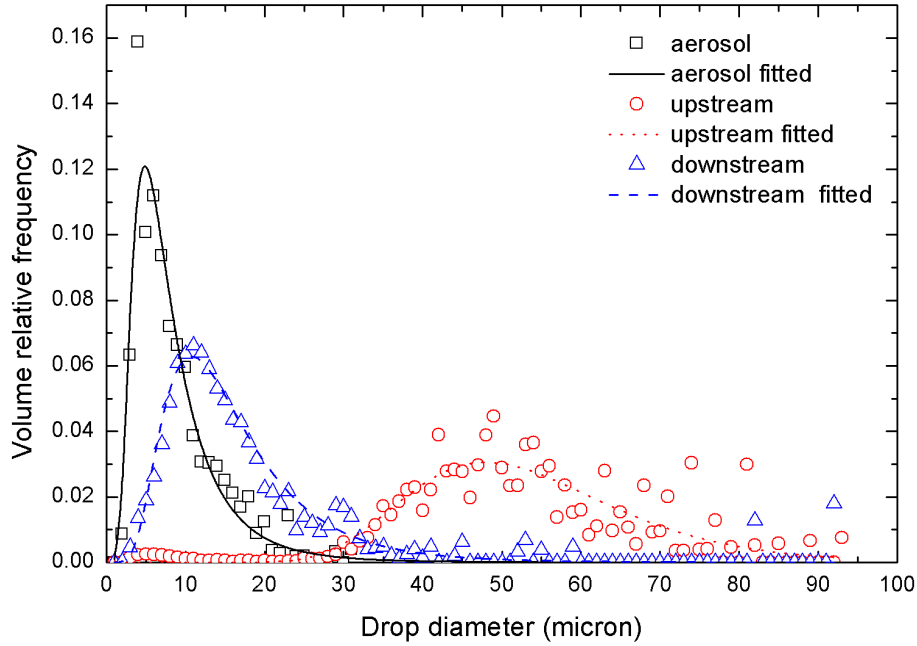


Figure 5.9 Measured drop size distributions in the aerosol, and on the upstream and downstream sides of the glass coupon at 1 m/s, Run 26

From Fig. 5.9, it can be noted that only the size distribution of deposits on the downstream side significantly overlaps with the size distribution in the aerosol (up to $D_p=25\ \mu\text{m}$). Therefore, reliable estimation of deposition coefficients should be possible in the region from 1–25 microns. On the upstream side, only droplets larger than about 28 microns deposit (by inertial impaction) and notably contribute to the mass of deposits. Hence, it was expected that the correct estimation of deposition coefficients would be difficult, since it includes calculations that require extrapolation of the aerosol size distribution curve.

5.3.1. Effect of drop diameter at different velocities, downstream side

The effect of drop diameter at different velocities was determined from experiments performed with the Hot Unit nozzle and Setup #2 (Section 5.1.2.2), using Eqs. (3.26) and (3.27). The results are presented in Figs. 5.10 and 5.11, and are given in

Table E.3. The fitted size distributions of droplets in the aerosol and coupon deposits were used in the calculations, and for that reason, the ‘experimental’ curves obtained appeared smooth. Over the whole range of velocities, the capture efficiencies and deposition coefficients show a definite increase with the drop diameter. The deposition coefficients at 1.5 m/s approach the deposition coefficients for gravitational settling (Fig. 5.11).

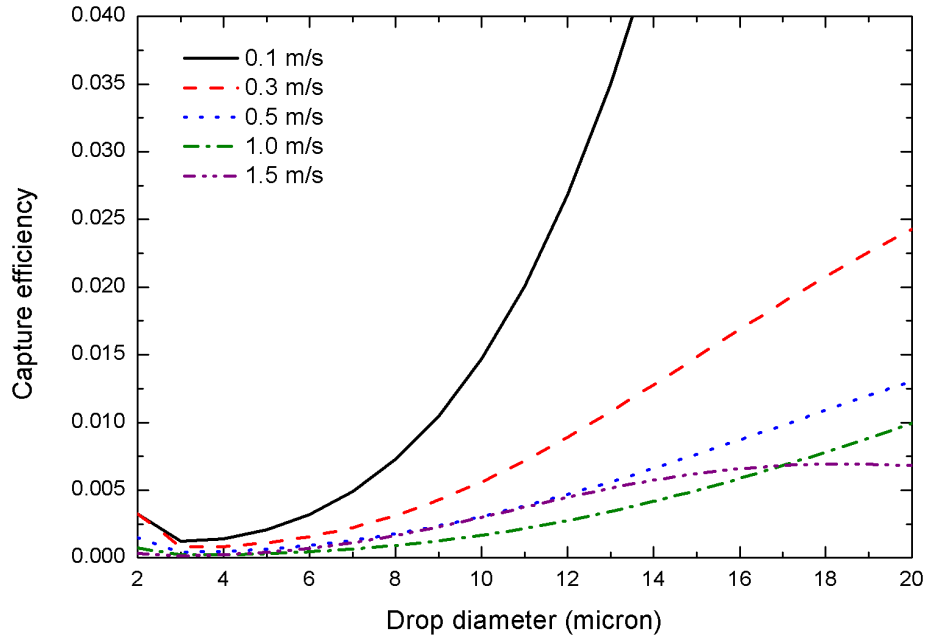


Figure 5.10 Calculated capture efficiencies vs. drop diameter for the downstream side, at different gas velocities

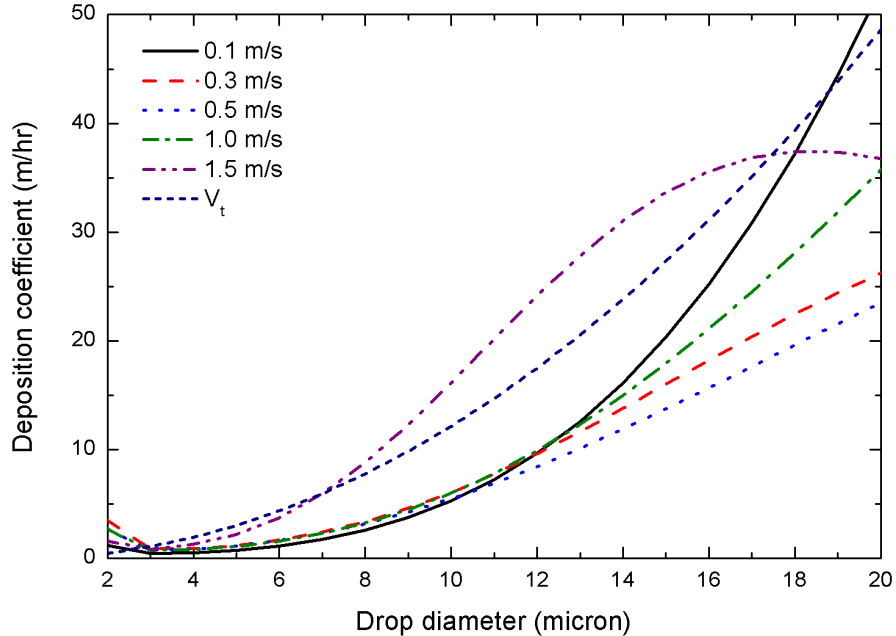


Figure 5.11 Calculated deposition coefficients vs. drop diameter for the downstream side, at different gas velocities

The results are shown for the range of drop sizes from 2–20 microns, since they are obtained by dividing the parts of distribution that are more accurate (significant overlap, Fig 5.9). Above $D_p=20$ –25 microns, the deposition coefficients and capture efficiencies still increase, but eventually must reach maximum and fall down to zero at higher Stokes numbers (at the highest velocity, $U=1.5$ m/s, the deposition coefficients reached a maximum at 17 microns and then start decreasing at $St=0.03$). This is because it is expected that droplets with high inertia would follow their original pathlines, and would not be entrained in the vortex behind the coupon (Fig. 3.1). From the results of the downstream deposit analysis (Table E.2), it can be seen that larger droplets were not entrained in the vortex behind the coupon (D_{max} for all runs is in the range from 27–40 microns, from at least 20,000 sampled droplets). If they were entrained, they would be deposited due to high inertia. At the same time, it is known that large droplets (>30 microns) are present in the aerosol, since some of them deposit on the upstream side. Therefore we may presume that large droplets with high inertia either deposit on the upstream side, or bypass the coupon, without being entrained in the vortex.

5.3.2. Effect of velocity for different drop diameters, downstream side

The capture efficiencies and deposition coefficients calculated in the previous section can be plotted versus velocity. The effect of velocity for different drop diameters is presented in Figs. 5.12 and 5.13. The results are given in Table E.4.

The capture efficiencies for all drop sizes show an exponential-like decrease with velocity, followed by a region of almost constant values. This is more pronounced for larger droplets. The results show good qualitative agreement with the results obtained using the size distribution of droplets (Fig. 5.5). The deposition coefficients for the smaller droplets (3, 5 micron) are almost constant over the range of velocities investigated, while for the larger droplets (10–25 microns), the deposition coefficients first decrease, then remain constant, and somewhere between 0.6 m/s and 1 m/s start to increase again. These trends are also in agreement with the results obtained in experiments with size distribution, using the Cold Unit nozzle and Setup #1 (Fig. 5.3).

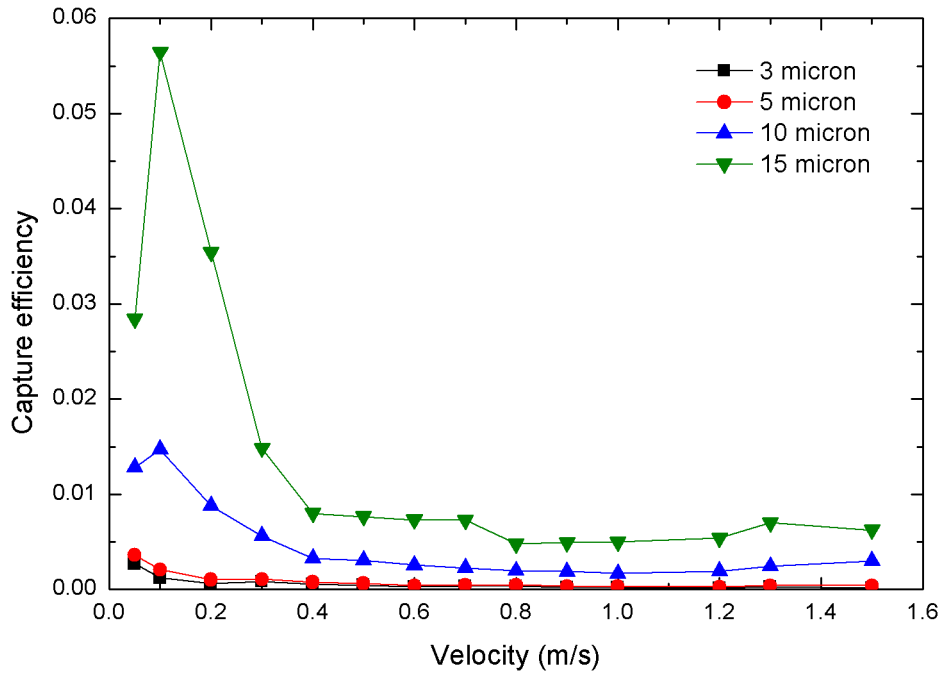


Figure 5.12 Calculated capture efficiencies vs. velocity for the downstream side, at different drop diameters

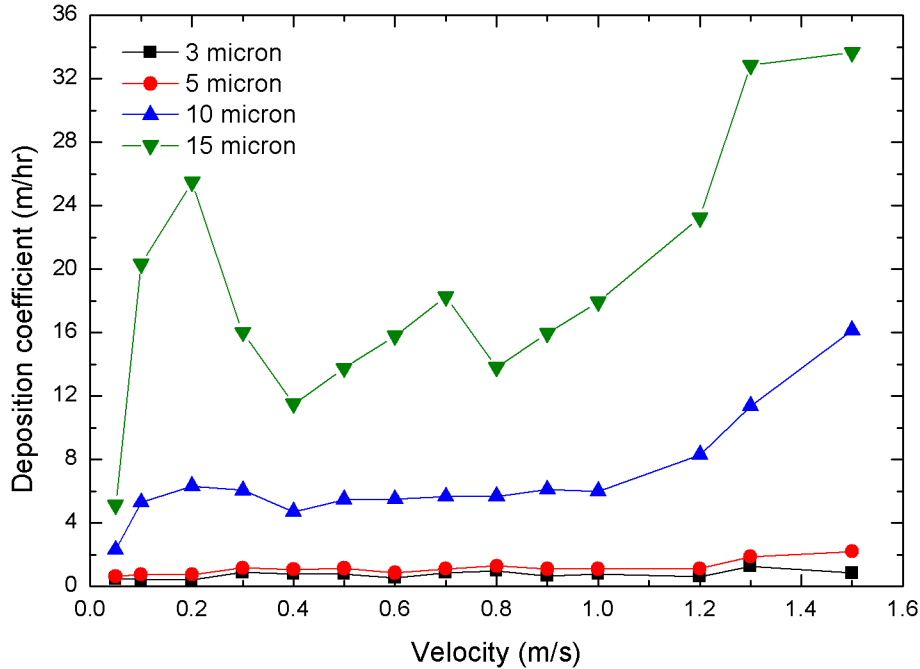


Figure 5.13 Calculated deposition coefficients vs. velocity for the downstream side, at different drop diameters

From Figs. 5.10–5.13, it can be definitively concluded that on the downstream side, deposition coefficients and capture efficiencies, in the range from 2–20 microns, increase with droplet size. The same trend was observed in experiments with drop size distribution (Fig. 5.7). Also, it can be concluded that for larger droplets (>10 microns), the deposition coefficients show a minimum value, somewhere between velocities of 0.5 m/s and 1 m/s. For smaller droplets, in the velocity range of 0.5–1 m/s, deposition coefficients are mainly constant, and at $U > 1$ m/s, they start to increase. As the drop diameter is increased, the increase in deposition coefficients occurs sooner, at lower velocities. All these phenomena can be explained by the mechanisms of inertial impaction and gravity in the flow direction, as is shown in the next two sections (Sections 5.4 and 5.5). Deposition coefficients for each drop size and velocity, obtained in this section, can be further used in the calculation of deposition coefficients for any drop size distribution at a given velocity. Knowing the aerosol concentration, deposition rates can be then easily calculated (Eq. (2.9)).

5.4. Simulations

In order to explain the experimental results of deposition on the upstream and downstream sides of the disk (coupon), the results of the simulations of inertial deposition, with and without gravity, are presented here. The results of calculating deposition due to turbulent particle transport are also presented.

5.4.1. Inertial particle transport

To simulate inertial deposition of droplets on the upstream side, the equations of particle motion in a potential flow field (Chapter 3) were solved analytically and numerically (*Appendices C and D*). The analytical solutions of droplet trajectories and capture efficiencies were obtained for Stokesian particles (*Appendix C*), while non-Stokesian particles required numerical calculations (*Appendix D*). In the following sections, the two solution methods, the validity of the potential flow approximation, and the effect of gravity on the inertial particle transport are discussed. To get a visual sense of the deposition phenomena, trajectories of particles before the coupon are presented first.

5.4.1.1. Particle trajectories

The droplet pathlines are shown in Fig. 5.14, for single droplets of different sizes, placed in the flow at a distance $\bar{x} = x/R_c = -0.5$, upstream of the disk. Initial velocity of injected droplets was equal to the superficial gas velocity, corrected for the droplet terminal velocity.

From Fig. 5.14a we can see that smaller droplets closely follow the fluid streamlines and do not reach the coupon surface via the inertial deposition mechanism ($D_p < 42$ microns). Intermediate size droplets (Fig. 5.14b) deposit on the surface ($42 < D_p < 135$ microns), while very large droplets (Fig. 5.14c), which are heavy enough, fall down before they reach the coupon surface ($D_p > 135$ microns). Start and end point diameters for inertial deposition (42 and 135 microns) are obtained from the simulations, using properties of tri-ethylene glycol droplets in air at room temperature. These values can be read from Fig. 5.19b, for the superficial velocity $U = 1$ m/s.

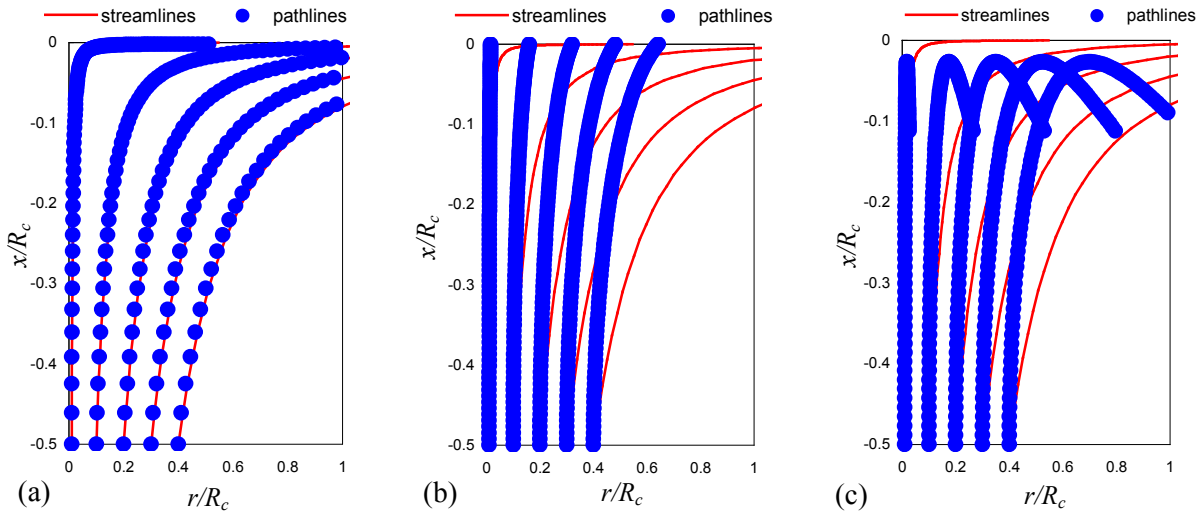


Figure 5.14 Trajectories of (a) 10, (b) 50 and (c) 140 micron droplets (pathlines) in the potential flow field (streamlines), for an upward flow at 1 m/s superficial gas velocity, using the Stokes drag force

5.4.1.2. Discussion of the model validity

To confirm the validity of the numerical procedure, analytical and numerical solutions for Stokesian particles were compared (section *a*). To compare the effect of different drag force, numerical solutions for Stokesian and non-Stokesian particles are presented as well. Since the potential flow is an approximation of the actual flow field, the results of potential flow simulations were compared with the CFD results [36], where a more faithful flow field was used (section *b*). To investigate the effect of the absence of a viscous sublayer in the potential flow model, deposition from a flow that includes a viscous sublayer was simulated too (section *c*).

a. Analytical vs. numerical solutions for Stokesian particles, and non-Stokesian vs. Stokesian particles

Analytical and numerical solutions for Stokesian particles, as well as the numerical solution for non-Stokesian particles are presented in Fig. 5.15.

From Fig. 5.15, it can be noted that,

1. The results of the numerical procedure for Stokesian particles (open “data” points) match analytical solutions for Stokesian particles (smooth curves). Hence, the numerical procedure is valid and can be used further for non-Stokesian particles.

2. For an upward flow, a higher drag force in the radial direction prevents droplets from reaching the coupon surface (non-Stokesian drag force–solid “data” points versus Stokes drag force–“open” data points) and shifts the onset of deposition toward larger droplets (from 42 to 45 microns). Also, the higher drag force is able to transport “heavier” droplets upward, so the end of deposition on the upstream surface is again shifted toward larger droplets (from 135 to 161 microns). According to the simulations, deposition due to inertia is confined to a range of Stokes numbers (drop diameters), at a given velocity. Below a certain minimum diameter (Stokes number), inertial effects are too small for deposition to occur. For droplets larger than some maximum diameter, upward flow is too slow to support droplets and transport them toward the coupon surface.

3. For horizontal and downward flows, at a given Stokes number (drop diameter), capture efficiencies calculated using the non-Stokesian drag force are from 1 to 5% lower than the capture efficiencies calculated using the Stokes drag force. Therefore, the Stokes drag force can be used as a relatively good approximation. For upward flow, non-Stokesian drag force should be used. The shapes of the obtained curves for all three flow orientations are further discussed in Section 5.4.1.3.

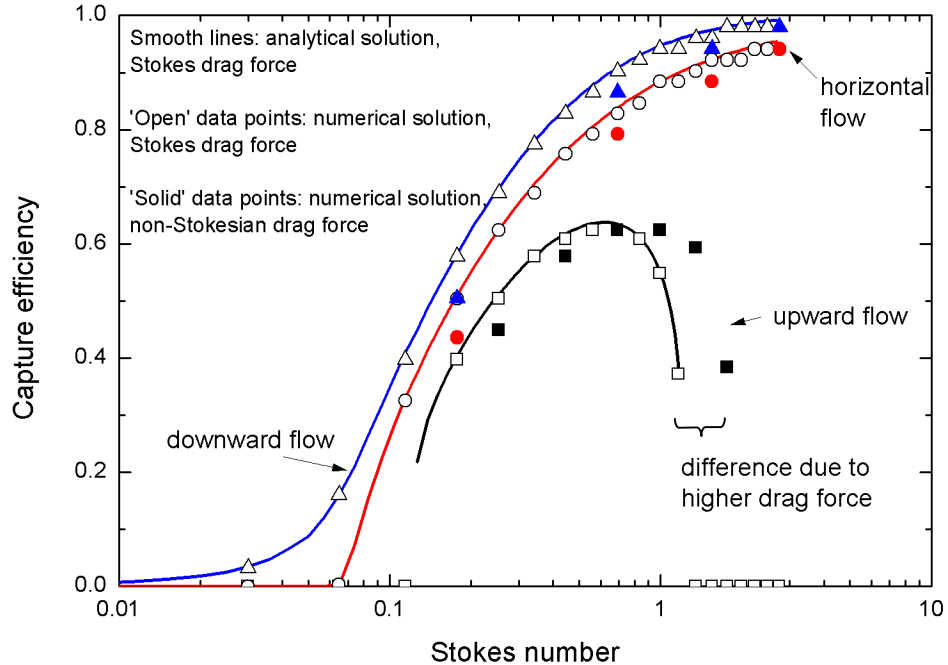


Figure 5.15 Comparison of analytical and numerical solutions for Stokesian particles, with numerical solutions for non-Stokesian particles, for upward, horizontal and downward flow, at 1 m/s superficial gas velocity

b. Comparison with the CFD results

Capture efficiencies calculated for potential flow and non-Stokesian drag force are compared with the CFD results of Lakghomi [36], at three velocities: 1, 2 and 5 m/s (Fig. 5.16). This was done in order to see how good an approximation potential flow is in terms of deposition.

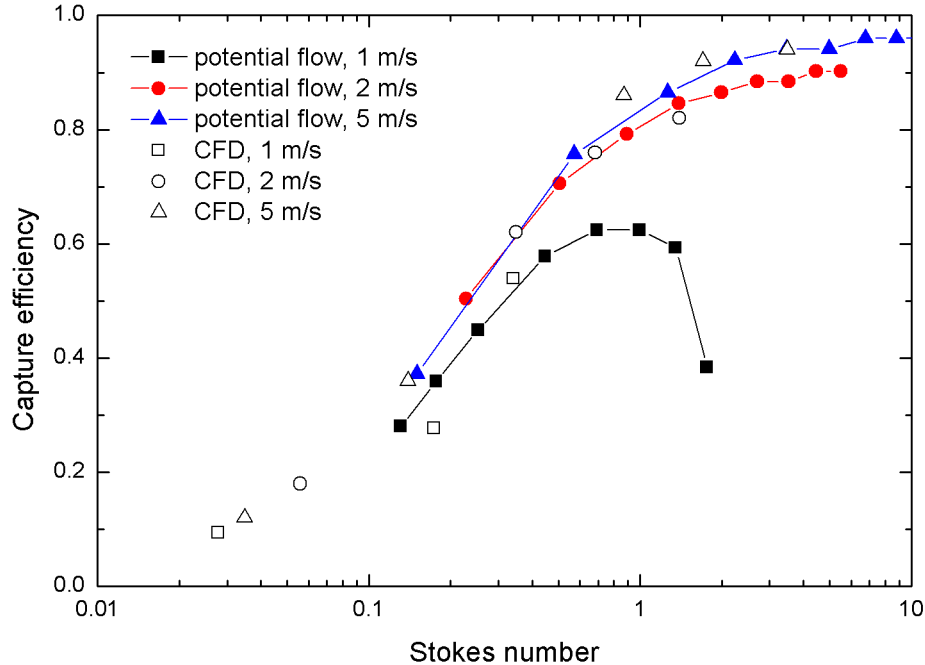


Fig. 5.16 Comparison of numerical solutions for non-Stokesian particles for upward flow, at different velocities, with the CFD results (by Lakghomi [36])

From Fig. 5.16, when comparing potential flow (open points) with CFD (solid points) capture efficiencies, there is a surprisingly good agreement between the two results, particularly for $St > 0.15$. Although the flow field is not the same as the one predicted by CFD, in terms of deposition, it gives a good match. The potential flow predictions are lower than the CFD results at lower Stokes numbers (below 0.13), probably since there is no viscous sublayer, or because deposition by turbulence is not included. These assumptions are investigated in the sections that follow (Sections 5.4.1.2.c and 5.4.2).

c. Potential flow with patched viscous sublayer

To investigate the effect of the presence of a viscous sublayer on the capture efficiency, a 5 mm thick viscous sublayer, defined by equations in Section 3.2.3, was added to the free-stream inviscid flow. The results of the simulations are presented in Fig. 5.17.

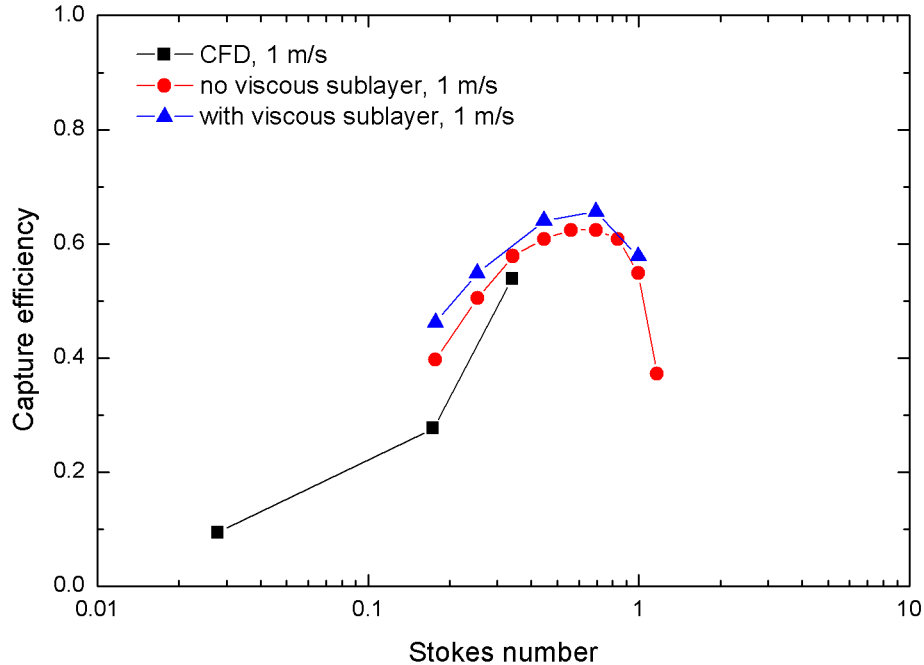


Figure 5.17 Comparison of the capture efficiencies on the upstream side from potential flow with and without a viscous sublayer, with CFD, for non-Stokesian particles (Lakghomi [36])

From Fig. 5.17, we can see that there is higher predicted capture efficiency (2–3%) with the included viscous sublayer than without it. This is the expected result since the intensity of radial velocity close to the disk surface, which moves droplets along the surface, is reduced (while the axial gas velocity component remained unchanged). Yet, there is still no deposition at low Stokes numbers. Therefore, an attempt was made to include convective diffusion and inertial impaction from turbulent parallel flow, as described in Section 3.4. The results are presented in Section 5.4.2, after all considerations of inertial deposition are completed.

5.4.1.3. Effect of gravity on inertial particle transport

As mentioned before, although the capture efficiencies from potential flow around a disk were known in the literature and were solved analytically, the effect of gravity was not considered (except Tsai and Liang [32]). Deposition due to inertial impaction from upward flow, as is the case in the Scrubber, has not been reported elsewhere to the best of

our knowledge. Therefore, the effect of gravity, i.e. flow orientation, on the inertial deposition on the upstream surface of a disk is presented here.

a. Capture efficiencies vs. Stokes number

The calculated capture efficiencies on the upstream side of a disk (side facing the flow), for all three cases of flow orientation (horizontal, upward and downward) are presented in Fig. 5.18.

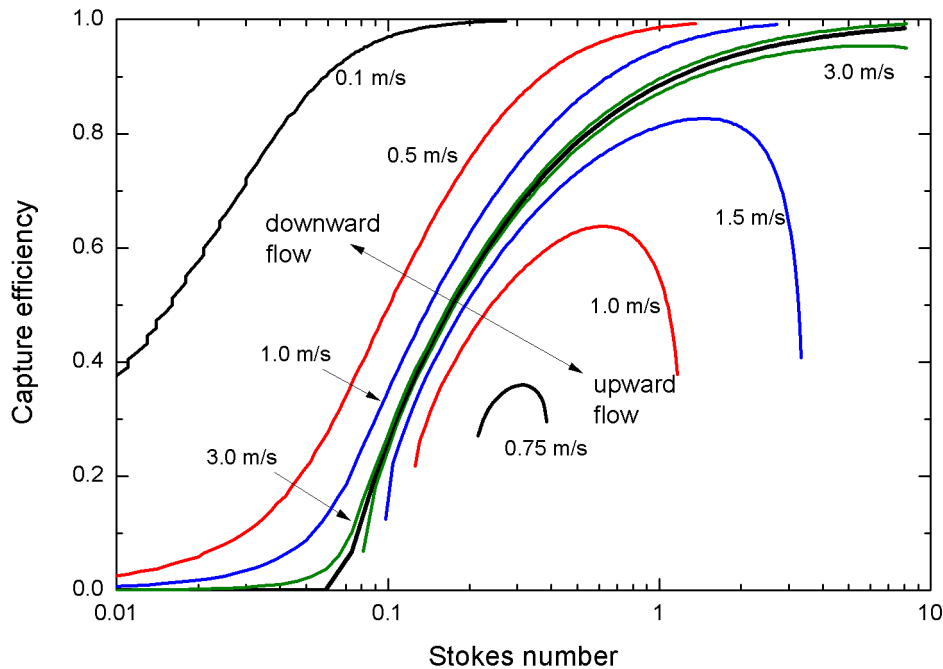


Figure 5.18 Calculated capture efficiencies vs. Stokes number for the horizontal, upward and downward flow, at different superficial gas velocities

For a *horizontal flow* (no gravity), the capture efficiency curves at all velocities overlap (thick line in the middle). This line separates efficiency curves for upward and downward flow. At higher velocities (above 2–3 m/s), curves for upward and downward flow approach the curve for horizontal flow. However, as already mentioned in Section 3.3, used particle motion equations (and thus their solutions) are not strictly valid for the horizontal (flow) orientation of our coupon-in-column system, since the problem is not axisymmetric anymore. Gravity will cause settling of larger droplets (e.g. at $St=2.2$ and $D_p=180\ \mu\text{m}$, terminal velocity is 1 m/s and the droplet will settle before it reaches the

coupon surface). It is expected that the capture efficiency curve for the disk inside the pipe will reach its maximum and start to fall down.

For an *upward flow* (gravity in direction opposite to the flow), at velocities below 0.735 m/s, there is no deposition on the upstream side. As the velocity is increased above this value, deposition starts taking place on the upstream side. As the velocity is increased further, the minimum drop diameter that deposits on the upstream side decreases, since smaller droplets have sufficient inertia to penetrate the gas layer in the vicinity of the coupon and reach the surface. Also, the maximum droplet diameter that is depositing is increased, since higher gas velocities are able to support and transport upward particles with larger terminal velocities. When the velocity becomes high enough and gravity forces become negligible compared to the inertial forces, the efficiency curve overlaps with the curve for horizontal flow.

For a *downward flow* (gravity in the flow direction) as the velocity is decreased, the capture efficiency curve is shifted toward unity, and when the gas velocity becomes zero (there is no gas flow), we have pure gravitational settling. There is no fluid to sweep particles away from the surface and capture efficiencies for all particles become equal to unity. As the velocity is increased, particles are swept away from the coupon surface and capture efficiencies first decrease. As the velocity approaches 2–3 m/s, gravitational forces become negligible compared to inertial forces and the capture efficiencies become equal to the capture efficiencies for the horizontal flow.

b. Capture efficiencies vs. drop diameter and velocity

The results of simulations (section *a*) can be presented as capture efficiencies vs. drop diameter and velocity (Figs. 5.19a-d). Deposition coefficients can be obtained by multiplying capture efficiencies by the gas velocity.

For a *horizontal flow* (Fig. 5.19a), it can be noted that the minimum droplet diameter that is deposited by inertia decreases as the velocity is increased, and there is no minimum velocity at which deposition on the upstream side occurs. Above 3 m/s, the capture efficiency curve would change only a little, in order to stay in agreement with the Fig. 5.18.

For an *upward flow* (Fig. 5.19b), at each velocity there exist a minimum and maximum drop diameter that deposits via the inertial impaction mechanism. There is no deposition on the upstream side below 0.735 m/s. At velocities higher than 3 m/s, the capture efficiency curve would change little, approaching the curve for horizontal flow (Fig. 5.18). At constant capture efficiencies, deposition coefficients would however increase linearly with velocity, according to Eq. (2.8).

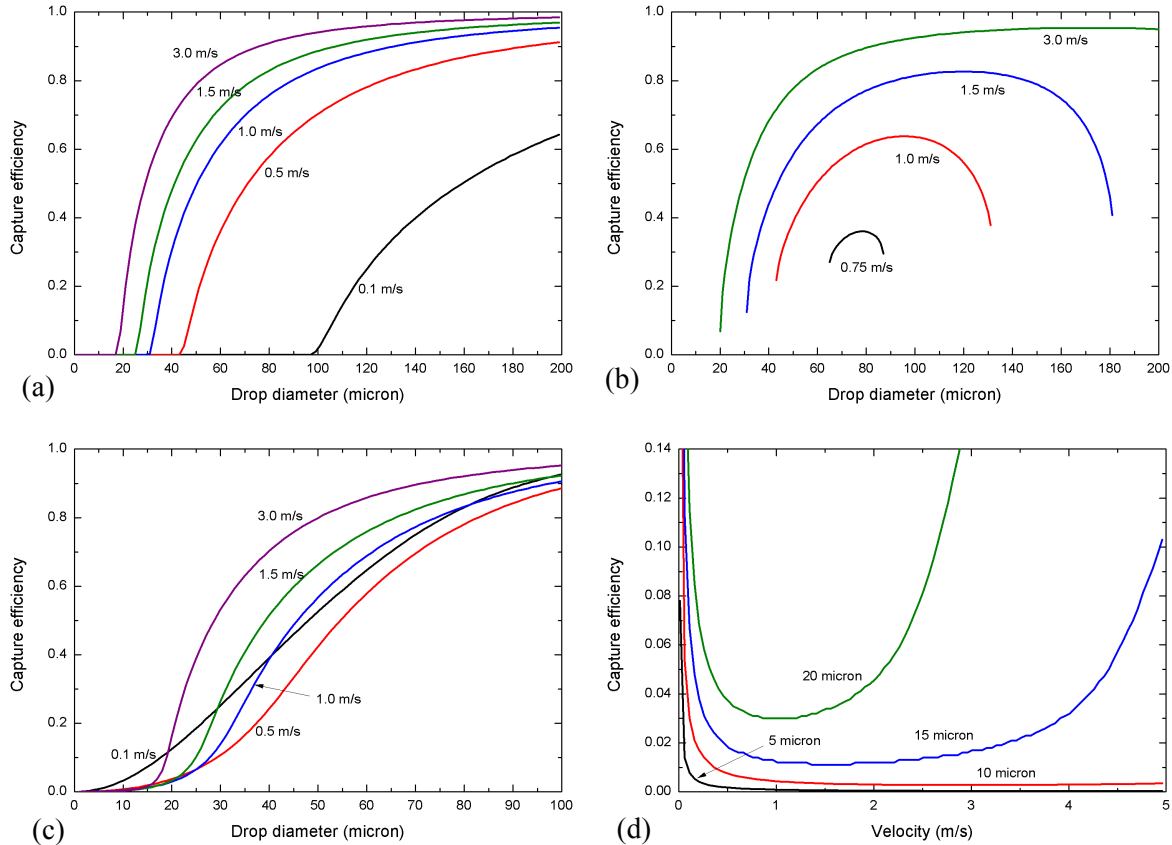


Figure 5.19 Capture efficiencies vs. drop diameter for (a) horizontal, (b) upward, and (c) downward flow, at different superficial gas velocities. Capture efficiencies vs. velocity for downward flow are presented in (d).

For a *downward flow*, the capture efficiencies increase with the drop diameter as given in Fig. 5.19c. As the velocity is increased, they first decrease and then increase toward capture efficiencies for horizontal flow. The results are somewhat different from what was observed in first two cases: capture efficiencies first decrease with velocity, and then increase. This is better seen in Fig. 5.19d.

From the calculated capture efficiencies for downward flow vs. velocity, there is a velocity for each drop size at which capture efficiency is minimal. Approaching $U=0$ m/s, capture efficiencies become very high, asymptotically approaching unity (not exactly shown in Fig. 5.19). This is in accordance with Fig. 5.18, and the explanation presented. As the velocity is increased, the capture efficiencies are reduced because the radial velocity removes particles from the surface and reduces deposition. When the inertial forces become significant, the capture efficiencies increase again, showing a similar dependence as for horizontal flow. As expected, at a given velocity, inertial effects first come into play for larger particles and therefore, a sharp increase for 20 micron droplet is seen at about 2 m/s, while for the 15 micron droplet, it happens at about 4 m/s.

Interestingly, the same trend was observed for capture efficiencies calculated from experimental data for the downstream side (Figs. 5.10, 5.12). This can be explained by the fact that the gravity in the simulation was oriented in the same direction as it is in the vortex (downward), and that flow field in a vortex could be somewhat similar to the potential flow field (see Fig. 5.22). Therefore, this simulation can help explain the mechanisms that govern deposition of droplets from the vortex. A quantitative comparison of the simulations and experimental data is given in Section 5.5 (Fig. 5.23).

5.4.2. Particle transport due to turbulence

To estimate deposition from parallel flow at low Stokes numbers, models described in Section 3.4 were used. Figure 5.20 represents calculated capture efficiencies from an assumed parallel flow to the disk surface, as described in Section 3.4. According to this model, in the range of Stokes numbers from 0.0001 to about 0.01, calculated capture efficiencies decrease, since the main mechanism of deposition is convective diffusion. The transport coefficient in this case is proportional to the Brownian diffusivity of the particles, which decreases as the Stokes number (droplet size) is increased. In this range, deposition from inertial effects is negligible, since the particles are too small (their relaxation time is small) so that the momentum transferred to them by turbulent eddies is dissipated in the viscous sublayer. At a Stokes number of about 0.008, or particle diameter of 11 microns, the equivalent non-dimensional particle relaxation time at $U=1$ m/s is about 0.23. In this region, inertia starts to dominate the deposition (see Fig. 2.1)

and we can observe an increase in deposition with an increase in the Stokes number (droplet size). Curves presented in Fig. 5.20 are summation curves of calculated convective diffusion and turbulent inertia over the whole range of Stokes numbers. Compared with the CFD results presented in Fig. 5.17, in the range of Stokes numbers 0.001–0.1, the capture efficiencies calculated here are significantly lower ($\sim 10^{-5}$ vs. $\sim 10^{-2}$). This could be due to the different flow field and different turbulence models used. Validity of the CFD predictions in this range of Stokes numbers was not verified experimentally; however, there are indications from this work that CFD over-predicts deposition in this range of Stokes numbers (experimental capture efficiencies at $St < 0.05$ are estimated to be less than 10^{-3} (0.1%)) and that the true capture efficiencies are between the two model predictions.

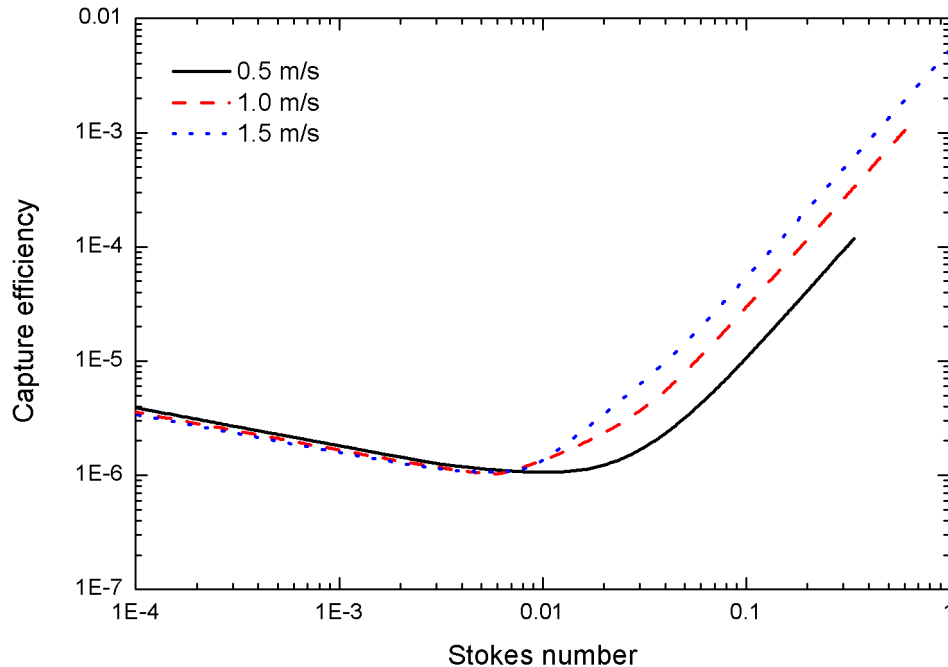


Figure 5.20 Simulation of deposition by convective diffusion and turbulent inertia from a flow parallel to the coupon surface, based on the modeling described in Section 3.4

In summary, for Stokes numbers larger than 0.1, the inertial deposition model using the potential flow approximation and a non-Stokesian drag force, proved to be very close to the CFD model (Lakghomi [36]). Gravity had an important effect on capture efficiency, and therefore, the flow orientation in the Scrubber could affect fouling. For upward and downward flows, capture efficiencies could be represented as a function of

the Stokes number and velocity; for a horizontal flow, capture efficiencies are only a function of the Stokes number. The results predicted by the turbulent deposition model (convective diffusion and turbulent inertia) are lower than the CFD model prediction [36] in the range of $St < 0.1$, most probably due to the different turbulence models and the flow field used in simulations. Measured capture efficiencies seem to be between the two model predictions.

5.5. Comparison with experimental data

In this section, experimental results for the upstream and downstream side (Sections 5.1 and 5.3) are compared with the results of simulations from the previous section (Section 5.4).

5.5.1. Upstream side

Simulation results for the upstream side presented in this section (Fig. 5.21) were obtained for an upward flow at the velocity $U=1$ m/s (Fig. 5.16). The experimental results (Fig. 5.21) were also obtained at superficial velocity $U=1$ m/s, and calculated from Eq. (3.27) by dividing the size distribution of the droplets on the coupon by that in the aerosol (Fig. 5.9). From Fig. 5.9, it is possible to observe that the distribution of deposits on the upstream side is bimodal: in the range of $D_p=1-27$ μm , there is a small amount of deposit due to turbulent diffusion (in 1 of 5 cases it is not even recorded), while for $D_p > 27$ microns, deposition is significant, as a result of inertial impaction. The measured critical diameter at which inertial impaction starts ($D_p=27$ μm) corresponds to the critical Stokes number $St_{cr}=0.05$, while calculations suggested a value of 43 microns ($St_{cr}=0.125$). This discrepancy can be explained with the fact that the real flow field is yet different (stronger) from the potential flow. This is since the potential flow approximation did not consider the presence of column walls, and it is known from the results of Salmanzadeh et. al. [56], that the increase in blockage ratio increases deposition.

Droplets that deposit on the upstream side are very rare in the aerosols used ($VMD=3.9-7.5$ microns), since from 5 aerosol samples (about 15,000–20,000 droplets recorded), no droplet was larger than 25–30 microns (Table E.1), although they must be present in the aerosol, since they deposited on the coupon. Therefore, their concentration

is estimated by extrapolation of the size distribution obtained from fitting the data in the range 1–30 microns, and used in calculation of capture efficiencies (Eq. (3.27)).

From Fig. 5.21, we can see that the experimental results overestimate the simulation results by a factor of 4–5. This suggests that the concentration of large droplets in the aerosol that deposit on the upstream side ($D_p > 27 \mu\text{m}$) is underestimated by shadowgraphy (4–5 times), most probably because its concentration is estimated from the extrapolated size distribution curve. The shape of the capture efficiency curve obtained, however, is similar to the efficiency curve predicted by the simulation, meaning that the trends of the size distributions in the aerosol and on the coupon are correct, while the main discrepancy is due to underestimating the concentration of larger droplets in the aerosol.

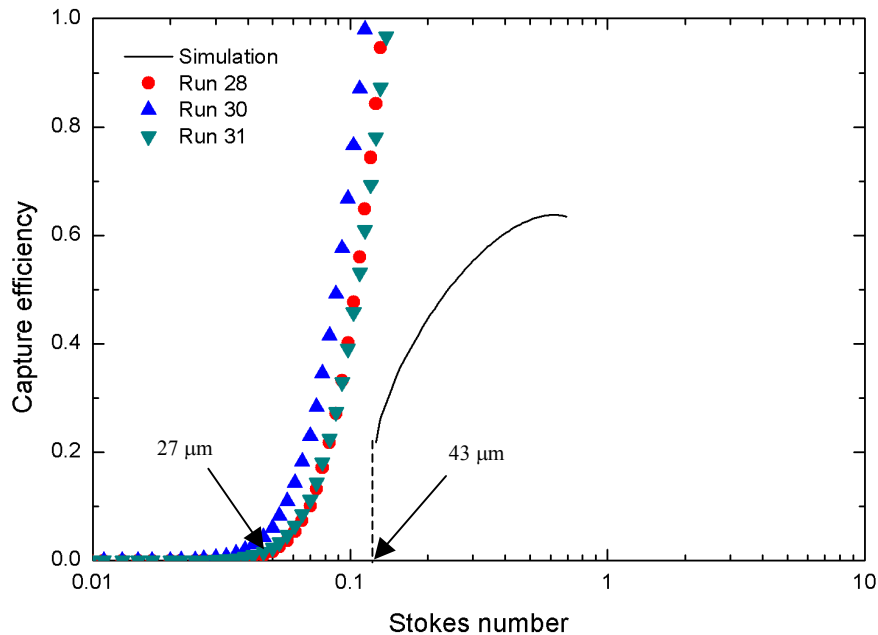


Figure 5.21 Comparison of the simulation and fitted experimental results for the upstream side at 1 m/s

5.5.2. Downstream side

Flow on the downstream side of the disk is represented by a vortex with turbulent fluctuations of velocity. Although certainly different from the real flow field, potential flow was tested in describing the flow in the vortex, due to some resemblance of the potential flow pattern to the actual flow pattern in the wake (Fig. 5.22). Also, the results

of simulations with gravity in the flow direction (Fig. 5.19d), indicated that this approach may be useful in explaining the experimental results (Fig. 5.12).

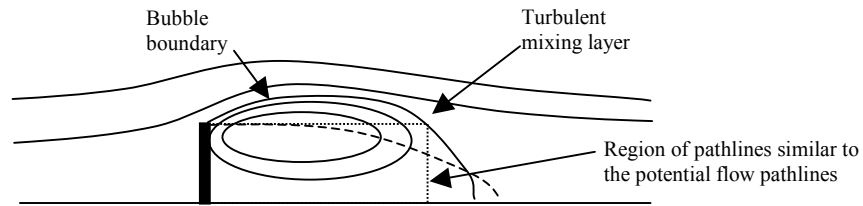


Figure 5.22 Axisymmetric flow pattern about a disk (adapted from Humphries and Vincent [73])

The results for the downstream side were obtained from the downward flow simulation ($p=1$), using the same potential flow field equations as for upward flow (Eqs. (3.6a,b)) at velocity $U=1$ m/s. For the downstream side, the size distribution of droplets in the aerosol and size distribution on the coupon overlap significantly (Fig. 5.9). It is believed that in this case, the experimental results are correct, and that the model is somewhat oversimplified. However, the model does seem capable of predicting the main trends and gives quantitative confirmation of the experimental results within a factor of 2.3 (Fig. 5.23).

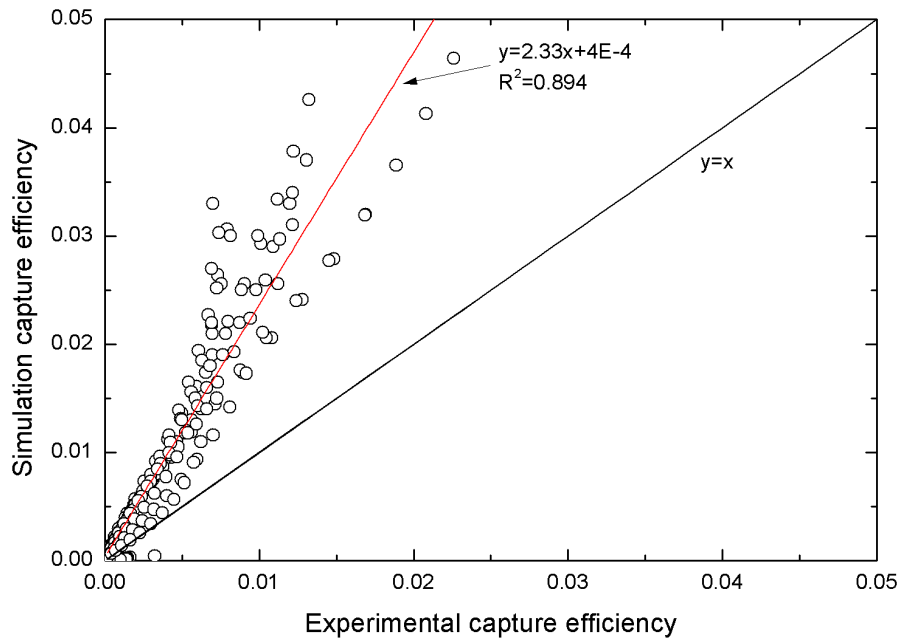


Figure 5.23 Correlation between calculated capture efficiencies from the downward flow and experimental data. Simulation over-predicts experimental data by a factor of 2.33

From Fig. 5.23, we can see that the simulation over-predicts the experimental data by a factor of 2.3. One reason for discrepancy is certainly because the real flow field in the wake is different from the potential flow field used in the simulations. The other reason is because the size distribution and concentration of droplets in the vortex is different from the size distribution and concentration in the aerosol (used in the simulations). The latter claim can be supported with the experimental data of Humphries and Vincent [72], who investigated transport and detention of airborne dusts in the near wake of a disk. Their experimental results showed that the dimensionless mean residence time of particles in the vortex (H_p) decreases with Stokes number, and is always lower than the residence time of inertialess particles ($H_p < H_f = 7.44$). Based on theoretical considerations, they suggested that the concentration of particles in the wake, c_{wake} , is related to the concentration in the bulk, c_b , according to, $c_{wake} = c_b (H_p / H_f)$. This implies that the concentration of particles in the wake is always lower than the concentration in the bulk (up to 1.6 times), particularly for larger particles. This explains to a certain degree why the simulation over-predicted the experimental results. Similar experimental findings, on the dispersion of large particles in the near wake of disks, were also reported by Sato et al. [74]. Apart from over-predicting the results by a constant factor (2.3), a good correlation between the simulation and experimental values exists ($R^2=0.89$), indicating that the model is capable of explaining the observed trends in the experimental data. From these considerations, we can postulate that inertial impaction and gravity in the flow direction, are governing mechanisms on the downstream side.

To summarize, deposition on the upstream side of a disk was simulated by the inertial impaction mechanism, using the potential flow approximation and gravity in the direction opposite to the flow. The model was able to describe deposition qualitatively. The main discrepancy was due to the underestimation of the concentration of large droplets in the aerosol ($D_p > 30$ microns), obtained by extrapolation of the log-normal distribution curve. For the downstream side, the same potential flow approximation with the inertial impaction mechanism and gravity in the flow direction proved capable of describing the deposition, but the simulation over-predicted experimental results by a factor of 2.3, mainly due to the actually lower concentration of droplets in the vortex than in the bulk stream.

5.6. Morphology of deposits and their distribution along the disk radius

From the images of deposits taken after each experiment, it can be noted that deposits on the upstream side were not uniformly distributed; more droplets were deposited toward the edge and less in the centre of the coupon (Fig. 5.24a). Also, because of the relatively large amounts of deposit that were collected (200–300 mg), droplets merged and formed grain-like shapes on the surface. Again, this was more pronounced close to the coupon edge. On the downstream side, deposits appeared to be uniformly distributed along the radius (Fig. 5.24b).

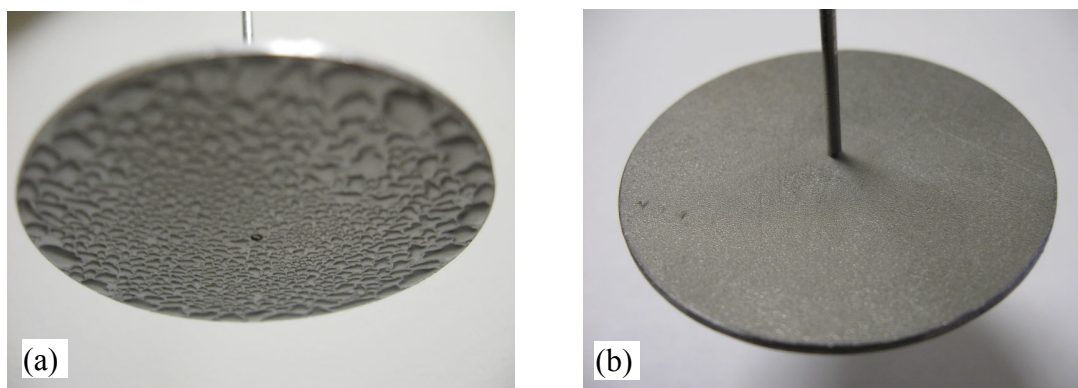


Figure 5.24 Typical appearance of (a) non-uniform distribution of deposits on the upstream side, and (b) uniform distribution on the downstream side

It is interesting to note that although the morphology of the surface was changing during the experiment from a flat coupon surface to a surface covered with a few mm size grains of liquid, the deposition rates remained constant (straight line in Fig. 4.33). This indicates that the changed morphology of the coupon surface did not change the flow field appreciably such that the deposition rates would be affected.

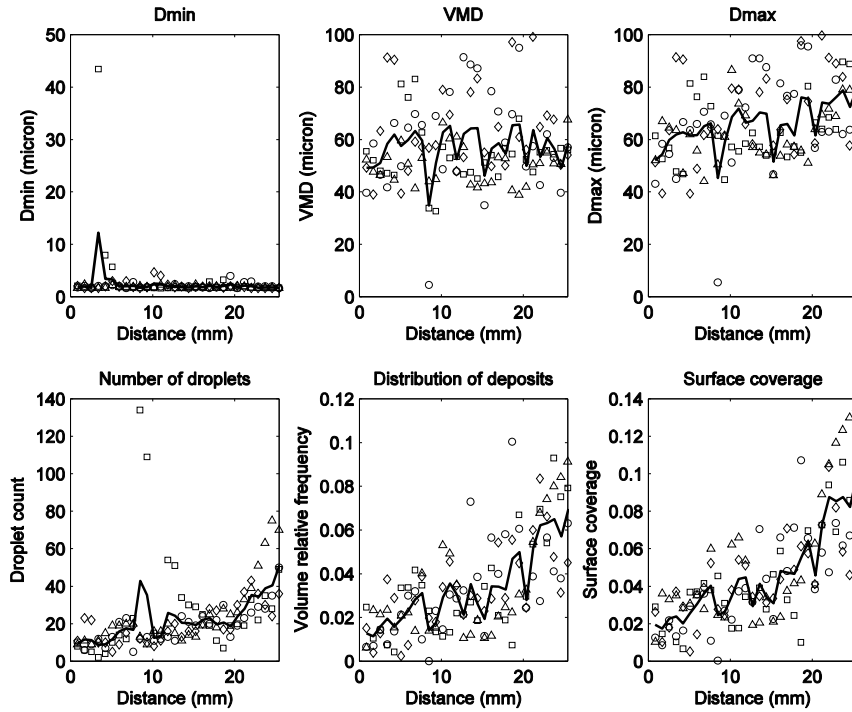
The distribution of deposits along the disk radius was determined by measuring the droplet number, size, and mass fraction of the deposits along the radius of a glass coupon, using the methodology and the setup described in Section 4.4.4. To collect the deposits for the measurement process, deposition on the coupon lasted from 10 to 60 seconds, depending on the experimental conditions. In any case, to avoid merging of

droplets and errors in the measurement process, the surface coverage should not exceed 10%.

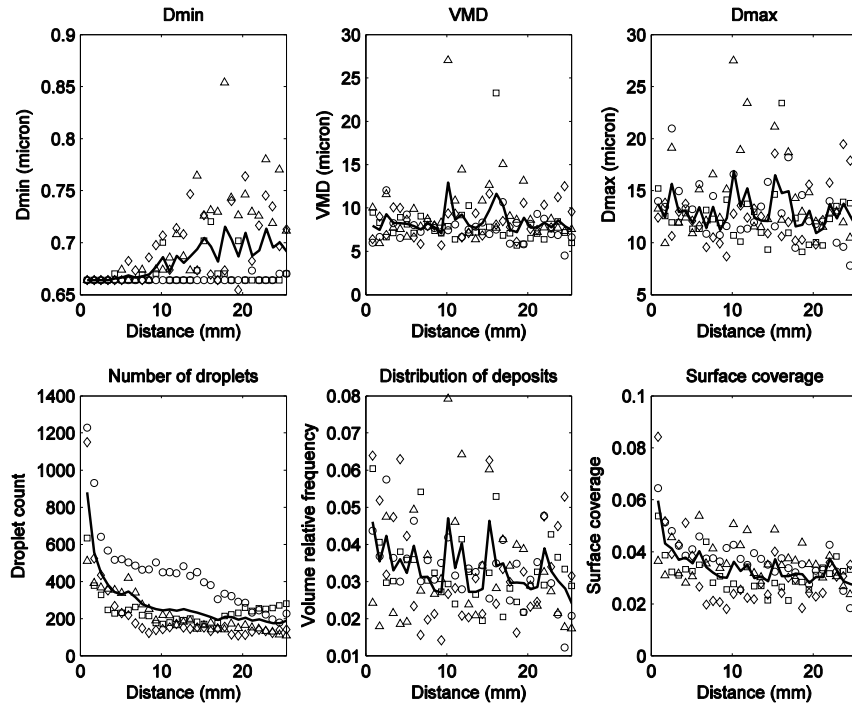
Typical distributions of deposits on the upstream and downstream side for Run 56 are shown in Fig. 5.25. Similar trends were obtained in all other experiments. For the upstream side (Fig. 5.25a), it can be noted that the volume median diameter of deposit of droplets did not vary along the coupon radius. The maximum diameter was about 20–30% larger at the coupon edge, due to the merging of droplets at the coupon edge, where the surface coverage was about 15%. The number of droplets, their mass distribution and surface coverage increased from the coupon centre toward the edge. In Fig. 5.25, the mass fraction of total deposits increased from about 1.8% close to the coupon centre, to about 6% at the coupon edge, which is more than a three-fold increase.

For the downstream side (Fig. 5.25b), the volume median diameter on the downstream side was constant along the coupon radius, as was the maximum drop diameter. The number of fine deposited droplets was usually higher close to the coupon centre, possibly due to the turbulence caused by the piece used for rod attachment. Mass distribution of deposits and surface coverage was constant along the radius, with surface coverage being somewhat higher close to the coupon centre, where many fine droplets were deposited.

Data on the mass distribution of deposits along the coupon radius, from all experiments with the Hot Unit nozzle and Setup #2 (Section 5.1.2.2), are given in Figs. 5.26a,b. The data were correlated with parabolic and linear functions respectively, and show that for the upstream side, more deposits were formed close to the coupon edge, and on the downstream side, the mass of deposits just slightly decreased along the coupon radius.



(a) Upstream side



(b) Downstream side

Figure 5.25 Distribution of deposits along the coupon radius on the (a) upstream and (b) downstream side, for Run 56. Solid lines were obtained by averaging measured values from four samples.

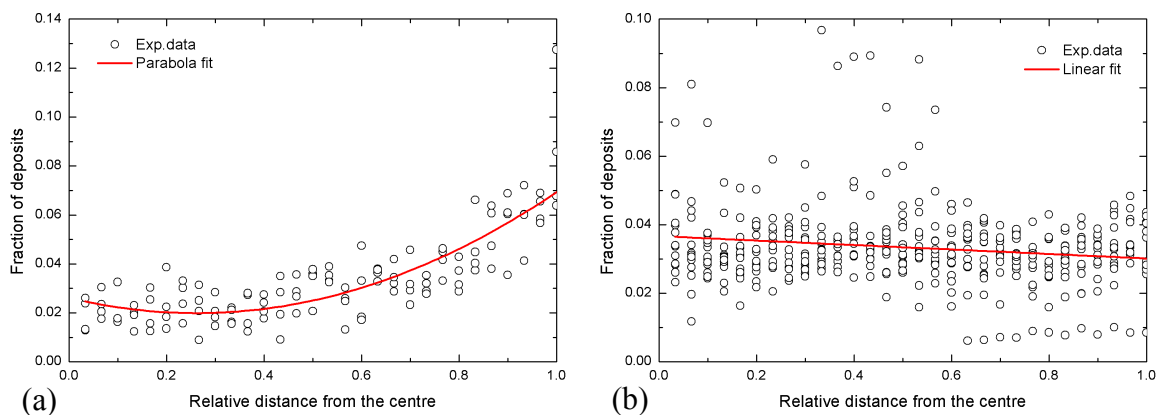


Figure 5.26 Mass distribution of deposits along the radius of the (a) upstream and (b) downstream surface of the coupon, in 30 classes, from Runs 46–59

Regarding the Scrubber, pictures of deposits on the surface of the packing elements (Fig. 1.3b) suggest that the coke is found everywhere across the packing elements, on both the downstream and upstream sides. The packing elements in the Scrubber are triangular sections with 3.3 cm long sides (equivalent disk diameter is 3.7 cm) [9]. If we assume a normal orientation of flow over these elements, and use the operating conditions and physical properties of vapour and droplets in the reactor (vapour viscosity 0.023 mPas, droplet density $\sim 900 \text{ kg/m}^3$, velocity 1.35 m/s, maximum droplet diameter 11 microns [8, 9]), the calculated Stokes number is $St \approx 0.01$. This value is 5 times smaller than the critical Stokes number at which inertial impaction would occur ($St_{cr} = 0.05$, Fig. 5.21). At the given conditions, the critical diameter of the obstacle positioned normal to the flow, for which $St_{cr} = 0.05$, would be around 7 mm. Therefore, inertial deposition probably takes place on the parts of the packing elements smaller than 7 mm. This includes parts of the triangular sections close to its vertices, but also the 2–3 mm thick metal sheets that support the packing elements. The deposits formed on these parts could cause early blockage of the reactor. However, the actual situation in the Scrubber, where the wash oil is poured from the top and over the packing, could prevent this from happening. Reliable predictions should be based on a more realistic fluid flow field, and consider the interaction with the wash oil. Based on the results for the downstream side, the back side of the packing should foul uniformly. Again, proper consideration should include the effect of the wash oil sprayed from the top, and the actual geometry of the packing.

5.7. Contact angle and dry vs. wet surface effect

To investigate the effect of contact angles on deposition, coupons made of different materials were used, while the liquid was kept the same (triethylene glycol). Short deposition experiments were performed in order to compare deposition rates between surfaces when part of the surface of the coupon is still dry. Longer duration runs allowed comparison with a wet surface.

To cover the widest range that we could attain with triethylene glycol, a glass, stainless steel and Teflon coupons were used (measured contact angles were 21°, 51° and 94° respectively). Short runs were performed to keep the coupon surface dry before it becomes covered with the layer of liquid.

Deposition rates from short runs (e.g. 30 seconds) vs. longer ones (e.g. 300 seconds) should show a difference between dry and liquid-covered coupon surface (if any). The operating conditions and the surface properties are provided in Tables 5.2 and 5.3 respectively.

Table 5.2 Operating conditions for contact angle tests

Parameter	Setting
Air to the nozzle	0.45 m/s (setting 75, PG 426 kPa)
Secondary air	0.57 m/s (setting 2.0, PG 34.6 kPa)
Liquid flow	95 ml/min (setting 9)
Nozzle	1/4QMJ+SUQ, Spraying Systems Co.

Table 5.3 Coupon material and roughness properties at initial dep. rate tests

	Glass	St. steel	Teflon
Contact angle	21°	51°	94°
Surface roughness	Polished glass	2B finish	Treated with sand paper

The weight of deposits after each experiment was measured on the analytical balance with 0.1 mg precision, and the results are given in Table E.5. It is estimated, however, that due to the sampling error, the deviation in the measurements is higher than 0.1 mg, especially for the short runs. Calculated integral deposition rates, $r_{d,i}^{\text{exp}}$ (Eq. (3.22)), are given in Table E.6, and plotted versus experiment duration in Figs. 5.27a–d.

It was expected that the lower contact angles would give higher deposition rates, but from the short duration tests in Figs. 5.27a–d, this could not be clearly concluded. No significant difference between the surfaces, for the upstream or downstream side, at $U=0.7$ m/s or $U=1.0$ m/s, could be observed. If any difference existed, it was within the experimental error. The exception is the Teflon coupon (at $U=1$ m/s, Fig. 5.27c,d), which was expected to yield lower, but showed higher deposition rates. We hypothesise that due to the higher surface roughness of the Teflon disk (after cutting, it was treated with sand paper), turbulence intensity increased and caused an increase in deposition rates. This difference is more pronounced at 1 m/s than at 0.7 m/s, since the tests at 1 m/s were performed first, and it is likely that by cleaning the Teflon coupon, surface roughness was diminished by friction. As a result, in Fig. 5.27b, there is no significant difference between the Teflon and other materials, as in Fig. 5.27d.

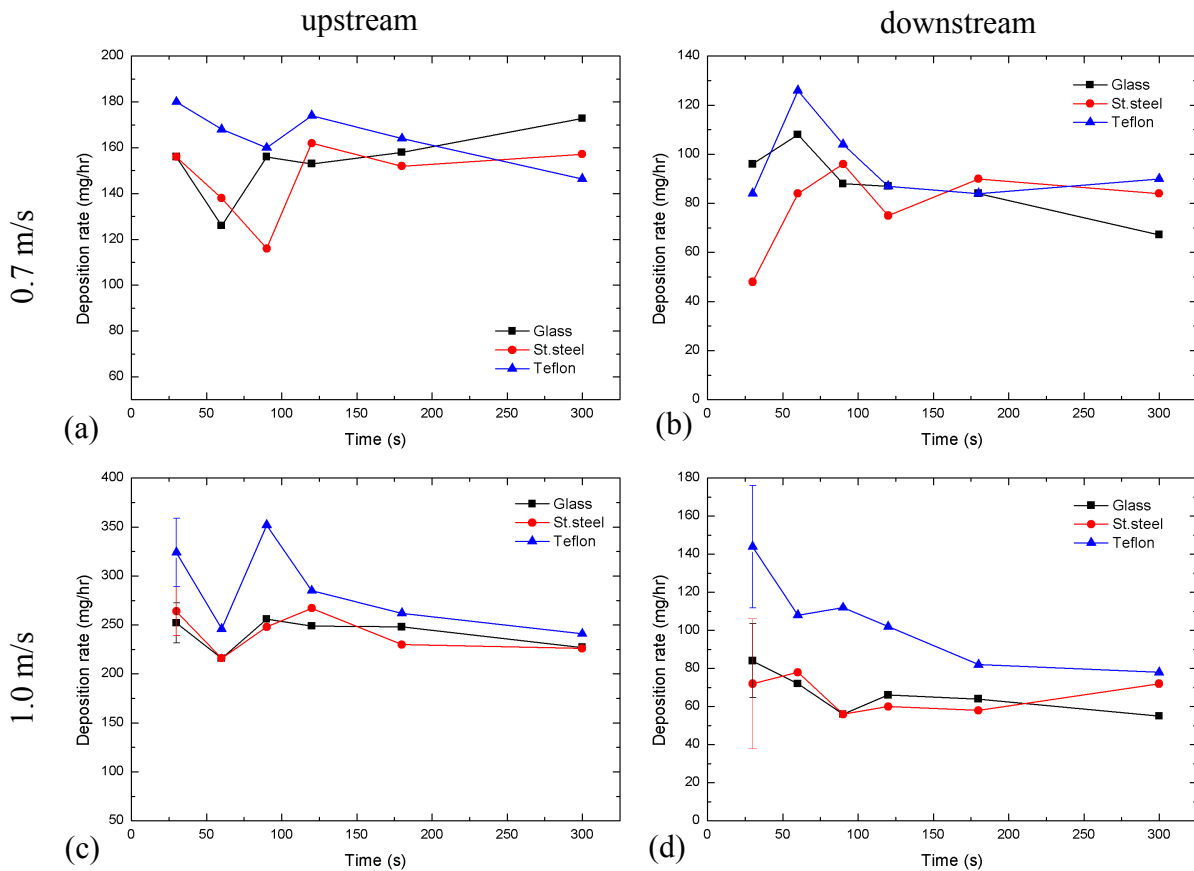


Figure 5.27 Experimental integral deposition rates, $r_{d,i}^{\text{exp}}$, at $U=0.7$ m/s and $U=1.0$ m/s, on different surfaces, for the upstream side (a, c) and downstream side (b, d) (Table E.6).

95% confidence intervals are estimated from 3 repeated experiments

Also, no significant difference between the deposition rates on a dry (short experiments) and already wet surface (longer experiments) could be observed (if any, it seems to be within the experimental error). The exception is the rough Teflon coupon (Fig. 5.27d), which showed higher deposition rates in the initial stages of deposition, on the presumably rough surface. However, after the first layer of deposits was formed, effect of surface roughness would no longer affect the deposition.

To summarize, even if the partial rebounding of droplets from different surface materials may have occurred and reduced deposition rates, the difference between surfaces with contact angles 20–94° and between the rough and smooth surface became insignificant after the initial layer of deposits was formed (1–2 minutes). For the glass and st. steel coupons, differences between deposition rates on a dry and wet surface were not significant, while for the Teflon coupon, the deposition rate on a roughened dry Teflon surface seemed to be higher than on the already wetted surface (downstream side).

Regarding the industrial case, it seems unlikely that changing the surface of the packing, with contact angle in the range 20–94°, could reduce the fouling rates. Although the effect of roughness requires a more detailed study, it seems that it does have effect on the deposition (especially on the downstream side), since it promotes turbulence and increases deposition. However, even an ideally smooth surface would be unable to prevent the formation of the first layer of deposits. After a layer of deposits has been formed, properties of the surface material (contact angle and surface roughness) become irrelevant for further deposition. Experimental investigation of superoleophobic materials, with contact angles higher than 150°, could show if the formation of the first layer of deposits could be prevented and the deposition reduced, if not eliminated.

Chapter 6. Application of the Results to the High Temperature Unit Conditions

Since experiments in the Cold Unit and the Hot Unit were performed for the same geometry (5 cm circular disk in a 7.5 cm circular column), deposition coefficients from the Cold Unit experiments were used to calculate deposition rates at high temperature conditions. This was done in order to support the validity of estimated deposition coefficients from the Cold Unit experiments, and perform an independent check of the results obtained in the Hot Unit.

Given that the droplet size distribution in the Hot Unit could not be easily measured, it was estimated from an empirical correlation and the experimental procedure described in Section 3.9. The concentration of droplets in the aerosol in the Hot Unit experiments was estimated from HYSYS simulations of the vapour-liquid equilibrium, as given by Lakghomi [36] and by Song [52]. Predictions were based on the Peng-Robinson equation of state; experimental TBP (True Boiling Point) curves for the hydrocarbon blending components Voltesso and MEBR were supplied to the HYSYS simulator.

6.1. Estimation of droplet size distribution in the Hot Unit

Measured and estimated volume median diameters from the procedure described in Section 3.9, are presented in Table E.7 in *Appendix E*. The correlation used (Eq. (3.37)) predicted about a 4 times larger volume median diameter than was measured in all experiments where liquid flow rate was 10 ml/min, and about 6 times larger in experiments where the liquid flow rate was 20 ml/min. This discrepancy is most likely due to the impaction of large droplets from the spray cone on the column walls close to the nozzle, and due to the ambiguous use of the dimension ‘ h ’ in the correlation (as already discussed in Section 3.9). Therefore, it was concluded that the correlation would always predict about a 4 or 6 times larger volume median diameter, depending on the liquid flow. A corrected diameter is then estimated by multiplying the estimated volume median diameter from the correlation with the correction factor 0.25 or 0.17 (last column of the Table E.7).

Volume median diameters in the Hot Unit, for experiments that investigated the effect of temperature and velocity, are shown in the last column of Table E.8 in *Appendix E*. These values are estimated at the temperature conditions in the nozzle. Depending on the temperatures in the chamber, a significant portion of droplets from the spray (from 94% to 98%) evaporated, reducing the droplet size. From the amount of evaporated liquid, a corrected volume median diameter is calculated and is shown in the last column.

Volume median diameters of droplets approaching the coupon are between 2.5 and 4.8 microns. From these values, log-normal size distributions were generated and used in further calculations.

6.2. Deposition coefficients for high temperature unit conditions

Deposition coefficients from the Cold Unit experiments are valid for tri-ethylene glycol droplets in air. In the high temperature unit experiments, the gas phase was a mixture of nitrogen and Voltesso vapours. The liquid phase feed was a mixture of heavy components of a volatile oil (Voltesso), and a heavy hydrocarbon stream (MEBR). The temperature varied between 295°C and 425°C and affected the physical properties of the gas and liquid, which were calculated using HYSYS. This required recalculation of deposition coefficients from the Cold Unit to different operating conditions.

In all Hot Unit experiments, the majority of deposits were formed on the downstream side of the coupon (Song [52]); therefore, only deposition coefficients for the downstream side were used in predicting deposition rates. From the comparison of experimental results and simulations of inertial impaction with gravity in the flow direction (Section 5.5.2), we can conclude that deposition on the downstream side, in the range of droplet sizes (1–20 microns) and velocities (0–1.5 m/s), is governed by the Stokes number and velocity. Figure 6.1 shows a plot of capture efficiencies (obtained by calculation from experimental results, Section 5.3) versus Stokes number. The dependence of capture efficiencies on Stokes number is almost linear over the wide range of Stokes numbers, at all velocities. At a given Stokes number, as the velocity is raised, the capture efficiencies decline.

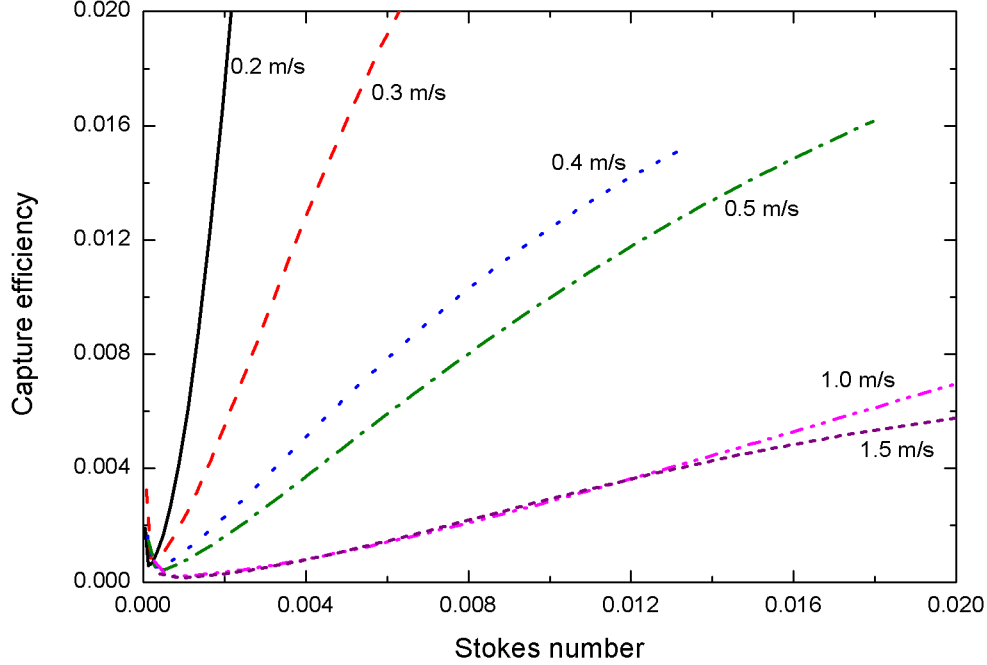


Figure 6.1 Capture efficiencies calculated from experimental results for the downstream side vs. Stokes number, in the range of droplet sizes (1–20 microns) and velocities (0–1.5 m/s)

Therefore, the change in the capture efficiencies at a given velocity can be predicted by the change in the Stokes number, due to the different gas viscosity and droplet density,

$$St_{HotUnit} = St_{ColdUnit} \cdot \frac{\mu_{air}}{\mu_{N_2}} \cdot \frac{\rho_{oil}}{\rho_{TEG}} \quad (6.1)$$

Over a wide range of Stokes numbers, capture efficiencies are close to a linear function of the Stokes number, $CE=k \cdot St$. The relative change in the capture efficiencies due to the change to the hot temperature unit conditions (different droplet density and gas viscosity) can be easily deduced from the relative change of the Stokes number according to,

$$\frac{E_{HotUnit}}{E_{ColdUnit}} = \frac{k \cdot St_{HotUnit}}{k \cdot St_{ColdUnit}} = \frac{\mu_{air}}{\mu_{N_2}} \cdot \frac{\rho_{oil}}{\rho_{TEG}} \quad (6.2)$$

The linear dependence does not strictly hold over the whole interval of Stokes numbers presented in Fig. 6.1, particularly at low Stokes numbers. However, since the relative

change in the Stokes numbers is not greater than 2 times, this dependence can be approximated with the linear function in this interval, and equation (6.2) will still hold.

6.3. Comparison of results

Predicted deposition rates in the Hot Unit are calculated from the Cold Unit deposition coefficients and presented in Figs. 6.2–6.4, along with the experimental Hot Unit deposition rates. Figure 6.2. represents the effect of temperature on deposition rates for 5% MEBR, and the effect of reaction. Deposition rates predicted from the Cold Unit experiments are higher than the deposition rates measured in the Hot Unit, except at 295°C, where the predicted deposition rates are lower. It is possible that the concentration of droplets at this temperature is underestimated by HYSYS. The reaction effect becomes important at temperatures above 370°C, and it can be noted that the two last points in the figure match well. Generally, we can say that a good match between the two sets of data can be observed. Also, predictions from the Cold Unit are close to the deposition rates predicted by CFD [36].

For the 10% MEBR (Fig. 6.3), deposition rates predicted from the Cold Unit deposition coefficients are up to 20% higher than deposition rates measured in the Hot Unit. Again, the reaction effect becomes important at temperatures above 370°C and good agreement between the trends of the two sets of data can be observed. The decrease in deposition rate with increasing temperature is attributed to a decrease in the concentration of aerosol droplets (Table E.9, *Appendix E*).

Comparison of the results for the effect of velocity is shown in Fig. 6.4. Predictions from the Cold Unit are within few percent of the Hot Unit data, with exception of the data point at 0.25 m/s, where Hot Unit deposition rates are underestimated by about 30%, and one data point at 0.92 m/s, which most probably contains error. Still, good agreement between the two sets of experimental results can be observed.

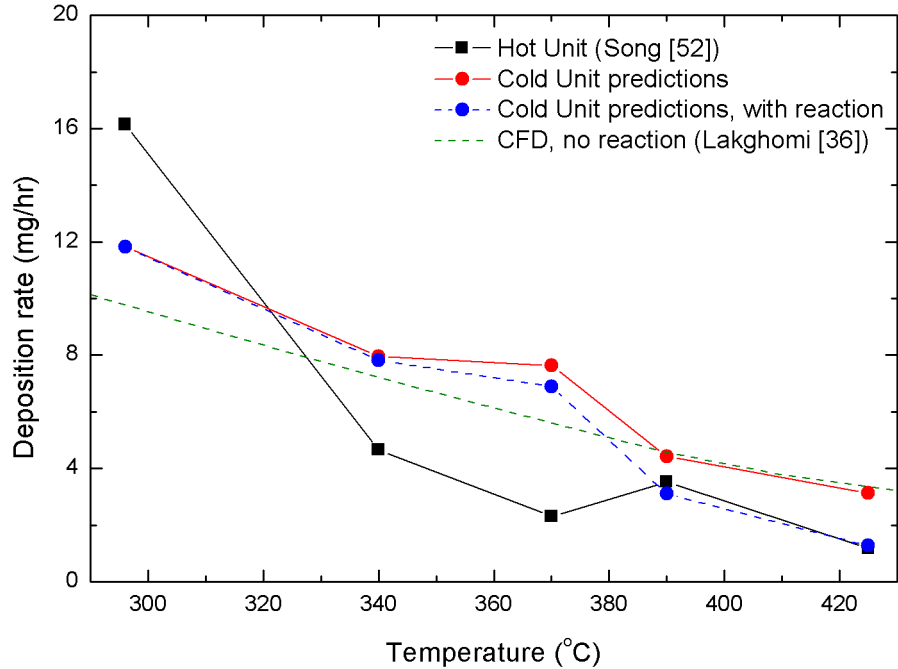


Figure 6.2 Comparison between Hot Unit deposition rates for 5% MEBR, with the predictions from the Cold Unit deposition coefficients, and CFD predictions

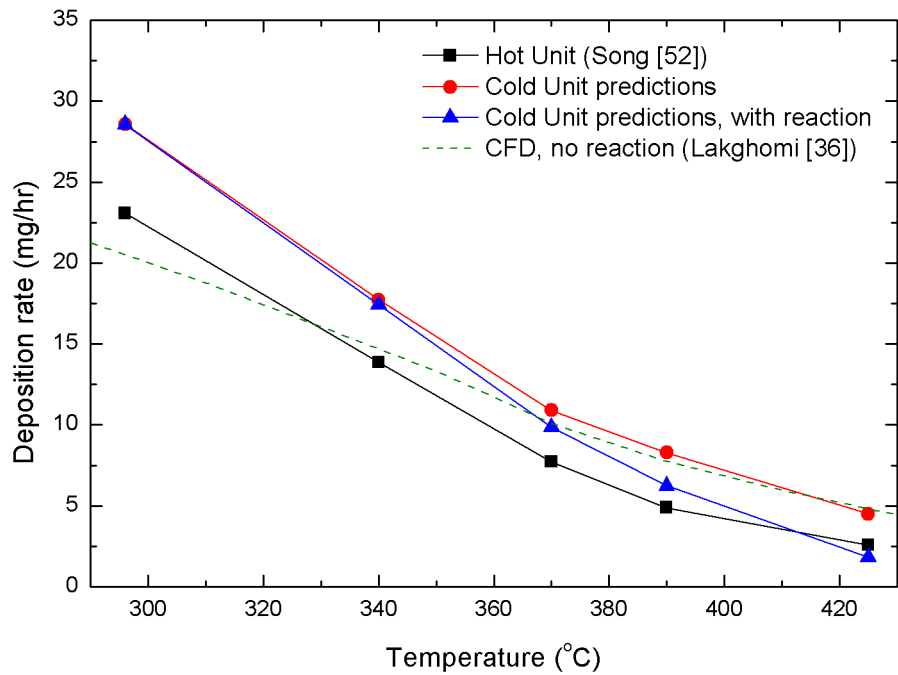


Figure 6.3 Comparison between Hot Unit deposition rates for 10% MEBR, with the predictions from the Cold Unit deposition coefficients, and CFD predictions

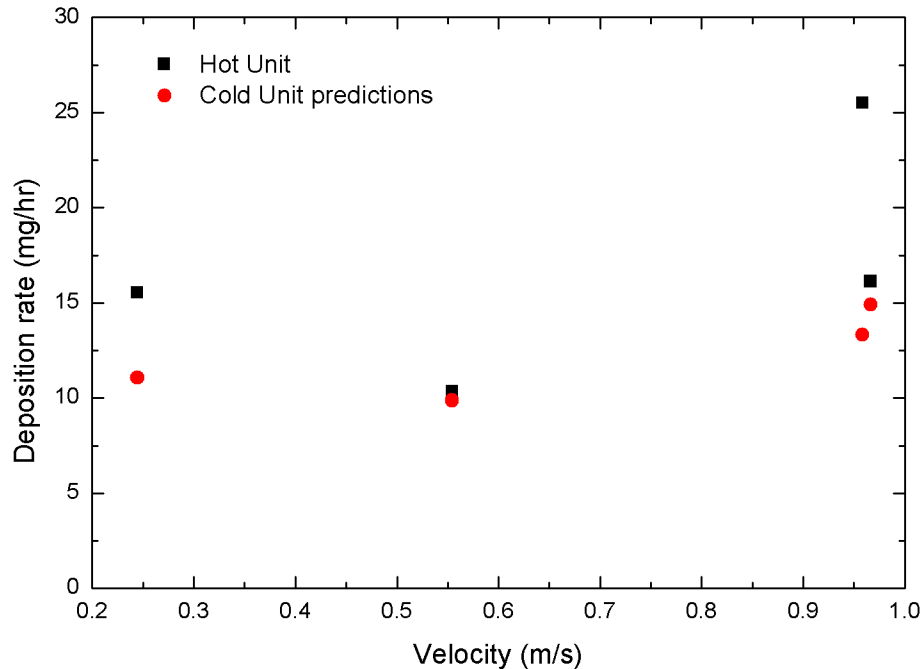


Figure 6.4. Comparison between Hot Unit deposition rates for the effect of velocity, with the predictions from the Cold Unit deposition coefficients

In summary, a good agreement between the Hot Unit experimental data [52], CFD results [36], and deposition rates predicted from the Cold Unit deposition coefficients was obtained. Given the fact that the deposition coefficients at the high temperature conditions were calculated from the change in the Stokes number (Eqs. (6.1), (6.2)), and that the main parameter governing the deposition due to inertial impaction is the Stokes number, the obtained results support the hypothesis, that the main mechanisms of deposition from the vortex on the downstream side, are inertial impaction and gravity.

Chapter 7. Conclusions and Recommendations

7.1. Conclusions

The objective of this work was to experimentally investigate the deposition of droplets from aerosol flow onto solid surfaces, namely a circular disk (coupon). The investigated factors included: (a) the effect of gas velocity, (b) the effect of droplet size, and (c) the effect of contact angle on deposition rates on the upstream (front) and downstream (back) side of a disk. In addition, morphology and distribution of deposits on the disk surface were studied as well.

For the purpose of this work, the Cold Unit apparatus, with complete measurement and data acquisition system was successfully designed and assembled. Experiments in the Unit were carried out for an upward flowing aerosol, for a 5 cm diameter circular disk, placed in the 7.5 cm diameter column. To measure the droplet size distribution in the aerosol, a shadowgraphy technique, with a modified image analysis procedure which was different from commercial systems, was developed and used with success. A technique for measuring size and mass distribution of deposits along the coupon radius was developed as well. Furthermore, a software code for complete analysis of the individual drop size data was developed and implemented in the MATLAB[®] environment.

To explain the experimental results, particle transport from a potential flow, in the presence of gravity, was modeled and simulated. To account for the effect of reaction at high temperature conditions [52], the effect of decomposition of heavy oil deposits was also included in the model.

The three main parameters that were used to describe deposition were: (a) deposition rates, which represent the rate of fouling at a given aerosol concentration, (b) deposition coefficients, which are independent of concentration and represent a direct measure of deposition rates and (c) capture efficiencies, which denote the extent of aerosol removal by deposition. Experiments performed with a size distribution of triethylene glycol droplets in air, showed that the main mechanism of deposition on the upstream side of the disk was inertial impaction. At superficial gas velocity of 1 m/s,

deposition on the upstream surface started at critical Stokes number $St_{cr}=0.05$, and droplet diameter $D_p=27$ microns. Simulations of the inertial impaction from the upward flow, obtained using the potential flow approximation, showed good qualitative agreement with the experimental results. According to the simulations, capture efficiencies are a function of the Stokes number and velocity, and increase as the velocity and Stokes numbers increase. It can be said that to reduce deposition due to inertial impaction, the Stokes number should be decreased, which means that velocity and droplet size should be reduced, or the diameter of the obstacle increased. Deposition by convective diffusion and inertia ('eddy impaction') from parallel flow seemed to be negligible compared to the deposition from inertial impaction. However, a more detailed study of these phenomena should be undertaken.

Experimental results for the downstream side, showed that for a given droplet size distribution, deposition coefficients showed a minimum with velocity. An increase in the volume median diameter of the size distribution, from 4 to 7 microns, resulted in an increase in deposition coefficients, by a factor of three. Calculated capture efficiencies and deposition coefficients, using size distributions in the aerosol and on the coupon (in the range $U=0-1.5$ m/s and $D_p=3-20$ microns), also showed an increasing trend with the drop diameter. At higher velocities and larger droplets, it is estimated that capture efficiencies and deposition coefficients will reach a maximum and start to decrease, since the droplets would be unable to follow the curvature behind the coupon and be entrained in the vortex. Simulations performed using potential flow approximation with gravity in the flow direction, showed a good correlation with the experimental results for the downstream side. Therefore, inertial impaction and gravity were postulated to be the governing mechanisms of deposition on the downstream side. To reduce deposition on the downstream side, droplet size should be reduced, and an optimum velocity, for a given droplet size distribution, should be calculated from the deposition coefficients for each drop size.

Investigation of the distribution of deposits along the radius of a glass coupon showed that, for the upstream side, deposits were more concentrated close to the edge of the coupon. On the downstream side, where the flow field is characterized by the vortex,

deposits were uniformly distributed along the radius. These results suggest that the downstream side of the packing would foul uniformly, while for the upstream side it is possible that the outer parts of packing elements would foul more rapidly than the inner parts. Therefore, inertial impaction on the upstream side should be avoided, if possible, by operating at lower superficial gas velocity and with smaller droplet sizes.

The effect of contact angle on deposition was investigated in the range of 20–95°, using glass, stainless steel and Teflon coupons. The results showed that there was no significant difference in deposition rates between the surfaces. If a difference existed, it was within the experimental error. The same can be said for the effect of dry vs. wet coupon surfaces: no significant differences between deposition rates could be observed; again, if there were any, they were within the experimental error. Although the effect of surface roughness requires a more detailed study, experiments with a roughened Teflon coupon suggested that surface roughness could have an impact on the deposition, by promoting turbulence and increasing deposition of fine droplets.

Lastly, results obtained from ambient temperature experiments (Cold Unit) were compared with an independent set of experimental data, obtained at high temperature conditions (Hot Unit, Song [52]). Using physical properties of the gas and liquid phase at high temperature conditions, and assuming that deposition in the wake is governed by inertial impaction and gravity in the flow direction, deposition coefficients from the ambient conditions were recalculated to the high temperature unit conditions. Good agreement between the two sets of experimental data was observed, indicating that the hypothesis of inertial impaction and gravity in the flow direction is correct.

7.2. Recommendations

7.2.1. Recommendations for further investigations in the Cold Unit

For the future work, investigation of deposition in the room temperature unit could be extended at velocities above 1.5 m/s. This should give information on the effect of velocity over a wider range, and confirm or disprove the assumption that on the downstream side, at high Stokes numbers, capture efficiencies and deposition coefficients reach their maximum and start decreasing.

Regarding the droplet size effect, it would be interesting to investigate experimentally deposition on the upstream side, due to turbulent diffusion solely. To properly measure small amounts of deposit from turbulent diffusion, experiments should be performed at such conditions, where inertial impaction would not occur. Using fine monodisperse aerosols, or polydisperse aerosols without any large droplets that would impact on the upstream surface, along with the larger coupons that would lead to a smaller Stokes numbers, could be a helpful strategy.

The effect of contact angle (and surface roughness) is important in the initial stages of deposition only, until the surface of the coupon becomes fully covered with the first layer of deposits (1–2 minutes). Hence, from a practical point of view, it is unlikely that increasing the contact angle in the range 20–94° could significantly reduce fouling rates in the Scrubber. The only possibility for deposit prevention via surface effects seems to be a complete repelling of bitumen droplets, or collection of bitumen droplets already deposited on the surface, with the washoil sprayed from the top (surface with the self-cleaning property). Such behaviour might be possible to achieve using superoleophobic surfaces, which exhibit contact angles higher than 150°. Experimental investigation would be the only way to prove or disprove this assumption. To find application in the Scrubber of a Fluid Coker reactor, these surfaces should maintain an oil repellent behaviour at elevated temperatures, and over a long period of time.

7.2.2. Recommendations for the industrial case

To minimize fouling in the Scrubber, one should operate under conditions of minimum deposition coefficients, but to maximize heavy component droplet removal, one should operate at highest capture efficiencies. These are two opposing requirements and entail that the optimum operating conditions are determined by minimizing a cost function, which includes the cost of fouling in the scrubber and the benefits having a heavy-component free product which enters the downstream equipment. The present work was, however, limited to understanding of the effects of phenomena that govern the deposition process. Knowledge from this investigation, along with the needed economic parameters, can be used in determining the optimal operating conditions.

Unfortunately, it seems unlikely that the velocity and droplet size in the reactor could be changed purposely in order to reduce fouling. Still, understanding of the velocity and droplet size effects could be useful in predicting the change in the rate of fouling in the Scrubber, if the rate of production (reactor throughput) is changed. For example, if the production rate increases, superficial gas velocity in the Scrubber will increase (from the current $U=1.35$ m/s), resulting in increased deposition coefficients and deposition rates on the packing elements. Since the gaseous product stream is treated in the cyclones before it enters the Scrubber, increase in the productivity would improve removal of droplets in the cyclones by means of inertial deposition. As a result, a decrease in the droplet size would be followed by a decrease in the deposition (fouling) rate. It is possible that the two opposite effects would cancel out and that the fouling rate would remain unchanged. Nevertheless, proper calculations should include a model for deposition of droplets in the cyclones [8], to account for the simultaneous changes in velocity and droplet size. In the case where the packing in the Scrubber section needs to be redesigned, knowledge of the velocity and droplet size effect can assist in understanding the effect of local velocities. For example, from the experimental results on the upstream and downstream side, we know that high velocity regions, which lead to high Stokes numbers and deposition by inertial impaction, should be avoided. Proper predictions of the deposition rates should, however, include a more realistic fluid mechanics model, specific to the geometry of the packing.

To discuss a possible fouling scenario in the Scrubber, consider an arrangement of surface elements (e.g. disks), one above the other, such as the arrangement of packing elements in the Scrubber. Capture efficiencies of disks are independent of concentration, and for a given droplet size, they are constant along the Scrubber height. Since the change in the aerosol concentration due to deposition on the packing elements is a first-order process, an exponential-like decrease in the aerosol concentration, from the bottom of the scrubber to the top, is expected. Furthermore, since capture efficiencies of larger droplets are higher than capture efficiencies of smaller droplets, it is expected that the size distribution of droplets in the aerosol will decrease along the Scrubber height. These two factors combined indicate that the fouling rate in the lower section of the Scrubber would be considerably higher than in the upper parts. Therefore, it is possible that fouling

in the lower section of the Scrubber could lead to early blockage of the grid. To avoid this situation, one could consider using larger packing elements at the bottom (lower Stokes number, and lower capture efficiencies), and allow more void space between the packing elements to distribute the fouling (deposition) rate more uniformly along the whole height of the Scrubber. Industrial data which indicates where the deposition starts would be useful.

From the above discussion, it seems unlikely that by changing some of the investigated parameters (gas velocity, droplet size, contact angle, degree of surface wetting), fouling rates could be wittingly reduced or eliminated. However, fouling could be reduced by using a new packing with a different geometry, but at the same time, this may lead to a lower collection efficiency and more heavy droplets in the product stream. Even if the redesigned packing would yield a somewhat lower fouling rate, the fouling problem would still persist. Thus, attention may be shifted toward wet scrubbers without internal elements, such as spray towers [75] or venturi scrubbers [76]. These scrubbers are used to remove particles by inertial impaction (spray tower) and additional deposition mechanisms (venturi scrubber). In the case of the spray tower, which is more similar to the existing design of the Scrubber, optimum drop diameter for the washoil could be determined. If the collection efficiency using the optimal drop diameter, and given scrubber height are not sufficient to remove heavy oil droplets from the product vapour, additional separation system, installed after the scrubber, could be considered. Fibrous filters made of the stainless steel fibers, used for air cleaning [20], could be employed for this purpose. Two such filters may be installed in parallel, and operate in turn, in order to allow continuous operation and maintenance. Downward orientation of the flow, with gravity aiding the deposition, would be the best of all three possibilities (upward, horizontal, downward).

References

1. Wikipedia, “Oil reserves”, http://en.wikipedia.org/wiki/Oil_reserves, Date of access: 09/15/2009.
2. Wikipedia, “Petroleum prices”, http://en.wikipedia.org/wiki/Price_of_petroleum, Date of access: 09/11/2009.
3. Wikipedia, “Unconventional oil”, http://en.wikipedia.org/wiki/Unconventional_oil, Date of access: 09/11/2009.
4. Wikipedia, “Petroleum production in Canada”, http://en.wikipedia.org/wiki/Petroleum_production_in_Canada, Date of access: 09/11/2009.
5. Mink, F. J., and Houlihan, R. N., “Tar sands”, Ullmann's Encyclopedia of Industrial Chemistry, John Wiley & Sons Inc., 2009.
6. Wikipedia, “Oil sands”, http://en.wikipedia.org/wiki/Oil_sands, Date of access: 09/15/2009.
7. Wikipedia, “Bitumen”, <http://en.wikipedia.org/wiki/Bitumen>, Date of access: 09/17/2009.
8. Jankovic, J., “Simulation of the Scrubber section of a Fluid Coker”, M.A.Sc. Thesis, University of British Columbia, 2005.
9. Subudhi, N., “Simulation of pressure drop and coke deposition in the grid of a scrubber”, M.A.Sc. Thesis, University of British Columbia, 2006.
10. Papavergos, P. G., and Hadley A.B., “Particle deposition behaviour from turbulent flows”, *Chemical Engineering Research and Design* 62, 275–295, 1984.
11. Cleaver, J. W., and Yates, B., “A sublayer model for the deposition of particles from a turbulent flow”, *Chemical Engineering Science* 30, 983–992, 1975.
12. Epstein, N., “Elements of particle deposition onto nonporous solid surfaces parallel to suspension flows”, *Experimental Thermal and Fluid Science* 14, 323–334, 1997.
13. Zhang, J., and Li, A., “CFD simulation of particle deposition in a horizontal turbulent duct flow”, *Chemical Engineering Research and Design* 86, 95–106, 2007.

14. Tian, L., and Ahmadi, G., "Particle deposition in turbulent duct flows-comparisons of different model predictions", *Aerosol Science* 38, 377–397, 2007.
15. Schlichting, H., "Boundary layer theory", McGraw-Hill, 7th Edition, 1979.
16. Lai, A. C. K., and Nazaroff, W. W., "Modeling indoor particle deposition from turbulent flow onto smooth surfaces", *Journal Of Aerosol Science* 31, No. 4, 463–476, 2000.
17. Sehmel, G. A., "Particle eddy diffusivities and deposition for isothermal flow and smooth surfaces", *Journal Of Aerosol Science* 4, 125–138, 1973.
18. Young, J., and Leeming, A., "A theory of particle deposition in turbulent pipe flow", *Journal of Fluid Mechanics* 340, 129–159, 1997.
19. Vincent, J. H., and Humphries, W., "The collection of airborne dusts by bluff bodies", *Chemical Engineering Science* 33, 1147–1155, 1978.
20. Hinds, W., "Aerosol technology: properties, behavior, and measurement of airborne particles", 2nd Edition, Wiley-Interscience, 1999.
21. Friedlander, S., "Smoke, dust, and haze: fundamentals of aerosol dynamics", 2nd Edition, Oxford University Press, 2000.
22. Albrecht, F., "Theoretische Untersuchungen über die Ablagerung von Staub aus strömender Luft und ihre Anwendung auf die Theorie der Staubfilter", *Physikalische Zeitschrift* 32, 48–56, 1931.
23. Sell, W., *Forsch Gebiete Ingenieur* 2, Supplement No. 347, August 1931.
24. Langmuir, J., and Blodgett K. B., "A mathematical investigations of water droplet trajectories," AAF Technical Report 5418, 1946.
25. Landhal, H. D., and Herrmann, R. G., "Sampling of liquid aerosols by wires, cylinders, and slides, and the efficiency of impaction of the droplets", *Journal of Colloid Science* 4, 103–136, 1949.
26. Ranz, W. E., and Wong, J. B., "Impaction of dust and smoke particles on surface and body collectors", *Industrial and Engineering Chemistry* 44, 1371–1381, 1952.

27. Wong, J. B., Ranz, W. E., and Johnstone, H. F., “Inertial impaction of aerosol particles on cylinders”, *Journal of Applied Physics* 26, No. 2, 244–249, 1955.
28. May, K. R., and Clifford, R., “The impaction of aerosol particles on cylinders, spheres, ribbons and discs”, *Annals of Occupational Hygiene* 10, 83–95, 1966.
29. Gregory, P. H., and Stedman, O. J., “Deposition of air-borne Lycopodium spores on plane surfaces”, *Annals of Applied Biology* 40, 651–674, 1953.
30. Golovin, M. N., and Putnam, A. A., “Inertial impaction on single elements”, *Industrial and Engineering Chemistry Fundamentals* 1, No. 4, 264–273, 1962.
31. Noll, K. E., and Pilat, M. J., “Inertial impaction of particles upon rectangular bodies”, *Journal of Colloid and Interface Science* 33, No. 2, 197–207, 1970.
32. Tsai, R., and Liang, L. J., “Inertial effect on aerosol particle deposition from an axisymmetric stagnation point flow approximation”, *International Communication Heat Mass Transfer* 29, No. 4, 489–496, 2002.
33. Amelin, A. G., and Beliyakov, M. I., *Doklady Akademii Nauk S.S.S.R.* 108, No. 1, 31–39, 1956.
34. Yeomans, A. H., Rogers, E. E., and Ball, W. H., “Deposition of aerosol particles”, *Journal Of Economic Entomology* 42, No. 4, 591–596, 1949.
35. Goldshmid, Y., and Calvert, S., “Small particle collection by supported liquid drops”, *A. I. Ch. E. Journal* 9, No. 3, 352–358, 1963.
36. Lakghomi, B., “CFD simulation of aerosol flow and hydrocarbon fouling on a circular disk”, M.A.Sc. Thesis, University of British Columbia, 2009.
37. Medout-Marere V., and Douillard, J.-M., “Studies of divided solids by immersion calorimetry”, *Encyclopedia of Surface and Colloid Science*, Marcel Dekker Inc., New York, 2002.
38. “Cleanliness measurements using contact angles”, FTA Application Notes, 2000, <http://www.firsttenangstroms.com/papers/papers.html>, Date of Acces: 03/05/2009.
39. Yarin, A. L., “Drop impact dynamics: splashing, spreading, receding, bouncing...”, *Annual Review of Fluid Mechanics* 38, 159–192, 2006.

40. Durickovic, B., and Varland K., “Between bouncing and splashing: water drops on a solid surface”, Term Paper, 2006, <http://pub.bojan.info/bounce.pdf>, Date Of Access: 03/05/2009.
41. Khatavkar, V. V., Anderson, P. D., and Meijer, H. E. H., “Impact of micro-drops on a solid surface”, Eindhoven University of Technology, <http://www.mate.tue.nl/mate/pdfs/4851.pdf>, Date Of Acces: 12/01/2009.
42. Rioboo, R., Tropea, C., Marengo, M., “Outcomes from a drop impact on solid surfaces”, *Atomization and Sprays* 11, 155–165, 2001.
43. Callies, M., and Quere, D., “On water repellency”, *Soft Matter* 1, 55–61, 2005.
44. Richard, D., and Quere, D., “Bouncing water drops”, *Europhysics Letters* 50, No. 6, 769–775, 2000.
45. Cheng, Y.-T., and Rodak, D. E., “Is the lotus leaf superhydrophobic?”, *Applied Physics Letters* 86, 144101, 2005.
46. Cheng, Y.-T., Rodak, D. E., Angelopoulos, A., and Gacek, T., “Microscopic observations of condensation of water on lotus leaves”, *Applied Physics Letters* 87, 194112, 2005.
47. Rioboo, R., Voue, M., Vaillant, A., and De Coninck, J., “Drop impact on porous superhydrophobic polymer surfaces”, *Langmuir* 24, 14074–14077, 2008.
48. Wang, Z., Lopez, C., and Koratkar, N., “Impact dynamics and rebound of water droplets on superhydrophobic carbon nanotube arrays”, *Applied Physics Letters* 91, 023105, 2007.
49. Tsujii, K., Yamamoto, T., Onda, T., and Shibuichi, S., “Super oil-repellent surfaces”, *Angewandte Chemie International Edition* 36, No. 9, 1011–1012, 1997.
50. Tuteja, A., Choi, W., Ma, M., Mabry, J. M., Mazzella, S. A., Rutledge, G. C., McKinley, G. H., Cohen, R. E., “Designing superoleophobic surfaces”, *Science* 318, 1618–1622, 2007.
51. Tuteja, A., Choi, W., McKinley, G. H., Cohen R. E., and Rubner, M. F., “Design parameters for superhydrophobicity and superolephobicity”, *MRS Bulletin* 33, 752–758, 2008.

52. Wu, W., Wang, X., Wang, D., Chen, M., Zhou, F., Liu, W., and Xue, Q., “Alumina nanowire forests via unconventional anodization and super-repellency plus low adhesion to diverse liquids”, *Chemical Communications* 9, 1043–1045, 2009.
52. Song, J., “Role of aerosols in coupon fouling-Hot Unit”, Final Syncrude Canada Ltd. Report, University Of British Columbia, 2009.
53. Lokare, S. S., “A mechanistic investigation of ash deposition in pulverized-coal and biomass combustion”, Ph.D. Dissertation, Brigham Young University, 2008.
54. Bird, R. B., Stewart, W. E., Lightfoot, E. N., “Transport phenomena”, 2nd Edition, Wiley, 2007.
55. Wilkes, J. O., “Fluid mechanics for chemical engineers”, Prentice Hall PTR, 1st Edition, 1998.
56. Salmanzadeh, M., Rahnama, M., and Ahmadi, G., “Particle transport and deposition in a duct flow with a rectangular obstruction”, *Particulate Science and Technology*, 25, 401–412, 2007.
57. Beg, S. A., “Forced convective mass transfer from circular disks”, *Wairme- und Stoffubertragung* 1, 45–51, Springer-Verlag, 1973.
58. Yue, C., Watkinson, A. P., Lucas, J. P., Chung, K. H., “Incipient coke formation during heating of heavy hydrocarbons”, *Fuel* 83, 1651–1658, 2004.
59. Wigg, L. D., “Drop-size prediction for twin-fluid atomisers”, *Journal of the Institute of Fuel* 11, 46–52, 1964.
60. Gupta, V. S., “Boiling point and critical temperature of n-paraffins”, *Journal of Chemical Physics* 24, 164–165, 1956.
61. Settles, G. S., “Schlieren and shadowgraph techniques: visualizing phenomena in transparent media”, Springer-Verlag Berlin Heidelberg New York, 2001.
62. Baron, P. A., and Willeke, K., “Aerosol measurement: principles, techniques and applications”, John Wiley & Sons Inc., 2001.
63. La Vision, “ParticleMaster Shadow manual”, LaVision GmbH, Gottingen, 2008.
64. Lee, S.-Y., Kim, Y. D., “Sizing of spray particles using image processing technique”, *KSME International Journal* 18, No. 6, 879–894, 2004.

65. Woodward, R. P., “Contact angle measurements using the drop shape method”, First Ten Angstroms, <http://www.firsttenangstroms.com/pdfdocs/CAPaper.pdf>, Date Of Access: 12/03/2009.
66. “Sessile drop interfacial tension measurements”, FTA Application Notes, <http://www.firsttenangstroms.com/pdfdocs/SessileDropIFT.pdf>, Date Of Access: 12/03/2009.
67. “Influence of drop’s volume on contact angle”, <http://www.firsttenangstroms.com/pdfdocs/DropVolumeAndCA.pdf>, Date Of Access: 12/03/2009.
68. “Cleanliness measurements using contact angles”, <http://www.firsttenangstroms.com/pdfdocs/Cleanliness.pdf>, Date Of Access: 12/03/2009.
69. Bergeron, V., and Quere, M., “Water droplets make an impact”, *Physics World* 14, No. 5, 27–31, 2001.
70. Cao., A., Cao, L., and Gao, D., “Fabrication of nanoaging superhydrophobic surfaces by packing flowerlike hematite particles”, *Applied Physics Letters* 91, 034102, 2007.
71. “Voltesso product data sheet”, http://www.imperialoil.com/Canada-English/Files/Products_Lubes/IOCAENWPOESVoltesso.pdf, Date Of Access: 08/12/2009.
72. Humphries, W., and Vincent, J., H., “The transport of airborne dusts in the near wakes of bluff bodies”, *Chemical Engineering Science* 33, 1141–1146, 1978.
73. Carmody, T., “Establishment of the wake behind a disk”, *Journal of Basic Engineering, Transactions of ASME*, 869–882, Dec. 1964.
74. Sato, S., Vincent, J. H., Pui, D. Y. H., “Dispersion of large particles in the near wake of a disc in a turbulent free stream”, *Journal of Aerosol Science* 27, No. 4, 559–573, 1996.
75. Wikipedia, “Spray tower”, http://en.wikipedia.org/wiki/Spray_tower, Date Of Access: 12/02/2009.
76. Wikipedia, “Venturi scrubber”, http://en.wikipedia.org/wiki/Venturi_scrubber, Date Of Access: 12/02/2009.

77. Schick R. J., “Spray technology reference guide: understanding drop size”, Spraying Systems Co., http://service.spray.com/web/register/view_lit.asp?code=B459B, Date of Access: 12/02/2009.
78. Limpert, E., Werner, S. A., Abbt, M., “Log-normal distributions across the sciences: keys and clues”, *Bioscience* 51, No. 5, 341–352, 2001.

Appendix A. Cold Unit Operating Procedure

A.1. Pre-experimental procedure

1. Turn the lights, fan, camera, and the balance on. Turn the computers on.
2. Place the 2.5 liter waste reservoir below the column, to collect the washdown waste stream from washing the column.
3. Wash the column from the top; clean the top flange and 30–40 cm of the column interior from the top.
4. Clean the nozzle by atomizing water (if previously worked with sugar solution) and switch to triethylene glycol for about 10–15 seconds.
5. Replace the reservoir that collected washdown waste with an empty one.
6. Fill the 4 liter reservoir on the balance with triethylene glycol.
7. Prepare softwares and file names for data logging;
 - PC #1: 1) RSImage for shadowgraphy
2) RS232 Data Logger for balance data
 - PC #2: 1) Transducer Technique software for Load Cell data
2) Hyper Terminal for temperature data logging.

A.2. Experimental procedure

1. Measure droplet size distribution with shadowgraphy
 - clean glass slides from deposits
 - turn the pump on
 - open the ball valve and introduce air
 - wait about 10 sec for the flow to stabilize and close the ball valve quickly
 - wait 5 sec and start acquiring images (130 images during 14 seconds, using 60 microseconds exposure at 6x magnification)
 - repeat this procedure 10 times to collect sufficient number of samples.
2. Place the coupon in the column and attach it to the Load Cell.
3. Make sure that the rod is not touching the constraint and the PVC cap on the top.
4. Start logging Load Cell and Temperature data. Do not open any other Load Cell log file while logging data since data in old files will be overwritten!

5. Wait about 15 min. for stable readings from the Load Cell and record the weight in the notebook.
6. Turn the pump on and introduce air.
7. Start logging balance data.
8. If the run will take longer than 30 min, connect the washdown reservoir on the balance with the large washdown reservoirs and make sure that all the valves are open.
9. Keep experiment running. Do not allow collecting more than 300–400mg of deposits on the coupon, since it will be difficult to remove it from the column without losing some deposits.
10. Take images of the coupon surface when change in the slope is noticed (increase or decrease).
11. At the end of experiment, stop the air and turn the pump off.
12. Wait about 15 min for stable readings and record the total weight in the notebook.
13. Stop the Load Cell and Temperature data logging.
14. Carefully remove the coupon from the column so that droplets from the coupon surface aren't lost.
15. Measure the weight of 7 nuts and wire (known mass) in the current load cell position, to allow load cell calibration check.
16. Take images of the upstream and downstream side of the coupon.
17. Measure coupon weight on the analytical balance:
 - weight of the stand
 - weight of the stand with the coupon and all deposits (all)
 - clean the rod and measure (all – rod deposits)
 - clean the upstream side and measure (all – rod – upstream deposits)
 - clean the downstream side and measure (all – rod – upstream – downstream deposits)
 - weight of the clean coupon

A.3. Post-experimental procedure

1. Empty the waste tank and pour the liquid from the reservoirs that collected triethylene glycol, back in the 4 liter reservoir.
2. Copy data files to the office computer.



Figure A.1 Picture of the Cold Unit apparatus

Appendix B. Calibrations

All measurement techniques (except the contact angle measurement technique) had to be calibrated. These included,

- a) Pump calibration for measurement of liquid flow to the nozzle and aerosol concentration (Section 4.3.1)
- b) Rotameter calibration for the gas velocity measurements (Section 4.3.2)
- c) Calibration of the shadowgraphy system for drop size distribution measurements, in the aerosol and on the coupon (Sections 4.3.3 and 4.3.4), and
- d) Load cell calibration for deposition rate measurements (Section 4.3.5)

All calibrations are presented here, with the exception of the shadowgraphy system calibrations, which, for the continuity of presentation, were retained in the main text (Section 4.3.3.6).

B.1. Pump calibration

For measuring flow of liquid to the aerosol (Section 4.3.1.1), the gear pump had to be calibrated. Full scale on the console drive was divided into 30 equidistant sections, further divided into 4 smaller sections each (Fig. 4.11).

The pump was calibrated without and with differential pressure (200–300 kPa) between the inlet and the outlet. Liquid was pumped from the reservoir placed on the balance, and the data from the balance were logged into a file. Mass flow rate of the liquid was estimated from the slope of the weight loss curve, and recalculated to the liquid volume flow. There was no significant difference (lower than 1 ml/min) between the liquid flow rates measured with and without differential pressure (Fig. B.1).

Although the manufacturer specified increase in the liquid flow over the entire range, above pump setting 9 (close to one third of the full scale), there was no additional increase in the liquid flow. This is most likely due to imperfect sealing of gears, or their imperfect placement in the pump casing. Therefore, each time after the gears are

replaced, the calibration should be checked. In the range 0–9, liquid flow proved to be linearly dependent on the pump setting.

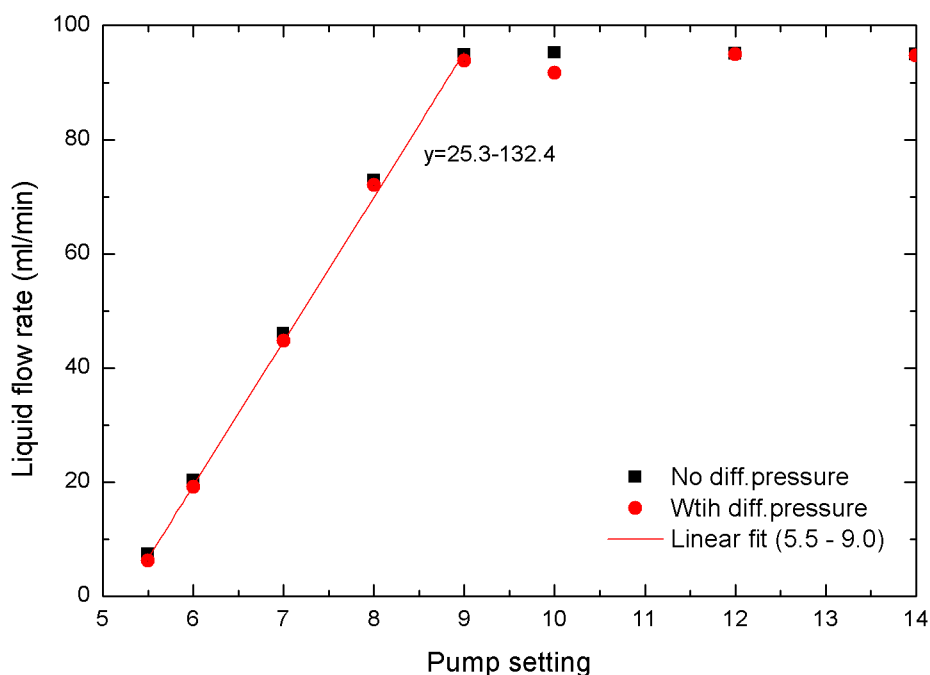


Figure B.1 Gear pump calibration curve, with and without differential pressure (200–300 kPa)

The details of the equipment used are as follows. The pump head was RK-07002-27 Micropump[®] A-mount Suction Shoe Pump Head from Cole Parmer, with graphite gears and PTFE seals. It was mounted on the RK-75211-10 Cole Parmer Console Drive. For measuring liquid flow rate to the aerosol, an Ohaus Ranger[™] balance, with 6 kg capacity and 0.1 g precision was used. The balance was connected to the serial port on the computer equipped with RS-232 Data Logging software. Communication setting in the software were set to: Baud rate: 300 bps, Data bits: 7, Parity: None, Stop bits: 1 and Flow control: None. Data from the balance were read each 0.5 seconds.

B.2. Rotameter calibration

All three rotameters on the Cold Unit Apparatus (Fig. 4.1) had to be calibrated. Rotameter #1 was Brooks model No. 8408-2193, 0–300 l/min, Rotameter #2 was Brooks type 9-1110, 0–300 l/min, and Rotameter #3 was from Cole Parmer, 0–100 l/min.

B.2.1. Theoretical background

Rotameter is a flow-measuring device that depends on the change of an annular area A_{an} between the float and the tube, which is a function of the vertical location of the float, to yield essentially fixed pressure drop at all flow rates (Fig. B.2)

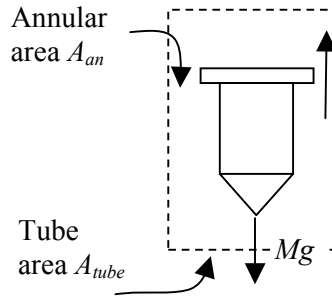


Figure B.2 Schematic representation of the rotameter float

After solving equations for conservation of mass, energy and upward momentum for the flow around the rotameter float [55], the flow rate can be expressed as,

$$Q = A_{an} \sqrt{\frac{2Mg}{\rho_f A_{tube}}} \quad (\text{B.1})$$

where M is the mass of the float, A_{tube} is the tube area, and ρ_f is the density of the fluid flowing through the rotameter. After replacing $\rho_f = \frac{PM_w}{RT}$, at each position of the float, at the constant temperature T , product $Q\sqrt{P}$ is a constant. The flow of air at pressure P , can be then calculated from the calibration data (Q_0 vs. P_0) as,

$$Q(P) = Q_0 \sqrt{\frac{P_0}{P}} = k_p \frac{1}{\sqrt{P}} \quad (\text{B.2})$$

where k_p is the rotameter constant, $k_p = Q_0 \sqrt{P_0}$. The flow of air in the column at $P_0 = 101.3$ kPa can be then calculated from the flow of air through the rotameter as,

$$Q_{column,p_0} = Q \frac{P}{P_0} \quad (\text{B.3})$$

B.2.2. Experimental

Rotameter #1 was calibrated by connecting it in series with the mass flow meter K-2908-23 from Cole Parmer, capacity 0–50 l/min. The inlet of the mass flow meter was connected to the outlet of the rotameter and readings at 15 points were recorded (Table B.1). Data were fitted with a second order polynomial. Limited flow range allowed calibration of only one part of the total scale (0–70), but the curve was extrapolated with confidence to the range (70–100).

Rotameter #2 was calibrated by connecting it in series with the high flow capacity rotameter, with the calibration curve from the manufacturer (Brooks rotameter type 1110-13B-A, tube size: R13M-25-1 BR-2-18G10, float: 13-RS-510, max. capacity approximately 3000 l/min). Schematic of the measurement setup is given in Fig. B.3, and the data points are given in Table B.2.

Rotameter #3 was calibrated using the above mentioned mass flow meter (K-2908-23). Calibration was performed for 12 points over the scale 0–50. Pressure did not increase appreciably above the atmospheric pressure, and no corrections were included. Values for the range 50–80 were obtained by extrapolation (Table B.3).

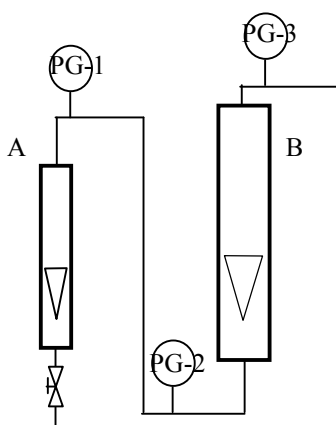


Figure B.3 Rotameter #2 calibration setup. Rotameter #2 (A) is connected in series with the rotameter with the calibration curve from the manufacturer (B).

Table B.1 Rotameter #1 calibration data

Setting	PG, (psi)	Flow of air at $P_0=14.7$ psi (l/min)	$k = Q \cdot \sqrt{(P_0+PG)}$, ($\text{m}^3 \cdot \text{s}^{-1} \cdot \text{psi}^{0.5}$)
0	0	3.37	0.00022
5	0	7.17	0.00046
10	0	10.91	0.00070
15	0.5	14.84	0.00093
20	1	18.67	0.00115
25	1	22.71	0.00140
30	1.5	26.76	0.00163
35	2	30.76	0.00184
40	2.5	34.6	0.00204
45	3	39.01	0.00227
50	3.2	43	0.00249
55	3.8	47.04	0.00268
60	4.2	51.29	0.00289
65	5	55.45	0.00306
70	5.5	60.29	0.00329
75		64.34	0.00346
80		68.74	0.00365
85		73.18	0.00383
90		77.66	0.00401
95		82.18	0.00418
100		86.74	0.00435

Table B.2 Rotameter #2 calibration data

Rot A setting	PG-1 (psi)	Rot B setting	PG-2 (psi)	PG-3 (psi)	k_B (m/hr)	Q (m ³ /s) at PG-3 (psi)	Q (m ³ /s) at PG-1 (psi)	$k_A=Q \cdot \sqrt{(P_0+PG)}$, (m ³ ·s ⁻¹ ·psi ^{0.5})
3.4	8.5	10.8	0.4	0	0.0175	0.0046	0.002891	0.013924
3.3	8.2	10.4	0.3	0	0.0169	0.0044	0.002835	0.013565
3.2	8	9.9	0.25	0	0.0162	0.0042	0.002741	0.013061
3.1	7.9	9.4	0.2	0	0.0155	0.0041	0.002635	0.012527
3	7.7	9.2	0.15	0	0.0153	0.0040	0.002611	0.012357
2.9	7.5	8.7	0.05	0	0.0146	0.0038	0.002514	0.011847
2.8	7	8.2	0	0	0.0139	0.0036	0.00245	0.011412
2.7	6.9	7.7	0	0	0.0132	0.0034	0.002338	0.010868
2.6	6.6	7.3	0	0	0.0126	0.0033	0.002272	0.010486
2.5	6.3	7	0	0	0.0122	0.0032	0.002229	0.010215
2.4	6	6.6	0	0	0.0117	0.0030	0.00216	0.009826
2.3	5.8	6.3	0	0	0.0112	0.0029	0.002104	0.009525
2.2	5.6	5.9	0	0	0.0107	0.0028	0.002021	0.009106
2.1	5.2	5.5	0	0	0.0102	0.0026	0.001957	0.008728
2	5	5.2	0	0	0.0097	0.0025	0.001897	0.008419
1.9	4.9	4.8	0	0	0.0092	0.0024	0.0018	0.00797
1.8	4.8	4.4	0	0	0.0087	0.0023	0.001703	0.007519
1.7	4.7	4.2	0	0	0.0084	0.0022	0.001658	0.007303
1.6	4.4	3.9	0	0	0.0080	0.0021	0.001603	0.007004
1.5	4.2	3.6	0	0	0.0076	0.0020	0.001537	0.006684
1.4	4.1	3.2	0	0	0.0070	0.0018	0.001436	0.006225
1.3	4	2.9	0	0	0.0066	0.0017	0.001361	0.005884
1.2	3.9	2.6	0	0	0.0062	0.0016	0.001285	0.005542
1.1	3.8	2.4	0	0	0.0060	0.0016	0.001237	0.005319
1	3.6	2.1	0	0	0.0056	0.0015	0.001166	0.004988
0.9	3.5	1.9	0	0	0.0053	0.0014	0.001116	0.004761
0.8	3.5	1.6	0	0	0.0049	0.0013	0.001032	0.004402
0.7	3.2	1.4	0	0	0.0046	0.0012	0.000992	0.004197

Table B.3 Rotameter #3 calibration data

Setting	Flow of air at $P_0=14.7$ psi (l/min)	$k=Q \cdot \sqrt{(P_0+PG)}$, ($\text{m}^3 \cdot \text{s}^{-1} \cdot \text{psi}^{0.5}$)
4	5.2	0.000332
6	7	0.000447
8	9	0.000575
10	11.1	0.000709
15	16.9	0.001080
20	22.6	0.001444
25	28.1	0.001796
30	34.1	0.002179
35	39.7	0.002537
40	46	0.002939
45	52.1	0.003329
50	58.3	0.003725
60	71.2	0.004401
70	84.4	0.005197
80	98.2	0.006013
90	112.3	0.006849
100	126.9	0.007705

B.3. Load cell calibration

Although the load cell was calibrated from the manufacturer, it was also calibrated in the laboratory, when installed on the Cold Unit. For this purpose, a wire with ten nuts, whose weight was determined on the analytical balance (0.1 mg precision), were used. Nuts were successively added to the load cell, and the total weight from the display was recorded, 2 minutes after each new nut was added. ‘True’ vs. measured values of the weight of nuts were plotted on the graph, and the calibration curve was determined by linear interpolation. Figure B.4 shows calibration curve for the second load cell. In addition, because of great sensitivity of the load cell to its position in the horizontal plane, after each run, a weight of known mass that is similar to the weight of the coupon and the rod (a wire and 7 nuts, ~25 g) was measured on the load cell, to correct the calibration curve for that position of the load cell. Calibration curve was determined for the each new load cell used.

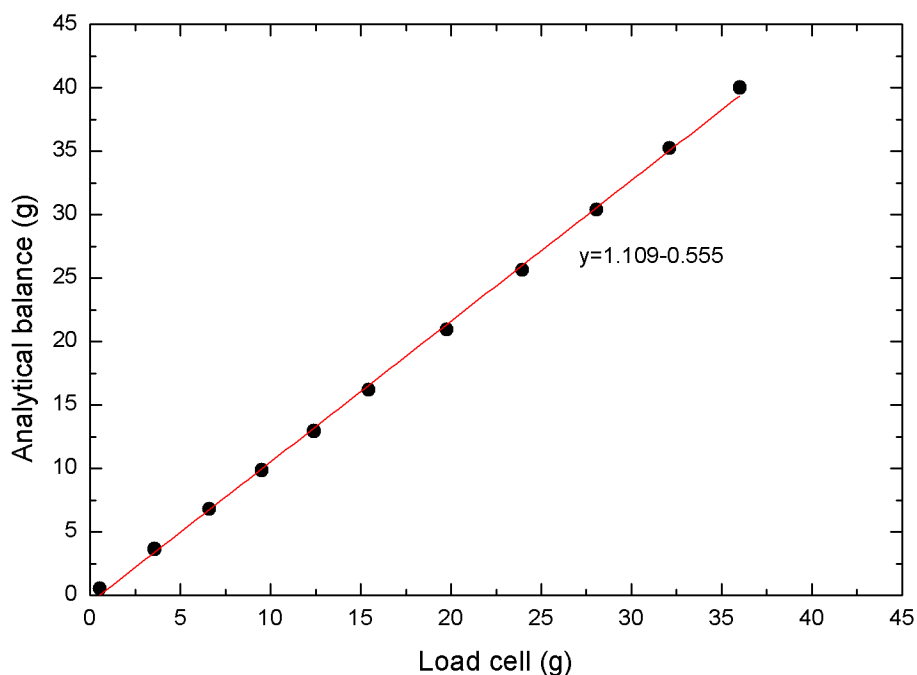


Figure B.4 Calibration curve for the second GSO-50 load cell used. The curve is approximately linear and it can be seen that, in this case, true values are about 11% larger than measured.

Appendix C. Equations Development

The following sections contain development of the equations that were deployed in this work. Derivations of the deposition model (Section 3.5.1), and the reaction model (Section 3.7), due to their brevity, were retained in the main text.

C.1. Inertial particle transport from potential flow

C.1.1. Equations of particle motion

Let us consider an axisymmetric flow around a disk, as presented in Fig. C.1,

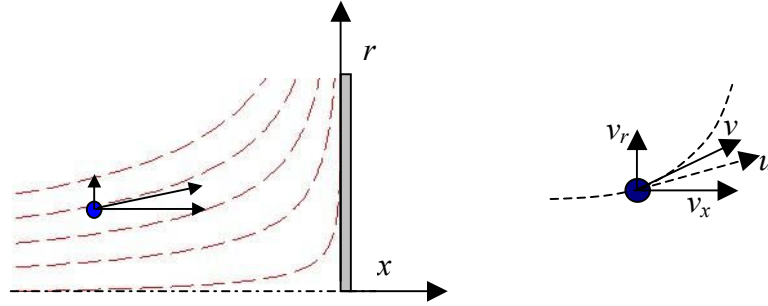


Figure C.1 Schematic representation of the flow field in front of the disk and fluid velocity components

The equation of particle motion in vector notation, in the presence of gravity field and under the assumption of Stokes drag force on the particle is given by,

$$\frac{d(m\vec{u})}{dt} = 3\pi\mu D_p (\vec{v} - \vec{u}) + m\vec{g} \quad (\text{C.1})$$

where \vec{u} is the particle velocity, \vec{v} is the fluid velocity, and $m\vec{g}$ is the gravity force. If the vector notation is removed, for each component we can write,

$$x: \frac{d(mu_x)}{dt} = 3\pi\mu D_p (v_x - u_x) + pmg \quad (\text{C.2a})$$

$$r: \frac{d(mu_r)}{dt} = 3\pi\mu D_p (v_r - u_r) \quad (\text{C.2b})$$

where parameter $p \in \{-1, 0, 1\}$ denotes a direction of the gravity field. The X-component can be further written as,

$$m \frac{d^2 x}{dt^2} + 3\pi\mu D_p \frac{dx}{dt} - 3\pi\mu D_p v_x - pmg = 0 \quad (\text{C.3})$$

or,

$$\underbrace{\frac{\rho D_p^2}{18\mu}}_{t_p} \frac{d^2 x}{dt^2} + \frac{dx}{dt} - v_x - \underbrace{\frac{\rho D_p^2}{18\mu}}_{t_p} pg = 0 \quad (\text{C.4})$$

Now we can introduce dimensionless coordinates $\bar{x} = \frac{x}{R_c}$, $\bar{r} = \frac{r}{R_c}$, dimensionless time

$\bar{t} = t \cdot \frac{v_0}{R_c}$, and dimensionless velocities $\bar{v}_x = \frac{v_x}{v_0}$, $\bar{v}_r = \frac{v_r}{v_0}$. After differentiation of the

first two relations, we get $d^2 x = R_c \cdot d^2 \bar{x}$ and $dt^2 = \left(\frac{R_c}{v_0}\right)^2 \cdot d\bar{t}^2$, which when used in the

X -component particle motion equation give,

$$x: 2St \frac{d^2 \bar{x}}{d\bar{t}^2} + \frac{d\bar{x}}{d\bar{t}} - \bar{v}_x - p \frac{t_p g}{v_0} = 0 \quad (\text{C.5})$$

where $St = \frac{t_p v_0}{2R_c}$ is the Stokes number. Similarly, for the r -component we get,

$$r: 2St \frac{d^2 \bar{r}}{d\bar{t}^2} + \frac{d\bar{r}}{d\bar{t}} - \bar{v}_r = 0. \quad (\text{C.6})$$

C.1.2. Flow field from potential flow approximation

The velocity components of the flow field around the coupon, from the potential flow approximation are given by [26, 31],

$$x: \bar{v}_x = -2\bar{x}, \quad -\frac{1}{2} < \bar{x} < 0 \quad (\text{C.7a})$$

$$r: \bar{v}_r = \bar{r}, \quad -1 < \bar{r} < 1 \quad (\text{C.7b})$$

These equations were obtained from the axisymmetric potential flow approximation around a disk. After integration of Eqs. (C.7a,b), axial and radial coordinates of the streamlines are,

$$\bar{x} = \bar{x}_0 \cdot e^{-2\bar{t}} \quad (\text{C.8a})$$

$$\bar{r} = \bar{r}_0 \cdot e^{-2\bar{t}} \quad (\text{C.8b})$$

where \bar{x}_0, \bar{r}_0 are initial positions at \bar{t}_0 .

C.1.3. Capture efficiencies for Stokesian particles

If we substitute equations of the flow field into the Eqs. (C.5), (C.6), we get,

$$x: 2St \frac{d^2 \bar{x}}{d\bar{t}^2} + \frac{d\bar{x}}{d\bar{t}} + 2\bar{x} - p \frac{t_p g}{v_0} = 0 \quad (\text{C.9a})$$

$$r: 2St \frac{d^2 \bar{r}}{d\bar{t}^2} + \frac{d\bar{r}}{d\bar{t}} - \bar{r} = 0 \quad (\text{C.9b})$$

These are two linear, second-order, ordinary differential equations, which can be solved separately. First equation is non-homogeneous and the second one is homogeneous equation.

C.1.3.1. X-component particle trajectory

For the first equation, solution can be found as a sum of homogeneous and particular solution,

$$\bar{x} = \bar{x}_H + \bar{x}_P \quad (\text{C.10})$$

Homogeneous solution can be found in the form,

$$\bar{x}_H = C_1 e^{z_1 \bar{t}} + C_2 e^{z_2 \bar{t}} \quad (\text{C.11})$$

where parameters z_1 and z_2 are obtained as a solution of the characteristic equation,

$$2St \cdot z^2 + z + 2 = 0 \quad (\text{C.12})$$

$$z_{1,2} = \frac{-1 \pm \sqrt{1-16St}}{4St} \quad (\text{C.13})$$

a. *Conjugate complex roots* ($St > 1/16$)

If we write $z_1 = \alpha + \beta i$ and $z_2 = \alpha - \beta i$, where $\alpha = -\frac{1}{4St}$ and $\beta = \frac{\sqrt{1-16St}}{4St}$,

homogeneous part of the solution is,

$$\begin{aligned} \bar{x}_H &= C_1 e^{(\alpha+\beta i)\bar{t}} + C_2 e^{(\alpha-\beta i)\bar{t}} \\ &= C_1 e^{\alpha\bar{t}} e^{i\beta\bar{t}} + C_2 e^{\alpha\bar{t}} e^{-i\beta\bar{t}} \\ &= A_0 e^{i\beta\bar{t}} + A_1 e^{-i\beta\bar{t}} \end{aligned} \quad (\text{C.14})$$

Components $e^{i\beta\bar{t}}$ and $e^{-i\beta\bar{t}}$ provide a basis for the two-dimensional "solution space" of the second order differential equation, meaning that the linear combinations of these solutions will also be solutions. From the Euler's formula, we can get $\cos(\varphi) = \frac{e^{i\varphi} + e^{-i\varphi}}{2}$

and $\sin(\varphi) = \frac{e^{i\varphi} - e^{-i\varphi}}{2i}$, meaning that homogeneous solution can be also written in the form,

$$\bar{x}_H = C_1 e^{\alpha\bar{t}} \cos(\beta\bar{t}) + C_2 e^{\alpha\bar{t}} \sin(\beta\bar{t}) \quad (\text{C.15})$$

Particular solution is equal to some constant, $\bar{x}_P = w$, which after differentiation and use in the characteristic equation leads to,

$$2St \cdot 0 + 0 + 2w = p \frac{t_p g}{v_0} \quad (\text{C.16})$$

$$w = \frac{1}{2} p \frac{t_p g}{v_0} \Rightarrow \bar{x}_P = \frac{1}{2} p \frac{t_p g}{v_0} \quad (\text{C.17})$$

The solution is finally,

$$\bar{x} = \bar{x}_H + \bar{x}_P = C_1 e^{\alpha\bar{t}} \cos(\beta\bar{t}) + C_2 e^{\alpha\bar{t}} \sin(\beta\bar{t}) + \frac{1}{2} p \frac{t_p g}{v_0} \quad (\text{C.18})$$

Constants C_1 and C_2 can be determined from the initial conditions at $\bar{t} = 0$. From $\bar{x}(0) = \bar{x}_0$ we get,

$$C_1 = \bar{x}_0 - \frac{1}{2} p \frac{t_p g}{v_0} \quad (\text{C.19})$$

and from $\frac{d^2 \bar{x}}{d\bar{t}^2}(0) = 0$ (velocity of the particle is equal to the fluid velocity), we have,

$$\frac{d\bar{x}}{d\bar{t}} + 2\bar{x}_0 = p \frac{t_p g}{v_0} \quad (\text{C.20a})$$

$$\frac{d\bar{x}}{d\bar{t}} = -2\bar{x}_0 + p \frac{t_p g}{v_0} = C_1 \alpha + C_2 \beta \quad (\text{C.20b})$$

$$C_2 = \frac{-(2 + \alpha)(\bar{x}_0 - \frac{1}{2} p \frac{t_p g}{v_0})}{\beta} \quad (\text{C.20c})$$

After rearranging, the solution is finally,

$$\bar{x}(\bar{t}) = e^{\alpha \bar{t}} \left(\bar{x}_0 - \frac{1}{2} p \frac{t_p g}{v_0} \right) \left(\cos(\beta \bar{t}) - \frac{2 + \alpha}{\beta} \sin(\beta \bar{t}) \right) + \frac{1}{2} p \frac{t_p g}{v_0} \quad (\text{C.21})$$

b. Real roots ($St < 1/16$)

The solution is a sum of homogeneous and particular solution,

$$\bar{x} = C_1 e^{z_1 \bar{t}} + C_2 e^{z_2 \bar{t}} + \frac{1}{2} p \frac{t_p g}{v_0} \quad (\text{C.22})$$

From the initial conditions at $\bar{t} = 0$, $\bar{x}(0) = \bar{x}_0$ we have,

$$\bar{x}_0 = C_1 + C_2 + \frac{1}{2} p \frac{t_p g}{v_0} \quad (\text{C.23a})$$

$$C_2 = \bar{x}_0 - C_1 - \frac{1}{2} p \frac{t_p g}{v_0} \quad (\text{C.23b})$$

and from $\frac{d^2 \bar{x}}{dt^2}(0) = 0$,

$$\frac{d\bar{x}_0}{dt} = -2\bar{x}_0 + p \frac{t_p \mathcal{G}}{v_0} = z_1 C_1 e^{z_1 \bar{t}} + z_2 C_2 e^{z_2 \bar{t}} \quad (\text{C.24a})$$

$$C_1 = \left(\frac{z_2 + 2}{z_2 - z_1} \right) \left(x_0 - \frac{1}{2} p \frac{t_p \mathcal{G}}{v_0} \right) \quad (\text{C.24b})$$

The constant C_2 can be then calculated as,

$$C_2 = \left(\frac{z_1 + 2}{z_1 - z_2} \right) \left(x_0 - \frac{1}{2} p \frac{t_p \mathcal{G}}{v_0} \right) \quad (\text{C.25})$$

The solution is finally,

$$\bar{x}(\bar{t}) = \left(x_0 - \frac{1}{2} p \frac{t_p \mathcal{G}}{v_0} \right) \left(\left(\frac{z_2 + 2}{z_2 - z_1} \right) e^{z_1 \bar{t}} + \left(\frac{z_1 + 2}{z_1 - z_2} \right) e^{z_2 \bar{t}} \right) + \frac{1}{2} p \frac{t_p \mathcal{G}}{v_0} \quad (\text{C.26})$$

C.1.3.2. *r*-component particle trajectory

For the *r*-component, there is only a homogeneous solution,

$$\bar{r}_H = C_1 e^{z_1 \bar{t}} + C_2 e^{z_2 \bar{t}} \quad (\text{C.27})$$

Initial condition $\bar{r}(0) = \bar{r}_0$ at $\bar{t} = 0$ gives,

$$\bar{r}_0 = C_1 e^{z_1 \bar{t}} + C_2 e^{z_2 \bar{t}} \quad (\text{C.28a})$$

$$\bar{r}_0 = C_1 + C_2 \quad (\text{C.28b})$$

$$C_2 = \bar{r}_0 - C_1 \quad (\text{C.28c})$$

And from the second initial condition, $\frac{d\bar{r}}{dt}(0) = 0$,

$$0 = C_1 z_1 e^{z_1 \bar{t}} + C_2 z_2 e^{z_2 \bar{t}} \quad (\text{C.29a})$$

$$C_1 z_1 = -C_2 z_2 \quad (\text{C.29b})$$

$$C_1 = \bar{r}_0 \left(\frac{z_2}{z_2 - z_1} \right) \quad (\text{C.29c})$$

The constant C_2 is then,

$$C_2 = \bar{r}_0 \left(\frac{z_1}{z_1 - z_2} \right) \quad (\text{C.29d})$$

The solution is finally,

$$\bar{r}(\bar{t}) = \bar{r}_0 \left(\frac{z_2}{z_2 - z_1} \right) e^{z_1 \bar{t}} + \bar{r}_0 \left(\frac{z_1}{z_1 - z_2} \right) e^{z_2 \bar{t}} \quad (\text{C.30})$$

C.1.3.3. Capture efficiencies

a. No gravity ($p = 0$)

In the case of no gravity ($p = 0$), capture efficiencies can be determined analytically. The X-component solution simplifies to,

$$\bar{x}(\bar{t}) = \bar{x}_0 e^{\alpha \bar{t}} \left(\cos(\beta \bar{t}) - \frac{2 + \alpha}{\beta} \sin(\beta \bar{t}) \right) \quad (\text{C.31})$$

If we set $\bar{x}(\bar{t}) = 0$, we will have $\cos(\beta \bar{t}) = \frac{2 + \alpha}{\beta} \sin(\beta \bar{t})$. The time needed for particle to

reach the surface plane at $\bar{x} = 0$ is given by,

$$\bar{t}' = \frac{1}{\beta} a \tan \left(\frac{\beta \cdot 4St}{8St - 1} \right) \quad (\text{C.32})$$

At the time \bar{t}' , the \bar{r} component will be,

$$\bar{r}(\bar{t}') = \bar{r}_0 \left(\frac{z_2}{z_2 - z_1} \right) e^{z_1 \bar{t}'} + \bar{r}_0 \left(\frac{z_1}{z_1 - z_2} \right) e^{z_2 \bar{t}'} \quad (\text{C.33})$$

We are interested in particles for which at time \bar{t}' , $\bar{r} \leq 1$, which means they have reached the coupon surface,

$$1 = \bar{r}_0 \left(\frac{z_2}{z_2 - z_1} \right) e^{z_1 \bar{t}'} + \bar{r}_0 \left(\frac{z_1}{z_1 - z_2} \right) e^{z_2 \bar{t}'} \quad (\text{C.34})$$

$$\bar{r}_0 = \frac{z_2 - z_1}{z_2 e^{z_1 \bar{t}'} - z_1 e^{z_2 \bar{t}'}} \quad (\text{C.35})$$

All particles, with r_0 lower than the value defined by Eq. (C.35), will reach the coupon surface. Fraction of particles approaching, which finally impacts the coupon surface (capture efficiency) is then,

$$E = \bar{r}_0^{-2} = \left(\frac{z_2 - z_1}{z_2 e^{z_1 \bar{t}'} - z_1 e^{z_2 \bar{t}'}} \right)^2 \quad (\text{C.36})$$

This equation is equivalent to the equation reported by Ranz and Wong [26]. Figure C.2. explains the calculation of capture efficiencies in 3-D, from the results obtained using the 2-D axysymmetric model.

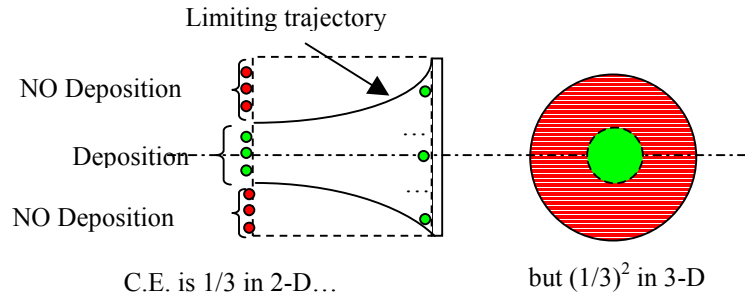


Figure C.2 Schematic representation of limiting droplet trajectories and the way that capture efficiencies for disk are obtained

b. With gravity ($p = 1, p = -1$)

When gravity is present, time needed for particles to reach the coupon surface plane at $\bar{x} = 0$ must be determined numerically, by solving the nonlinear equation for \bar{t} ,

$$\bar{x}(\bar{t}) = e^{\alpha \bar{t}} \left(\bar{x}_0 - \frac{1}{2} p \frac{t_p g}{v_0} \right) \left(\cos(\beta \bar{t}) - \frac{2 + \alpha}{\beta} \sin(\beta \bar{t}) \right) + \frac{1}{2} p \frac{t_p g}{v_0} = 0 \quad (\text{C.37})$$

Once the time \bar{t} is determined, capture efficiency can be calculated from the Eq. (C.36).

C.1.4. Capture efficiencies for non-Stokesian particles

Non-Stokesian drag force is better representation of the real drag force, especially for larger particles. In this case, differential equations are nonlinear, and particle trajectories must be obtained by numerical integration of the system of two, second order, nonlinear ordinary differential equations (C.38a,b),

$$x: \frac{2St}{k_D} \frac{d^2 \bar{x}}{dt^2} + \frac{d\bar{x}}{dt} - \bar{v}_x - \frac{1}{k_D} p \frac{t_p \mathcal{G}}{v_0} = 0 \quad (\text{C.38a})$$

$$r: \frac{2St}{k_D} \frac{d^2 \bar{r}}{dt^2} + \frac{d\bar{r}}{dt} - \bar{v}_r = 0 \quad (\text{C.38b})$$

where for the coefficient k_D , we use $k_D = \frac{C_D \text{Re}}{24} = 1 + \frac{1}{6} \text{Re}^{2/3} = 1 + \frac{1}{6} \left(\frac{D_p \rho_a (v-u)}{\mu_a} \right)^{2/3}$.

Detailed equations are then,

$$x: \frac{2St}{1 + \frac{1}{6} \left(\frac{D_p \rho_a}{\mu_a} \left(\frac{d\bar{x}}{dt} - \bar{v}_x \right) \right)^{2/3}} \frac{d^2 \bar{x}}{dt^2} + \frac{d\bar{x}}{dt} - \bar{v}_x - \frac{1}{1 + \frac{1}{6} \left(\frac{D_p \rho_a}{\mu_a} \left(\frac{d\bar{x}}{dt} - \bar{v}_x \right) \right)^{2/3}} p \frac{t_p \mathcal{G}}{v_0} = 0 \quad (\text{C.39a})$$

$$r: \frac{2St}{1 + \frac{1}{6} \left(\frac{D_p \rho_a}{\mu_a} \left(\frac{d\bar{r}}{dt} - \bar{v}_r \right) \right)^{2/3}} \frac{d^2 \bar{r}}{dt^2} + \frac{d\bar{r}}{dt} - \bar{v}_r = 0 \quad (\text{C.39.b})$$

After incorporating equations of the flow field (Eqs. (C.8a,b)), we get,

$$x: \frac{2St}{1 + \frac{1}{6} \left(\frac{D_p \rho_a}{\mu_a} \left(\frac{d\bar{x}}{dt} + 2\bar{x} \right) \right)^{2/3}} \frac{d^2 \bar{x}}{dt^2} + \frac{d\bar{x}}{dt} + 2\bar{x} - \frac{1}{1 + \frac{1}{6} \left(\frac{D_p \rho_a}{\mu_a} \left(\frac{d\bar{x}}{dt} + 2\bar{x} \right) \right)^{2/3}} p \frac{t_p \mathcal{G}}{v_0} = 0 \quad (\text{C.40a})$$

$$r: \frac{2St}{1 + \frac{1}{6} \left(\frac{D_p \rho_a}{\mu_a} \left(\frac{d\bar{r}}{dt} - \bar{r} \right) \right)^{2/3}} \frac{d^2 \bar{r}}{dt^2} + \frac{d\bar{r}}{dt} - \bar{r} = 0 \quad (\text{C.40b})$$

This system can be transformed into the system of 4 ODE's,

$$\begin{aligned}
 \bar{x} &= \bar{x}_0 \\
 \frac{d\bar{x}_0}{d\bar{t}} &= \bar{x}_1 \\
 \frac{d^2\bar{x}_0}{d\bar{t}^2} &= \frac{d\bar{x}_1}{d\bar{t}} = \frac{k_{D,x}}{2St} \left(-\bar{x}_1 - 2\bar{x}_0 + \frac{1}{k_x} p \frac{t_p g}{v_0} \right) = \frac{k_{D,x}}{2St} (-\bar{x}_1 - 2\bar{x}_0) + \frac{1}{2St} p \frac{t_p g}{v_0} \quad (C.41) \\
 \bar{r} &= \bar{x}_2 \\
 \frac{d\bar{x}_2}{d\bar{t}} &= \bar{x}_3 \\
 \frac{d^2\bar{x}_2}{d\bar{t}^2} &= \frac{d\bar{x}_3}{d\bar{t}} = \frac{k_{D,r}}{2St} (-\bar{x}_3 + \bar{x}_2)
 \end{aligned}$$

where,

$$k_{D,x} = 1 + \frac{1}{6} \left(\frac{D_p \rho_a}{\mu_a} \left(\frac{d\bar{x}}{d\bar{t}} + 2\bar{x} \right) \right)^{2/3}, \text{ and } k_{D,r} = 1 + \frac{1}{6} \left(\frac{D_p \rho_a}{\mu_a} \left(\frac{d\bar{r}}{d\bar{t}} - \bar{r} \right) \right)^{2/3}. \text{ Initial conditions}$$

are,

$$\begin{aligned}
 \bar{x}_0 &= \bar{x}_0 \\
 \bar{x}_1 &= -2\bar{x}_0 + \frac{1}{|k_{D,x}|} p \frac{t_p g}{v_0} \\
 \bar{x}_2 &= \bar{r}_0 \\
 \bar{x}_3 &= 0
 \end{aligned} \quad (C.42)$$

To calculate capture efficiencies for this case, trajectories of 100 particles, positioned at a distance $\bar{x} = -0.5$, and $\bar{r} = 0, 0.01, 0.02, \dots, 1$ were calculated. A particle was counted as deposited if at the time when it reached $\bar{x} = 0$, its radial position was $\bar{r} \leq 1$, meaning that it did not go around the disk. Number of deposited particles was then divided by the total number of particles (one hundred) and squared to yield the capture efficiency (see Fig. C.2). This procedure in the form of *pseudocode* is given below, while its implementation in the Mathcad Professional 2001 software is given in *Appendix D*.

```

-----
%Integrates system of differential equations from time t=0 to t=tmax, from the position
%(x0,r0), for particle diameter Dp and fluid velocity V0. Orientation of gravity is
%determined by parameter p.
function xr(tmax,Dp,V0,x0,r0,p)
    Integrate ODE system with the given initial condition, from t=0 to t=tmax
    (function 'Rkadapt' in Mathcad, Runge-Kutta method of 4th order)
    Return x,r coordinates of the last point at t=tmax
end
-----
%Solves nonlinear equation and returns time at which x = 0
function time(t0,Dp,V0,x0,r0,p)
    Solve nonlinear equation xr(t,Dp,V0,x0,r0,p)1 = 0 for t, with the initial guess
    t=t0 (Solve block in Mathcad, Levenberg-Marquardt method).
    Return obtained time, t
end
-----
%Calculates capture efficiency by simulating particle trajectories of 100 particles
%injected at equidistant points, starting from (x,r) = (-1,0) to (x,r) = (-1,1).
function efficiency (Dp,V0,x0,r0,p)
    Guess the time needed for particle to reach the coupon surface (t0 = 1)
    Calculate the time needed for particle to reach x = 0 (call function 'time') and
    assign the result to tmax
    for i = 1 to 100
        Integrate ODE system (call function 'xr', with obtained tmax)
        Assign the obtained result to xfinal and rfinal
        if (rfinal<1) and (xfinal>0.0001)
            Increase number of particles that reached the coupon surface
            n = n + 1
        end
        Calculate the efficiency: Efficiency = (n/100)^2
    end
end
-----

```

C.1.5. Distribution of deposits along the coupon radius

If we use time needed for particle to reach the coupon surface from Eq. (C.32) and substitute it into Eq. (C.30), we get,

$$\bar{r}(\bar{t}') = \bar{r}_0 \left(\frac{z_2}{z_2 - z_1} \right) e^{z_1 \bar{t}'} + \bar{r}_0 \left(\frac{z_1}{z_1 - z_2} \right) e^{z_2 \bar{t}'} \quad (\text{C.43})$$

This value is constant for a given droplet size and velocity. It can be restated as,

$$\bar{r}(\bar{r}_0) = \bar{r}_0 \left(\frac{z_2}{z_2 - z_1} \right) e^{z_1 \bar{t}'} + \bar{r}_0 \left(\frac{z_1}{z_1 - z_2} \right) e^{z_2 \bar{t}'} = \text{const} \cdot \bar{r}_0 \quad (\text{C.44})$$

This equation states that the final position of the particle on the disk is linear function of its initial radial position where the particle is injected. This leads to the conclusion that, according to this model, deposits should be uniformly distributed along the coupon radius.

C.2. Drop diameter on a surface

In each case when the contact angle of droplet sitting on a solid surface is less than 180° (which means always), the measured droplet diameter is larger than the diameter of the same droplet before deposition. If the spherical cap is assumed, and the contact angle of droplets on the surface is known, real droplet diameter can be calculated. Geometry of the drop on a surface is schematically shown in Fig. C.3.

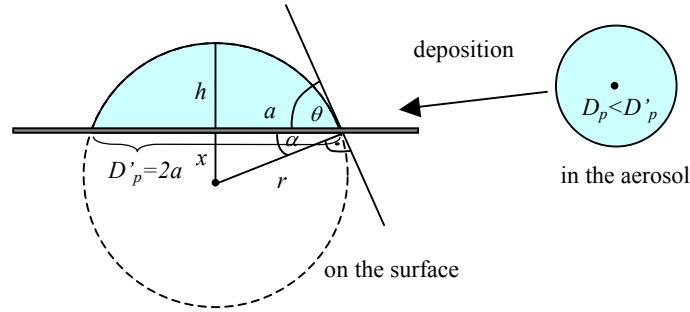


Figure C.3 Spherical cap model for droplets deposited on the coupon surface

Volume of the spherical cap, V , is given by,

$$V = \frac{\pi}{6} \cdot (3 \cdot a^2 + h^2) \cdot h, \quad (\text{C.45})$$

and from the figure we can see that,

$$h = r - x = r - r \cdot \sin(90 - \theta), \quad (\text{C.46})$$

which is equivalent to,

$$h = r - r \cdot \cos(\theta) = r \cdot (1 - \cos(\theta)). \quad (\text{C.47})$$

Also it can be noted that,

$$a = r \cdot \cos(90 - \theta) = r \cdot \sin(\theta). \quad (\text{C.48})$$

This gives,

$$h = \frac{D_p'}{2} \cdot \frac{1 - \cos(\theta)}{\sin(\theta)} \quad (\text{C.49})$$

which by the use of half-angle identities, can be presented as, $h = \frac{D_p'}{2} \cdot \tan\left(\frac{\theta}{2}\right)$. After

incorporating this into the equation for the volume we get,

$$V = \frac{D_p'^3 \pi}{48} \cdot \left(3 \cdot \tan\left(\frac{\theta}{2}\right) + \left(\tan\left(\frac{\theta}{2}\right) \right)^3 \right) \quad (\text{C.50})$$

If we equate this expression with the expression for the volume of the spherical droplet

$V = \frac{D_p^3 \pi}{6}$, we arrive to the following expression for the droplet diameter,

$$D_p = D_p' \cdot \underbrace{\left(\frac{1}{2} \sqrt[3]{3 \tan\left(\frac{\theta}{2}\right) + \left(\tan\left(\frac{\theta}{2}\right) \right)^3} \right)}_{k(\theta)}. \quad (\text{C.51})$$

This equation was used in the Matlab codes *shadow.m* and *coupon.m* (Appendix D). Some correction factors $k(\theta)$, for several contact angles θ , are given in Table C.1. In this work, droplets of tri-ethylene glycol on the glass or acrylic plate with contact angles 20° and 43° were observed.

Table C.1 Correction factor for different contact angles

Angle, θ ($^\circ$)	20	40	60	90
$k(\theta)$	0.406	0.522	0.622	0.794

Appendix D. Software codes

D.1. Image Pro Plus macros

Macros written in the Image Pro Plus software were used for automatization of the image analysis process. If the image analysis process was not programmed, analysis of shadowgraphy images would be a tedious and practically impossible task.

Macro procedure *'coupon'* analyzes images of coupon deposits; it opens sequences of 120 images recorded along the coupon radius and extracts every fourth image. It flattens images, loads Image Pro Plus environment settings and histogram ranges for the image segmentation and performs analysis. It measures object area, maximum, minimum and median diameter, and writes results into files. Macro procedure *'shadowgraphy'* analyzes shadowgraphy images of droplets in the aerosol; opens sequences of 130 images and performs analysis. It measures and reports the same variables as the macro procedure *'coupon'*.

The structure of the input and output files are described inside the code and should be strictly followed. Parameters regarding the number of runs to be processed automatically, and the number of samples that are supplied, should be changed in the code, accordingly.

coupon

```
'Analyzes images of coupon deposits. Opens image sequence of 120 images along the coupon
'radius and takes every fourth image from it. Flattens image, loads environment settings
'and histogram ranges and performs analysis. Measures Area, Dmax, Dmin, and Dmean and
'writes results into files.
```

```
Sub coupon()
```

```
'Input: For each run provide 4 image sequences with 120 images each, for upstream and
'downstream side both. Files should be named as 1-u-1.tif, 1-u-2.tif, ... 1-d-1.tif, ...,
'1-d-4.tif where the first letter is the run number, second denotes upstream or
'downstream side, and the third letter represents the sample number (1-4).
```

```
'Output: 1)30 files for each image (window) along the coupon radius (e.g. 1-u-1-1.txt,
'... 1-u-1-30.txt), 2) 1 file for each sample-image sequence (e.g. 1-u-1.txt), 3) 1 file
'for all 4 samples on the upstream and downstream surface (e.g. 1-u.txt, 1-d.txt)
```

```
'Parameters: 'r1' and 'r2' are first and last run number, and 'samples' is the number of
'samples
```

```
'Declaration of variables and definition of constants'
Const N = 120 'adjust to the number of images in the frame sequence'
Dim i, j, k, m, r1, r2, samples As Integer
Dim side As String
```

```
'first and the last run number'
r1 = 1
r2 = 10
'number of samples of image sequences on the coupon side'
samples = 4

For i = r1 To r2

    For m = 1 To 2
        If m = 1 Then
            side = "u"
        Else
            side = "d"
        End If

        For j = 1 To samples

            For k = 1 To N
                'Opening the sequence'
                ret = IpSeqOpen("C:\My Documents\WORK\images\" +
Right$(Str(i), Len(Str(i))-1) + "-" + side + "-" + Right$(Str(j), Len(Str(j))-1) +
".tif", "tif", (k-1)*4, 1)

                'Image processing'
                ret = IpFltFlatten(0, 15)
                ret = IpFltFlatten(0, 15)

                'Loading environment settings and histogram ranges'
                If side = "u" Then
                    ret = IpBlbLoadSetting("C:\My Documents\WORK\coupon-
settings\environmentsettings-convexhull.env")
                Else
                    ret = IpBlbLoadSetting("C:\My Documents\WORK\coupon-
settings\environmentsettings.env")
                End If
                ret = IpSegLoad("C:\My Documents\WORK\coupon-
settings\colorsettingsR(255)G(200)B(255).rge")

                'Counting'
                ret = IpBlbCount()
                ret = IpBlbUpdate(0)

                'Writing data to a file'
                ret = IpBlbSaveData("C:\My Documents\WORK\coupon-results\"
+ Right$(Str(i), Len(Str(i))-1) + "-" + side + "-" + Right$(Str(j), Len(Str(j))-1) + "-"
+ Right$(Str(k), Len(Str(k))-1) + ".txt", S_DATA)
                ret = IpBlbSaveData("C:\My Documents\WORK\coupon-results\"
+ Right$(Str(i), Len(Str(i))-1) + "-" + side + "-" + Right$(Str(j), Len(Str(j))-1) +
".txt" , S_APPEND)
                ret = IpBlbSaveData("C:\My Documents\WORK\coupon-results\"
+ Right$(Str(i), Len(Str(i))-1) + "-" + side + ".txt" , S_APPEND)

                'Close the image from the sequence'
                ret = IpDocClose()
            Next k
        Next j
    Next m
Next i
End Sub
```

shadowgraphy

```
'Analyzes shadowgraphy images of droplets in the aerosol or on the coupon. Opens image
'sequence of 130 images, flattens images, loads environment settings and histogram ranges
'and performs analysis. Measures Area, Dmax, Dmin, and Dmean and writes results into
'files.
```

```
Sub shadowgraphy()
```

```
'Input: For each run provide 10 samples (image sequences) with 130 images each. Files
'should be named as 1-1.tif, 1-2.tif...1-10.tif where the first is the run number and
'the second is the sample number

'Output: 1) 5 files with results of 2 adjacent samples joined into one new sample (e.g.
` 1-1.txt,...,1-5.txt) and 2) 1 file of all samples joined together (e.g. 1.txt)

'Parameters: change 'r1' and 'r2' for first and last run number, and 'samples' to the
'number of samples

'Declaration of variables and constant definition'
Const N = 130 'adjust to the current number of pictures in the frame sequence - 1'
Dim i, j, k, s, r1, r2, samples As Integer

'first and last run number'
r1 = 1
r2 = 10
'number of samples (of image sequences) in the aerosol'
samples = 10

For i = r1 To r2 Step 1
    For j = 1 To samples
        'Choosing folder name for the each sample'
        If (j=1) Or (j=2) Then
            s=1
        ElseIf (j=3) Or (j=4) Then
            s=2
        ElseIf (j=5) Or (j=6) Then
            s=3
        ElseIf (j=7) Or (j=8) Then
            s=4
        ElseIf (j=9) Or (j=10) Then
            s=5
        End If

        For k = 0 To N-1
            'Opening the sequence'
            ret = IpSeqOpen("C:\My Documents\WORK\images\" + Right$(Str(i),
Len(Str(i))-1) + "-" + Right$(Str(j), Len(Str(j))-1) + ".tif", "tif", k, 1)

            'Image processing'
            ret = IpFltFlatten(0, 15)
            ret = IpFltFlatten(0, 15)

            'Loading environment settings and histogram ranges'
            ret = IpBlbLoadSetting("C:\My Documents\WORK\shadow-
settings\environmentsettings.env")
            ret = IpSegLoad("C:\My Documents\WORK\shadow-
settings\colorsettingsR(255)G(200)B(255).rge")

            'Counting'
            ret = IpBlbCount()
            ret = IpBlbUpdate(0)

            'Writting data to a file'
            ret = IpBlbSaveData("C:\My Documents\WORK\shadow-results\" +
Right$(Str(i), Len(Str(i))-1) + "-" +Right$(Str(s), Len(Str(s))-1) + ".txt", S_APPEND)
            ret = IpBlbSaveData("C:\My Documents\WORK\shadow-results\" +
Right$(Str(i), Len(Str(i))-1) + ".txt" , S_APPEND)

            'Close image from the image sequence'
            ret = IpDocClose()
        Next k
    Next j
Next i
End Sub
```

D.2. MATLAB[®] codes

To analyze results on the size of individual droplets reported by Image Pro Plus, script files in the MATLAB[®] software were programmed.

Script file '*shadow.m*' generates size distribution from the data reported by Image Pro Plus. Firstly, it recalculates drop size from pixels into microns and computes size distribution based on the specified number of classes or class width. Then, it applies border and depth of field correction and deals with the outliers. It performs curve fitting with the log-normal distribution function ('*fdist.m*'). Finally, it reports the main results on the screen and plots results for relative and cumulative frequencies of the distribution curve. All results are then written into files. This script is used for analysis of drop size distribution in the aerosol and on the coupon (it covers fitting modal and bimodal size distribution for the upstream side).

Script file '*coupon.m*' processes data on the individual droplet sizes of coupon deposits and generates size distribution. It calculates minimum, maximum and median diameter, number of droplets, mass fraction and surface coverage along the coupon radius, for both upstream and downstream side. It displays results on the screen and writes results into files.

Script file '*eff.m*' is used to calculate deposition coefficients of individual drop sizes at given velocity (Section 5.3). All other scripts (functions) used, '*eff.m*', '*f2normlognormalcdf.m*', '*f2normlognormalpdf.m*', '*fcdf.m*', '*fdist.m*', '*fdmean.m*', '*flognormalcdf.m*', '*flognormalpdf.m*' and '*fpdf.m*', are called from these three main scripts.

coupon.m

```
%Calculates: Dmin, Dmax, Dv50, Number of droplets, Mass fraction and Surface coverage
%along the coupon radius, for both upstream and downstream side. Displays results on the
%screen and plots the figures, then writes results into files.
```

%%INPUT SECTION

```
%Input the run number only (e.g. 1). Program automatically goes through all downstream
%and upstream files (e.g. 1-u-1-1.txt, 1-u-1-2.txt...1-d-1-1.txt etc.)
%Files must be provided by Image Pro Plus and placed in the directory defined by datapath
%File naming e.g.: 1-d-2-3.txt (1-run number, d-downstream side ('d' or 'u'), 2-sample
%number (1-4), window number (1-30)).
```

```
clear all;
```

```
sample = input ('1.Sample number: ','s');
magnification = input ('2.Magnifications used [upstream, downstream]: ');
```

```

choice = input('3.Size distribution of: (1)Dmax, (2)Dmin, (3)Dmean: ');
nwchoice = input('3.Define: (1)Number of Classes, (2)Class Width: ');
if nwchoice == 1
    nclasses = input('3a.Number of classes: ');
    nw0 = [nclasses; 0]; %set zero where not defined
else
    cwidth = input('3b.Class width(um): ');
    nw0 = [0; cwidth]; %set zero where not defined
end
outlier = input('4.Remove outliers larger than (default is 100 um):');
if isempty(outlier)
    outlier = 100;
end
diam = 2*0.0254; %coupon diameter

N = 30; %number of images in the sample sequence
datapath = 'C:\Documents\WORK\coupon-results\';

%calculate no. of microns per pixel (from the calibration data)
teta = 20; %TEG on glass, 20 deg contact angle
k1 = (3*tan((teta/2)*(2*pi/360)) + tan((teta/2)*(2*pi/360))^3)^(1/3)/2;%correction due to
the contact angle
k2 = 1/(0.2173*magnification - 0.0030); %microns per pixel
k12 = k1*k2;
W = k2 * 1392;
H = k2 * 1040;

%% HERE START LOADING ALL FILES OBTAINED WITH IMAGE PRO PLUS
samplename = sample;
column = 1;
%i walks through upstream and downstream
for i = ['u','d']
    %j walks through 4 samples and samples 5 containing all samples joined together
    for j = ['1', '2', '3', '4', '5']
        %k walks through all N images (windows)
        k = 1;
        samplename = strcat(sample, '-', i, '-', j, '-', num2str(k), '.txt');
        while (exist(samplename, 'file')==2)

            data = load(strcat(datapath, samplename));
            %pick appropriate column for diameter
            if i == 'u'
                x = k12(1)*data(:, choice + 1);
            else
                x = k12(2)*data(:, choice + 1);
            end

            %% CALCULATION OF THE DISTRIBUTION AND POSTPROCESSING OF THE RESULTS
            %calculate the distribution and remove outliers
            [dcmax, dcmed, nw, d, vol] = fdist(x, nw0);
            Dv50 = fdmean(0.5, dcmax, fcdf(vol/sum(vol)));
            for t = 1:max(size(x))
                if x(t) > outlier
                    x(t) = 1;
                end
            end
            [dcmax, dcmed, nw, d, vol] = fdist(x, nw0);
            vpdf = vol/sum(vol);
            if i=='u'
                surfacecoverage = sum((x/k1).^2*pi/4)/(W(1)*H(1));
            else
                surfacecoverage = sum((x/k1).^2*pi/4)/(W(2)*H(2));
            end

            %% CALCULATING CHARACTERISTIC DIAMETERS
            Dmin = min(x);
            Dmax = max(x);
            Dv50 = fdmean(0.5, dcmax, vcdf);

            %write data into matrix

```

```

        results(k, (column-1)*6+1 : (column)*6) = [Dmin, Dv50, Dmax, sum(d),
sum(vol)*10^-9, surfacecoverage];

        %increase image number and update sample name
        k = k + 1;
        samplename = strcat(sample, '-', i, '-', j, '-', num2str(k), '.txt');
    end
    column = column + 1;
end
end
window = (1:N)';
results = [window , results];
%average values of all 4 samples
%upstream
results(:,26) = (results(:,2) + results(:,8) + results(:,14) + results(:,20))/4;
results(:,27) = (results(:,3) + results(:,9) + results(:,15) + results(:,21))/4;
results(:,28) = (results(:,4) + results(:,10) + results(:,16) + results(:,22))/4;
results(:,29) = (results(:,5) + results(:,11) + results(:,17) + results(:,23))/4;
results(:,30) = (results(:,6) + results(:,12) + results(:,18) + results(:,24))/4;
results(:,31) = (results(:,7) + results(:,13) + results(:,19) + results(:,25))/4;

t = size(results);
if t(1,2)>31
%downstream
results(:,56) = (results(:,32) + results(:,38) + results(:,44) + results(:,50))/4;
results(:,57) = (results(:,33) + results(:,39) + results(:,45) + results(:,51))/4;
results(:,58) = (results(:,34) + results(:,40) + results(:,46) + results(:,52))/4;
results(:,59) = (results(:,35) + results(:,41) + results(:,47) + results(:,53))/4;
results(:,60) = (results(:,36) + results(:,42) + results(:,48) + results(:,54))/4;
results(:,61) = (results(:,37) + results(:,43) + results(:,49) + results(:,55))/4;
end

%results are in the form:
%[window#, Dmin-upstreamsample1, Dv50-upstreamsample1, Dmax-upstreamsample1, n-
upstreamsample1,
%vol-upstreamsample1, surfacecoverage-upstreamsample1, and continues for ...
%...us2, us3, us4, uALL, ds1, ds2, ds3, ds4, dALL]

%% WRITTING RESULTS INTO FILES
A = {'Window#', 'Dmin-u1', 'Dv50-u1', 'Dmax-u1', 'N%-u1', 'V%-u1', 'Area%-u1',...
'Dmin-u2', 'Dv50-u2', 'Dmax-u2', 'N%-u2', 'V%-u2', 'Area%-u2',...
'Dmin-u3', 'Dv50-u3', 'Dmax-u3', 'N%-u3', 'V%-u3', 'Area%-u3',...
'Dmin-u4', 'Dv50-u4', 'Dmax-u4', 'N%-u4', 'V%-u4', 'Area%-u4',...
'Dmin-uALL', 'Dv50-uALL', 'Dmax-uALL', 'N%-uALL', 'V%-uALL', 'Area%-uALL',...
'Dmin-d1', 'Dv50-d1', 'Dmax-d1', 'N%-d1', 'V%-d1', 'Area%-d1',...
'Dmin-d2', 'Dv50-d2', 'Dmax-d2', 'N%-d2', 'V%-d2', 'Area%-d2',...
'Dmin-d3', 'Dv50-d3', 'Dmax-d3', 'N%-d3', 'V%-d3', 'Area%-d3',...
'Dmin-d4', 'Dv50-d4', 'Dmax-d4', 'N%-d4', 'V%-d4', 'Area%-d4',...
'Dmin-dALL', 'Dv50-dALL', 'Dmax-dALL', 'N%-dALL', 'V%-dALL', 'Area%-dALL'};
xlswrite(strcat(datapath, sample, '-distribution','.xls'), A);
xlswrite(strcat(datapath, sample, '-distribution','.xls'), results, 'Sheet1', 'A2');

%% PLOT RESULTS
%UPSTREAM SIDE
h1 = figure(1);

%Dmin
subplot(2,3,1)
plot(1000*(diam/2)*(window/max(window)), results(:,2) , 'ro', 'MarkerSize', 5); hold on;
plot(1000*(diam/2)*(window/max(window)), results(:,8) , 'bs', 'MarkerSize', 5);
plot(1000*(diam/2)*(window/max(window)), results(:,14) , 'gd', 'MarkerSize', 5);
plot(1000*(diam/2)*(window/max(window)), results(:,20) , 'm^', 'MarkerSize', 5);
plot(1000*(diam/2)*(window/max(window)), results(:,26) , 'kx-', 'LineWidth', 1.5 ,
'MarkerSize', 5); hold off;
%setting the axis properties
xlim([0, 25.4]);
title('Dmin, upstream');
xlabel('Distance (mm)');
ylabel('Dmin (microns)');
%legend ('sample 1', 'sample 2', 'sample 3', 'sample4');

```

```

%Dv50
subplot(2,3,2)
plot(1000*(diam/2)*(window/max(window)), results(:,3) , 'ro', 'MarkerSize', 5); hold on;
plot(1000*(diam/2)*(window/max(window)), results(:,9) , 'bs', 'MarkerSize', 5);
plot(1000*(diam/2)*(window/max(window)), results(:,15) , 'gd', 'MarkerSize', 5);
plot(1000*(diam/2)*(window/max(window)), results(:,21) , 'm^', 'MarkerSize', 5);
plot(1000*(diam/2)*(window/max(window)), results(:,27) , 'kx-', 'LineWidth', 1.5,
'MarkerSize', 5); hold off;
%setting the axis properties
xlim([0, 25.4]);
title('Dv50, upstream');
xlabel('Distance (mm)');
ylabel('Dv50 (microns)');
%legend ('sample 1', 'sample 2', 'sample 3', 'sample4');

%Dmax
subplot(2,3,3)
plot(1000*(diam/2)*(window/max(window)), results(:,4) , 'ro', 'MarkerSize', 5); hold on;
plot(1000*(diam/2)*(window/max(window)), results(:,10) , 'bs', 'MarkerSize', 5);
plot(1000*(diam/2)*(window/max(window)), results(:,16) , 'gd', 'MarkerSize', 5);
plot(1000*(diam/2)*(window/max(window)), results(:,22) , 'm^', 'MarkerSize', 5);
plot(1000*(diam/2)*(window/max(window)), results(:,28) , 'kx-', 'LineWidth', 1.5,
'MarkerSize', 5); hold off;
%setting the axis properties
xlim([0, 25.4]);
title('Dmax, upstream');
xlabel('Distance (mm)');
ylabel('Dmax (microns)');
%legend ('sample 1', 'sample 2', 'sample 3', 'sample4');

%Number of Droplets
subplot(2,3,4)
plot(1000*(diam/2)*(window/max(window)), results(:,5) , 'ro', 'MarkerSize', 5); hold on;
plot(1000*(diam/2)*(window/max(window)), results(:,11) , 'bs', 'MarkerSize', 5);
plot(1000*(diam/2)*(window/max(window)), results(:,17) , 'gd', 'MarkerSize', 5);
plot(1000*(diam/2)*(window/max(window)), results(:,23) , 'm^', 'MarkerSize', 5);
plot(1000*(diam/2)*(window/max(window)), results(:,29) , 'kx-', 'LineWidth', 1.5,
'MarkerSize', 5); hold off;
%setting the axis properties
xlim([0, 25.4]);
title('Number of droplets, upstream');
xlabel('Distance (mm)');
ylabel('Number of droplets');
%legend ('sample 1', 'sample 2', 'sample 3', 'sample4');

%Mass Distribution
subplot(2,3,5)
plot(1000*(diam/2)*(window/max(window)), results(:,6)/sum(results(:,6)) , 'ro',
'MarkerSize', 5); hold on;
plot(1000*(diam/2)*(window/max(window)), results(:,12)/sum(results(:,12)) , 'bs',
'MarkerSize', 5);
plot(1000*(diam/2)*(window/max(window)), results(:,18)/sum(results(:,18)) , 'gd',
'MarkerSize', 5);
plot(1000*(diam/2)*(window/max(window)), results(:,24)/sum(results(:,24)) , 'm^',
'MarkerSize', 5);
plot(1000*(diam/2)*(window/max(window)), results(:,30)/sum(results(:,30)) , 'kx-',
'LineWidth', 1.5, 'MarkerSize', 5); hold off;
%setting the axis properties
xlim([0, 25.4]);
title('Mass fraction, upstream');
xlabel('Distance (mm)');
ylabel('Mass fraction');
%legend ('sample 1', 'sample 2', 'sample 3', 'sample4');

%Surface Coverage
subplot(2,3,6)
plot(1000*(diam/2)*(window/max(window)), results(:,7) , 'ro', 'MarkerSize', 5); hold on;
plot(1000*(diam/2)*(window/max(window)), results(:,13) , 'bs', 'MarkerSize', 5);
plot(1000*(diam/2)*(window/max(window)), results(:,19) , 'gd', 'MarkerSize', 5);
plot(1000*(diam/2)*(window/max(window)), results(:,25) , 'm^', 'MarkerSize', 5);

```

```

plot(1000*(diam/2)*(window/max(window)), results(:,31) , 'kx-', 'LineWidth', 1.5,
'MarkerSize', 5); hold off;
%setting the axis properties
xlim([0, 25.4]);
title('Surface coverage, upstream');
xlabel('Distance (mm)');
ylabel('Surface coverage');
%legend ('sample 1', 'sample 2', 'sample 3', 'sample4');

%position it right
left = 10; bottom = 10; width = 1000; height = 750;
set(h1, 'Position', [left, bottom, width, height]);

%write figure(1) in the file
saveas(h1, strcat(datapath, sample, '-upstream', '.bmp'));

%=====
%DOWNSTREAM SIDE
t = size(results);

if t(1,2)>31

h2 = figure(2);

%Dmin
subplot(2,3,1)
plot(1000*(diam/2)*(window/max(window)), results(:,32) , 'ro', 'MarkerSize', 5); hold on;
plot(1000*(diam/2)*(window/max(window)), results(:,38) , 'bs', 'MarkerSize', 5);
plot(1000*(diam/2)*(window/max(window)), results(:,44) , 'gd', 'MarkerSize', 5);
plot(1000*(diam/2)*(window/max(window)), results(:,50) , 'm^', 'MarkerSize', 5);
plot(1000*(diam/2)*(window/max(window)), results(:,56) , 'kx-', 'LineWidth', 1.5,
'MarkerSize', 5); hold off;

%setting the axis properties
xlim([0, 25.4]);
title('Dmin, downstream');
xlabel('Distance (mm)');
ylabel('Dmin (microns)');
%legend ('sample 1', 'sample 2', 'sample 3', 'sample4');

%Dv50
subplot(2,3,2)
plot(1000*(diam/2)*(window/max(window)), results(:,33) , 'ro', 'MarkerFaceColor', 'r',
'MarkerSize', 5); hold on;
plot(1000*(diam/2)*(window/max(window)), results(:,39) , 'bs', 'MarkerFaceColor', 'b',
'MarkerSize', 5);
plot(1000*(diam/2)*(window/max(window)), results(:,45) , 'gd', 'MarkerFaceColor', 'g',
'MarkerSize', 5);
plot(1000*(diam/2)*(window/max(window)), results(:,51) , 'm^', 'MarkerFaceColor', 'y',
'MarkerSize', 5);
plot(1000*(diam/2)*(window/max(window)), results(:,57) , 'kx-', 'LineWidth', 1.5,
'MarkerSize', 5); hold off;

%setting the axis properties
xlim([0, 25.4]);
title('Dv50, downstream');
xlabel('Distance (mm)');
ylabel('Dv50 (microns)');
%legend ('sample 1', 'sample 2', 'sample 3', 'sample4');

%Dmax
subplot(2,3,3)
plot(1000*(diam/2)*(window/max(window)), results(:,34) , 'ro', 'MarkerSize', 5); hold on;
plot(1000*(diam/2)*(window/max(window)), results(:,40) , 'bs', 'MarkerSize', 5);
plot(1000*(diam/2)*(window/max(window)), results(:,46) , 'gd', 'MarkerSize', 5);
plot(1000*(diam/2)*(window/max(window)), results(:,52) , 'm^', 'MarkerSize', 5);
plot(1000*(diam/2)*(window/max(window)), results(:,58) , 'kx-', 'LineWidth', 1.5,
'MarkerSize', 5); hold off;

%setting the axis properties
xlim([0, 25.4]);

```

```

title('Dmax, downstream');
xlabel('Distance (mm)');
ylabel('Dmax (microns)');
%legend ('sample 1', 'sample 2', 'sample 3', 'sample4');

%Number of droplets
subplot(2,3,4)
plot(1000*(diam/2)*(window/max(window)), results(:,35) , 'ro', 'MarkerSize', 5); hold on;
plot(1000*(diam/2)*(window/max(window)), results(:,41) , 'bs', 'MarkerSize', 5);
plot(1000*(diam/2)*(window/max(window)), results(:,47) , 'gd', 'MarkerSize', 5);
plot(1000*(diam/2)*(window/max(window)), results(:,53) , 'm^', 'MarkerSize', 5);
plot(1000*(diam/2)*(window/max(window)), results(:,59) , 'kx-', 'LineWidth', 1.5,
'MarkerSize', 5); hold off;

%setting the axis properties
xlim([0, 25.4]);
title('Number of droplets, downstream');
xlabel('Distance (mm)');
ylabel('Number of droplets');
%legend ('sample 1', 'sample 2', 'sample 3', 'sample4');

%Mass Distribution
subplot(2,3,5)
plot(1000*(diam/2)*(window/max(window)), results(:,36)/sum(results(:,36)) , 'ro',
'MarkerFaceColor', 'r', 'MarkerSize', 5); hold on;
plot(1000*(diam/2)*(window/max(window)), results(:,42)/sum(results(:,42)) , 'bs',
'MarkerFaceColor', 'b', 'MarkerSize', 5);
plot(1000*(diam/2)*(window/max(window)), results(:,48)/sum(results(:,48)) , 'gd',
'MarkerFaceColor', 'g', 'MarkerSize', 5);
plot(1000*(diam/2)*(window/max(window)), results(:,54)/sum(results(:,54)) , 'm^',
'MarkerFaceColor', 'y', 'MarkerSize', 5);
plot(1000*(diam/2)*(window/max(window)), results(:,60)/sum(results(:,60)) , 'kx-',
'LineWidth', 1.5, 'MarkerSize', 5); hold off;

%setting the axis properties
xlim([0, 25.4]);
title('Mass fraction, downstream');
xlabel('Distance (mm)');
ylabel('Mass fraction');
%legend ('sample 1', 'sample 2', 'sample 3', 'sample4');

%Surface coverage
subplot(2,3,6)
plot(1000*(diam/2)*(window/max(window)), results(:,37) , 'ro', 'MarkerSize', 5); hold on;
plot(1000*(diam/2)*(window/max(window)), results(:,43) , 'bs', 'MarkerSize', 5);
plot(1000*(diam/2)*(window/max(window)), results(:,49) , 'gd', 'MarkerSize', 5);
plot(1000*(diam/2)*(window/max(window)), results(:,55) , 'm^', 'MarkerSize', 5);
plot(1000*(diam/2)*(window/max(window)), results(:,61) , 'kx-', 'LineWidth', 1.5,
'MarkerSize', 5); hold off;

%setting the axis properties
title('Surface coverage, downstream');
xlabel('Distance (mm)');
ylabel('Surface coverage');
%legend ('sample 1', 'sample 2', 'sample 3', 'sample4');

%position it right
left = 10; bottom = 10; width = 1000; height = 750;
set(h2, 'Position', [left, bottom, width, height]);

%write figure(2) in the file
saveas(h2, strcat(datapath, sample, '-downstream' ,'.bmp'));
end

```

eff.m

```

%Calculates k-values and capture efficiencies for each droplet size, based on the size
%distribution results in the aerosol and on the coupon

```

```

%% INPUT SECTION

```

```

%Input: run number, velocity(m/s), droplet flow(g/min), and upstream and downstream
%deposition rates(mg/hr). Supply aerosol and coupon distribution data in
%the directory specified by datapath.
%Output: k-values and capture efficiencies for each droplet size, written
%in files and plotted

clear all;

%Input parameters and change to SI units
sample = input('Run number:', 's');
U = input('Velocity(m/s):');
F = input('Droplet flow(g/min):'); F = F * 0.001/60; %kg/s
ru = input('Upstream dep.rate(mg/hr):'); ru = ru*10^(-6)/3600; %kg/s
rd = input('Downstream dep.rate(mg/hr):'); rd = rd*10^(-6)/3600; %kg/s

A = 0.0254^2*pi; %coupon area
C = F/(U*((3*0.0254)^2*pi/4)); %kg/m3

%% READ DISTRIBUTION DATA AND CALCULATE K-values and EFFICIENCIES FOR EACH DROPLET SIZE
%aerosol data
datapath = 'C:\Documents\WORK\shadow-results\';
dataa = xlsread(strcat(datapath, sample, '-distribution.xls'));
dmaxa = dataa(:,1);
vpdfcorra = dataa(:,6);
vpdfcorrfita = dataa(:,8);
clear dataa;

%coupon data
datapath = 'C:\Documents\WORK\coupon-results\';
%upstream distribution
try
u = xlsread(strcat(datapath, sample, '-u-distribution.xls'));
dmaxu = u(:,1);
vpdfcorru = u(:,6);
vpdfcorrfitu = u(:,8);
clear u;
catch
disp('Warning: file for upstream distribution not found!');
dmaxu = (1:60)';
vpdfcorru = zeros(60,1);
vpdfcorrfitu = zeros(60,1);
end

n = min(max(size(vpdfcorrfitu)),max(size(vpdfcorrfita)));
vpdfcorru = vpdfcorru(1:n); vpdfcorrfitu = vpdfcorrfitu(1:n);
vpdfcorrfita = vpdfcorrfita(1:n); vpdfcorra = vpdfcorra(1:n); dmaxu = dmaxu(1:n);

Eu = ru/(U*A*C)*(vpdfcorrfitu./vpdfcorrfita);
ku = Eu*U;

%downstream distribution
d = xlsread(strcat(datapath, sample, '-d-distribution.xls'));
dmaxd = d(:,1);
vpdfcorrd = d(:,6);
vpdfcorrfitd = d(:,8);

n = min(max(size(vpdfcorrfitd)),max(size(vpdfcorrfita)));
vpdfcorrd = vpdfcorrfitd(1:n); vpdfcorra = vpdfcorra(1:n);
vpdfcorrfitd = vpdfcorrfitd(1:n); vpdfcorrfita = vpdfcorrfita(1:n); dmaxd = dmaxd(1:n);

Ed = rd/(U*A*C)*(vpdfcorrd./vpdfcorrfita);
kd = Ed*U;

%% DISPLAY RESULTS
disp('Concentration(g/m3):'); disp (C*1000);
disp('Upstream k-value(m/hr):'); disp (ru/(A*C)*3600);
disp('Downstream k-value(m/hr):'); disp (rd/(A*C)*3600);
disp('Upstream capture efficiency:'); disp (ru/(U*A*C));
disp('Downstream capture efficiency:'); disp (rd/(U*A*C));

%% PLOT THE RESULTS

```

```

h1 = figure(1);
plot(dmaxu, ku*3600, 'r-', dmaxd, kd*3600, 'b--' );
%title and labels
title('Deposition coefficients');
xlabel('Drop diameter (micron)');
ylabel('k-values (m/hr)');
left = 20; bottom = 300; width = 560; height = 420;
set(h1, 'Position', [left, bottom, width, height]);
legend('k-upstream', 'k-downstream', 'Location', 'NorthWest'); legend('boxoff');
ylim ([0 max(max(ku*3600, kd*3600))]);

h2 = figure(2);
plot(dmaxu, Eu, 'r-', dmaxd, Ed, 'b--' );
%title and labels
title('Capture efficiencies');
xlabel('Drop diameter (micron)');
ylabel('Capture efficiency');
left = 600; bottom = 300; width = 560; height = 420;
set(h2, 'Position', [left, bottom, width, height]);
legend('CE-upstream', 'CE-downstream', 'Location', 'NorthWest', 'boxoff'); legend('boxoff');
ylim ([0 max(max(Eu, Ed))]);

%% SAVE THE RESULTS
filepath = 'C:\Documents\WORK\';
%write deposition coefficients and figure(1) into file
saveas(h1, strcat(filepath, sample, '-k', '.bmp'));
xlswrite(strcat(filepath, sample, '.xls'), {'dmax', 'k-u(m/hr)', 'k-d (m/hr)'});
xlswrite(strcat(filepath, sample, '.xls'), [dmaxu, ku*3600, kd*3600], 'Sheet1', 'A2');

%write capture efficiencies and figure(2) into file
saveas(h2, strcat(filepath, sample, '-ce', '.bmp'));
xlswrite(strcat(filepath, sample, '.xls'), {'CE-u', 'CE-d'}, 'Sheet1', 'D1');
xlswrite(strcat(filepath, sample, '.xls'), [Eu, Ed], 'Sheet1', 'D2');

%write data into files
B = {'Input:', ' ';
     'Run', sample;
     'Velocity(m/s)', U;
     'Droplet flow(g/min)', F*60*1000;
     'Upstream dep.rate(mg/hr)', ru*3600*10^6;
     'Downstream dep.rate(mg/hr)', rd*3600*10^6;
     'Output:', ' ';
     'Concentration(g/m3)', C*1000;
     'k-upstream(m/hr)', ru/(A*C)*3600;
     'k-downstream(m/hr)', rd/(A*C)*3600;
     'CE-upstream', ru/(U*A*C);
     'CE-downstream', rd/(U*A*C)};
xlswrite(strcat(filepath, sample, '.xls'), B, 'Sheet1', 'G1');

```

f2normlognormalcdf.m

```

%Calculates 2-norm (sum of squares) of differences between data and curve for cumulative
%log-normal distribution with 4 parameters
%Input: Initial guess vector a, vector of diameters xdata and vector of frequencies
%(relative or cumulative), ydata
%Output: sum of squares

function f = f2normlognormalcdf(a, xdata, ydata)
a(1) = 1;
f = norm(((1/2)*erf((1/2)*sqrt(2)/a(4)*log(xdata-a(2)))-(1/2)*(a(3)/a(4))*sqrt(2))*a(1) -
ydata);
end

```

f2normlognormalpdf.m

```

%Calculates 2-norm (sum of squares) of differences between data and log-normal
%distribution curve with 4 parameters

```

```

%Input: Initial guess vector a, vector of diameters xdata and vector of frequencies
%relative or cumulative), ydata
%Output: sum of squares

function f = f2normlognormalpdf(a, xdata, ydata)
a(1) = 1; %reduce number of parameters from 4 to 3 by setting this coefficient to 1
f = norm(((a(1)*(1./((xdata-a(2))*a(4)*sqrt(2*pi))))).*exp(-((log(xdata-a(2))-
a(3)).^2)/(2*a(4)^2)))) - ydata);
end

```

fcdf.m

```

%Calculates cumulative frequencies from relative frequencies.
%Input: vector of relative frequencies, x
%Output: vector of cumulative frequencies, y

```

```

function y = fcdf(x)
n = max(size(x));
for i = 1:n
    y(i) = sum(x(1:i));
end
y;
end

```

fdist.m

```

%Calculates size distribution from the vector of drop diameters x.
%Input: nw is a vector that defines whether the size distribution will be calculated in a
%number of points or with defined class width.
%Output: xmax is vector of the maximum class diameter, xmed is vector of median
%diameter of the class, nx is the new nw vector, d is the count distribution, and vol is
%the volume distribution vector.

```

```

function [xmax, xmed, nw, d, vol] = fdist(x,nw)

n = max(size(x));

%determine max and min element and correct them a little to avoid problems in counting
[xmax,row] = max(x);
x(row) = 0.99999*xmax;
[xmin,row] = min(x);
x(row) = 1.00001*xmin;

%volume of droplets
v = x.^3.*pi/6;

%class width is defined, calculate number of classes
if nw(1) == 0
    nw(1) = ceil(xmax/nw(2)); %number of classes
    xmin = 0;
    xmax = nw(1) * nw(2);
    xclass = linspace(xmin, xmax, nw(1) + 1);
else
%number of classes is defined
    xclass = linspace(xmin, xmax, nw(1) + 1);
    nw(2) = (xmax-xmin) / nw(1);
end

%set numbers of droplets and volume in each class to zero
d = zeros(nw(1),1);
vol = zeros(nw(1),1);

try
for i = 1:n
    j = ceil((x(i)-xmin)/nw(2)); %class number
    d(j) = d(j)+1; %increase number of droplets in the class for 1
    vol(j) = vol(j)+v(i); %add droplet volume to the class total volume
end
catch

```

```

    %just to skip potential problems due to droplets that could fall out of range
end

%maximum and medium class diameter
xcmax = xclass(2 : nw(1) + 1)';
xcmed = xcmax - nw(2)/2;

end

```

fdmean.m

```

%Calculates mean diameter by linear interpolation between two adjacent points
%a is desired mean diameter (e.g. for Dv50, a=0.5), x is vector of droplet size classes
%and V is vector of volume relative frequencies

```

```

function y = fdmean(a,x,V)
n = max(size(x));
V = V/max(V);
for i = 1:n
    if V(i) > a
        if i==1
            result = V(i);
        else
            result = x(i-1)+(a-V(i-1))*(x(i)-x(i-1))/(V(i)-V(i-1));
        end
        break;
    end
end
y = result;
end

```

flognormalcdf.m

```

%Four-parameter cumulative log normal distribution

```

```

function f = flognormalcdf(a, xcmax)
f = (1/2)*erf((1/2)*sqrt(2)/a(4)*log(xcmax-a(2))-(1/2)*(a(3)/a(4))*sqrt(2))*a(1);
end

```

flognormalpdf.m

```

%Four-parameter log normal distribution

```

```

function f = flognormalpdf(a, xcmax)
f = (a(1)*(1./((xcmax-a(2))*a(4)*sqrt(2*pi))))*exp(-((log(xcmax-a(2))-a(3)).^2)/(2*a(4)^2));
end

```

fpdf.m

```

%Calculates relative frequencies from cumulative frequencies (probability density
%function), from the cumulative frequencies (cumulative density function).

```

```

%Input: vector of cumulative frequencies, x
%Output: vector of relative frequencies, y

```

```

function y = fpdf(x)
n = max(size(x));
for i = 1:n
    if i == 1
        y(i) = x(i);
    else
        y(i) = x(i) - x(i-1);
    end
end
y;
end

```

shadow.m

```

%Analyzes individual drop size data, reported from Image Pro Plus. Calculates drop size
%from pixels into microns, and computes size distribution based on the specified number
%of classes or class width. Applies border and depth of field correction and deals with
%outliers. It is used for analysis of drop size distribution in the aerosol and on the
%coupon (one or two separated distributions). It also performs curve fitting using
%function 'fdist.m'. Finally, it reports results on the screen and plots results for
%relative and cumulative frequencies. All the results and graphs are written into files.

%% INPUT SECTION
%Input file name(run number or sample number) e.g. 1, 1-u, or 1-d
%Files should be placed in the folder defined by variable datapath

clear all;
sample = input ('1.Sample number: ','s');
ac = input ('2.Size distribution (1)In the Aerosol (2)On the Coupon: ');
    if ac == 2
        minpoint = input ('2a.Minimum point that separates two distributions (enter for
none):');
    else
        minpoint = [];
    end
magnification = input('3.Magnification used: ');
choice = input('4.Size distribution of: (1)Dmax, (2)Dmin, (3)Dmean: ');
nwchoice = input('5.Define: (1)Number of Classes, (2)Class Width: ');
    if nwchoice == 1
        nclasses = input('5a.Number of classes: ');
        nw0 = [nclasses; 0];
    else
        cwidth = input('5b.Class width(um): ');
        nw0 = [0; cwidth];
    end
fitting = input ('6.Fit volume distribution: (1)Cumulative, (2)Relative: ');

outlier = input ('7.Remove outliers X times larger than Dv50, or >Dmax (default is 10x
and Dmax = 150):');
    if isempty(outlier)
        outlier = 10;
    end

%% LOADING DATA AND INITIAL PROCESSING
%load data obtained by Image Pro Plus
if ac == 1
    datapath = 'C:\Documents\WORK\shadow-results\';
else
    datapath = 'C:\Documents\WORK\coupon-results\';
end
data = load(strcat(datapath, sample, '.txt'));
%calculate no. of microns per pixel (from the calibration data)
teta = 20; %TEG on glass, 20deg contact angle
if ac == 1
    k1 = 1;
    k2 = 1/(0.3257*magnification - 0.0004);
elseif ac ==2
    k1 = (3*tan((teta/2)*(2*pi/360)) + tan((teta/2)*(2*pi/360))^3)^(1/3)/2;
    k2 = 1/(0.2173*magnification - 0.0030);
end

%width and height of the view field
k = k1 * k2;
W = k2 * 1392;
H = k2 * 1040;
%pick appropriate column for diameter
x = k*data(:, choice + 1);

%% CALCULATING THE DISTRIBUTION AND POSTPROCESSING OF THE RESULTS
%calculate the distribution and remove outliers
[dcmax, dcmed, nw, d, vol] = fdist(x, nw0);
Dv50 = fdmean(0.5, dcmax, fcdf(vol/sum(vol)));

```

```

for i = 1:max(size(x))
    if or(x(i)> outlier*Dv50, x(i)>150)
        x(i) = 1;
    end
end
[dcmax, dcmed, nw, d, vol] = fdist(x, nw0);
nclasses = nw(1);
deltad = nw(2);

%aerosol distribution and non-separated coupon distribution
nclasses1 = nclasses;
dcmax1 = dcmax;
dcmed1 = dcmed;
d1 = d;
vol1 = vol;

%separated distributions on the coupon (if it exists on the upstream side)
if not(isempty(minpoint))
    %first distribution from turbulent diffusion
    nclasses1 = minpoint;
    dcmax1 = dcmax(1:minpoint);
    dcmed1 = dcmed(1:minpoint);
    d1 = d(1:minpoint);
    vol1 = vol(1:minpoint);
    %second distribution from inertial impaction
    nclasses2 = nclasses - minpoint;
    dcmax2 = dcmax(minpoint + 1 : nclasses);
    dcmed2 = dcmed(minpoint + 1 : nclasses);
    d2 = d(minpoint + 1 : nclasses);
    vol2 = vol(minpoint + 1 : nclasses);
end

%%DEPTH OF FIELD AND BORDER CORRECTION
if ac == 1 %(aerosol)
    %border and DOF corrections
    p1 = ((W-dcmax1).*(H-dcmax1)/(W*H)) .* (dcmax1/dcmax1(nclasses1));
    %depth of field in microns for the largest droplet, calibrated at 2x3magnification
    DOF = 40.5*dcmax1(nclasses1);
elseif ac == 2 %(coupon)
    %only border correction
    DOF = 0;
    if not(isempty(minpoint))
        p1 = ((W-dcmax1).*(H-dcmax1)/(W*H));
        p2 = ((W-dcmax2).*(H-dcmax2)/(W*H));
    else
        p1 = ((W-dcmax1).*(H-dcmax1)/(W*H));
    end
end

%aerosol and non-separated coupon distribution: corrected number of droplets and volume
dlcorr = round((1./p1).*d1);
vollcorr = (dcmed1.^3*pi/6).*dlcorr;
vpdf1 = voll/sum(voll);
vcdf1 = fcdf(vpdf1)';
vpdf1corr = vollcorr/sum(vollcorr);
vcdf1corr = fcdf(vpdf1corr)';

%volume and concentration
V = W*H*DOF; %um3
C = 1127*sum(vollcorr)/(1300*V); %for 1300 images, kg/m3
C = C*1000; %g/m3

%separated distributions on the coupon: corrected number of droplets and volume
if not(isempty(minpoint))
    %first distribution
    dlcorr = round((1./p1).*d1);
    vollcorr = (dcmed1.^3*pi/6).*dlcorr;
    vpdf1 = voll/sum(voll);
    vcdf1 = fcdf(vpdf1)';
    %second distribution
    d2corr = round((1./p2).*d2);
end

```

```

vol2corr = (dcmed2.^3*pi/6).*d2corr;
vpdf2 = vol2/sum(vol);
vcdf2 = fcdf(vpdf2)';
%first and second distribution
vpdf1corr = vollcorr/(sum(vollcorr)+sum(vol2corr));
vcdf1corr = fcdf(vpdf1corr)';
vpdf2corr = vol2corr/(sum(vollcorr)+sum(vol2corr));
vcdf2corr = fcdf(vpdf2corr)';
end

%%CHARACTERISTIC DIAMETERS
%aerosol, non-separated distribution and first of two separated distributions
Dmin1 = min(x);
Dmax1 = max(dcmx1);
Damd1 = sum(d1.*dcmx1)/(sum(d1)); Damd1corr = sum(d1corr.*dcmx1)/(sum(d1corr));
Dv101 = fdmean(0.1, dcmx1, vcdf1); Dv101corr = fdmean(0.1, dcmx1, vcdf1corr);
Dv501 = fdmean(0.5, dcmx1, vcdf1); Dv501corr = fdmean(0.5, dcmx1, vcdf1corr);
Dv901 = fdmean(0.9, dcmx1, vcdf1); Dv901corr = fdmean(0.9, dcmx1, vcdf1corr);
RSF1 = (Dv901-Dv101)/Dv501; RSF1corr = (Dv901corr-Dv101corr)/Dv501corr;

%second separated distribution
if not isempty(minpoint)
    Dmin2 = min(dcmx2);
    Dmax2 = max(d2);
    Damd2 = sum(d2.*dcmx2)/(sum(d2)); Damd2corr = sum(d2corr.*dcmx2)/(sum(d2corr));
    Dv102 = fdmean(0.1, dcmx2, vcdf2); Dv102corr = fdmean(0.1, dcmx2, vcdf2corr);
    Dv502 = fdmean(0.5, dcmx2, vcdf2); Dv502corr = fdmean(0.5, dcmx2, vcdf2corr);
    Dv902 = fdmean(0.9, dcmx2, vcdf2); Dv902corr = fdmean(0.9, dcmx2, vcdf2corr);
    RSF2 = (Dv902-Dv102)/Dv502; RSF2corr = (Dv902corr-Dv102corr)/Dv502corr;
end

%FITTING AND DISTRIBUTION CURVE BASED ON FITTING
a0 = [1, 0.1, 2.2, 0.6]; %initial guess
%select fitting relative or cumulative frequencies
switch fitting
case 1 %cumulative frequencies
    %aerosol, non-separated distribution and first of two separated distributions
    %[a1, fval1] = lsqcurvefit(@flognormalcdf, a0, dcmx1, vcdf1corr);
    f = @(a)f2normlognormalcdf(a, dcmx1, vcdf1corr);
    [a1, fval1] = fminunc(f, a0);
    vcdf1corrfit = flognormalcdf(a1, dcmx1);
    vpdf1corrfit = fpdf(vcdf1corrfit)';
    SSE1corr = sum((vcdf1corr - vcdf1corrfit).^2);
    RMSE1corr = (SSE1corr/(max(size(dcmx1))))^0.5;

    %second separated distribution
    if (ac == 2)&&(not isempty(minpoint))
        %[a2, fval2] = lsqcurvefit(@flognormalcdf, a0, dcmx2, vcdf2corr);
        f = @(a)f2normlognormalcdf(a, dcmx2, vcdf2corr);
        a0(2) = a0(2) + minpoint; %better initial guess for the shift along x-axis
        [a2, fval2] = fminunc(f, a0);
        vcdf2corrfit = flognormalcdf(a2, dcmx2);
        vpdf2corrfit = fpdf(vcdf2corrfit)';
        SSE2corr = sum((vcdf2corr - vcdf2corrfit).^2);
        RMSE2corr = (SSE2corr/(max(size(dcmx2))))^0.5;
    end
case 2 %relative frequencies
    %aerosol, non-separated distribution and first of two separated distributions
    %[a1, fval1] = lsqcurvefit(@flognormalpdf, a0, dcmx1, vpdf1corr);
    f = @(a)f2normlognormalpdf(a, dcmx1, vpdf1corr);
    [a1, fval1] = fminunc(f, a0);
    vpdf1corrfit = flognormalpdf(a1, dcmx1);
    vcdf1corrfit = fcdf(vpdf1corrfit)';
    SSE1corr = sum((vpdf1corr - vpdf1corrfit).^2);
    RMSE1corr = (SSE1corr/(max(size(dcmx1))))^0.5;

    %non-corrected distribution (only for the aerosol and first coupon distribution)
    f = @(a)f2normlognormalpdf(a, dcmx1, vpdf1);
    [a11, fval11] = fminunc(f, a0);
    vpdf1fit = flognormalpdf(a11, dcmx1);
    vcdf1fit = fcdf(vpdf1fit)';

```

```

SSE1 = sum((vpdf1 - vpdf1fit).^2);
RMSE1 = (SSE1/(max(size(dcmax1))))^0.5;

%second separated distribution
if (ac == 2) && (not(isempty(minpoint)))
    [a2, fval2] = lsqcurvefit(@flognormalpdf, a0, dcmax2, vpdf2corr);
    f = @(a)f2normlognormalpdf(a, dcmax2, vpdf2corr);
    a0(2) = a0(2) + minpoint; %better initial guess for the shift along x-axis
    [a2, fval2] = fminunc(f, a0);
    vpdf2corrfit = flognormalpdf(a2, dcmax2);
    vcdf2corrfit = fcdf(vpdf2corrfit)';
    SSE2corr = sum((vpdf2corr - vpdf2corrfit).^2);
    RMSE2corr = (SSE2corr/(max(size(dcmax2))))^0.5;
end

end

%% DISPLAY RESULTS
disp('-----');
disp('                                R E S U L T S:');
disp('-----');
disp('Distribution:');
disp(sprintf('%15s', '#1', '    #1corrected', '    #2', '    #2corrected'));
if (ac == 2) && not(isempty(minpoint))
    disp('Number of droplets:');
    disp(sprintf('%15.0f', sum(d1), sum(d2), sum(d1corr), sum(d2corr)));
    disp('Volume of droplets(um3):');
    disp(sprintf('%15.0f', sum(vol1), sum(vol2), sum(vol1corr), sum(vol2corr)));
    disp('Class width(um):');
    disp(sprintf('%15.2f', deltad, deltad, deltad, deltad));
    disp('Arithmetic mean diameter, Damd(um):');
    disp(sprintf('%15.2f', Damd1, Damd2, Damd1corr, Damd2corr));
    disp('Minimum diameter, Dmin(um):');
    disp(sprintf('%15.2f', Dmin1, Dmin2, Dmin1, Dmin2));
    disp('10 percent volume diameter, Dv10(um):');
    disp(sprintf('%15.2f', Dv101, Dv102, Dv101corr, Dv102corr));
    disp('50 percent volume diameter (VMD), Dv50(um):');
    disp(sprintf('%15.2f', Dv501, Dv502, Dv501corr, Dv502corr));
    disp('90 percent volume diameter, Dv90(um):');
    disp(sprintf('%15.2f', Dv901, Dv902, Dv901corr, Dv902corr));
    disp('Maximum diameter, Dmax(um):');
    disp(sprintf('%15.2f', Dmax1, Dmax2, Dmax1, Dmax2));
    disp('Relative Span Factor, RSF = (Dv90-Dv10)/Dv50:');
    disp(sprintf('%15.2f', RSF1, RSF2, RSF1corr, RSF2corr));
else
    disp('Number of droplets:');
    disp(sprintf('%15.0f', sum(d1), sum(d1corr)));
    disp('Volume of droplets(um3):');
    disp(sprintf('%15.0f', sum(vol1), sum(vol1corr)));
    disp('Class width(um):');
    disp(sprintf('%15.2f', deltad, deltad));
    disp('Arithmetic mean diameter, Damd(um):');
    disp(sprintf('%15.2f', Damd1, Damd1corr));
    disp('Minimum diameter, Dmin(um):');
    disp(sprintf('%15.2f', Dmin1, Dmin1));
    disp('10 percent volume diameter, Dv10(um):');
    disp(sprintf('%15.2f', Dv101, Dv101corr));
    disp('50 percent volume diameter (VMD), Dv50(um):');
    disp(sprintf('%15.2f', Dv501, Dv501corr));
    disp('90 percent volume diameter, Dv90(um):');
    disp(sprintf('%15.2f', Dv901, Dv901corr));
    disp('Maximum diameter, Dmax(um):');
    disp(sprintf('%15.2f', Dmax1, Dmax1));
    disp('Relative Span Factor, RSF = (Dv90-Dv10)/Dv50:');
    disp(sprintf('%15.2f', RSF1, RSF1corr));
end
disp('-----');
disp('                                F I T T I N G   R E S U L T S:');
disp('-----');
if (ac == 2) && not(isempty(minpoint))
    disp('Parameters a(1), a(2), a(3), a(4): ');
    disp('Distribution 1: ');

```

```

disp(sprintf('%15.5f', a1(1), a1(2), a1(3), a1(4)));
disp('Distribution 2: ');
disp(sprintf('%15.5f', a2(1), a2(2), a2(3), a2(4)));
disp('Sum of Squares of Errors, SSE: ');
disp(sprintf('%15.5f', SSE1corr, SSE2corr));
disp('Root Mean Square Error, RMSE: ');
disp(sprintf('%15.5f', RMSE1corr, RMSE2corr));
else
disp('Parameters a(1), a(2), a(3), a(4)');
disp('Corrected distribution: ');
disp(num2str(a1(1), '%15.5f')); disp(num2str(a1(2), '%15.5f'));
disp(num2str(a1(3), '%15.5f')); disp(num2str(a1(4), '%15.5f'));
disp('Noncorrected distribution: ');
disp(num2str(a11(1), '%15.5f')); disp(num2str(a11(2), '%15.5f'));
disp(num2str(a11(3), '%15.5f')); disp(num2str(a11(4), '%15.5f'));
disp('Sum of Squares of Errors, SSE: ');
disp(sprintf('%15.5f', SSE1corr));
disp('Root Mean Square Error, RMSE: ');
disp(sprintf('%15.5f', RMSE1corr));
end

disp('Sample volume(mm3): ');
disp(sprintf('%15.3f', V*10^(-9)));
disp('Concentration(g/m3): ');
disp(sprintf('%15.2f', C));

%% WRITTING RESULTS INTO FILES
% separated distributions on the coupon
if (ac == 2) && not(isempty(minpoint))
A= {'Magnification', magnification, magnification, magnification, magnification;
' (1)Dmax, (2)Dmin, (3)Dmean', choice, choice, choice, choice;
' Fitting (1)cum, (2)rel', fitting, fitting, fitting, fitting;
' Outlier (times>Dv50)', outlier, outlier, outlier, outlier;
' Distribution ', '#1', '#1corrected', '#2', '#2corrected';
' Ntot', sum(d1), sum(d2), sum(d1corr), sum(d2corr);
' Vtot(um3)', sprintf('%15.0f',sum(voll)), sprintf('%15.0f', sum(vol2)),
sprintf('%15.0f', sum(vollcorr)), sprintf('%15.0f', sum(vol2corr));
' deltad(um)', sprintf('%15.2f',deltad), sprintf('%15.2f', deltad),
sprintf('%15.2f',deltad), sprintf('%15.2f', deltad);
' Damd(um)', sprintf('%15.2f',Damd1), sprintf('%15.2f', Damd2), sprintf('%15.2f',
Damd1corr), sprintf('%15.2f', Damd2corr);
' Dmin(um)', sprintf('%15.2f',Dmin1), sprintf('%15.2f',Dmin2), sprintf('%15.2f',
Dmin1), sprintf('%15.2f', Dmin2);
' Dv10(um)', sprintf('%15.2f',Dv101), sprintf('%15.2f',Dv102), sprintf('%15.2f',
Dv101corr), sprintf('%15.2f', Dv102corr);
' Dv50(um)', sprintf('%15.2f',Dv501), sprintf('%15.2f',Dv502), sprintf('%15.2f',
Dv501corr), sprintf('%15.2f', Dv502corr);
' Dv90(um)', sprintf('%15.2f',Dv901), sprintf('%15.2f',Dv902),
sprintf('%15.2f',Dv901corr), sprintf('%15.2f',Dv902corr);
' Dmax(um)', sprintf('%15.2f',Dmax1), sprintf('%15.2f',Dmax2), sprintf('%15.2f',Dmax1),
sprintf('%15.2f',Dmax2);
' RSF', sprintf('%15.2f',RSF1), sprintf('%15.2f', RSF2), sprintf('%15.2f',RSF1corr),
sprintf('%15.2f',RSF2corr);
' F I T T I N G ', '', '', '', '';
' a(1),a(2),a(3),a(4)', sprintf('%15.5f', a1(1)), sprintf('%15.5f', a1(2)),
sprintf('%15.5f', a1(3)), sprintf('%15.5f',a1(4));
' SSE', sprintf('%15.5f', SSE1corr), sprintf('%15.5f', SSE2corr), sprintf('%15.5f',
SSE1corr), sprintf('%15.5f', SSE2corr);
' RMSE', sprintf('%15.5f', RMSE1corr), sprintf('%15.5f',RMSE2corr), sprintf('%15.5f',
RMSE1corr), sprintf('%15.5f',RMSE2corr)
' Sample vol (mm3)', sprintf('%15.5f', V*10^(-9)), sprintf('%15.5f',V*10^(-9));
' Conc. (g/m3)', sprintf('%15.5f', C), sprintf('%15.5f',C));

% write distribution data into xls files
xlswrite(strcat(datapath, sample, '.xls'),A);
B0 = {'dcmx', 'd', 'vpdf', 'vcdf', 'dcorr', 'vpdfcorr', 'vcdfcorr', 'vpdfcorrfit',
'vcdfcorrfit'};
B = {[dcmx1;dcmx2], [d1;d2], [vpdf1;vpdf2], [vcdf1;vcdf2], [d1corr;d2corr],
[vpdf1corr;vpdf2corr],
[vcdf1corr;vcdf2corr], [vpdf1corrfit;vpdf2corrfit], [vcdf1corrfit;vcdf2corrfit]};
xlswrite(strcat(datapath, sample, '-distribution', '.xls'), B0);

```

```

xlswrite(strcat(datapath, sample, '-distribution','.xls'), B, 'Sheet1', 'A2');

else
%aerosol and nonseparated coupon distribution
A= {'Magnification', magnification, magnification;
' (1)Dmax, (2)Dmin, (3)Dmean', choice, choice;
'Fitting (1)cum, (2)rel', fitting, fitting;
'Outlier (times>Dv50)', outlier, outlier;
'Distribution ', '#1', '#1corrected';
'Ntot', sum(dl), sum(dlcorr);
'Vtot (um3)',sprintf('%15.0f',sum(voll)), sprintf('%15.0f', sum(vollcorr));
'deltad (um)',sprintf('%15.2f',deltad), sprintf('%15.2f',deltad);
'Damd (um)',sprintf('%15.2f',Damdl), sprintf('%15.2f', Damdlcorr);
'Dmin (um)',sprintf('%15.2f',Dminl), sprintf('%15.2f', Dminl);
'Dv10 (um)',sprintf('%15.2f',Dv10l), sprintf('%15.2f', Dv10lcorr);
'Dv50 (um)',sprintf('%15.2f',Dv50l), sprintf('%15.2f', Dv50lcorr);
'Dv90 (um)',sprintf('%15.2f',Dv90l), sprintf('%15.2f', Dv90lcorr);
'Dmax (um)',sprintf('%15.2f',Dmaxl) sprintf('%15.2f', Dmaxl);
'RSF', sprintf('%15.2f',RSF1), sprintf('%15.2f',RSF1corr);
'F I T T I N G', '', '';
'noncorrected', '', '';
'a (1), a (2)',sprintf('%15.5f', a1(1)), sprintf('%15.5f', a1(2));
'a (3), a (4)',sprintf('%15.5f', a1(3)), sprintf('%15.5f', a1(4));
'SSE',sprintf('%15.5f', SSE1lcorr), '';
'RMSE',sprintf('%15.5f', RMSE1lcorr), '';
'corrected', '', '';
'a (1), a (2)',sprintf('%15.5f', a1(1)), sprintf('%15.5f', a1(2));
'a (3), a (4)',sprintf('%15.5f', a1(3)), sprintf('%15.5f', a1(4));
'SSE', '', sprintf('%15.5f', SSE1corr);
'RMSE', '', sprintf('%15.5f', RMSE1corr);

'Sample vol (mm3)',sprintf('%15.5f', V*10^(-9)), sprintf('%15.5f',V*10^(-9));
'Conc. (g/m3)',sprintf('%15.5f', C), sprintf('%15.5f',C));

% distribution data into xls files
xlswrite(strcat(datapath, sample, '.xls'),A);
B0 = {'dcmx', 'd', 'vpdf', 'vcdf', 'dcorr', 'vpdfcorr', 'vcdfcorr', 'vpdfcorrfit',
'vcdfcorrfit'};
B = [dcmx1, dl, vpdf1, vcdf1, dlcrr, vpdf1corr, vcdf1corr, vpdf1corrfit, vcdf1corrfit];
xlswrite(strcat(datapath, sample, '-distribution','.xls'), B0);
xlswrite(strcat(datapath, sample, '-distribution','.xls'), B, 'Sheet1', 'A2');

end

%% PLOTTING THE DATA
% FIGURE 1
%volume pdf distribution
h1 = figure(1);
plot (dcmx, vol/sum(vol), 'rs', 'MarkerSize', 5); hold on;
plot (dcmx1, vpdf1corr, 'bo', 'MarkerFaceColor', 'b', 'MarkerSize', 5);
plot (dcmx1, vpdf1corrfit, 'k-', 'LineWidth', 1);
plot (dcmx1, vpdf1fit, 'k-', 'LineWidth', 1);
if not isempty(minpoint)
    plot (dcmx2, vpdf2corr, 'bo', 'MarkerFaceColor', 'b', 'MarkerSize', 5);
    plot (dcmx2, vpdf2corrfit, 'k--', 'LineWidth', 1); hold off;
end
ylim ([0, max(max(vpdf1corr), max(vpdf1corrfit))*1.2]);
%title and labels
title('Volume distribution');
xlabel('Droplet diameter (micron)');
ylabel('Volume %');
%position it left
left = 20; bottom = 300; width = 560; height = 420;
set(h1, 'Position', [left, bottom, width, height]);

%FIGURE 2
%volume cdf distribution
h2 = figure(2);
plot (dcmx, fcdf(vol/sum(vol)), 'rs', 'MarkerSize', 5); hold on;
plot (dcmx1, vcdf1corr, 'bo', 'MarkerFaceColor', 'b', 'MarkerSize', 5);
plot (dcmx1, vcdf1corrfit, 'k-', 'LineWidth', 1);

```

```
plot (dcmxl, vcdf1fit, 'k-', 'LineWidth', 1);
if not(isempty(minpoint))
    plot (dcmxl, vcdf2corr + max(vcdf1corr), 'bo', 'MarkerFaceColor', 'b', 'MarkerSize',
5);
    plot (dcmxl, vcdf2corrfit + max(vcdf1corrfit), 'k--', 'LineWidth', 1); hold off;
end
ylim ([0 1]);
%title and labels
title('Cumulative volume distribution');
xlabel('Droplet diameter (micron)');
ylabel('Volume %');
%position it right
left = 600; bottom = 300; width = 560; height = 420;
set(h2, 'Position', [left, bottom, width, height]);

%% WRITING FIGURES INTO FILES
%write figure(1) in the file
saveas(h1, strcat(datapath, sample, '-vpdf', '.bmp'));

%write figure(2) in the file
saveas(h2, strcat(datapath, sample, '-vcdf' ,'.bmp'));
```

D.3. Mathcad code

To calculate capture efficiencies for non-Stokesian drag force, system of nonlinear differential equations was solved in the program written in the Mathcad Professional 2001 software. The ODE's system was solved using function 'Rkadapt', which implements the Runge-Kutta method of the 4th order, while nonlinear equations were solved in the 'Solve block', using Levenberg-Marquardt algorithm.

Parameters

$\rho := 1127$	TEG density, kg/m ³
$\mu := 1.815 \cdot 10^{-5}$	air viscosity, Pas
$\rho_a := 1.203$	air density, kg/m ³
$R_c := 0.0254$	coupon radius, m

$$St(D_p, V_0) := \frac{\rho \cdot D_p^2}{18 \cdot \mu} \cdot \frac{V_0}{2 \cdot R_c} \quad \text{Stokes number function}$$

Flow field from potential flow

$$x(t, x_0) := x_0 \cdot e^{-2 \cdot t} \quad y(t, y_0) := y_0 \cdot e^t$$

Particle motion equations

Parameter definition (must be defined before the function definition). In SI units:

$D_p := 50 \cdot 10^{-6}$	particle diameter
$V_0 := 1$	initial velocity
$x_0 := -0.5$	nondimensional x distance
$y_0 := 0.1$	nondimensional y distance (y=r, radial component)
$p := -1$	gravity in negative direction (upward flow)

Initial velocity calculation (different from fluid velocity due to the gravity effect):

Given

$$x_1 = -2 \cdot x_0 + \frac{p}{\left[1 + \frac{1}{6} \cdot \left(\frac{D_p \cdot \rho_a}{\mu} \cdot |x_1 + 2 \cdot x_0| \right)^{\frac{2}{3}} \right]} \cdot \left[\frac{\rho \cdot (D_p)^2}{18 \cdot \mu} \cdot \frac{9.81}{V_0} \right]$$

$$\text{init}(x_0, x_1, D_p, V_0, p) := \text{Find}(x_1)$$

$$\text{init} \left[x_0, -2 \cdot x_0 + p \cdot \left[\frac{\rho \cdot (D_p)^2}{18 \cdot \mu} \cdot \frac{9.81}{V_0} \right], D_p, V_0, p \right] = 0.921$$

Initial conditions and system of diff.equations definition:

$$X := \begin{bmatrix} x_0 \\ \text{init} \left[x_0, -2 \cdot x_0 + p \cdot \left[\frac{\rho \cdot (D_p)^2}{18 \cdot \mu} \cdot \frac{9.81}{V_0} \right], D_p, V_0, p \right] \\ y_0 \\ 0 \\ D_p \\ V_0 \\ p \end{bmatrix}$$

$$D(t, X) := \begin{bmatrix} X_1 \\ \frac{1 + \frac{1}{6} \cdot \left(\frac{D_p \cdot \rho_a}{\mu} \cdot |X_1 + 2 \cdot X_0| \right)^{\frac{2}{3}}}{2 \cdot \text{St}(X_4, X_5)} \cdot (-X_1 - 2 \cdot X_0) + \frac{1}{2 \cdot \text{St}(X_4, X_5)} \cdot X_6 \cdot \left[\frac{\rho \cdot (X_4)^2}{18 \cdot \mu} \cdot \frac{9.81}{X_5} \right] \\ X_3 \\ \frac{1 + \frac{1}{6} \cdot \left(\frac{D_p \cdot \rho_a}{\mu} \cdot |X_3 - X_2| \right)^{\frac{2}{3}}}{2 \cdot \text{St}(X_4, X_5)} \cdot (-X_3 + X_2) \\ 0 \\ 0 \\ 0 \end{bmatrix}$$

Function *xyp* returns (x,y) position of a particle of size D_p , at time t , starting from the initial position (x_0, y_0) , with initial velocity V_0 , and gravity orientation p .

$$\text{xyp}(t, D_p, V_0, x_0, y_0, p) := \left[\begin{array}{l} n \leftarrow 100 \\ \\ X \leftarrow \left[\begin{array}{c} x_0 \\ \text{init} \left[x_0, -2 \cdot x_0 + p \cdot \left[\frac{\rho \cdot (D_p)^2}{18 \cdot \mu} \cdot \frac{9.81}{V_0} \right], D_p, V_0, p \right] \\ y_0 \\ 0 \\ D_p \\ V_0 \\ p \end{array} \right] \\ \\ \text{res} \leftarrow \text{rkfixed}(X, 0, t, n, D) \text{ on error Rkadapt}(X, 0, t, n, D) \\ \text{xp} \leftarrow \text{res}_{n,1} \\ \text{yp} \leftarrow \text{res}_{n,3} \\ \left(\begin{array}{c} \text{xp} \\ \text{yp} \end{array} \right) \end{array} \right]$$

Function *timexyp* returns the time needed for particle to reach the coupon surface ($x=0$).

TOL := 10^{-3}

Given

$\text{xyp}(t, D_p, V_0, x_0, y_0, p)_0 = 0$

$t > 0$

$\text{timexyp}(t, D_p, V_0, x_0, y_0, p) := \text{Find}(t)$

Function *E* calculates capture efficiency for particle size D_p , starting with initial velocity V_0 , from position (x_0, y_0) , with gravity orientation p .

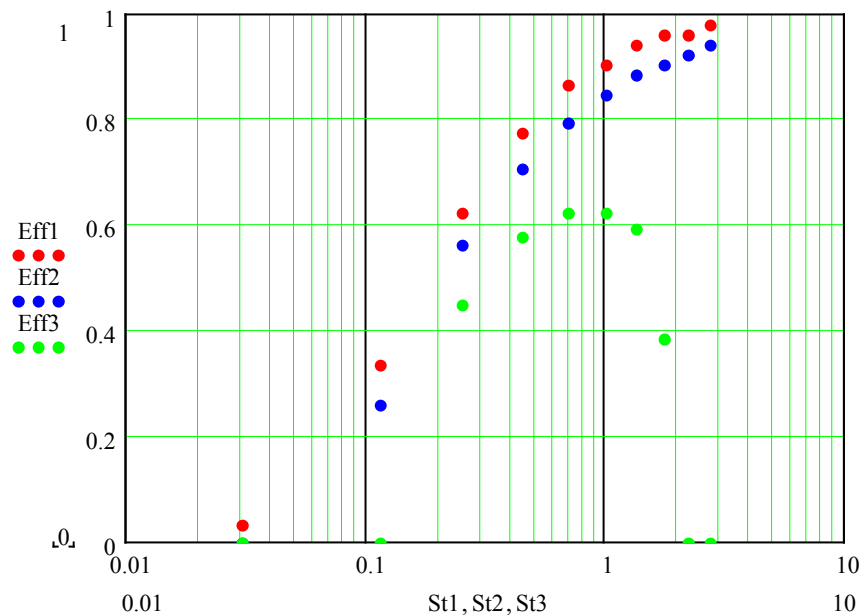
$$E(D_p, V_0, x_0, y_0, p) := \left| \begin{array}{l} n \leftarrow 0 \\ N \leftarrow 100 \\ \text{tmax} \leftarrow 0 \text{ on error } \text{tmax} \leftarrow \text{timexp}(1, D_p, V_0, x_0, y_0, p) \\ \text{for } y_0 \in \frac{1}{N}, \frac{2}{N} \dots 1 \\ \quad \left| \begin{array}{l} x \leftarrow -1 \text{ on error } x \leftarrow \text{ryp}(\text{tmax}, D_p, V_0, x_0, y_0, p)_0 \\ y \leftarrow 0 \text{ on error } y \leftarrow \text{ryp}(\text{tmax}, D_p, V_0, x_0, y_0, p)_1 \\ n \leftarrow n + 1 \text{ if } (y < 1) \wedge (x > -0.001) \\ \text{break otherwise} \end{array} \right. \\ \left(\frac{n}{N} \right)^2 \end{array} \right.$$

Function *Ecurve* calculates capture efficiencies for particles starting with initial velocity V_0 , from position (x_0, y_0) , with gravity orientation p .

$$Ecurve(V_0, x_0, y_0, p) := \left| \begin{array}{l} M \leftarrow (\text{"Stokes" "Capture efficiency" }) \\ \text{for } D \in 1, 21 \dots 201 \\ \quad \left| \begin{array}{l} D_p \leftarrow D \cdot 10^{-6} \\ M \leftarrow \text{stack}[M, (\text{St}(D_p, V_0) \ E(D_p, V_0, x_0, y_0, p))] \end{array} \right. \\ \text{submatrix}(M, 1, \text{rows}(M) - 1, 0, \text{cols}(M) - 1) \end{array} \right.$$

$$M1 := Ecurve(V_0, x_0, y_0, 1) \quad M2 := Ecurve(V_0, x_0, y_0, 0) \quad M3 := Ecurve(V_0, x_0, y_0, -1)$$

$$St1 := M1^{(0)} \quad Eff1 := M1^{(1)} \quad St2 := M2^{(0)} \quad Eff2 := M2^{(1)} \quad St3 := M3^{(0)} \quad Eff3 := M3^{(1)}$$



Appendix E. Tables

Table E.1 Summary results for the effect of velocity, triethylene glycol, Cold Unit nozzle, Setup #1

Run	14	43	37	38	17	39	40	41	21	19	20
Run time (min)	45.5	60.0	27.3	23.0	20.0	10.0	10.0	10.0	10.0	15.0	15.0
Air and liquid settings											
Rotameter 1	90/39	90/38	90/37	90/37	90/39	90/37	90/37	90/37	90/39	91/40.1	91/40
Rotameter 2	0/0	0/0	0.5/2	1.0/3	1.5/4.8	2.0/5	2.4/9	2.7/11	3.13/11.	3.13/11.	3.14/11.
Rotameter 3	0/0	30/1	0/0	0/0	0/0	0/0	0/0	0/0	0/0	0/0	0/0
Pump setting	8	8	8	8	8	8	8	8	8	8	8
Velocity											
Air to nozzle (m/s)	0.438	0.430	0.430	0.430	0.438	0.430	0.430	0.430	0.438	0.446	0.446
Secondary air (m/s)	0	0.12	0.211	0.320	0.433	0.552	0.713	0.832	0.972	0.973	0.977
Total air (m/s)	0.44	0.55	0.64	0.75	0.87	0.98	1.14	1.26	1.41	1.42	1.42
Liquid											
Liquid flow rate (g/min)	68.2	70	70	70	68.1	70	70	70	68.1	68.1	68.1
Liquid flow rate to aerosol (g/min)	1.02	1.46	1.60	2.03	2.44	3.19	3.35	3.79	3.52	3.72	3.44
Aerosol concentration from washdown (g/m ³)	8.49	9.73	9.10	9.88	10.20	11.88	10.71	10.98	9.11	9.58	8.85
Aerosol concentration from shadowgraphy (g/m ³)	6.00	6.31	6.34	5.16	7.33	5.1	4.64	4.95	5.07	2.94	4.37
Aerosol shadowgraphy											
Number of 260 image samples	1	5	5	5	1	5	5	5	1	1	1
Uncorrected											
Number of droplets	2011	10993	10377	9066	2148	9222	8961	9548	1775	1199	1493
D _{min} (μm)	0.99	0.51	0.91	0.94	0.97	0.94	0.72	0.85	0.9	1.14	0.99
D _{V,10} (μm)	3.92	3.88	4.08	3.9	4.65	3.83	3.62	3.62	3.76	3.63	3.91
D _{V,50} (μm)	10.84	10.25	11.35	10.9	12.67	10.22	8.83	9.19	9.47	9.42	10.46
D _{V,50} st.dev. (μm)	–	0.71	0.723	0.742	–	0.624	0.326	0.468	–	–	–
D _{V,90} (μm)	27.48	21.55	25.05	23.46	24.58	22.02	19.92	20.47	18.57	16.52	17.38
D _{max} (μm)	30	33	32	32	29	28	29	32	21	23	23
Log-normal distribution parameters a ₂ , a ₃ , a ₄	1.10009, 2.34139, 0.83173	1.09535, 2.2716, 0.80057	0.99316, 2.40646, 0.81847	0.80759, 2.3736, 0.79407	-0.5288, 2.6324, 0.66471	1.0953, 2.27252, 0.81418	1.0994, 2.09936, 0.7545	1.09528, 2.13731, 0.78397	1.08816, 1.6958, 0.68193	-3.6326, 2.59415, 0.41959	1.07643, 1.84745, 0.78458
SSE	0.01108	0.00247	0.00365	0.00445	0.00979	0.00378	0.00526	0.00312	0.00723	0.0153	0.00617
RMSE	0.01922	0.00866	0.01069	0.01179	0.01837	0.01162	0.01347	0.00988	0.01856	0.02579	0.01638
Corrected											
Number of droplets	16473	101010	92030	82055	17021	72739	73365	86829	10182	8207	9724
D _{V,10} (μm)	3.12	3.09	3.14	3.05	3.22	3.04	3.02	3	3.12	2.78	3.03
D _{V,50} (μm)	6.59	6.27	6.74	6.52	7.53	6.22	5.84	5.8	6.12	6.03	7.15
D _{V,50} st.dev. (μm)	–	0.17	0.19	0.12	–	0.18	0.09	0.15	–	–	–
D _{V,90} (μm)	17.78	16.08	18.08	16.71	19.5	15.95	13.74	14.15	14.56	13.52	14.09
Log-normal distribution parameters a ₂ , a ₃ , a ₄	1.08402, 1.74506, 0.71937	1.08446, 1.72098, 0.70602	1.08273, 1.78901, 0.74361	1.07873, 1.74996, 0.74785	1.08192, 1.92377, 0.79304	1.08191, 1.70306, 0.71071	1.08535, 1.62847, 0.65976	1.08329, 1.62282, 0.67139	1.08816, 1.6958, 0.68193	1.07369, 1.69518, 0.74402	1.07643, 1.84745, 0.78458
SSE	0.00683	0.00439	0.00439	0.00473	0.00627	0.00379	0.00526	0.00567	0.00723	0.00569	0.00617
RMSE	0.01509	0.01153	0.01172	0.01216	0.0147	0.01164	0.01347	0.01331	0.01856	0.01573	0.01638
Weight of deposits											
Upstream (mg)	0.1	1.0	62.0	143.6	187.6	148.9	174.8	231.2	168.0	279.0	231.1
Downstream (mg)	77.7	88.0	36.8	41.5	40.0	21.0	22.7	25.4	22.0	33.0	34.5
Deposition rates											
Upstream deposition rate from A.B.* (mg/hr)	0.13	1.0	136.3	374.3	562.8	893.4	1045.3	1387.2	1008	1116	924.4
Downstream deposition rate from A.B. (mg/hr)	103	88.0	80.9	108.2	120	126	135.7	152.4	132	132	138
k upstream (m/hr)	0.01	0.05	7.39	18.69	27.2	37.1	48.18	62.33	54.6	57.5	51.6
k downstream (m/hr)	6.01	4.46	4.39	5.40	5.81	5.23	6.26	6.85	7.15	6.80	7.70
E upstream	0	0	0.0032	0.0069	0.0087	0.0105	0.0117	0.0137	0.0108	0.0113	0.0101
E downstream	0.00381	0.00225	0.00190	0.00200	0.00185	0.00148	0.00152	0.00151	0.00141	0.00133	0.00150
k upstream (m/hr)	0.01	0.08	10.61	35.79	37.89	86.42	111.2	138.3	98.1	187.3	104.4
k downstream (m/hr)	8.50	6.88	6.30	10.34	8.08	12.18	14.45	15.19	12.85	22.16	15.59
E upstream	0	0	0.0046	0.0133	0.0121	0.0244	0.0270	0.0304	0.0193	0.0367	0.0204
E downstream	0.00539	0.00347	0.00273	0.00383	0.00258	0.00345	0.00351	0.00334	0.00253	0.00434	0.00304

Table E.2 Summary results for the effect of velocity, triethylene glycol, Hot Unit nozzle, Setup #2

Run	55	54	48	46	47	50	49	52	51	56	53	57	58	59
Run time (min)	120	130	120	120	120	120	120	150	123	120	120	40	40	40
Air and liquid settings														
Rotameter 1	11/5	21/15 .5	34/41	44/67	44/67	44/67	44/67	44/67	44/67	44/67	44/67	43/67	44/67	44/67
Rotameter 2	0/0	0/0	0/0	0/0	0/0	0/0	0.9/3. 5	1.32/ 5.5	1.7/7	1.98/ 9	2.28/ 10.5	2.72/ 15	2.92/ 17.5	3.25/ 22
Rotameter 3	0/0	0/0	0/0	0/0	25/0	47/0	0/0	0/0	0/0	0/0	0/0	0/0	0/0	0/0
Pump setting	6	6	6	6	6	6	6	6	6	6	6	6	6	6
Velocity														
Air to nozzle (m/s)	0.05	0.10	0.20	0.30	0.30	0.30	0.30	0.30	0.30	0.30	0.30	0.30	0.30	0.30
Secondary air (m/s)	0.00	0.00	0.00	0.00	0.10	0.20	0.30	0.40	0.50	0.60	0.70	0.90	1.00	1.10
Total air (m/s)	0.05	0.10	0.20	0.30	0.40	0.50	0.60	0.70	0.80	0.90	1.00	1.20	1.30	1.40
Liquid														
Liquid flow rate (g/min)	19	19	19	19	19	19	19	19	19	19	19	19	19	19
Liquid flow rate to aerosol (g/min)	0.131	0.281	0.451	0.484	0.679	0.834	1.188	1.452	1.661	1.80	1.98	2.586	3.043	3.504
Aerosol conc. from washdown (g/m ³)	9.57	10.27	8.24	5.99	6.2	6.1	7.24	7.58	7.59	7.155	7.24	7.876	8.55	8.54
Aerosol conc. from shadowgraphy (g/m ³)	9.68	10.16	5.75	4.95	6.94	6.96	8	6.93	8.27	6.23	7.99	6.36	7.72	7.62
Aerosol shadowgraphy														
Number of 260 image samples	5	5	5	5	5	5	5	5	5	5	5	5	5	5
Uncorrected														
Number of droplets	14256	2317 2	1960 9	1803 1	1634 6	1584 4	1876 8	1757 0	1823 5	1502 6	1751 3	1405 7	1679 6	1585 3
D _{min} (μm)	0.9	0.73	0.73	0.76	0.81	0.73	0.91	0.92	0.81	0.91	0.72	0.73	0.94	0.81
D _{V,10} (μm)	4.39	3.35	3.18	3.22	3.29	3.3	3.28	3.21	3.38	3.25	3.37	3.4	3.36	3.45
D _{V,50} (μm)	12.06	7.79	6.7	6.67	7.21	7.15	7.1	6.6	7.78	7.33	7.73	8.09	7.4	8.21
D _{V,50} st.dev. (μm)	0.58	0.47	0.17	0.145	0.199	0.368	0.291	0.218	0.508	0.273	0.237	0.304	0.406	0.439
D _{V,90} (μm)	24.37	20.66	16.9	14.94	15.31	17.09	16.32	15.55	18.14	16.35	16.8	17.48	16.46	18.37
D _{max} (μm)	34	31	27	22	22	23	24	23	37	27	24	25	26	27
Log-normal distribution parameters	0.7259 9, 2.4818	1.088 09, 1.955	1.087 44, 1.803	1.092 97, 1.797	1.093 19, 1.893	1.091 2, 1.874	1.090 49, 1.863	1.090 52, 1.780	1.090 51, 1.935	1.088 68, 1.888	1.092 81, 1.951	1.092 58, 2.006	1.095 21, 1.906	1.094 65, 2.009
a ₂ , a ₃ , a ₄	7, 0.7820 4	84, 0.783 88	08, 0.721 67	16, 0.691 94	61, 0.718 55	31, 0.742 61	7, 0.739 08	03, 0.706 26	18, 0.769 78	23, 0.737 15	84, 0.76 237	23, 0.764 67	33, 0.731 74	22, 0.772 46
SSE	0.0023 2	0.003 58	0.004 11	0.003 7	0.002 94	0.006 11	0.005 18	0.006 98	0.005 92	0.003 57	0.005 48	0.002 41	0.004 26	0.004 0
RMSE	0.0082 7	0.010 74	0.012 33	0.012 96	0.011 56	0.016 3	0.014 69	0.017 43	0.012 65	0.011 5	0.015 11	0.009 83	0.012 81	0.012 17
Corrected														
Number of droplets	129454	2101 95	1605 59	1165 08	1073 71	1049 35	1320 10	1173 71	1944 19	1206 43	1214 48	1032 21	1238 80	1215 01
D _{V,10} (μm)	3.23	2.76	2.59	2.7	2.72	2.89	2.8	2.75	2.98	2.65	2.97	2.78	2.92	3
D _{V,50} (μm)	7.16	5.18	4.87	4.92	5.2	5.03	4.97	4.78	5.11	5.09	5.22	5.41	5.19	5.4
D _{V,50} st.dev. (μm)	0.17	0.105	0.07	0.064	0.11	0.12	0.06	0.091	0.135	0.064	0.051	0.143	0.096	0.136
D _{V,90} (μm)	19.22	13.1	11.49	10.76	11.73	12.46	12.03	11.45	13.33	11.48	13.24	12.94	12.26	13.41
Log-normal distribution parameters	1.0863 1, 1.8593	1.082 55, 1.469	1.079 9, 1.407	1.084 36, 1.427	1.081 47, 1.490	1.088 57, 1.436	1.086 3, 1.435	1.087 27, 1.388	1.089 81, 1.458	1.079 04, 1.457	1.087 55, 1.484	1.080 56, 1.532	1.088 37, 1.479	1.087 02, 1.525
a ₂ , a ₃ , a ₄	0.7534 1	89, 0.606 27	05, 0.587 16	8, 0.576 65	38, 0.617 05	54, 0.563 89	11, 0.572 69	1, 0.546 3	37, 0.568 03	06, 0.621 95	15, 0.592 44	19, 0.645 38	86, 0.584 25	3, 0.613 63
SSE	0.0031 5	0.006 08	0.005 96	0.006 51	0.005 35	0.011 04	0.008 77	0.011 22	0.010 06	0.006 58	0.010 24	0.005 15	0.007 25	0.008 12
RMSE	0.0096 2	0.014	0.014 85	0.017 21	0.015 6	0.021 91	0.019 12	0.022 08	0.016 49	0.015 61	0.020 66	0.014 35	0.016 7	0.017 34

Run	55	54	48	46	47	50	49	52	51	56	53	57	58	59
Coupon deposits														
Upstream, corrected														
Number of 30 image samples	0	0	0	0	0	0	0	4	4	4	4	0	0	0
Number of droplets	-	-	-	-	-	-	-	8790	2453	2829	7052	-	-	-
D_{min} (μm)	-	-	-	-	-	-	-	1	1.78	1	0.94	-	-	-
$D_{min,inertial}$ (μm)	-	-	-	-	-	-	-	-	-	-	-	-	-	-
$D_{V,10}$ (μm)	-	-	-	-	-	-	-	48.57	44.02	41.2	41.37	-	-	-
$D_{V,50}$ (μm)	-	-	-	-	-	-	-	71.9	72.59	68.8	84.28	-	-	-
$D_{V,90}$ (μm)	-	-	-	-	-	-	-	106.1	108.6	119.9	132.5	-	-	-
D_{max} (μm)	-	-	-	-	-	-	-	144	138	131	150	-	-	-
Log-normal distribution parameters a_2, a_3, a_4	-	-	-	-	-	-	-	3.325	-	2.990	-	-	-	-
								17,	14.10	27,	85.36			
								4.232	942,	4.211	634,			
								76,	4.471	14,	5.157			
								0.299	61,	0.413	49,			
								77	0.310	03	0.233			
									5		18			
SSE	-	-	-	-	-	-	-	0.004	0.006	0.002	0.002	-	-	-
								25	44	92	27			
RMSE	-	-	-	-	-	-	-	0.005	0.006	0.004	0.003	-	-	-
								43	83	72	89			
Downstream, corrected														
Number of 30 image samples	4	4	4	4	4	4	4	4	4	4	4	4	4	4
Number of droplets	7861	6081	3500	4341	3921	3900	2828	1454	1329	3404	1324	2350	5473	1957
	0	4	5	3	9	9	2	92	886	8	43	8	4	6
D_{min} (μm)	0.56	0.37	0.56	0.56	0.67	0.42	0.56	0.53	0.56	0.67	0.42	0.67	0.67	0.53
$D_{V,10}$ (μm)	5.74	5.12	4.54	3.15	3.45	3.47	3.84	3.07	3.3	4.01	4.01	5.11	4.04	4.98
$D_{V,50}$ (μm)	14.55	12.74	11.04	8.42	9.18	8.1	9.1	7.93	8.22	9.67	9.95	11.12	9.67	9.66
$D_{V,90}$ (μm)	28.7	25.49	20.74	15.94	18.28	15.31	16.66	16.41	18.82	18.76	19.49	18.97	19.33	17.11
D_{max} (μm)	46	37	32	34	30	28	29	31	37	33	35	32	38	33
Log-normal distribution parameters a_2, a_3, a_4	-	-	-	-	-	-	-	-	-	-	-	-	-	-
	4.762	2.717	6.657	6.133	4.189	2.335	6.233	1.762	3.195	4.684	3.832	12.95	5.841	4.331
	39,	66,	09,	36,	25,	43,	66,	16,	7,	68,	99,	815,	46,	5,
	2.993	2.780	2.904	2.696	2.619	2.388	2.754	2.320	2.455	2.693	2.656	3.193	2.765	2.671
	04,	91,	8,	29,	81,	34,	55,	35,	93,	31,	28,	8,	34,	83,
	0.463	0.508	0.348	0.338	0.411	0.427	0.317	0.506	0.408	0.377	0.423	0.219	0.337	0.302
	37	27	3	06	5	18	42	21	17	41	26	54	04	65
SSE	0.001	0.000	0.000	0.001	0.002	0.001	0.001	0.000	0.002	0.000	0.000	0.001	0.001	0.000
	21	74	99	42	12	01	5	42	28	67	35	14	11	64
RMSE	0.005	0.004	0.005	0.006	0.008	0.006	0.007	0.003	0.007	0.004	0.003	0.005	0.005	0.004
	12	48	57	46	41		18	66	85	52	18	96	41	41
Weight of deposits														
Upstream (mg)	0	0	0	0	0	0	1.2	14.0	28.2	59.3	308.5	484.5	2493	5103
													*	
Downstream (mg)	102.4	158.2	100.8	66.5	66.6	61.1	69.0	95.0	87.6	90.5	120.7	47.9-	70.5-	88.2-
												2.5	5.7	5.6
Deposition rates														
Upstream deposition rate from A.B. (mg/hr)	0	0	0	0	0	0	0.6	5.6	13.8	29.65	123.4	726.7	3740	7650
												5		
Downstream deposition rate from A.B. (mg/hr)	51.2	72.9	50.04	33.25	33.3	30.55	34.5	38	42.73	45.25	48.28	68.11	97.2	123.9
Deposition coefficients from washdown concentration														
k upstream (m/hr)	0	0	0	0	0	0	0.04	0.36	0.90	2.04	8.41	45.53	215.8	441.9
k downstream (m/hr)	2.64	3.50	2.99	2.78	2.65	2.47	2.35	2.47	2.78	3.12	3.29	4.27	5.61	7.16
Capture efficiencies from washdown concentration														
E upstream	0	0	0	0	0	0	0.000	0.000	0.000	0.000	0.002	0.010	0.046	0.081
							0189	145	311	63	34	5	1	8
E downstream	0.014	0.009	0.004	0.002	0.001	0.001	0.001	0.000	0.000	0.000	0.000	0.000	0.001	0.001
	6	73	15	57	84	37	09	981	965	962	914	988	19	33

* calculated from the load cell data

Table E.3 Summary results for the effect of droplet size distribution, triethylene glycol, Cold Unit nozzle, Setup #1

Run	23	24	25	31	26	33	28	29	30
Run time (min)	123	76.4	60	20	15	10	13	11	10
Air and liquid settings									
Rotameter 1	96/33	95/33	91.5/37	91/37	90/38	88/39	89.5/40	88.7/39.8	89/40
Rotameter 2	2.02/6.5	2.02/6.5	2.03/6.4	1.98/7.2	2.02/6.2	1.98/7.1	2/6.2	2.01/6.2	2.02/6.2
Rotameter 3	0/0	0/0	0/0	0/0	0/0	0/0	0/0	0/0	0/0
Pump setting	5.5	6	7	7.33	8	9	10	12	14
Velocity									
Air to nozzle (m/s)	0.433	0.431	0.419	0.434	0.434	0.430	0.440	0.436	0.438
Secondary air (m/s)	0.577	0.573	0.579	0.577	0.573	0.576	0.568	0.571	0.573
Total air (m/s)	1.01	1.00	1.00	1.01	1.01	1.01	1.01	1.01	1.01
Liquid									
Liquid flow rate (g/min)	7.2	20.3	46.4	54.1	72	94	92	95	95
Liquid flow rate to aerosol (g/min)	0.60	2.34	4.08	3.14	7.61	4.65	2.81	2.87	3.14
Aerosol concentration from washdown (g/m ³)	2.18	8.52	14.94	11.36	27.61	16.91	10.18	10.41	11.36
Aerosol concentration from shadowgraphy (g/m ³)	1.09	2.93	5.76	5.15	4.8	5.59	5.66	6.13	5.54
Aerosol shadowgraphy									
Number of 260 image samples	1	1	3	1	1	10	1	1	1
Uncorrected									
Number of droplets	685	1438	6568	1882	1810	18521	1732	1815	1733
D _{min} (μm)	0.99	0.91	0.94	0.97	0.87	0.79	0.99	0.99	1.05
D _{v,10} (μm)	2.81	3.2	3.7	3.83	3.79	4.04	4.32	4.29	4.13
D _{v,50} (μm)	4.76	6.32	9.18	9.6	10.37	10.87	12.04	10.93	10.95
D _{v,50} st.dev. (μm)	-	-	-	-	-	-	-	-	-
D _{v,90} (μm)	8.64	17.04	19.43	24.23	34.31	24.2	22.27	23.54	21.97
D _{max} (μm)	10	19	28	26	35	42	25	26	28
Log-normal distribution parameters a ₂ , a ₃ , a ₄	1.0948, 1.44027, 0.52844	1.09277, 1.75241, 0.68363	1.09006, 2.15188, 0.76024	1.0978, 2.22714, 0.7864	1.0941, 2.27518, 0.85806	1.10066, 2.33014, 0.82339	-0.47964, 2.56818, 0.65273	0.89148, 2.42341, 0.76659	0.3632, 2.44412, 0.71741
SSE	0.00846	0.01346	0.00409	0.00814	0.03168	0.00259	0.00931	0.00786	0.00654
RMSE	0.02908	0.02662	0.01209	0.01769	0.03009	0.00785	0.0193	0.01738	0.01528
Corrected									
Number of droplets	2093	8001	52113	13820	18045	213365	11796	12456	13003
D _{v,10} (μm)	2.45	2.71	2.96	2.97	2.97	3.12	3.18	3.27	3.19
D _{v,50} (μm)	3.93	4.87	5.96	6.25	6.05	6.5	7.14	7.11	6.86
D _{v,50} st.dev. (μm)	-	-	n/a	-	-	n/a	-	-	-
D _{v,90} (μm)	7.31	11.36	13.77	15.37	14.72	17.41	17.61	17.5	17.2
Log-normal distribution parameters a ₂ , a ₃ , a ₄	1.08832, 1.2311, 0.45211	1.08723, 1.40511, 0.54452	1.08264, 1.66709, 0.68653	1.08097, 1.71144, 0.70952	1.0804, 1.66653, 0.70145	1.10066, 2.33014, 0.82339	1.08339, 1.87036, 0.7667	1.09103, 1.83889, 0.72186	1.08652, 1.80964, 0.73229
SSE	0.00757	0.00958	0.00291	0.0028	0.00781	0.00259	0.00627	0.0048	0.00527
RMSE	0.02751	0.02245	0.01019	0.01039	0.01494	0.00785	0.01584	0.01359	0.01372
Coupon deposits									
Weight of deposits									
Upstream (mg)	25.2	67	273.8	154.6	159.6	207.7	277.5	231.2	230.5
Downstream (mg)	21.5	40.6	73.1	31.5	24.9	22.9	24.4	22.0	20.0
Deposition rates									
Upstream deposition rate from A.B. (mg/hr)	12.29	52.60	273.8	463.8	638.4	1246	1281	1261	1383
Downstream deposition rate from A.B. (mg/hr)	10.5	31.9	73.1	94.5	100	137	113	120	120
Deposition coefficients from washdown concentration									
k upstream (m/hr)	2.8	3.1	9.0	20.1	11.4	36.4	62.1	59.8	60.0
k downstream (m/hr)	2.37	1.85	2.41	4.10	1.78	4.01	5.46	5.69	5.21
Capture efficiencies from washdown concentration									
E upstream	0.0008	0.0008	0.0025	0.0055	0.0031	0.0101	0.0171	0.0165	0.0165
E downstream	0.00065	0.00051	0.00067	0.00113	0.00049	0.00111	0.00150	0.00157	0.00143

Table E.4 Deposition coefficients for the downstream side, m/hr

D_p (μm)	Run	55	54	48	46	47	50	49	52	51	56	53	57	58	59
	U (m/s)	0.05	0.1	0.2	0.3	0.4	0.5	0.6	0.7	0.8	0.9	1	1.2	1.3	1.5
2	1.09	1.08	1.17	1.35	3.50	2.35	2.65	2.06	3.67	4.00	1.63	2.68	1.57	4.71	1.62
3	1.94	0.48	0.43	0.43	0.89	0.78	0.77	0.55	0.87	1.00	0.65	0.77	0.63	1.28	0.84
4	3.04	0.51	0.51	0.49	0.88	0.81	0.83	0.59	0.85	0.98	0.76	0.81	0.75	1.34	1.27
5	4.37	0.65	0.75	0.74	1.17	1.07	1.14	0.85	1.12	1.29	1.10	1.10	1.13	1.88	2.21
6	5.95	0.86	1.16	1.19	1.68	1.49	1.64	1.30	1.57	1.79	1.64	1.60	1.79	2.81	3.74
7	7.78	1.13	1.76	1.89	2.41	2.07	2.32	1.96	2.22	2.48	2.40	2.31	2.79	4.17	5.95
8	9.84	1.47	2.61	2.92	3.38	2.80	3.19	2.87	3.10	3.37	3.40	3.26	4.18	6.03	8.83
9	12.15	1.86	3.77	4.38	4.60	3.68	4.25	4.05	4.24	4.43	4.63	4.48	6.02	8.43	12.29
10	14.70	2.31	5.29	6.33	6.06	4.72	5.48	5.50	5.66	5.68	6.10	5.99	8.30	11.38	16.16
11	17.50	2.80	7.24	8.85	7.75	5.88	6.89	7.20	7.42	7.08	7.79	7.80	10.97	14.86	20.19
12	20.53	3.34	9.65	12.00	9.63	7.16	8.44	9.14	9.52	8.62	9.65	9.90	13.94	18.84	24.16
13	23.81	3.91	12.61	15.81	11.67	8.54	10.12	11.26	12.02	10.27	11.67	12.30	17.08	23.22	27.84
14	27.34	4.50	16.15	20.31	13.81	10.00	11.90	13.50	14.93	12.01	13.78	14.99	20.23	27.93	31.05
15	31.10	5.12	20.33	25.49	16.02	11.50	13.76	15.80	18.28	13.81	15.96	17.93	23.25	32.85	33.66
16	35.11	5.74	25.20	31.33	18.22	13.04	15.68	18.11	22.09	15.64	18.15	21.12	25.97	37.87	35.60
17	39.36	6.37	30.81	37.78	20.39	14.58	17.64	20.36	26.40	17.48	20.32	24.52	28.28	42.89	36.85
18	43.86	7.00	37.20	44.77	22.47	16.11	19.61	22.49	31.22	19.30	22.42	28.11	30.08	47.79	37.42
19	48.60	7.61	44.41	52.24	24.42	17.60	21.58	24.46	36.57	21.09	24.43	31.85	31.32	52.49	37.37
20	53.58	8.22	52.47	60.10	26.22	19.05	23.52	26.23	42.48	22.82	26.32	35.71	31.97	56.90	36.77
21	58.80	8.80	61.42	68.24	27.83	20.44	25.43	27.78	48.95	24.49	28.07	39.67	32.06	60.95	35.71
22	64.27	9.37	71.28	76.59	29.25	21.76	27.29	29.08	56.00	26.07	29.65	43.68	31.62	64.60	34.29
23	69.98	9.90	82.08	85.03			29.08	30.13	63.65	27.56	31.06	47.74	30.72	67.80	32.58
24	75.93	10.41	93.83	93.47			36.28	30.92		28.95	32.30	51.79	29.43	70.53	30.68
25	82.13	10.89	106.56	101.83			38.58			30.23	33.35		27.84	72.78	28.65
26	88.57	11.34	120.27	110.00						31.41	34.22			74.55	26.56
27	95.25	11.75	134.99	117.93						32.48	34.92				24.46
28	102.18	12.13	150.72							33.43					
29	109.34	12.48	167.46							34.28					
30	194.39	12.79	185.21							35.02					
31		13.07	203.99							35.65					
32		13.31	62.18							36.18					
33		13.53	66.13							36.61					
34		13.71								36.95					
35										37.20					
36										37.37					
37										37.46					

Table E.5 Weight of deposits (± 0.1 mg) at the end of experiment, $m(\tau_i)$, mg

Time, τ_i (sec)	0.7 m/s						1.0 m/s					
	Downstream			Upstream			Downstream			Upstream		
	Glass	St.steel	Teflon	Glass	St.steel	Teflon	Glass	St.steel	Teflon	Glass	St.steel	Teflon
30	0.8	0.4	0.7	1.3	1.3	1.5	0.7	0.6	1.2	2.1	2.2	2.7
60	1.8	1.4	2.1	2.1	2.3	2.8	1.2	1.3	1.8	3.6	3.6	4.1
90	2.2	2.4	2.6	3.9	2.9	4	1.4	1.4	2.8	6.4	6.2	8.8
120	2.9	2.5	2.9	5.1	5.4	5.8	2.2	2	3.4	8.3	8.9	9.5
180	4.2	4.5	4.2	7.9	7.6	8.2	3.2	2.9	4.1	12.4	11.5	13.1
300	5.6	7	7.5	14.4	13.1	12.2	4.6	6	6.5	18.9	18.8	20.1

Table E.6 Experimental integral deposition rates, $r_{d,i}^{\text{exp}}$, mg/hr

Time, τ_i (sec)	0.7 m/s						1.0 m/s					
	Downstream			Upstream			Downstream			Upstream		
	Glass	St.steel	Teflon	Glass	St.steel	Teflon	Glass	St.steel	Teflon	Glass	St.steel	Teflon
30	96	48	84	156	156	180	84	72	144	252	264	324
60	108	84	126	126	138	168	72	78	108	216	216	246
90	88	96	104	156	116	160	56	56	112	256	248	352
120	87	75	87	153	162	174	66	60	102	249	267	285
180	84	90	84	158	152	164	64	58	82	248	230	262
300	67	84	90	172.8	157	146.4	55	72	78	227	226	241

Table E.7 Correction factors (last column) obtained from several Cold Unit runs

Equivalent Hot Unit Run*	Nozzle			Liquid flow to			St. dev. of $D_{V,50,corr}$	Estimated $D_{V,50}$ from the correlation, $D_{V,50,est}$ (μm)	Correction factor, $k = \frac{D_{V,50,corr}}{D_{V,50,est}}$	
	Cold Unit test	air velocity (m/s)	Sec. air velocity (m/s)	Total velocity (m/s)	the nozzle (ml/min)	$D_{V,50}$ (μm)				$D_{V,50,corr}$ (μm)
S-5	T-1	0.162	0.090	0.25	10.9	7.37	5.52	0.26	23.8	0.232
S-17	T-2	0.151	0.099	0.25	10.9	9.02	6.28	0.10	25.3	0.248
S-18	T-3	0.162	0.099	0.26	10.9	7.97	5.87	0.04	23.8	0.247
S-19	T-4	0.162	0.000	0.16	10.9	8.09	5.97	0.07	23.8	0.251
S-20	T-5	0.151	0.050	0.20	10.9	8.36	6.07	0.07	25.3	0.240
S-21	T-6	0.139	0.270	0.41	10.9	9.61	6.52	0.25	26.7	0.244
S-27	T-7	0.151	0.107	0.26	21.5	10.58	6.88	0.15	37.6	0.183
S-34	T-8	0.112	0.847	0.96	21.5	11.31	7.81	0.23	49.8	0.157
S-36	T-9	0.151	0.406	0.56	10.9	7.94	5.97	0.10	25.3	0.236

*Hot Unit run with the same air velocity and liquid flow as used in the Cold unit test

Table E.8 Estimated volume median diameter after evaporation

Run	$D_{V,50,est}$ (μm)	Correction factor, k	$k \cdot D_{V,50,est}$ (μm)	Final $k \cdot D_{V,50,est}$ after evaporation (μm)
5% MEBR CONCENTRATION (effect of temperature)				
S-5	44.8	0.23	10.4	3.30
S-17	47.5	0.25	11.8	3.31
S-18	52.2	0.25	12.9	3.47
S-7	37.9	0.25	9.5	2.46
S-11	40.2	0.25	10.1	2.34
10% MEBR CONCENTRATION (effect of temperature)				
S-14	48.3	0.25	12.1	4.84
S-15	46.5	0.25	11.6	4.08
S-16	44.9	0.25	11.2	3.58
S-13	44.9	0.25	11.2	3.31
S-12	40.5	0.25	10.1	2.61
<i>Effect of velocity</i>				
S-34	75.4	0.16	11.8	4.55
S-35	85.5	0.16	13.7	5.27
S-36	46.9	0.24	11.1	4.25
S-37	35.6	0.26	9.3	3.33

Table E.9 Estimation of deposition rates at high temperature conditions from the deposition coefficients in the Cold Unit

Run	T ($^{\circ}\text{C}$)	Hot Unit dep.rate (mg/hr)	Oil density (g/cm^3)	Gas viscosity (Pa-s)	Aerosol conc. (g/m^3)	$\frac{St_{Hot Unit}}{St_{Cold Unit}}$	Relative change in C.E. due to St number	Relative change in C.E. due to decrease in $D_{V,50}$	Total relative change in C.E., k-values or dep. rates	k-value for $D_{V,50}=5.0$ μm in the Cold Unit, at a given velocity (mg/hr)	Dep. rate from the Cold Unit (mg/hr)	Dep. rate at the Hot Unit (mg/hr)
5% MEBR effect of temperature												
S-5	296	16.15	0.88	2.8E-05	4.47	0.51	0.51	0.9	0.461	2.83	25.64	11.83
S-17	340	4.66	0.88	3E-05	3.14	0.49	0.49	0.9	0.439	2.85	18.12	7.96
S-18	370	2.31	0.88	3E-05	3.14	0.47	0.47	0.9	0.426	2.82	17.94	7.64
S-7	390	3.53	0.88	3.1E-05	2.00	0.46	0.46	0.85	0.395	2.77	11.22	4.43
S-11	425	1.18	0.88	3.2E-05	1.46	0.45	0.45	0.85	0.382	2.77	8.21	3.14
10% MEBR effect of temperature												
S-14	296	23.08	0.89	2.8E-05	9.55	0.52	0.52	1	0.517	2.86	55.27	28.59
S-15	340	13.85	0.89	3E-05	6.54	0.49	0.49	0.95	0.468	2.86	37.91	17.73
S-16	370	7.73	0.89	3E-05	4.45	0.48	0.48	0.9	0.430	2.81	25.39	10.91
S-13	390	4.89	0.89	3.1E-05	3.47	0.47	0.47	0.9	0.421	2.80	19.69	8.30
S-12	425	2.58	0.89	3.2E-05	2.08	0.45	0.45	0.85	0.385	2.77	11.69	4.50
Effect of velocity												
S-19	344	7.02	0.88	3E-05	5.44	0.49	0.49	0.9	0.437	3.26	35.94	15.72
S-20	333	4.15	0.88	2.9E-05	4.63	0.49	0.49	0.9	0.443	2.97	27.90	12.35
S-17	340	4.66	0.88	3E-05	3.14	0.49	0.49	0.9	0.439	2.85	18.12	7.96
S-21	315	1.50	0.88	2.9E-05	2.31	0.50	0.50	0.9	0.451	2.64	12.34	5.57